RAS and STM Investigations of Pentacene Molecules on Metal and Semiconductor Surfaces

Darren Carty (B.Sc.)
School of Physical Sciences
Dublin City University

A thesis submitted to

For the degree of
Doctor of Philosophy

Research Supervisor
Dr. A. A. Cafolla

July 2004

Declaration

I hereby certify that this material, which I now submit for assessment on the programme of study leading to the award of Doctor of Philosophy is entirely my own work and has not been taken from the work of others save and to the extent that such work has not been cited and acknowledged within the text of my own work.

Signed: Karen Canty ID Number: 50161571

Date: 19th July 2004

Contents

Abstract

In this study the electronic surface states and surface reconstructions of an organic molecule on semiconductor and metal surfaces were investigated with Reflectance Anisotropy Spectroscopy (RAS), Scanning Tunnelling Microscopy (STM) and photoemission techniques.

The design, construction and operation of a Reflectance Anisotropy Spectrometer are described in detail. The RAS technique was applied to the investigation of pentacene on the Au(110)-(2×1) surface. It was found that the pentacene molecules adsorbed on this surface shows three observable electronic transitions in the 1.6 eV-5 eV photon energy range. At monolayer coverage there are distinct changes in the RAS spectrum that can be associated with a change in the orientation of the molecule on the gold surface.

STM was applied to the investigation of pentacene adsorbed on the Au(110)-(2×1) and the Ag/Si(111)-(7×7) surface. It was found that on the Au(110)-(2×1) surface, below a monolayer the pentacene molecule adsorbs parallel to and between the Au rows in the $[1\bar{1}0]$ direction. While above a monolayer the molecule changes direction and preferentially adsorbs across the gold rows. This change in orientation accounts for the changes in the RAS spectra above a monolayer. The effect of annealing on the molecular ordering was also studied. These interfaces were also studied by core level and valence band photoemission using a synchrotron light source. Deposition of pentacene on the Ag/Si(111)-($\sqrt{3}\times\sqrt{3}$) surface produced three distinct ordered structures for coverages up to one monolayer. It is concluded from the RAS, STM, synchrotron studies that the molecule lies flat on the Au(110) and Ag/Si(111) surfaces.

Chapter 1 Introduction

About 20 years ago there was a growing interest in what came to be called 'molecular electronics'. The idea in general terms was to create assemblies of molecules to create complex functional units, for example, transistors. Before the advent of STM there was no way to proceed. Indeed, until recently there was not a single organic molecule-silicon surface system well understood. True molecular devices still remain elusive but the collection of knowledge is growing rapidly. Presently we are at the stage of understanding various options for molecular linkages to surfaces.

Presently, there is substantial interest in the growth of organic semiconductors such as pentacene and other acenes with atomic masses above 200amu because of their high mobilities and the potential to employ thin film depositions of these materials to fabricate electronic devices [1]. Room temperature mobilities in the range of $1cm^2/V$ s can be achieved in pentacene thin film transistors [1] making this material a possible alternative to amorphous silicon. The possibility that grain boundaries and other defects formed during growth may limit the mobility has motivated experimental studies of the growth morphology of organics on different surfaces. For the structural optimization of the organic substrate interface a detailed knowledge of the adsorption and ordering of pentacene on different substrate surfaces is essential. The growth of organic films on surfaces is generally controlled by the competition between molecule-substrate and molecule-molecule interactions. On atomically clean silicon surfaces the molecule-substrate interactions are most important, as the molecule is generally chemisorbed to the substrate and unable to diffuse at room temperatures. On metallic surfaces and the surfaces used in the course of this work the molecules are bound to the substrate usually by the weaker van der Waals type interactions. The molecules are able to diffuse at room temperatures. In this case the molecule-molecule interactions are no longer negligible and may influence the molecular arrangement in the film.

In the course of this work reflectance anisotropy spectroscopy (RAS), scanning tunnelling microscopy (STM), photoelectron spectroscopy (PES) and low energy electron diffraction were used to structurally investigate the formation of two interfaces; (i) the Au(110)-(2×1)/pentacene and (ii) the Ag/Si(111)-($\sqrt{3}\times\sqrt{3}$)/pentacene.

Reflectance Anisotropy is a technique that uses polarized light to measure optical properties of a surface. Since its original inception by Aspnes et. al. [2] in 1985, RAS has become a significant surface science technique. The original design has been improved upon over the years by Aspnes et. al, Berkovits et. al. [3] and Luo et. al. [4] making it possible to perform qualitative experiments.

Since Aspnes [2] pioneering work there have been many experiments performed using the RAS technique. For example Zettler et. al. [5] employed RAS as a growth sensor for real time monitoring of Metal Oxide Vapour Phase Epitaxy (MOVPE) device growth on III/V semiconductors. Sobiesierski et. al. [6] measured the RAS response to MBE evaporation rates *in-situ*. Frederick et. al. [7] determined the azimuthal orientation of an organic molecule on a metal surface using RAS. Sheridan et. al. [8] applied RAS to a solid-liquid interface and presented results for the Au(110)/0.1M H_2SO_4 electrolyte interface. The diversity of these experiments performed indicates the flexibility of this technique to many different environments. The main feature of the RAS is that it can be used *ex-situ* and *in-situ*.

The design, construction and implementation of a RAS spectrometer forms a major part of this work. This RAS spectrometer was used to monitor surface states and interband bulk transitions on a single crystal Au(110)-(2×1) surface. It was also used to study the deposition of pentacene on Au(110)-(2×1). It is shown that RAS can be used to monitor azimuthal molecular alignment changes on the gold surface associated with the optical and vibrational transitions in the pentacene molecule. Scanning Tunnelling Microscopy is used in this work to identify the surface reconstructions of the pentacene molecule on the two substrates at varying pentacene coverages. Photoelectron spectroscopy is used to ascertain the molecular bonding environments and also to detect the orientation of the molecular plane with respect to the substrate. Low energy electron diffraction is used to describe the change in reconstructions with increasing pentacene coverages. These complementary techniques provide structural information on the system being studied.

In Chapter Two, a brief history of the development of RAS with details of current experiments being performed is described. RAS theory is presented in sections 2.1 and 2.2. These sections illustrate how a polarised light beam can be affected by the optical components placed in its path. From this theory two RAS equations are developed one that is theoretical and used for performing model calculations and simulations of RAS spectra, the second equation is in a form suitable for analysis of experimental data. These equations allow surface characteristics to be explored with RAS. The theory of STM is introduced in section 2.3. Growth modes and surface sensitivity suitable for photoelectron experiments are summarised in section 2.4. Photoemission theory is presented in section 2.5. This section describes how the photoemission process works and how a photon of certain energy can eject an electron from an atom. Also briefly discussed is the importance of analysing core levels and

valence bands to obtain information as to the chemical environment of the surface or adsorbate on the surface. LEED theory is described in section 2.6. Diffraction theory and reciprocal space are introduced to help explain the operation of the LEED system. In section 2.7 a brief discussion on group theory is presented. This discussion begins with operator assignments and point group identification. From selection rules associated with the character tables for each point group, electronic energy levels and molecular orientations are investigated. Finally surface and bulk states of the fcc Au(110) surface are presented in section 2.8.

Chapter three describes the four experimental techniques used in the study of pentacene/Au(110) and pentacene/Ag/Si(111)-($\sqrt{3}\times\sqrt{3}$). Several configurations of RAS are presented including common components that are essential for the working of every RAS spectrometer. The design of the RAS spectrometer is discussed in relation to space limitations for the most compact setup of RAS. The components that make up the spectrometer are discussed and requirements for optimum selection of each component are presented. Details of the software are also presented. The calibration, operation and a procedure for performing experiments are outlined. The sequence of operations that the RAS must perform to obtain the real and imaginary signals is also explained. Details of the necessary equipment needed for connecting the RAS spectrometer to a UHV system is described. The experimental details of the Scanning Tunnelling Microscope (STM) and Low Energy Electron Diffraction (LEED) are discussed. A description is also given of this synchrotron-based photoemission technique.

Chapter four describes the deposition of pentacene ($C_{22}H_{14}$) on Au(110) by organic molecular-beam deposition (OMBD) under ultra high vacuum conditions at a base pressure of 1×10^{-10} mbar. In the monolayer regime, three orientations of pentacene exist. These were investigated by scanning tunnelling microscopy (STM) and low energy electron diffraction (LEED). Investigations of the interface at low molecular coverage show that these unique molecular arrangements are a direct consequence of pentacene induced Au(110)-(1×3) missing row reconstruction. Above several monolayers the growth of a highly ordered, multilayer, a π-stacked pentacene film on the Au(110) surface is observed.

Chapter five combines the theory presented in chapter 2 and the construction of the RAS spectrometer in chapter 3 into an experimentally useable technique to measure the RAS response of an organic molecule adsorbed onto a Au(110)-(2×1) surface in situ. The first experiment obtains RAS spectra of the clean surface and interprets the spectra with reference to surface state transitions and interband bulk transitions

introduced in chapter 2. The second experiment is a surface disordering experiment. By annealing an already reconstructed (2×1) surface to increasing temperatures the (2×1) periodicity of the Au(110) surface becomes disordered and a (1×1) reconstruction dominates. The change in reconstruction is detected using RAS. The changes in the RA spectra can be used to distinguish between surface state transitions and interband bulk transitions. In a third experiment surface roughening is introduced by Ar^+ bombarding the Au(110)-(2×1) surface. In this experiment RAS is used distinguish how the surface states and interband bulk transitions are affected by the surface roughening. The fourth experiment is a RAS study of pentacene adsorbed on the Au(110)-(2×1) surface. A brief description of the pentacene absorption spectra and allowed transitions for peak assignments is presented. Results are then presented for the pentacene adsorption on the Au(110)-(2×1) surface. Surface related features in the spectra are correlated to the optical transitions of the pentacene. The surface was then annealed to achieve the long range ordering of the molecule, as was seen using STM in chapter 4.

A scanning tunnelling microscopy study of the ordering of pentacene ($C_{22}H_{14}$) molecules on the Ag/Si(111)-($\sqrt{3}\times\sqrt{3}$)R30° surface at room temperature is presented in chapter six. Three distinct solid phases are observed, S1, S2 and S3 at coverages of ~0.35 monolayer (ML), ~1.0 ML and >1.0 ML respectively. At low coverages it is shown that in the solid phase, S1, the molecules adopt a head-to-head orientation forming a molecular row structure. This phase has a high order commensurate lattice, Ag/Si(111)-(25×25)-pentacene, containing 75 molecules. The structure of this phase is determined from STM measurements at low coverages where it is possible to image both the pentacene molecules and the Ag/Si(111) substrate. Two adsorption sites are identified, a three fold hollow site at the centre of a Ag trimer (CA-site) and a six-fold hollow site at the centre of the hexagonal arrangement of silver atoms (CB-site). In the second phase occurring at a pentacene coverage of ~1ML, the molecules adsorb between the rows to adopt a close packed side-by-side orientation, which is mediated by the van der Waals interaction. This reconstruction forms a new commensurate structure Ag/Si(111)-(2×3)-pentacene, containing two pentacene molecules per unit cell. Low energy electron diffraction patterns were not obtainable for this system, therefore the structure of the second phase is determined by using the bias voltage as a tuneable parameter to focus on either the molecular film or the on the substrate. In this phase adsorption takes place exclusively on the Ag trimer (CA-site) and the CB-site is lost due to strong lateral molecule-molecule interactions. The third phase occurring at pentacene coverages >1.0 ML leads to a molecular reorganization and a higher molecular density

than the second phase, which can be interpretated in two ways. The first interpretation is a tilting of the pentacene molecules from a planer to an upright configuration with increasing pentacene deposition. The second interpretation is that the tilting of the pentacene molecules it is due to a STM tip induced effect.

Chapter 1 References

[1] C.D. Dimitrakopulos, J. of Appl. Phys., 80, (1996), 2501

[2] D.E. Aspnes, J. Vac. Sci. Technol. B3 (5), (1985) 1498 and D.E. Aspnes, J.P. Harbison, A.A. Studna, L.T. Florez, J. Vac. Sci. Technol. A6 (1988) 1327.

[3] V.L. Berkovitz, I.V. Makarenko, T.A. Minishvili, V.I. Safarov, Solid State Comms. 56 (1985) 449.

[4] J.S. Luo, J.M. Olson, K.A. Bertness, M.E. Raikh, E.V. Tsiper, J. Vac. Sci. Technol., B 12(4), (1994), 2552.

[5] J-T. Zettler, K. Haberland, M.Zorn, M.Pristovsek, W.Richter, P.Kurpas, M.Weyers, J. of Crys. Growth, 195 (1998) 151.

[6] Z. Sobiesierski, D.I. Westwood, Thin Solid Films, 318 (1998) 140.

[7] B.G. Frederick, J.R. Power, R.J. Cole, C.C. Perry, Q. Chen, S. Haq, Th. Bertrams, N.V. Richardson, P. Weightman, Phys. Rev. Lett. 80(20), (1998) 4490.

[8] B. Sheridan, D.S. Martin, J.R. Power, S.D. Barret, C.I. Smith, C.A. Lucas, R.J. Nichols, P. Weightman, Phys. Rev. Lett. 85 (2000) 4618.

2.1 Reflectance Anisotropy Spectroscopy (RAS)

Many surface analysis techniques exist but the majority of these are non-optical methods, for example Reflection High Energy Electron Diffraction (RHEED), Low Energy Electron Diffraction (LEED), Auger Electron Spectroscopy (AES), Scanning Tunnelling Microscopy (STM) and Ultraviolet Photoelectron Spectroscopy (UPS). These non-optical techniques employ charged particle beams to probe the surface, which can result in damage to the surface or the adsorbed layer, especially adsorbed organic overlayers.

The study of a surface using optical techniques offers several advantages over conventional non-optical techniques.

1. The material damage and contamination associated with charged particle beams are eliminated.
2. All pressure ranges are accessible, even ex-situ and liquid measurements are possible.
3. Buried interfaces are accessible owing to the relatively large penetration depth of the optical radiation.
4. Insulators can be studied without the problem of charging effects.

Reflectance Anisotropy Spectroscopy (RAS) is an optical technique that employs photons to act as both probe and signal for passive analysis of a surface. The penetration depth [1] of optical radiation into condensed matter is large. However, with an understanding of the physics of the optical response (section 2.1.3) and advances in instrumentation (chapter 3), the surface contribution can be identified and enhanced. Most important of all has been the recognition that symmetry differences between the bulk and surface interfaces can be exploited [1].

The theory and experimental setup for Ellipsometry and RAS are very similar. In this section the theoretical aspects of ellipsometry are explained. It is then shown how this theory relates to RAS.

2.1.1 Matter & Light

The interaction of electromagnetic radiation with a material is called the "optical response" of the material. Information about the surface can be obtained by analysing the properties of the light after an interaction has taken place. In general, when a surface is subjected to an electromagnetic wave, the internal charge distribution is distorted under its influence. This corresponds to the generation of electric dipole moment within the material, which in turn contributes to the total internal field. More simply stated, the

external field separates positive and negative charges in the surface. The resultant dipole moment per unit volume is called the electric polarization, **P**. The interaction of an electromagnetic wave of optical frequency, ω, and wave vector, **k**, with condensed matter, is described in terms of a general polarisation amplitude, **P**(**k**,ω, 2ω, ….), induced by the field of amplitude **E**(**k**, ω) [1] :

$$\mathbf{P}(\mathbf{k}, \omega, 2\omega, \ldots.) = \varepsilon_0[\, \chi^{(1)}(\mathbf{k}, \omega) \,.\, \mathbf{E}(\mathbf{k}, \omega) + \chi^{(2)}(\mathbf{k}, \omega, 2\omega) : \mathbf{E}^2(\mathbf{k}, \omega) + \ldots\ldots\ldots\ldots] \tag{2.1}$$

where $\chi^{(i)}$ is the i^{th} order dielectric susceptibility tensor, which describes the material's tendency to polarise in, or its degree of reaction to, an electromagnetic field [1]. In general, the susceptibility tensor would show both frequency and spatial dispersion [1].

In an anisotropic, linear medium, the dielectric tensor, ε, is related to the susceptibility by

$$\varepsilon = \varepsilon_0 (\mathbf{1} + \chi^{(1)}) \tag{2.2}$$

where **1** is the unit tensor.

There are also higher harmonics present in the polarisation field. These are caused by lattice imperfections and other symmetry disruptions that distort it, and are represented in equation 2.2 by χ^n, where $n > 1$, resulting in harmonics of nω [1]. These non-linear terms may become significant at high EM field strengths. RAS is a linear technique, and therefore is only concerned with $\chi^{(1)}$. Normally $\chi^{(1)} >> \chi^n$ for $n > 1$ and the higher harmonics can be ignored.

2.1.2 Null Ellipsometry

Ellipsometry can be defined as the measurement of the state of polarisation of a polarised wave vector. A polarised light-wave probe is allowed to interact with the sample under investigation. This interaction changes the state of the polarisation of the reflected wave [2]. The optical properties of a homogenous isotropic medium at any photon energy are determined by two quantities, the real and imaginary parts of the relative dielectric constant. Thus two quantities must be measured to determine the optical properties of a system. This can be done by measuring the two polarisations; one in the plane of incidence (p-polarised) and a second perpendicular to the plane of incidence (s-polarised) at an angle of incidence close to the Brewster angle, usually between 60° and 80°. Ellipsometry studies the ratio of the amplitude of the reflectivities for p and s polarised light $r = r_p / r_s$. This is in general a complex number since there is

a phase shift between the p and s reflected waves. Ellipsometry performed at one angle of incidence yields two quantities from which the surface dielectric constant and other optical properties can be determined [3], [4], [5].

When ellipsometry is performed at normal incidence the plane of incidence is no longer defined. In the following discussion close to normal incidence means any angle of incidence smaller than 5° [2], [5]. The bulk properties of most cubic crystals are isotropic, therefore the amplitude ratios and phase difference of the polarisations perpendicular and parallel to the plane of incidence approach the values of 1 and 0 respectively. When an ellipsometer is operating under these conditions it is called "Absolute Null Ellipsometry" and no signal is detected. If the reconstructed surface is anisotropic the values of the amplitude ratio and the phase difference do not approach the values of 1 and 0 and then a signal that is related to the surface anisotropy can be measured.

The RAS technique exploits symmetry differences to gain information about a surface. Information obtained in this way can be used in the calculation of a surface dielectric response of a material [1].

2.1.3 Reflectance Techniques

RAS measures the difference, in near normal incidence reflectance of linearly polarised light along two orthogonal axes. The geometry of the incident and reflected polarisations are shown in figure 2.1 [1].

P-polarisation describes an electric vector in the plane of incidence (the xz-plane); s-polarisation describes an electric vector perpendicular to the plane of incidence (y-direction). The angle of incidence is ϕ_0. Applying the boundary conditions at the interface yields the well-known Fresnel equations [7] for the complex amplitude of the reflected wave. This is expressed in normalised form as the complex reflection coefficient $r_{12} = E_{12}^r / E_{12}^i$, which is the ratio of reflected to incident electric field amplitude. The reflectance $R_{12}(\omega) = |r_{12}|^2$ is the ratio of the reflected to incident beam intensity [1].

The surface is considered to be an interface between two crystals with dielectric tensor components ε_{ixx}, ε_{iyy} and ε_{izz} (i = 1, 2). ε_{ixx} is the x response of the dielectric tensor to x components of the incident beam in medium i, where i = 1 (surface or thin film) or 2 (substrate or bulk material).

It is useful to divide the surface into a 3 phase system comprising vacuum (medium 0), thin film (medium 1), and substrate (medium 2) [2]. It is assumed that medium 1 is anisotropic and medium 2 is isotropic. For reflection at an interface between medium 1 and medium 2, both the tangential components of the electric and magnetic fields, and the normal components of the electric displacement and magnetic flux density, are required to be continuous across the interface, according to Maxwells' equations.

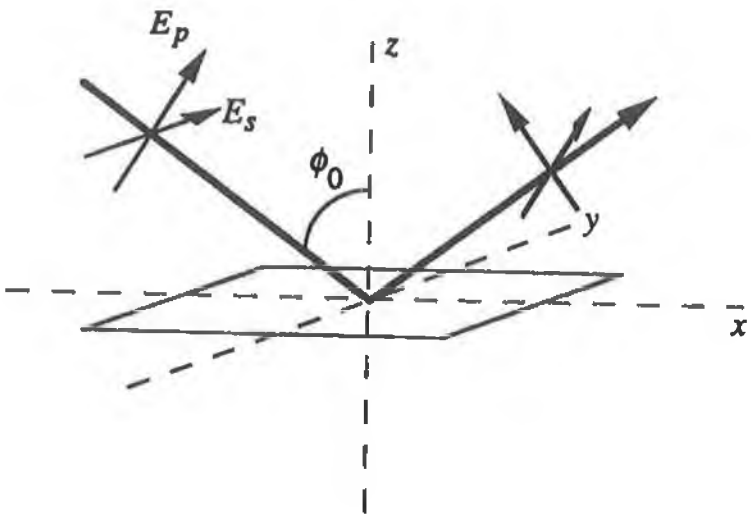

Figure 2.1 *Geometry of incident and reflected polarisations.*

In the three-phase system, where medium 0 is vacuum, d is the depth of the surface reconstruction (medium 1) and λ the wavelength of the incident light, the reflection coefficient is found to be [8]

$$r_{012} = \frac{r_{01} + r_{12}e^{-i2\beta}}{1 + r_{01}r_{12}e^{-i2\beta}} \tag{2.3}$$

where the time dependence of the field is taken as $e^{+i\omega t}$, and β the phase change on a single pass through medium 1, is given by

$$\beta = \frac{2\pi d}{\lambda}\cos\phi_1\sqrt{\varepsilon_{1jj}} \tag{2.4}$$

where j = x, y, depending on the polarisation. When applying equation 2.4 to surfaces the condition $d << \lambda/4\pi\cos\phi_1\sqrt{\varepsilon_{1jj}}$ is always satisfied, which allows the exponential terms in equation 2.3 to be replaced by a first order approximation, $(1 - i2\beta)$ [9]. In addition, if the bulk material is isotropic, then the tensor components are equal along each of the material axes. Thus ε_{2jj} can be replaced by the single component ε_b, the isotropic bulk value [10]. The z-axis of the film is assumed to be perpendicular to the

interface and the x-axis of the film is at an azimuthal angle ψ with respect to the plane of incidence.

RAS is only concerned with the reflectance of p-polarised reflected light resulting from a p-polarised incident beam [11], then the equation obtained is [1]

$$\frac{r_{pp}(\phi_0,\psi)}{r_{pp}^0} = \left[1+\frac{i4\pi d\cos\phi_0}{\lambda(\varepsilon_b-1)(\varepsilon_b\cos^2\phi_0-\sin^2\phi_0)}\left[(\varepsilon_b-\bar{\varepsilon})\varepsilon_b - \left(\left(\frac{\varepsilon_b^2}{\varepsilon_{zz}}\right)-\bar{\varepsilon}\right)\sin^2\phi_0+\Delta\varepsilon(\varepsilon_b-\sin^2\phi_0)\cos 2\psi\right]\right] \quad (2.5)$$

where $\bar{\varepsilon}=\frac{\varepsilon_{xx}+\varepsilon_{yy}}{2}$, $\Delta\varepsilon=\frac{\varepsilon_{yy}-\varepsilon_{xx}}{2}$ and r_{pp}^0 is the complex reflection coefficient of the bulk.

Three general comments can now be made based on above equation [8]

1) The contribution from the interface region depends on the difference between the bulk and the interface dielectric response, or on the interface anisotropy.
2) If $|\varepsilon_{zz}|$ is comparable to in size to $|\varepsilon_b|$, then the main contribution to r_{pp} comes from ε_{xx}. The linear optical response from interfaces is expected to be dominated by ε_{xx} and ε_{yy}. This comes from a continuity condition on the displacement field arising from deriving equation 2.5.
3) At optical wavelengths the contribution from single atomic layers should be detectable as reflectivity changes below 10^{-4} are measurable.

RAS measures the difference between the (near) normal incidence values of r_{pp} for $\phi_0 = 0$, $\psi = 0°$ and $\phi_0 = 0$, $\psi = 90°$ as shown in figure 2.2. The r_{pp}^0 component in equation 2.5 reduces to 1. The equation can then be written as

$$r_{pp}(\phi_0,\psi) = 1+\frac{i4\pi d}{\lambda(\varepsilon_b-1)}[\varepsilon_b-\bar{\varepsilon}+\Delta\varepsilon\cos 2\psi] \quad (2.6)$$

The RAS equation may be defined as [1] (see figure 2.2)

$$\left.\frac{\Delta r}{r}\right|_{RAS} = 2\frac{r_{pp}(0°,90°)-r_{pp}(0°,0°)}{r_{pp}(0°,90°)+r_{pp}(0°,0°)} \quad (2.7)$$

and since

$$r_{pp}(0°,90°) = 1 + \frac{i4\pi d}{\lambda(\varepsilon_b - 1)}\varepsilon_b - \varepsilon_{yy} \tag{2.8}$$

and

$$r_{pp}(0°,0°) = 1 + \frac{i4\pi d}{\lambda(\varepsilon_b - 1)}\varepsilon_b - \varepsilon_{xx} \tag{2.9}$$

then substitution yields the following equation:

$$\frac{\Delta r}{r} = \frac{i4\pi d}{\lambda}\frac{(\varepsilon_{xx} - \varepsilon_{yy})}{(\varepsilon_b - 1)} \tag{2.10}$$

This is a theoretical RAS equation. If calculations of the surface dielectric tensor components or model calculations of RAS spectra are being performed, then equation 2.10 should be used. In section 2.2 a RAS equation relating $\Delta r/r$ to experimentally measured parameters is derived.

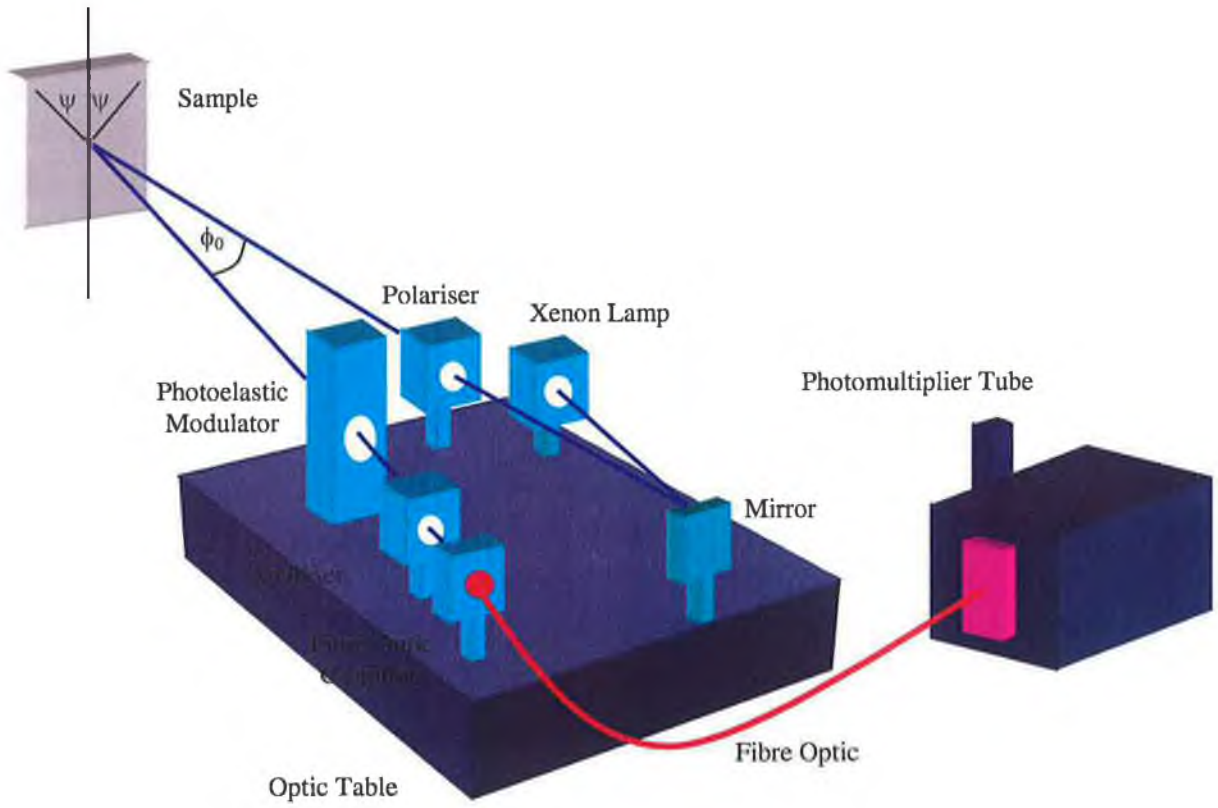

Figure 2.2 *RAS spectrometer layout on Optic Table.*

2.2 Derivation of RAS Equation

The RAS spectrometer operates by measuring the ellipticity of the light after it has been reflected from the surface. The 'tilt' of the polarization ellipse corresponds to the real part of the anisotropy and the width or semi-minor axis of the ellipse corresponds to the imaginary part of the anisotropy [6]. The elliptically polarized light reflected from the sample is directed through a photoelastic modulator where the polarization modulated signal is converted to a phase-modulated signal. The light beam then passes through an analyser where the phase-modulated signal is converted to an intensity-modulated signal, which can be detected and recorded. The layout for the RAS spectrometer is shown in figure 2.2 and will be described in more detail in chapter 3. The real and imaginary parts of the surface anisotropy can be obtained directly from the intensity-modulated signal.

2.2.1 Polarization & Jones Calculus

Jones calculus is a matrix method used to describe the state of polarisation of polarised light beams before and after optical devices are encountered [2], [12]. In this section the basic theory of Jones calculus is described.

If a beam of light is propagating along the z-axis, with electric field components E_x along the x-axis and E_y along the y-axis, it can be represented by the vector

$$\vec{E} = \begin{pmatrix} E_x \\ E_y \end{pmatrix} \tag{2.11}$$

Therefore the standard normalised vectors representing horizontally and vertically polarized light along the z-axis are, respectively

$$\vec{E}_x = \begin{pmatrix} 1 \\ 0 \end{pmatrix} \quad , \quad \vec{E}_y = \begin{pmatrix} 0 \\ 1 \end{pmatrix} \tag{2.12}$$

If a phase difference of 90° between the components of polarization is introduced, a vector representing the electric field of the light is obtained but its direction changes in time so that the tip of the vector maps out a circular path rotating left or right over time. This is called left and right circularly polarized light and it is represented in Jones notation by [12]

$$\vec{E}_{left} = \frac{1}{\sqrt{2}} \begin{pmatrix} 1 \\ -i \end{pmatrix} \qquad \vec{E}_{right} = \frac{1}{\sqrt{2}} \begin{pmatrix} 1 \\ i \end{pmatrix} \tag{2.13}$$

If arbitrary amplitudes and phase differences are introduced between the components of polarization, a vector representing the electric field of the light is obtained but its

direction changes in time so that the tip of the vector maps out an elliptical path over time.

The effect of a transmission or reflection type optical device on a polarised beam can be represented by the product of two Jones Matrices. The optical device influences the polarised beam by either rotating it through an angle α or retarding it by a phase δ or both. For example, if an optical device has rotated the polarisation of the beam by an angle α, then this is represented by a Jones matrix of the form

$$\begin{pmatrix} \cos\alpha & \sin\alpha \\ -\sin\alpha & \cos\alpha \end{pmatrix} \tag{2.14}$$

Therefore the electric field vector $\vec{E}_0$ after encountering an optical device is given by

$$\vec{E}_1 = \begin{pmatrix} \cos\alpha & \sin\alpha \\ -\sin\alpha & \cos\alpha \end{pmatrix} \begin{pmatrix} E_{0x} \\ E_{0y} \end{pmatrix} \tag{2.15}$$

This resultant vector is then used as the initial vector when the light beam encounters another optical device. This method is applied to each of the optical components shown in figure 2.2 to find the final state of polarisation of the light in the RAS spectrometer.

2.2.2 The RAS Signal

To describe the signal that is measured in RAS all optical components of the setup have to be considered. As described earlier and shown in figure 2.2, light passes through a polariser followed by an optical viewport and is then reflected by the sample. On the return path the light passes through the viewport followed by a phase shifting element, the Photoelastic Modulator, and another polariser which functions as the analyzer. The polarization state of the light beam, which enters the monochromator and photomultiplier after passing through all the optical components can be evaluated either graphically or theoretically using the Jones-formalism described in section 2.2.1. In this approach, every optical component is defined by a matrix, which describes the effect of the component. The electric field vector produced after passing through the optical component is then given by the product of that particular matrix with the incident electric field vector:

The basic matrices needed to describe the RAS setup are

$\begin{pmatrix} 1 & 0 \\ 0 & 1 \end{pmatrix}$ optical element which does not have any influence (2.16)

$\begin{pmatrix} 1 & 0 \\ 0 & 0 \end{pmatrix}$ ideal polarizer for the x-plane (2.17)

$\begin{pmatrix} e^{i\varphi} & 0 \\ 0 & 1 \end{pmatrix}$ phase shifting element which retards the phase in x by φ (2.18)

$\begin{pmatrix} r_a & 0 \\ 0 & r_b \end{pmatrix}$ the sample with its reflection coefficients (2.19)

In the RAS experiments, as they were performed in this work, the main crystal directions of the Au(110)-(2×1) sample were found along the $[1\bar{1}0]$ and the [001] directions. If one of these planes is aligned parallel to the polarization plane of the incident light, the anisotropy of the Au(110)-(2×1) surface cannot be detected. Therefore the sample is rotated to $\theta = 45°$ to maximise the sensitivity of RAS to the anisotropy. The matrices for the optical elements are as follows.

$$\vec{E}_{\text{polariser}} = \begin{pmatrix} 1 \\ ia_p - \Delta P \end{pmatrix} \tag{2.20}$$

is the matrix for the polariser, where a_p is a measure of the birefringence in the polarising crystal, and ΔP represents any slight misalignment of the polariser relative to the optical axis.

$$\vec{E}_{\text{window}} = \begin{pmatrix} 1+F_{1c} & F_{1s} \\ F_{1s} & 1+F_{1c} \end{pmatrix} \tag{2.21}$$

is the matrix for the window as light enters the chamber, where $F_{1c} = i\frac{\delta_1}{2}\cos 2\vartheta_1$ and $F_{1s} = i\frac{\delta_1}{2}\sin 2\vartheta_1$. The phase difference between the fast and slow axes is δ_1, and the angle θ_1 is the orientation of the fast and slow axes with the sample axes.

$$\vec{E}_{\text{sample}} = \begin{pmatrix} \bar{r} & \Delta r/2 \\ \Delta r/2 & \bar{r} \end{pmatrix} \tag{2.22}$$

is the matrix for the sample, where $\bar{r} = (r_s + r_p)/2$ and $\Delta r = r_s - r_p$.

$$\vec{E}_{\text{window}} = \begin{pmatrix} 1+F_{2c} & F_{2s} \\ F_{2s} & 1+F_{2c} \end{pmatrix} \tag{2.23}$$

is the matrix for the window as light exits the chamber, where $F_{2c} = i\frac{\delta_2}{2}\cos 2\vartheta_2$ and $F_{2s} = i\frac{\delta_2}{2}\sin 2\vartheta_2$. The phase difference between the fast and slow axes is δ_2, and the angle θ_2 is the orientation of the fast and slow axes with the sample axes.

$$\vec{E}_{PEM} = \begin{pmatrix} e^{i\varphi/2} & \Delta M(e^{i\varphi/2} - e^{-i\varphi/2}) \\ \Delta M(e^{i\varphi/2} - e^{i\varphi/2}) & e^{-i\varphi/2} \end{pmatrix} \tag{2.24}$$

is the matrix for the PEM, where ΔM is included to account for any misalignment between the modulator axis and the optic axis and $\varphi = \delta_m \sin\omega t$, where δ_m is the phase amplitude. For example $\delta_m = \pi$ corresponds to half wave modulation.

$$\vec{E}_{analyser} = \frac{1}{\sqrt{2}} \begin{pmatrix} 1-\Delta A & 1+\Delta A \\ -ia_a & ia_a \end{pmatrix} \tag{2.25}$$

is the matrix element for the analyser, where ΔA is the misalignment of the analyser relative to the optical axis and a_a is a measure of the birefringence in the polarising crystal.

The final equation for the resulting electric field is obtained by taking the product of all the optical components, which gives

$$E_{result} = (\text{Analyser})(\text{PEM})(\text{Window} - \text{Exit})(\text{Sample})(\text{Window} - \text{Entry})(\text{Polariser})E \tag{2.26}$$

The ratio of the change in intensity to the average intensity can then be found according to [6], [13], [14],

$$\frac{\Delta I}{I} = \begin{bmatrix} 2\left(-\text{Im}\left(\frac{\Delta\hat{r}}{\hat{r}}\right) + \delta_1\cos 2\vartheta_1 + \delta_2\cos 2\vartheta_2 - 2a_p\right)J_1(\delta_m)\sin\omega t \\ +2\left(\text{Re}\left(\frac{\Delta\hat{r}}{\hat{r}}\right) + 2\Delta P + 2\Delta M\right)J_2(\delta_m)\cos 2\omega t \end{bmatrix} \tag{2.27}$$

where,

J_1, J_2 are Bessel Functions

Throughout this thesis this result is referred to as **'The RAS Equation'**

The RAS Equation has many important features and useful properties. The normalised, intensity modulated, output signal from the system, ΔI/I, is directly proportional to the real and imaginary parts of the reflectance anisotropy ratio Δr/r. The real and imaginary parts of Δr/r appear in the 2ω and ω frequency components of the signal respectively. Therefore, it is possible to distinguishing between the real and imaginary components.

From the RAS Equation it is clear that there are no contributions from window strain in the real part of the signal. If the sample being examined is in UHV then it is

useful to neglect the imaginary part and concentrate on the real component because there are fewer errors in the setup for the real component.

The imperfections of the polarizer are taken into account in the RAS Equation in the form of first order polariser birefringence a_p. The imperfections of the analyser do not contribute in the equation; therefore if there is a difference in quality between the two polarising crystals it is advantageous to use the superior one as the polariser and the inferior one as the analyser.

When a misalignment is present it can mean that the incident light may have a greater component along a certain direction, permitting the modulator to let more light through in that direction. This would imply that the surface is anisotropic when in fact it is isotropic. Therefore even a small misalignment of the polariser or modulator can offset the signal. However it can be seen that if the modulator itself were misaligned by the same amount, $\Delta M = -\Delta P$, then the misalignments cancel each other out. Therefore accurate RAS alignment is essential for good quality spectra.

2.2.3 Signal Analysis

From the RAS Equation it can be seen that the real and imaginary components contain a constant multiplier $J(\delta_m)$, which is the value of the relevant Bessel function at the retardation of the modulator.

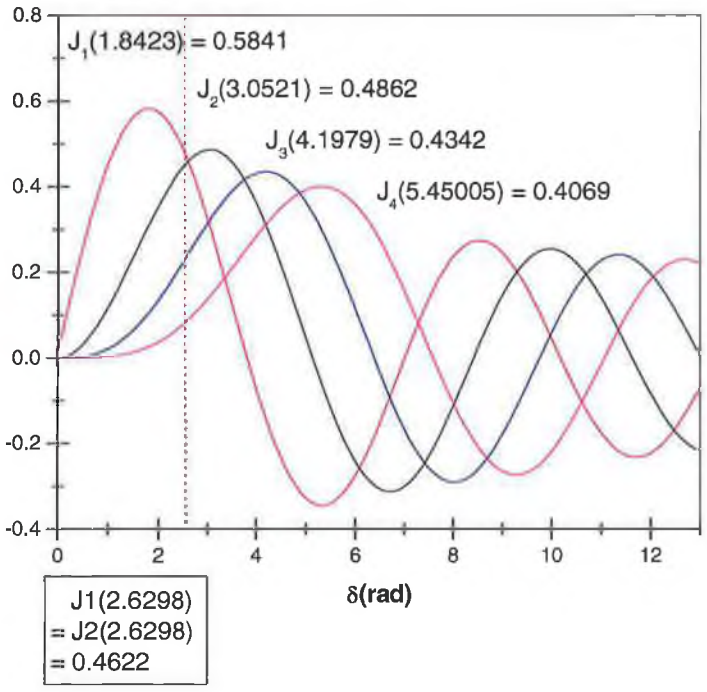

Figure 2.3 *Shows the first four Bessel Functions.*

To maximise ΔI/I and hence improve the signal-to-noise ratio, it is necessary to select δ_m such as to give the maximum value at the modulated frequency or twice the frequency. Therefore, the value of J_1 and J_2 should be maximised to obtain the most favourable value for the ω and 2ω components respectively.

Figure 2.3 shows the peak positions of the first four Bessel functions. We are only concerned with the first two harmonics, J_1 and J_2, but the third and fourth harmonics are included to give an estimate of their strength.

A photomultiplier tube detects the intensity modulated light beam. The detected current is converted to a voltage that is read into the lock-in amplifier to measure the signals at ω and 2ω. Referring back to the RAS equation, the DC component is proportional to the intensity I and the AC component is proportional to the modulation ΔI. Therefore the voltages ΔU_ω and $\Delta U_{2\omega}$ are proportional to the intensities ΔI_ω and $\Delta I_{2\omega}$ as shown in figure 2.4. For calculation of (Δr / r) a peak amplitude is needed, the RMS voltage from the lock-in amplifier must be multiplied by $\sqrt{2}$.

$$\Delta I_\omega \propto \sqrt{2}.\Delta U_\omega \qquad \Delta I_{2\omega} \propto \sqrt{2}.\Delta U_{2\omega} \tag{2.28}$$

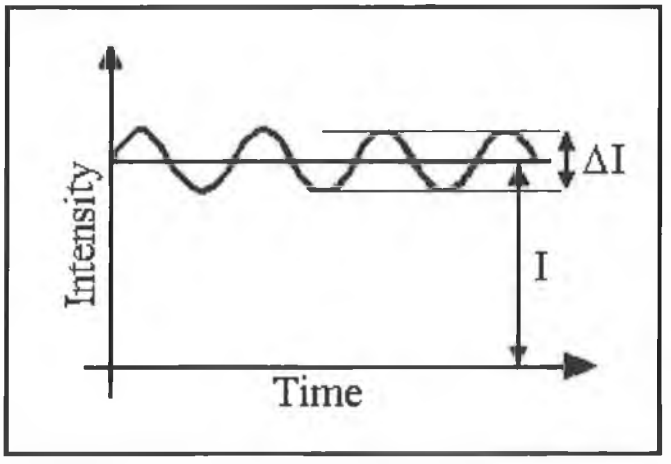

***Figure 2.4** DC signal superimposed on AC signal for $\Delta I_{\omega,2\omega}$.*

The DC modulated voltage U_{dc} is filtered out with a buffered low-pass filter and is measured by a digital to analog converter (DAC) on the lock-in amplifier. This voltage is directly proportional to *I*.

The RAS signal is therefore,

$$\mathrm{Re}\left(\frac{\Delta r}{r}\right)=\frac{1}{2J_2(\delta_m)}.\frac{\Delta I_{2\omega}}{I} \quad , \quad \mathrm{Im}\left(\frac{\Delta r}{r}\right)=\frac{1}{2J_1(\delta_m)}.\frac{\Delta I_{\omega}}{I} \tag{2.29}$$

When Re(Δr/r) and Im(Δr/r) are measured at the peak positions of J_1 and J_2, the correction factors are given by inserting the Bessel function values into equations above to give

$$\mathrm{Re}\left(\frac{\Delta r}{r}\right) = \frac{1}{2J_2(3.0521)} \cdot \frac{\Delta U_{2\omega}}{U_{dc}} \qquad \mathrm{Im}\left(\frac{\Delta r}{r}\right) = \frac{1}{2J_1(1.8423)} \cdot \frac{\Delta U_{\omega}}{U_{dc}}$$

$$= 1.4544. \frac{\Delta U_{2\omega}}{U_{dc}} \qquad = 1.2162. \frac{\Delta U_{\omega}}{U_{dc}} \tag{2.30}$$

If the PEM can change phase when the lock-in changes from ω to 2ω mode then the phase modulations should be set to the maximum values J_1 and J_2 respectively. If the PEM cannot change phase modulations then a compromise is made, and the modulator is set to the point in figure 2.4 where $J_1 = J_2$, the appropriate factor is then

$$\mathrm{Re,\ Im}\left(\frac{\Delta r}{r}\right) = \frac{\sqrt{2}}{2J_{1,2}(2.6298)} \cdot \frac{\Delta U_{2\omega,\omega}}{U_{dc}}$$

$$= 1.5299 \frac{\Delta U_{2\omega,\omega}}{U_{dc}} \tag{2.31}$$

This is the phase setting that will maximise the intensity of the first two harmonics, if the RAS spectrometer is acquiring both real and imaginary parts of the signal simultaneously.

2.3 Scanning Tunnelling Microscopy (STM)

G. Binnig, H. Rohrer, and co-workers at the IBM Zurich Research Laboratory developed the Scanning Tunneling Microscope in March 1981 [15], [16], [17]. The concept is relatively simple. A metal tip is moved very close to a conducting sample surface, so close that the wave functions of the closest atom in the tip and the surface atom overlap. If a potential is applied between the tip and the surface then a tunnel current will flow. By varying the potential or separation or both, the local density of states can be probed. By scanning the tip across the surface an image of the surface topography can be formed from variations of the tunnel current or from variations in the tip height necessary to maintain constant tunneling current and therefore constant tip-surface separation.

Before the development of the STM there was growing debate about the reconstructions of two silicon surfaces, the Si(111)-(7×7) and the Si(100)-(2×1). One of

the first applications of STM, and certainly one that caused the most impact was the solution to the problem of the atomic arrangement of the reconstructed (7×7) surface on silicon (111) [18].

2.3.1 Tunneling Theory

An understanding of STM follows from considering the solution of the Schrödinger equation for a one-dimensional square barrier of height V_0 as shown in figure 2.5.

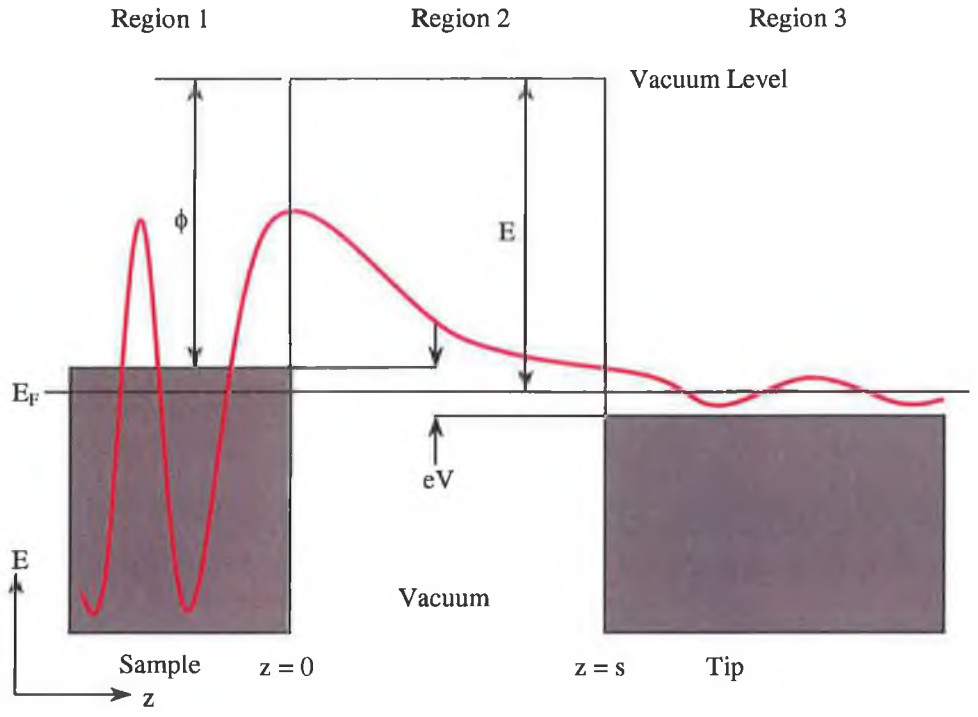

Figure 2.5 *one-dimensional metal-vacuum-metal tunnelling junction. The bias voltage V is assumed to be small (eV<< ϕ) and the work functions of both electrodes are identical so the vacuum level is effectively the same for both electrodes.*

A very simple elementary one-dimensional model [19] may be used to describe and illustrate the basic concepts of electron tunneling. In classical mechanics, the energy E of an electron moving in a potential U(z) with momentum p is given by

$$\frac{p_z^2}{2m} + U(z) = E \qquad (2.32)$$

where m is the mass of the electron. The electron has a nonzero momentum and can move in regions where E>U(z) but cannot penetrate into any region where E < U(z), i.e. a potential barrier. The equivalent quantum mechanical expression for the state of the

same electron is Schrödinger's equation, where the electron is described by a wavefunction $\psi(z)$, which satisfies Schrödinger's equation [19],

$$-\frac{\hbar^2}{2m}\frac{d^2}{dz^2}\psi(z) + U(z)\psi(z) = E\psi(z) \tag{2.33}$$

where $\hbar = h/2\pi$ and h is Planck's constant. Consider the case of a piecewise constant potential, as shown in figure 2.5. In the classically allowed region, E > U, the electron is represented by a traveling wave and equation 2.34 has solutions [19]

$$\psi(z) = \psi(0)e^{\pm ikz} \tag{2.34}$$

where $$k = \frac{\sqrt{2m(E-U)}}{\hbar}$$

is the wave vector. The electron is moving (in either the positive or the negative direction) with a constant momentum $p_z = \hbar k = [2m(E-U)]^{1/2}$, or a constant velocity $v_z = p_z/m$, the same as the classical case. In the classically forbidden barrier region, E<U (region 2 in figure 2.5) the wavefunction is a decaying exponential [20]

$$\psi(z) = \psi(0)e^{-\kappa z} \tag{2.35}$$

where $$\kappa = \frac{\sqrt{2m(U-E)}}{\hbar}$$

is the decay constant. The probability density of observing an electron near a point z is proportional to [20]

$$|\psi(0)|^2 e^{-2\kappa z} \tag{2.36}$$

which has a nonzero value in the barrier region.

From this elementary model some basic features of metal-vacuum-metal tunneling can be explained. If the vacuum level is taken as the zero point for energy, then the Fermi level is $E_F = -\phi$, where ϕ is the work function, i.e. the energy required to remove an electron from the surface of a metal [19], [20], [21]. The work functions of the two electrodes are assumed to be equal. For materials commonly encounter in STM experiments, typical values of the work function lie between 4.0 and 5.5eV. By applying a bias V to the junction, a net tunneling current can flow due to tunneling from states between $E_F - eV$ and E_F. For small bias voltages ($eV << \phi$), the energy levels of the tunneling states are approximately equal to the Fermi Energy. Thus, the energy of the n^{th} tunneling state E_n can be approximated by $E_n \approx -\phi$ and the probability P of an electron from this state reaching the tip can be written as [19], [20]

$$P \propto |\psi(s)|^2 = |\psi(0)|^2 e^{-2\kappa s} \tag{2.37}$$

where $$\kappa = \frac{\sqrt{2m\phi}}{\hbar}$$

is the decay constant of a sample near the Fermi level in the barrier region, and s is the gap between the electrodes, as shown in figure 2.5. Using eV as the unit of the work function, and Å^{-1} as the unit of the decay constant, the numerical value of κ is

$$\kappa = 0.51\sqrt{\phi(\text{eV})}\ \text{Å}^{-1} \tag{2.38}$$

For a typical work function value of 4eV, this implies that $\kappa = 1.025\ \text{Å}^{-1}$ so the current will fall by a factor of $e^{2\kappa} \approx 7.75$ times if the gap width is increased by 1 Å. The total tunneling current *I*, reaching the tip, can be calculated by summing over all the states between $E_F - eV$ and E_F [20].

$$I(V) \propto \sum_{E_n = E_F - eV}^{E_F} |\psi_n(0)|^2\, e^{-2\kappa s} \tag{2.39}$$

For small bias voltages, the density of states of a metal is constant between $E_F - eV$ and E_F and the current can be written in terms of the local density of states (LDOS) of the sample at the Fermi level. At a location z and energy E, the LDOS $\rho_s(z=0, E=E_F)$ of the sample is defined as [26]

$$\rho(z,E) \equiv \lim_{\varepsilon \to 0} \frac{1}{\varepsilon} \sum_{E_n = E-\varepsilon}^{E} |\psi_n(z)|^2 \tag{2.40}$$

for a sufficiently small energy, ε. The tunneling current at the tip can then be written in terms of the LDOS of the sample as [20]

$$I(V) \propto V\rho_S(0, E_F)e^{-2\kappa s} \tag{2.41}$$

2.4 Growth Modes [22]

Due to scientific and technological interest, many studies are concerned with growth modes of adsorbates on metal and semiconductor substrates. Temperature, deposition rate and defects of both the substrate and of the growing film can influence the growth modes in metals and semiconductors. For heterogeneous systems, the lattice mismatch must also be accommodated during growth by the formation of either (a) epitaxial or overlayer structures or (b) surface alloy structures.

(a) Epitaxial Growth

The term epitaxial growth describes an ordered overlayer structure formed on a single crystal surface. In many cases, such as the adsorption of organics on metal or semiconductor surfaces, the adsorption does not terminate upon the completion of a single monolayer and multilayer structures may be formed.

Epitaxial growth is broadly classified into three different growth modes, based on their original investigators, namely, (i) Frank-van der Merwe, (ii) Volmer Weber (VW) and (iii) Stranski-Krastanov (SK) modes as shown in figure 2.6. These growth modes are governed by the surface free energies of the deposited adatoms (γ_A), the substrate (γ_S) and the interface (γ_{A-S}) according to the parameter:

$$\Delta\gamma = \gamma_A + \gamma_{A-S} - \gamma_S$$

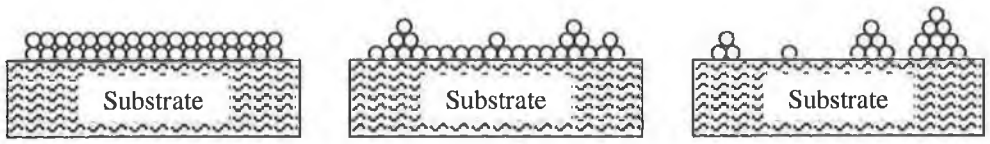

a) Frank van der Merve b) Stranski-Krastanov c) Volmer-Weber

Figure 2.6 *Epitaxial Growth Modes: (a) Frank van der Merve, (b) Stranski-Krastanov; and (c) Volmer Weber.*

(i) *Frank van der Merve (FM): monolayer-by-monolayer growth*

$$\Delta\gamma \leq 0$$

If there is a large difference between the two surface free energies then the parameters γ_A and γ_S will strongly influence the growth mechanism. In FM growth the adatoms are more strongly bound to the substrate than to each other. The initial adatoms condense to form a complete monolayer. Then a less tightly bound second layer covers this. If the decrease in bonding is monotonic towards the value of the bulk crystal then layer growth may occur. Whether FM growth continues to high coverages is strongly dependent on the strain energy, that is the lattice mismatch between the substrate and the adsorbate atoms. If is mismatch is large then continued FM growth is unlikely, however it is possible in systems with large lattice mismatch provided that the strain can be relieved, usually by a defect mechanism.

(ii) *Volmer-Webber (VW): Island Growth*

$$\Delta\gamma > 0$$

In this mode adatoms grow as three-dimensional islands. The adatoms are more strongly bound to each other than to the substrate and small clusters nucleate directly on the surface as adsorbate growth continues.

(iii) *Stranski-Krastanov (SK): Monolayer plus Islanding Growth*

$$\Delta\gamma < 0$$

SK growth refers to growth of islands following the deposition of one or more complete monolayers. Any factor that disrupts the monotonic decrease in binding

energy with coverage, thereby resulting in high free energy of the adlayer surface, may cause layer growth to become unfavourable. The bonding energies of a system, large lattice mismatches and the method of adsorbate growth are the major influences on the development of a SK growth mode.

2.4.1 Surface Sensitivity

The surface sensitivity of an analytical technique depends on the depth of origin of the detected species. For example in XPS, X-ray photons, which bombard the surface can penetrate deep into the solid, the resultant emitted electrons, which can be detected without loss of energy arise from within 1-8nm of the surface. Electrons generated deeper in the solid may escape but in propagating to the surface they will have collided with other atoms and lost energy through inelastic collisions. Therefore the surface sensitivity of electron-based probes arises from the very strong inelastic scattering of low energy electrons in the range 40-150eV, in solids. An electron travelling through a solid will have a certain inelastic mean free path (IMFP), which is a distinctive length that the electron can travel without an energy loss due to a collision. Seah and Dench [23] have comprehensively studied the IMFP in solids for energies in the range 0-10 keV. They derive a universal inelastic mean free path length curve, IMFP versus electron kinetic energy, shown in figure 2.7

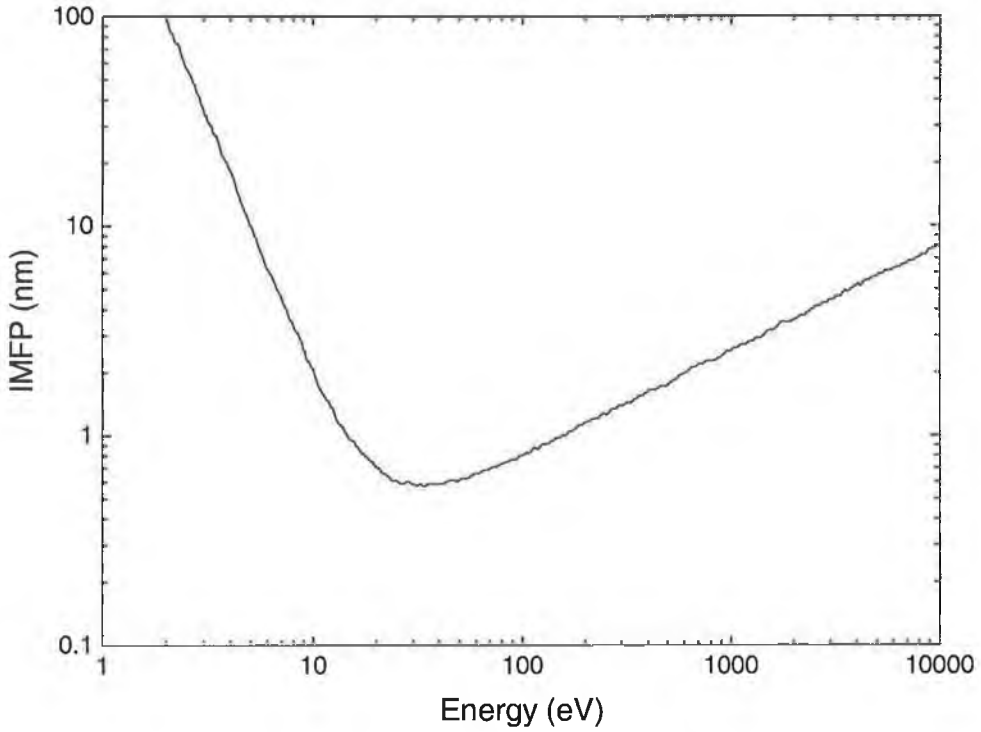

Figure 2.7 *Universal Inelastic Mean Free Path versus electron kinetic energy for solids* [23]

Seah and Dench [23] have also developed equations that relates the IMFP to electron energy and the type of material in which the electron is traversing.

$$\text{IMFP} = \lambda = 538\text{KE}^{-2} + 0.41(\text{aKE})^{0.5} \quad \text{for solids}$$

$$\text{IMFP} = \lambda_d = 49\text{KE}^{-2} + 0.11\text{KE}^{0.5} \quad \text{for organic compounds}$$

where KE is the electron energy above the Fermi level (eV) and a is the thickness of a monolayer in nanometers. From figure 2.7 it can be seen that the IMFP varies considerably with the kinetic energy of the electron. At very low kinetic energies the electrons are unable to excite any of the loss mechanisms (plasmon excitations) and therefore the IMFP is very long. At very high energies the cross section for these losses is again low and the IMFP is long. What is most important about figure 2.8 is that in the energy range 40-150 eV electrons have the shortest inelastic mean free paths < 1 nm and thus are highly surface sensitive.

2.5 Photoelectron Spectroscopy

The technique of photoelectron spectroscopy to study the chemical and electronic structure of solids was developed as an analytical tool by Siegbahn [24] in the 1950's and 1960's. It was found that accurate measurements of the electronic binding energies could provide information about the electric structure of a sample. From an analysis of the binding energies it is possible to build up a chemical classification of the solid.

From section 2.4 it can be seen that with the correct choice of experimental parameters, photoelectron spectroscopy can be used to probe only the surface of a solid. The lowest escape depth corresponds to electrons which have kinetic energy of about 40 eV. The surface sensitivity of the experiment can therefore be optimised by selecting a photon energy so that the photoelectrons have the smallest mean free path length.

Synchrotron sources [26], which provide a continuous range of photon energies, are commonly used in modern day high-resolution photoemission experiments. Photoemission measurements are divided into two regimes (a) core level photoemission and (b) valence band photoemission.

2.5.1 Photoemission Theory

The basic process in both core level and valence band photoemission is the absorption of a photon of energy $h\nu$ by an atomic orbital electron with total transfer of the photon energy to an electron with binding energy E_b, and the emission of the

electron from the solid. The kinetic energy E_{kin} of the emitted photoelectron, can be expressed by the Einstein equation [25]

$$E_{kin} = h\nu - E_b - \phi \tag{2.42}$$

where ϕ is the work function of the material. If the difference $(h\nu - E_b)$ is larger than the work function, the electron will have enough energy to leave the solid with kinetic energy E_{kin} as shown in figure 2.8.

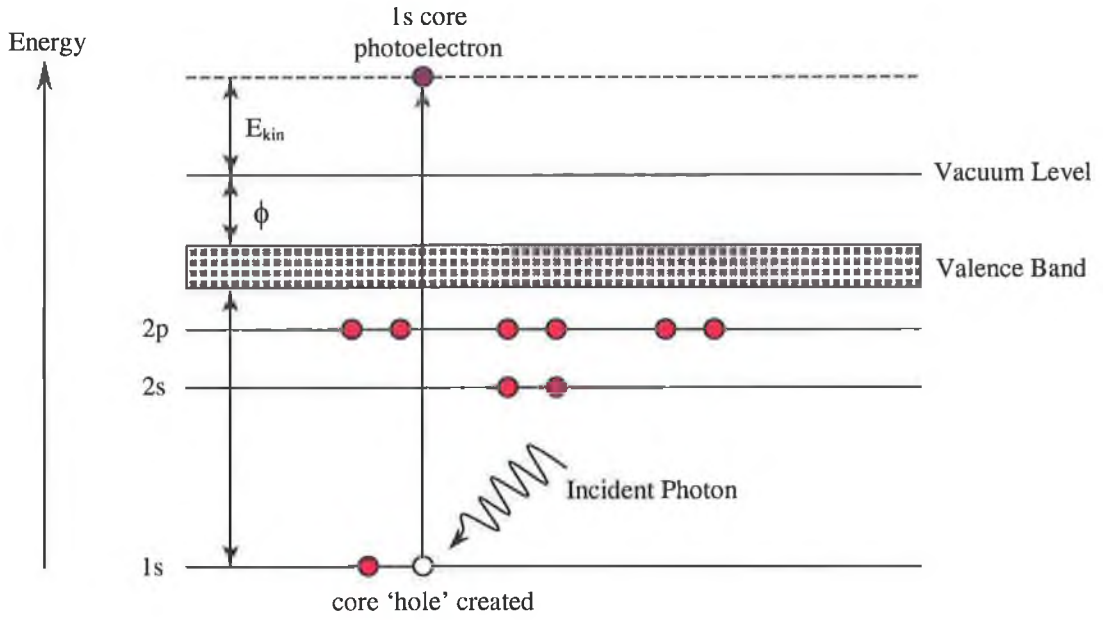

Figure 2.8 *An example of a photoemission process, where an incident photon transfers all its energy to a 1s core level electron.*

2.5.2 Core Level Spectroscopy

A core level spectrum is obtained by exciting photoelectrons from a deep atomic level. Some of the excited core level photoelectrons are involved in collisions giving rise to an inelastically scattered background. Core level peaks produced by elastically scattered electrons can sit on top of this background. Since each element has a characteristic core level spectrum, it is possible to carry out chemical identification in photoemission. Also, atoms in different chemical environments give rise to core levels that are shifted in energy.

2.5.3 Analysis of Core Level Spectra

There is a natural line width associated with the finite lifetime of the core hole, which leads to a Lorentzian broadening of each core level peak. Using a photoemission technique like synchrotron radiation [26] the overall lineshape is a convolution of the

Lorentzian profile with the Gaussian broadening which arises due to the limited resolution of the monochromator and detector and also surface inhomogeneities. This type of line profile is called a Voigt profile and is of the form [27].

$$I(E) = \int_{-\infty}^{+\infty} \frac{\left(\frac{1}{2}\omega_L\right)^2}{\left(\frac{1}{2}\omega_L\right)^2 + (E - E_0)^2} \exp\left[-\frac{1}{2}\left(\frac{\sqrt{8}\ln 2.\,\tilde{E} - E}{\omega_G}\right)^2\right] d\tilde{E} \qquad (2.43)$$

where I is the intensity measured at the energy E, ω_L and ω_G are the full width at half maximum (FWHM) of the Lorentzian and Gaussian respectively. E_0 is the peak position of the Voigt function and $\tilde{E}$ represents the energy values over which the integration is carried out.

The function must be calculated by numerical integration for every point of the spectrum since the results cannot be given in an analytical form.

Atoms at the surface of a crystal do not have the same coordination as atoms in the bulk of the sample due to a missing next atomic layer. Thus, their coordination number and hence their binding energy is generally different. The different binding energy of electrons from surface atoms gives rise to additional spectral components, which are shifted in energy. This effect is for example observable for surface reconstructions [25]. Atoms at the outermost layers which do not have a binding partner, and thus have unsaturated bonds, will minimize their potential energy by possibly rearranging and forming new bonds with other surface atoms. On a clean surface core level spectra usually have two components, one from the bulk atoms and the second from the surface atoms [28].

Chemical shifts are of similar origin [25]. When adsorbing a layer of atoms of a different species onto the surface, the surface atoms rearrange to incorporate the new atom species to minimise their potential energy. Two features can appear in the photoelectron emission spectra. Firstly, emission from the core level of the newly adsorbed species itself can be detected and secondly a shifted additional component for the original surface atom can appear. The number of additional components depends on the number of different chemical states present [28].

2.5.4 Valence Band Spectroscopy

As discussed in section 2.5.3 core level spectra are comprised of relatively sharp intense peaks that can be used to identify different chemical environments. The valence band electrons are electrons in the outer shell of an atom that are directly involved in bond formation. Information regarding the electronic and interface properties can be

obtained from the valence band measurements, such as the valence band offset and the position of the highest occupied molecular orbital (HOMO) of an organic film. Work functions can be deduced from changes in the secondary electron cutoff position and measurements regarding band bending and interface dipoles can be deduced [28].

2.5.5 Evaluating Valence Band Spectra

Valence band analysis can provide additional electronic and structural information that cannot be obtained from a core level analysis. It is also possible to obtain molecular orientational information from valence band spectra. For the valence band spectra in chapters four and six, group theory has been applied to try to determine the molecular orientation of a pentacene molecule on the Au(110) and Ag/Si(111)-($\sqrt{3}\times\sqrt{3}$) surfaces.

2.6 Low Energy Electron Diffraction (LEED)

The diffraction of electrons from a crystal surface is a standard method for determining the structure of crystal surfaces. The incident electron may have low energy ~10-500 eV (LEED) or high energy ~10-20 keV (RHEED). The low energy electrons have wavelengths of 1.0-0.1Å, which are of the same order of magnitude as the inter-atomic spacing at the surface of a single crystal [29]. Nearly all of the elastic collisions that lead to diffraction peaks take place in the one or two atomic layers close to the surface. For this reason LEED is a surface sensitive technique.

$$\lambda = \left({}^{150.6}\!/_{\mathrm{E(eV)}} \right) \text{Å} \qquad (2.44)$$

where E is the electron beam energy.

The elastically scattered electrons produce a diffraction pattern, from which the two dimensional periodicity of the surface can be deduced. Variations in the unit cell size induced by adsorption can also be observed. From the variations of the spot intensities with beam energy, the complete surface geometry can be determined, this technique is referred to as I(V)-LEED.

2.6.1 Diffraction / LEED Theory

Any plane of atoms in a crystal structure can be defined by three coordinates called Miller Indices, (h, k, l). These Miller indices are obtained by calculating the intercepts of a plane with the **a, b, c,** axes as a fraction of a, b, c, then taking reciprocals of these numbers, and expressing the result in the form of the smallest whole numbers.

The Miller indices of a plane has a reciprocal relationship to the real intercepts of the plane with the axes; in the same way the wavelength of an x-ray beam (a real distance) has a reciprocal relationship to the wavevector, **k**, of the beam, whose magnitude is defined as [30]

$$|\mathbf{k}| = 2\pi/\lambda \tag{2.45}$$

The wavevector is a measure of the momentum of the incident and diffracted beams. The change in wavevector of a beam on scattering from a plane of atoms will determine the direction of any emergent diffracted beams. A diffracted beam of electrons emerges from a crystal whenever constructive interference occurs between electrons scattered from successive planes of atoms in the real lattice. By applying the law of conservation of momentum to a reciprocal lattice, where distances are directly proportional to momentum, it is possible to find where constructive interference occurs. The geometrical construction employed is known as the Ewald sphere construction. This is shown in reciprocal space in figure 2.9 for a cubic lattice, where the distance between adjacent lattice points is $2\pi/d$, with d the distance between points in the real lattice. A wavevector $\boldsymbol{k}_0$ is drawn on the diagram with its tip pointing towards the origin of reciprocal space, (000), representing the wavevector of the incident electron beam. A sphere is drawn with radius $|\boldsymbol{k}_0|$, with the origin at point P. This is the Ewald sphere [30].

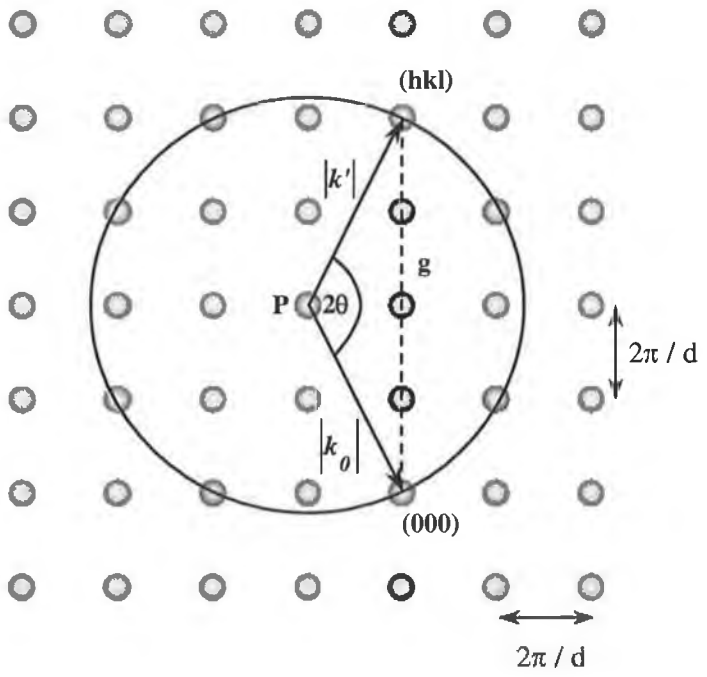

Figure 2.9 *Ewald sphere construction for a cubic lattice, (hkl) are the Miller indices of the point on the Ewald sphere.*

If any of the reciprocal lattice points are intersected by the sphere then the condition for elastic scattering is satisfied (i.e. there is a change in momentum of the beam but there is no change in energy) with the scattered beam having a wavevector $|\boldsymbol{k}'|$. By conservation of momentum [30]

$$|\boldsymbol{k}_0| = |\boldsymbol{k}'| + \boldsymbol{g} \tag{2.46}$$

where the change in momentum on scattering is represented by the reciprocal lattice vector $\boldsymbol{g}$. For elastic scattering $|\boldsymbol{k}_0| = |\boldsymbol{k}'|$. From figure 2.9 it can be seen that [28]

$$\sin\theta = \frac{|\boldsymbol{k}_0|}{|\boldsymbol{g}|/2} \tag{2.47}$$

and

$$|g| = (h^2 + k^2 + l^2)^{1/2} 2\pi / d \tag{2.48}$$

therefore

$$\sin\theta = (h^2 + k^2 + l^2)^{1/2} \lambda / 2d \tag{2.49}$$

where λ is the deBroglie wavelength of the electron. The wavelengths of the low energy electrons are a few angstroms, which is slightly smaller than the interatomic spacing and therefore suitable for diffraction experiments. Equation 2.49 is the familiar Bragg condition [19]

$$n\lambda = 2d\sin\theta \tag{2.50}$$

where $n = (h^2 + k^2 + l^2)^{1/2}$, known as the order of diffraction.

2.6.2 Elements of LEED Theory

Constructing an Ewald sphere in two dimensions does not reproduce the same construction as in three dimensions. It can be shown that instead of showing reciprocal lattice points, in two-dimensions a diagram would show reciprocal lattice rods. This arises because if the surface forms a completely two-dimensional net the periodic repeat distance normal to the surface is infinite. As was seen in previous section, the distance between adjacent points in three dimensions in a reciprocal lattice is inversely proportional to the corresponding distance in the real space. Therefore in two-dimensions the reciprocal lattice points normal to the surface are infinitely dense forming rods. The diffraction condition is satisfied for every beam that emerges in a direction along which the sphere intersects a reciprocal rod [30].

In LEED experiments diffracted beams may occur at all energies, provided the corresponding rod lies within the Ewald sphere. Changing the incident beam energy will

change the radius of the sphere, $|k_0|$, and the number and directions of scattered beams will vary. It can be shown that the LEED pattern condenses towards the specularly (0,0) reflected beam as the incident electron beam energy is increased.

2.7 Group Theory

The physical and chemical applications of group theory are usually based on the geometric symmetries of atoms, molecules and crystals. A connection between spectroscopy and molecular structure may be formed by utilizing these symmetry relations.

For the characterization of photoemission spectra and RAS spectra a terminology is used that will be introduced in this section. It is possible to classify molecules into symmetry types or "point groups". A point group classifies the type and number of symmetry operations that can be carried out on the molecule as shown in table 2.1 [36].

Symmetry Operators		**Symmetry Operations**
Symbol	**Description**	
E	Identity	No change
σ_v	Plane of symmetry	Reflection through vertical plane
σ_h	Plane of symmetry	Reflection through horizontal plane
i	Center of symmetry - inversion	Inversion through the center
C_n	Axis of Rotation	Rotation about the axis by 360°/n
S_n	Improper Rotation – rotation-reflection axis of symmetry	Rotation about the axis by 360°/n followed by reflection through the plane

Table 2.1 *Symmetry elements and symmetry operations* [31].

In this section group theory is used to determine the point group and associated selection rules for a pentacene molecule, shown in figure 2.10. Each of the above symmetry elements listed in table 2.1 can be applied to the molecule. All the symmetry operations that can be performed on the pentacene molecule are shown in figure 2.10. For example a rotation about the C_2 y-axis of the pentacene molecule causes the

molecule to rotate about the y-axis by 180°, therefore the displacement x vector points in the negative x-direction and the displacement z vector points in the negative z-direction. This result can be written as [31]

$$C_y(T_y)=(-1)(T_y) \qquad (2.51)$$

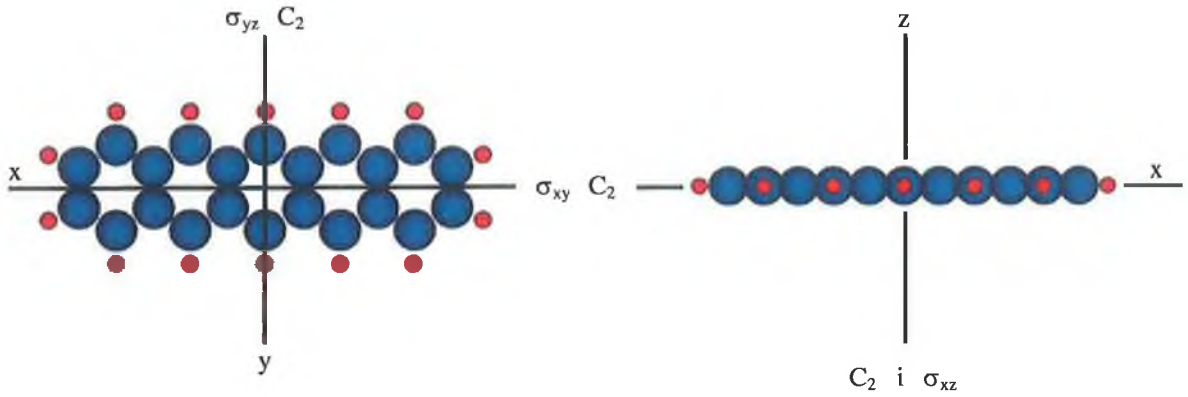

Figure 2.10 *diagram of pentacene molecule showing all the operations on the molecule.*

The transformation matrices that characterize the motions of a molecule belonging to a given point group can be arranged in table form and are termed "character tables".

The pentacene molecule belongs to the D_{2h} point group as it has three C_2 axes, a single C_2 axis along the z-direction and perpendicular to the σ_{xy} plane and two further C_2 axes along the x and y-axes. It also has a horizontal plane σ_h. The character table for the D_{2h} symmetry group and therefore the pentacene molecule is shown in table 2.2 [31].

D_{2h}	E	$C_2(x)$	$C_2(y)$	$C_2(z)$	i	σ(xy)	σ(xz)	σ(yz)		
A_g	1	1	1	1	1	1	1	1		x^2, y^2, z^2
B_{1g}	1	1	-1	-1	1	1	-1	-1	R_z	xy
B_{2g}	1	-1	1	-1	1	-1	1	-1	R_y	xz
B_{3g}	1	-1	-1	1	1	-1	-1	1	R_x	yz
A_u	1	1	1	1	-1	-1	-1	-1		
B_{1u}	1	1	-1	-1	-1	-1	1	1	z	
B_{2u}	1	-1	1	-1	-1	1	-1	1	y	
B_{3u}	1	-1	-1	1	-1	1	1	-1	x	

Table 2.2 *Character table for D_{2h} symmetry* [31]

Conventionally, the letters A, B, E and T are used in the left column of table 2.2. A and B are one-dimensional, E is two-dimensional and T is three-dimensional. The dimension of the irreducible representation is the dimension of any of its matrices. The

subscript which may appear with A, B, E or T are arbitrary labels, the subscript u represents antisymmetric with respect to inversion and the subscript g represents symmetric with respect to inversion. The superscripts ' and '' denote irreducible representations which are respectively, symmetric and antisymmetric with respect to reflection through a horizontal mirror plane [31]. The three columns on the right of the table contain the basis functions for the irreducible representations. These basis functions have the same symmetry properties as the atomic orbitals, which bear the same names.

2.7.1 Selection Rules

In general the study of symmetry can help to decide which transitions between energy levels are possible, a molecule may not be able to absorb light even if that light has precisely the correct energy to cause a transition between two energy levels of the molecule. The symmetries of the states involved must be compatible in order that the molecule may absorb the light. The selection rules which discriminate between allowed and forbidden transitions are one of the most important uses of symmetry.

The selection rules governing the uv-photoemission process from the clean and pentacene covered Au(110)-(2×1) surface and the Ag/Si(111)-($\sqrt{3}\times\sqrt{3}$)R30°, as a consequence of the symmetry properties of the system will be discussed.

Using a simplified one-dimensional model, it can be shown that the probability that a transition between two states will be induced by the oscillating electric field of a light wave is proportional to the square of the transition moment integral. For an electronic transition, the transition moment integral has the form [32]

$$M = \int \psi_{v'}^{*} \psi_{v} d\tau_{n} \int \psi_{e'}^{*} \hat{\mu} \psi_{e} d\tau_{e} \int \psi_{s'}^{*} \psi_{s} d\tau_{s} \qquad (2.52)$$

Franck-Condon Factor — Basis of orbital selection rules — Basis of spin selection

Equation 2.52 is the basis of the electronic selection rules and is composed of three parts. The vibrational integral is labeled the Franck-Condon principal in equation 2.52, it represents the overlap of vibrational wavefunctions between the ground and excited electronic states. The spin integral is also shown in equation 2.52. The orbital selection

rules integral part of equation 2.52 is generally used on its own for calculating the electronic transitions.

The selection rules state that the integral $\int \psi_{e'}^{*} \hat{\mu} \psi_{e} d\tau_{e}$ must be nonzero if the transition is to be orbitally allowed. Also an electronic transition is orbitally allowed if and only if the triple direct product $\Gamma(\psi_{e'}) \times \Gamma(\hat{\mu}_{e'}) \times \Gamma(\psi_{e})$ contains the totally symmetric irreducible representation of the point group of the molecule. The dipole moment operator has three components which transform as x, y and z [32]. A_g is the totally symmetric irreducible representation of the D_{2h} point group.

In chapters 4, 5 and 6 the selection rules governing the electronic transitions of the D_{2h} molecule are calculated and related to transitions in the valence band spectra. From this analysis the orientation of the molecule on the two surfaces studied is determined.

2.8 Electronic States at Surfaces

I. Tamm [33] showed that the termination of a one dimensional Kronig-Penney potential resulted in the formation of localised states at the surface which were at energies forbidden to electrons in the bulk. In 1939 W. Shockley [34] found that the surface states depend on how the periodic bulk potential was terminated and extended his results to three dimensions where the surface states become surface bands. In the late 1940's experimental evidence was found that confirmed the existence of these predicted surface states [35].

These first theoretical studies dealt with surfaces which were ideal terminations of the bulk. This is very rarely found on real surfaces, normally the surface will experience some relaxation or reconstruction, there may also be contamination on the surface or there may be an adsorbed overlayer present. The treatment of these surfaces is essentially the same, once a potential is found to describe the presence of the surface, the energy states can be calculated. There are two types of states, which may appear in addition to the bulk states. True surface states which are at energies forbidden to the electrons in the bulk crystal. These are localized at the surface, decaying exponentially into the crystal. States which overlap in the projection of the bulk bands, can mix with the bulk states and will decay much more slowly into the crystal, these states are known as surface resonances.

2.8.1 The Au(110) fcc Surface Structure

Gold has an electronic configuration of [Xe] $4f^{14}$ $5d^{10}$ $6s^1$ and crystallises with an f.c.c. structure. An f.c.c lattice is not the primitive cell as it contains four lattice points: one at the origin and three others at the centre of the cube faces with coordinates (½, ½, 0), (½, 0, ½) and (0, ½, ½). The Brillouin Zone of the f.c.c lattice is therefore not a cube but the shape shown in figure 2.11 [36].

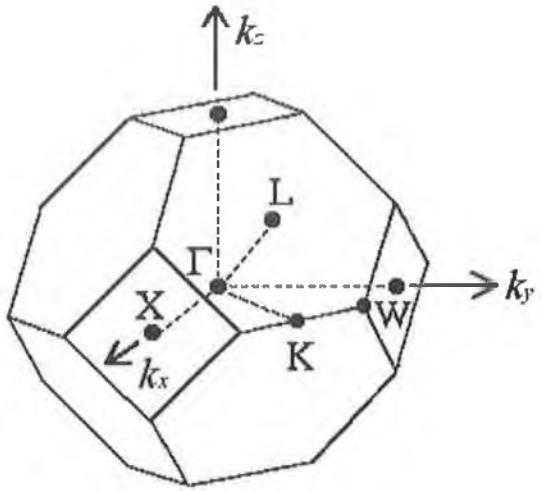

Figure 2.11 *Bulk Brillouin Zone of an f.c.c. lattice. a is the size of the cubic unit cell in the crystal. High symmetry points within the Brillouin zone are given symbolic names derived from group theory. The origin at* $\mathbf{k}$ *=(0, 0, 0) is called the Γ-point. The X-point at* $(2\pi/a)(1,0,0)$ *identifies the zone edge along the six equivalent (100) directions. The L-point at* $(\pi/a)(1,1,1)$ *is at the zone edge along the eight equivalent (111) directions. An arbitrary point along the Γ→X direction is labelled Δ, while an arbitrary point along the Γ→L direction is labelled Λ. The K-point corresponds to the zone edge along the (110) direction, while the W-point is at the intersection of the square and hexagonal faces of the polygon. The X-point corresponds to a wave vector of* $(2\pi/a)$ *rather than* (π/a).

The band structure of the transition metal gold is complicated because of the need to include the dispersion of both the 3d and 4s bands, which overlap in energy. The 4s bands are approximately parabolic, but the 3d bands are fairly flat. This is a consequence of the strong localization of the d electrons, which means that their orbitals do not overlap much in the crystal. The low dispersion d-bands are the origin of the high density of states within a relatively narrow range of energies. These states are very important for the magnetic and optical properties of the crystal, and some of these states will be probed with the RAS technique.

2.8.2 Surface States on the Au(110) Face [37], [38], [39]

There has been much discussion in the literature [39], [37] as to the number of sp surface states which may exist in a single band gap of a metal. It is generally agreed that in gaps at the centre of the Surface Brillouin Zone (SBZ) at least one free electron state may exist. Away from the centre of the Brillouin Zone, however, band gaps often occur at points of low symmetry. The topology of the underlying bulk bands then introduces the possibility of having more than one crystal-induced surface state in a single band gap, even within a nearly free electron model.

The three-dimensional Bulk Brillouin Zone for the f.c.c. crystal (see figure 2.11) can be reoriented to give a two dimensional projection onto the (110) surface, as shown in figure 2.12. This is the Surface Brillouin Zone (SBZ) and from this it is possible to calculate the surface and bulk states along specific crystal directions. The SBZ is rectangular with its long side ($\bar{\Gamma} \rightarrow \bar{X}$) parallel to the $<\bar{1}10>$ direction and the short side $\bar{\Gamma} \rightarrow \bar{Y}$ parallel to the <001> direction. The top panel shows (a) the real space geometry of the f.c.c (110) surface, and (b) the SBZ. The dashed lines in the k-space diagram depict the SBZ when a (1×2) reconstruction is present [39].

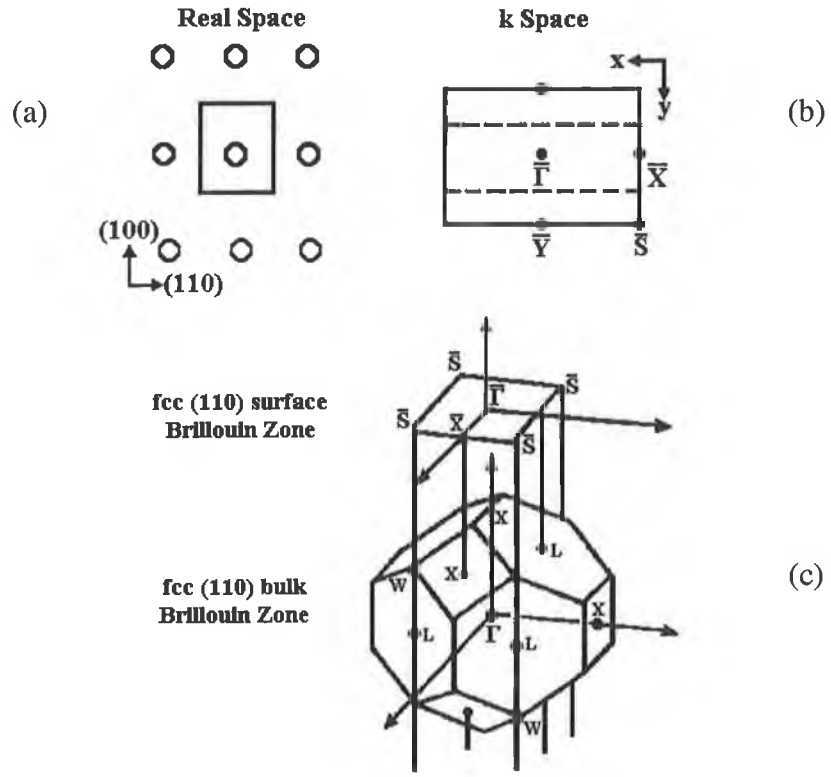

Figure 2.12 *(a) Real Space geometry of f.c.c (110) surface (b) Surface Brillouin Zone of f.c.c. (110) surface (c) three dimensional Bulk Brillouin Zone of f.c.c. (110) surface and the projected two dimensional Surface Brillouin Zone of that surface* [39].

Photoemission [40],[39] and inverse photoemission[39] respectively have been employed to observe and study occupied and unoccupied surface states of Au. Since most sp bands lie partially or entirely above E_F, a combination of these two experiments opens up the possibility to study the entire energy range of these gaps and explore the surface states.

Bartynski et. al. [39] used photoemission, inverse photoemission and a surface state calculation employing an analytical model within the nearly free electron approximation to study the (110) faces of several noble metals. Along the $\bar{\Gamma} \rightarrow \bar{X}$ azimuth of Au(110), two peaks at 0.2 eV and 1.6 eV above E_F at $\bar{\Gamma}$ are found from normal incidence photoemission. At larger angles two more peaks appeared at energies of ~ 4.75 eV and ~2.25 eV at $\bar{X}$. These higher energy peaks are identified as even and odd surface states. These peaks should be sensitive to surface contamination. Along the $\bar{\Gamma} \rightarrow \bar{Y}$ azimuth of Au(110), two peaks at 0.2 eV and 1.6 eV above E_F were found at normal incidence as shown in figure 2.13.

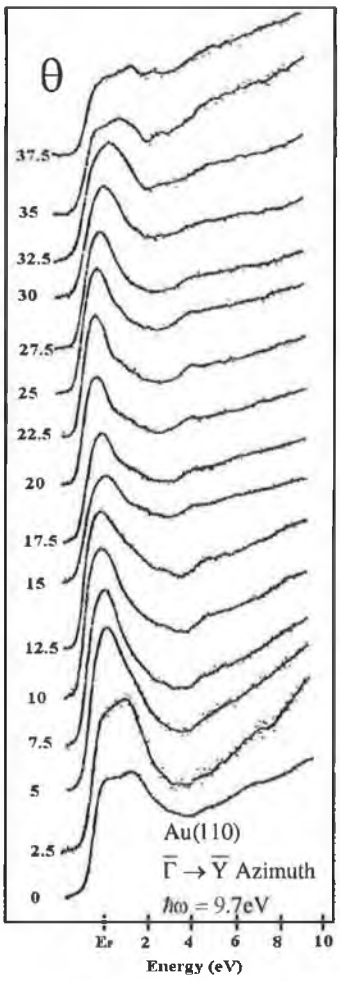

Figure 2.13 *Inverse photoemission spectra from the* $\bar{\Gamma} \rightarrow \bar{Y}$ *azimuth of Au(110)* [39].

The higher lying peak disperses towards E_F becoming the dominant feature in the spectra for nearly all angles investigated. This higher lying peak reaches a maximum energy of about 0.2 eV above E_F. The 1.6 eV spectral feature is interpreted as a direct transition. In addition, this feature is relatively insensitive to surface contamination. They interpret the peak at 0.2 eV near E_F as the surface state at $\bar{Y}$ backfolded by the reconstruction. The arguments in favour of this assignment are that the energy of this feature coincides with that of the surface state at $\bar{Y}$, no bulk transitions are predicted at that energy, and the two states behave very similarly upon contamination. The theoretical values for the surface states and the experimentally obtained values are not consistent. The reasons suggested are that the reconstructed (1×2) surface is not included in the model, and the relativistic effects are not accounted for.

Heimann et. al. [38] using angle resolved photoemission of Au(112), Au(100) and Au(110) determined experimentally the existence of occupied surface state bands which are located in sp gaps of the projected bulk band structure. It has been shown that for each of the surfaces; where the polar angle θ and consequently $k_{||}$ has been varied, a peak in the vicinity of the Fermi level E_F emerges at a certain polar angle on top of the step like background of emission from bulk sp bands. This peak becomes more intense with increasing θ and finally disappears on further increasing θ. Figure 2.14 shows the surface state S and its dispersion across the Fermi Level E_F for increasing θ.

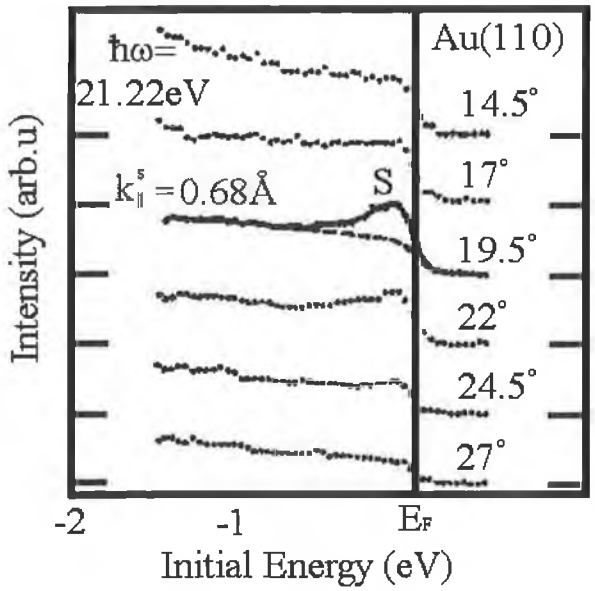

Figure 2.14 *Angle resolved photoemission from a Au(110) single crystal for 21.22 eV. This shows the existence of a surface state below the Fermi edge* [38].

Xu et. al. [37] determined more accurately the surface bands and bulk band structures along the $\bar{\Gamma} \rightarrow \bar{X} \rightarrow \bar{S}' \rightarrow \bar{Y}' \rightarrow \bar{\Gamma}$ directions in the two dimensional Brillouin

Zone for the Au(110)-(2×1) reconstructed surface using a first principal calculation. Results for the projected band structure along various symmetry lines are displayed in figure 2.15 [37].

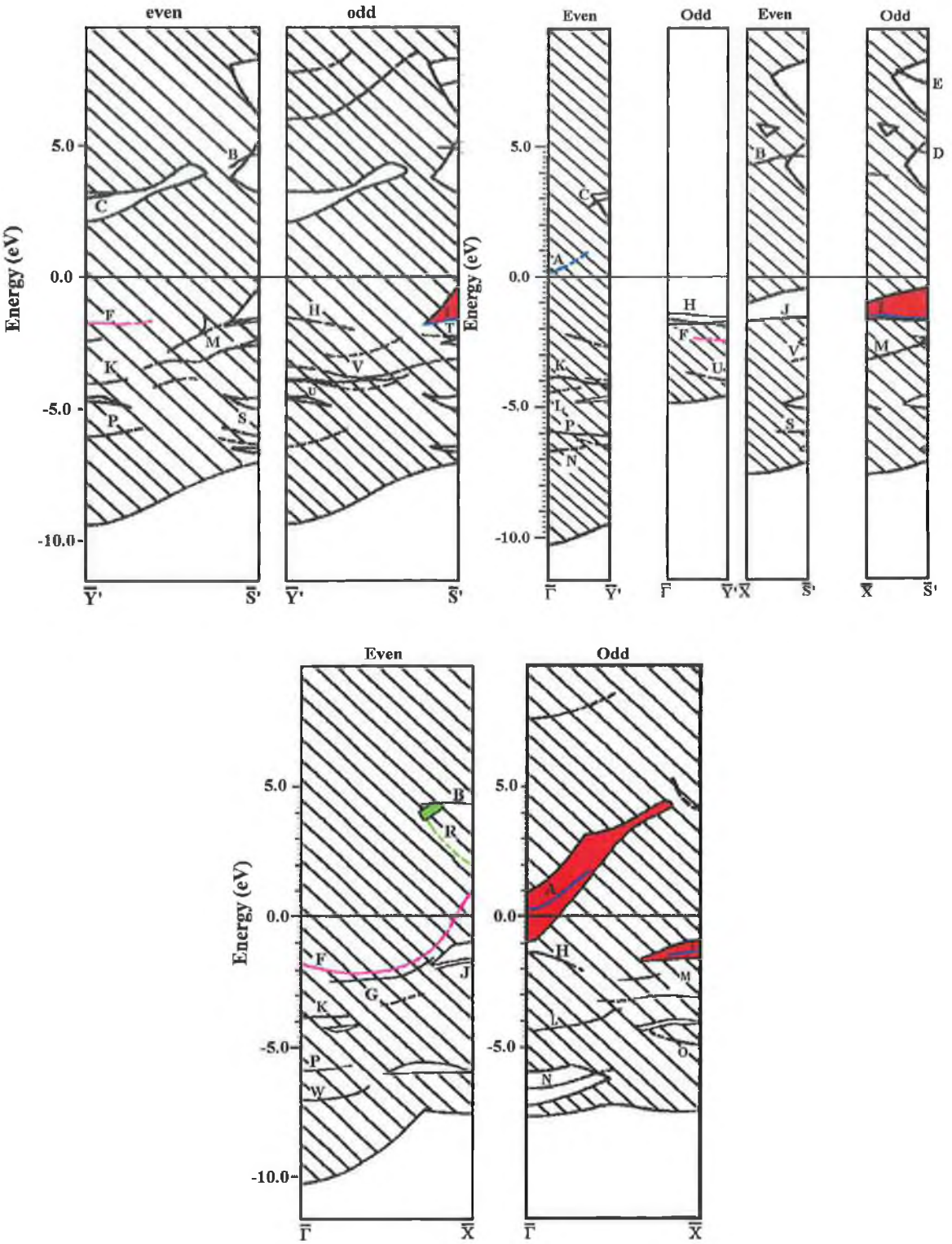

Figure 2.15 *Projected bulk band structures of Au together with dispersions of surface states for Au(110)-(1×2) reconstructed structure (displayed as solid or dashed lines) along symmetry lines* $\bar{\Gamma}-\bar{X}, \bar{\Gamma}-\bar{Y}', \bar{X}-\bar{S}'$, and $\bar{Y}'-\bar{S}'$ *of Au(110)-(1×2) SBZ. The pair panels of each figure show band structures and surface dispersions with even and odd symmetries, respectively* [37].

The shaded areas indicate the projection of the bulk states onto the (110) SBZ. The Hamiltonian matrix along the symmetry lines has reflection symmetry about the (001) ($\bar{\Gamma}\to\bar{X},\bar{\Gamma}\to\bar{S}'$) or ($1\bar{1}0$) ($\bar{\Gamma}\to\bar{Y}',\bar{Y}'\to\bar{S}'$) planes. Thus electronic states with wave vectors along these symmetry lines can be separated into two groups with even and odd symmetries. Figure 2.15 indicates the filled and empty surface and bulk states.

A prominent surface band is ***A***, it exists just above the Fermi level ~0.2 eV above E_F near $\bar{\Gamma}$ along the $\bar{\Gamma}\to\bar{X}$ line. ***A*** is mainly p-like in character.

The state ***F*** lies mostly within the bulk band region starting at ~1.8 eV below E_F near $\bar{\Gamma}$ along the $\bar{\Gamma}\to\bar{X}$ line and having a minimum energy of ~2.1 eV. It is therefore characterised as a surface resonance.

Band ***I*** is a surface band of predominantly d-character, it lies within the bulk band region starting at ~1.3 eV below E_F near $\bar{X}$ along the $\bar{\Gamma}\to\bar{X}$ line and having a minimum energy of ~1.5 eV.

The band ***R*** is a surface resonance, it lies ~2.0 eV above E_F near $\bar{X}$ along the $\bar{\Gamma}\to\bar{X}$ line and having a maximum energy of ~3.7 eV.

Results from inverse photoemission [39] experiments are only available along the symmetry lines $\bar{\Gamma}$ to $\bar{X}$ and $\bar{\Gamma}$ to $\bar{Y}'$. Along the $\bar{\Gamma}\to\bar{X}$ line for the Au(110)-(2×1) surface, all the experimentally observed surface features can be described as surface bands or resonances in the first principle calculation: surface band ***A*** near $\bar{\Gamma}$, surface band ***B*** and surface resonance ***R*** near $\bar{X}$.

Heimann et. al. [38] have reported the observation of a surface state near $\bar{\Gamma}$ just below Fermi level using photoemission. Xu et. al. [37] found no evidence of this surface state and they propose two reasons for this discrepancy:

1. Scanning Tunnelling Microscopy experiments of the Au(110)-(2×1) surface have shown substantial disorder of this surface with the occurrence of (1×3) reconstruction in local areas. The effect of this disorder is to introduce a broadening of the surface band ***A*** just above the Fermi level so that this band will be slightly extended below the Fermi level and give a photoemission signal, therefore accounting for a surface state detected just below the Fermi energy.
2. The occurrence of local areas of (1×3) geometry exposes small regions of (111) like facets that can introduce surface defect states just below the Fermi level. It is well known that Au(111) has a surface state just below the Fermi level [46].

For the Au(110)-(2×1) surface all the experimentally observed surface features can be described from surface bands or resonances in figure 2.15.

2.9 Summary

Sections 2.2 and 2.3 introduced basic ideas about the general optical response of a surface and the RAS technique. An equation that may be used in a practical spectrometer has been derived and presented. Although there are many consequences of this expression that may be apparent, they have not been presented in this chapter, but are detailed and explained along with the design, construction and operation of a RAS spectrometer in chapter 3.

The STM section (2.4) has introduced some general ideas about quantum mechanical theory, and applied them to describe the tunneling phenomenon between two closely separated surfaces. The main feature was the fact that there is an exponential decay of the tunnelling current with the distance between the two separated surfaces. This discovery has lead to the invention of the Scanning Tunneling Microscope, which uses the tunnel current dependence on the separation between two metal electrodes to image the atomic structure of a surface.

Section 2.5 provides a basis for the theory of photoemission spectroscopy. In the following chapter the theory presented here will be used to analyze and interpret the results for the pentacene/Au(110)-(2×1) and the Ag/Si(111)-$\sqrt{3}$ pentacene interfaces.

In section 2.6 a brief presentation of diffraction theory and how it relates to the theory and the operation of the LEED apparatus.

Elements of group theory have been briefly described in section 2.7. From this brief discussion it was found that all molecules could be classified according to a point group. After identifying the point group the selection rules for that particular point group can be used to seek information regarding the electronic energy levels and/or orientations of the molecule on a surface. The basic concepts presented in section 2.7 will be developed upon in chapters 4, 5 and 6 to determine the orientation of the pentacene molecule.

Section 2.8 introduced surface and bulk states of the fcc(110) surface of gold. This surface is used extensively in chapters 4 and 5 and a brief discussion of this surface is necessary.

Chapter Two References

1. J.F. Mc Gilp, Prog. in Surf. Sci. 49 (1995) 1–106
2. R.M.A. Azzam and N.M. Bashara, ***Ellipsometry and Polarized Light***, North Holland, Amsterdam (1987)
3. http://www.uuw.ac.nz/
4. A. Zangwill, ***Physics at Surfaces***, Cambridge Univ. Press, 1988.
5. J. Rumberg, Diploma Thesis in Physics, TU Berlin, (1996).
6. Dr. Steve Morris, Thesis.
7. E. Hecht, ***Optics, 2nd Edition***, Addison-Wesley Publishing Company (1990).
8. J.F. Mc Gilp, D. Weaire, C.H. Patterson, ***Epioptics Linear and Nonlinear Optical Spectroscopy of Surfaces and Interfaces***, Springer-Verlag, (1995).
9. J.D.E. McIntyre, D.E. Aspnes, Surf. Sci. 24, (1971), 417.
10. K. Hingerl, D.E. Aspnes, I. Kamiya, L.T. Florez, Applied Physics Letters, 63, (1993), 885.
11. D.E. Aspnes, J. of Vac. Sci. Technol., B3, (1985), 1498.
12. D.S. Kliger, J.W. Lewis and C.E. Randall, ***Polarized Light in Optics and Spectroscopy***, Academic Press, (1990).
13. D.E. Aspnes, J.P. Harbison, A.A. Studna, L.L. Florez, J. Vac. Sci. Technol, A 6(3), 1327, (1998).
14. D.E. Aspnes, J.P. Harbison, A.A. Studna, L.L. Florez, Appl. Phys. Lett. 52, (12), 957, (1988).
15. G. Binnig, H. Rohrer, Ch. Gerber, E. Weidel, Phys Rev Lett, 49, 57, (1982).
16. G. Binnig, H. Rohrer, Helv. Phys. Acta 55, (1982) 726.
17. G. Binnig, H. Rohrer, Ch. Gerber, E. Weidel, Phys Rev Lett, 40, (1982) 178.
18. R.M. Tromp, R.J. Hamers, J.E. Demuth, Phys Rev, B34 (1986) 1388.
19. H.C. O'Hanian, ***Modern Physics, Second Edition***, Prentice Hall International Editions,1987.
20. R. Weisendanger, ***Scanning Probe Microscopy and Spectroscopy, Methods and Applications***, Cambridge University Press, 1994.
21. C.J. Chen, ***Introduction to Scanning Tunneling Microscopy***, Oxford University Press, 1993.
22. E. Mc. Loughlin, ***Structural Investigations of Metal and Semiconductor Interfaces***, Phd Thesis, 2000.
23. M.P. Seah, W.A. Dench, Surf. Interface, Anal. 1, 2-11, (1979).
24. K. Siegbahn, Science, 217, (1982), 111.

25. L. Ley, M. Cardona, ***Topics in Applied Physics Vol 27, Photoemission in Solids I and II***, Springer-Verlag 1979.
26. G. Margaritondo, ***Introduction to Synchrotron Radiation***, Oxford University Press, 1988.
27. J.J. Joyce, M. Del Guidice, J.H. Weaver, J. Electron Spectroscopy and Related Phenomena, 49, 31, (1989).
28. E.W. Plummer, W. Eberhardt, Advances in Chem. Phys., 49, 533, (1982).
29. F. Jona, J.A. Strozier, W.S. Wang, Rep. Prog. Phys., 45, 527, (1982).
30. C. Barnes, G. Attard, ***Surfaces***, New York: Oxford University Press (1998).
31. A. Vincent, ***Molecular Symmetry and Group Theory: A programmed Introduction to Chemical Applications***, J. Wiley and Sons, (1977).
32. D.C. Harris, M.D. Bertolucci, ***Symmetry and Spectroscopy: An Introduction to Vibrational and Electronic Spectroscopy***, Dover Publications Inc., 1978.
33. I.E. Tamm, Z Physik, 76, (1932).
34. W. Shockley, Phys. Rev, 56, 317, (1939).
35. W.H. Brittain, W. Shockley, Phys. Rev 72, 345, (1947).
36. M.N. Rudden, J. Wilson, ***Elements of Solid State Physics, Second Edition***, John Wiley and Sons, 1993.
37. C.H. Xu, K.M. Ho, K.P. Bohnen, Physical Review B, 39, 9, 5599 (1989).
38. P.Heimann, H. Miosga, H. Neddermeyer, Phsical Review Letters, 42, 12 (1979).
39. R.A. Barynski, T. Gustafsson, Physical Review B, 33, 10 , 6588 (1986).
40. K. Strahrenberg, Th. Hermann, N. Esser, W. Richter, S.V. Hoffmann, Ph. Hofmann, Physical Review B, 65, 035407, (2001).
41. G.V. Hansson, S.V. Flodström, Physical Reviev B, 18, 1572, (1978).

Chapter 3 Experimental Details

3.1 Spectrometer Construction

Since its original inception by Aspnes et. al. [1] in 1985 many reviews regarding the performance of various configurations of RAS have been published [2], [3], [4], [5]. While performing an accuracy analysis, Aspnes et. al. [6] tested several possible configurations of reflectance anisotropy spectrometers and eventually achieved a sensitivity limit of 5×10^{-5} with the "near null optical bridge" configuration [6].

Since Aspnes pioneering work there have been many experiments performed with the RAS technique. For example Zettler et. al. [7] employed RAS as a growth sensor for real time monitoring of Metal Oxide Vapour Phase Epitaxy (MOVPE) device growth on III/V semiconductors. The MOVPE growth rate was controlled via the variable group III-partial pressure and a fixed group-V partial pressure. The RAS spectra taken with time indicated a corresponding change of the surface stoichiometry during growth, demonstrating the ability of RAS to act as a growth rate sensor. This group also measured the RAS response to doping levels, surface temperatures, bulk compositions, surface morphology, overlayers and bulk ordering [7].

Sobiesierski et. al. [8] measured the RAS response to MBE evaporation rates *in-situ*. RAS has proved to be extremely sensitive to both surface reconstructions and ultrathin coverages of adsorbates on semiconductor surfaces. The deposition of submonolayer coverages of Si, to form Si δ-layers within GaAs was studied by this group, and it was found that RAS is sensitive to coverages ~0.005 ML Si on GaAs surfaces.

Frederick et. al. [9] determined the azimuthal orientation of an organic molecule on a metal surface using RAS. Early applications of the technique to metal surfaces exhibited strong anisotropy of fcc (110) surfaces associated with transitions between surface states as well as interband transitions in the near surface region [10]. Recently, there have been several attempts to follow the effects of molecular adsorption on metal surfaces [11]. Prior to this experiment, none of the molecular adsorbates studied had a intramolecular transition in the 1.5-5.5 eV energy range available to the RAS spectrometer, therefore Frederick et. al. chose a larger conjugated molecule so as to shift the intramolecular electronic transitions into the visible region. They used 9-Anthracene carboxylic acid and showed that analysis of the reflectance signal permitted a determination of the orientation of the aromatic ring relative to the surface.

Sheridan et. al. [12] applied RAS to a solid-liquid interface and presented results for the Au(110)/0.1M H_2SO_4 electrolyte interface. This group demonstrated that RAS was sensitive to phase transitions, step morphology, and electronic surface states. Rates

of adsorption and desorption of adlayers on the surface in an electrolyte solution with respect to a varying sample bias were performed. As a result of monitoring the rates of desorption experimental measurements of the "sticking coefficients" for the adlayer were possible.

3.1.1 RAS Configurations

Several types of RA spectrometers have been implemented in the past and over the years the design has steadily evolved. The most important variations of the RAS setup are sketched in figure 3.1. In the first RAS setup developed by Aspnes and Studna, figure 3.1(a), a rotating sample is used [13], [14]. This configuration is incompatible with most semiconductor growth environments as well as most UHV chambers. On most UHV manipulators the sample has limited rotation, but for RAS the rotation must be wobble free and should be of the order of 10 Hz or above to obtain a good signal. Hence this system can only be used properly *ex-situ*.

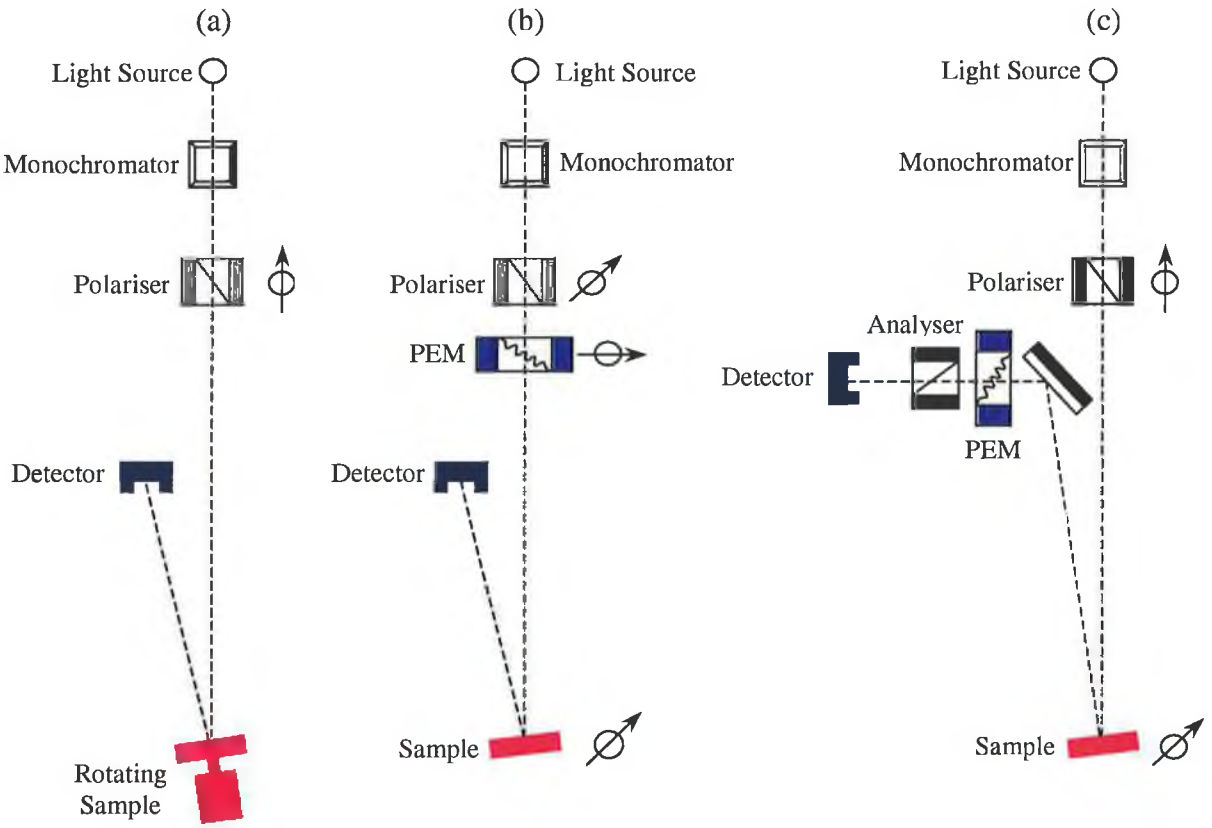

Figure 3.1 *Alternative RAS designs as used by several groups: (a) first design by Aspnes et. al. [1] with rotating sample, (b) alternative design by Berkovits et. al. [15] with PEM, (c) the additional mirror design by Luo et. al [16].*

A significant modification of the apparatus, which removed the necessity for a rotating sample was implemented by Berkovits et. al. [15] with the use of a photoelastic modulator (PEM), and a single polarizer, (figure 3.1(b)). Such a configuration can be used for all RAS experiments, both *in-situ* and *ex-situ*, but this configuration can only measure Re(Δr/r). An alternative to this design is achieved by placing the PEM and the polarizer in the reflected beam, therefore the polarizer acts as an analyser. The signal to noise ratio of this system is of the same order of the setup by Aspnes et. al. [1] showing a resolution of $\pm 3\times10^{-5}$ [1].

In the setup of Luo et. al. [16], (figure 3.1(c)), the monochromator is also placed in front of the lamp although it could be placed before the detector without changing the rest of the configuration. The configuration is similar to that of Aspnes et. al. [1] but the beam direction is changed with the addition of a mirror after the sample. This is because of space limitations in their experiment. Usually additional optical components cause a problem if placed between the polarizer, sample and PEM because reflection reduces intensity of the signal and can also change the polarisation. This setup has poor signal to noise ratio and has a resolution of $\pm 1\times10^{-3}$ [14].

The configurations in figure 3.1, all have some common components which include light source, polariser, sample, modulator, analyser, monochromator, detector and mirrors.

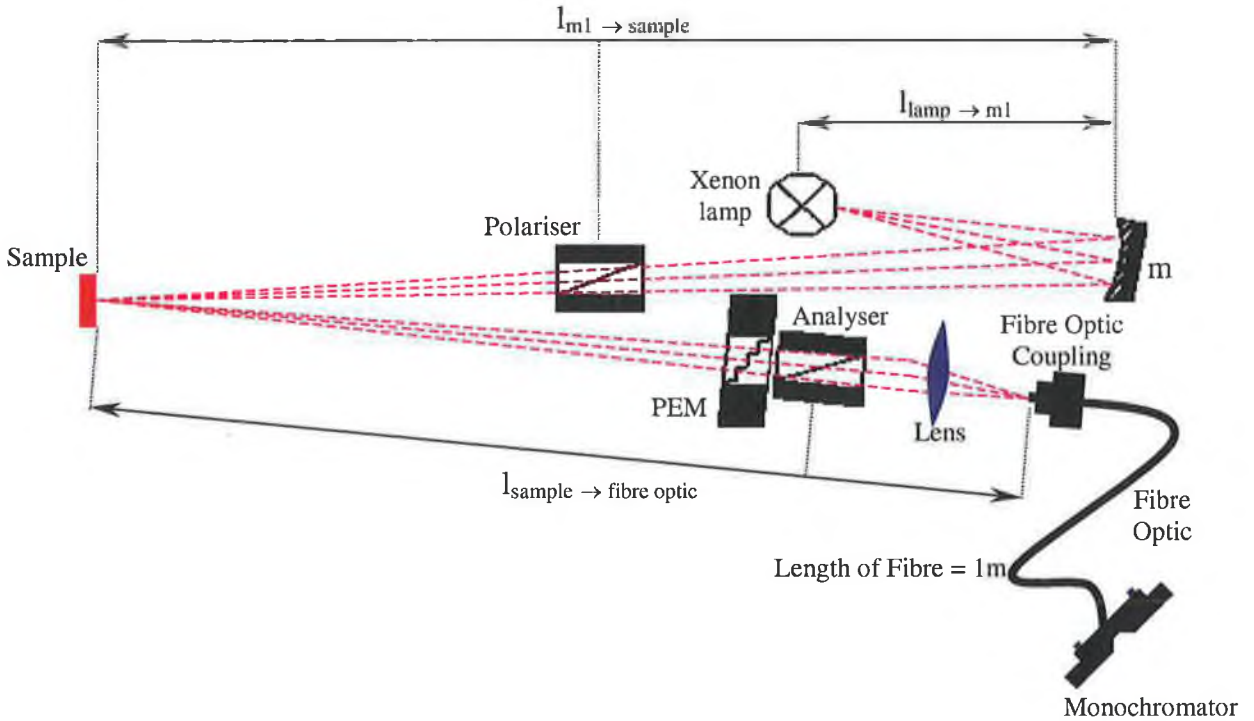

Figure 3.2 *Diagram of RAS setup showing notation that will be used throughout chapter* [2].

Figure 3.2 [2] shows the setup for phase modulated RAS as introduced by Aspnes et. al. [2] and is the basis for the design of most RAS systems currently in operation. It employs a photoelastic modulator (PEM) to analyse the polarization of the light that is reflected from the sample. The PEM is found to increase the signal to noise ratio by an order of magnitude.

3.1.2 Realization of a RAS System

The apparatus shown in figure 3.2 includes a light source (Xenon lamp), a concave mirror m, a polariser (Glan Taylor Prism), sample, an analyser (Glan Taylor Prism), a grating monochromator, (Acton Research Inc.) with a variable entrance and exit slit and a photoelastic modulator (Hinds PEM 90 with I/FS50 oscillator head). The parameters that define the layout are space limitations and optics. It is necessary to have a compact configuration and to keep absorption low. Therefore increasing the number of mirrors to fold the optical beam into a smaller space increases absorption by the mirrors and decreases the signal detected. A trade off between the compact configuration and the number of mirrors used is essential.

The aperture of the monochromator, the acceptance angles of the polariser and analyser and distance from the fibre optic coupling to the monochromator are fixed. Variable parameters include the focal lengths of the mirrors, the distance from light source to mirror, the distance from the mirror to sample and distance from sample to fibre optic coupling.

The distance from the mirror to the sample is the most important distance from the point of view of performing experiments, especially *in-situ* experiments where the distance from the UHV flange to the centre of the chamber is fixed. With this measurement as a starting point, all components on the optic table can be correctly positioned.

3.2 Component Description

3.2.1 Light Source

As with most surface sensitive optical techniques, RAS requires measurement of the signal over a wide range of photon energies. Therefore the initial requirement is a suitable light source. Listed below are all the necessary requirements for selecting a suitable light source:

1. This spectral range of interest in RAS is from approximately 1.5 eV to about 5.0 eV (λ = 830 nm to λ = 248 nm). The light source should provide light from the infrared through to the near ultraviolet. This range has been chosen, because it covers the intermolecular electronic transitions of large conjugated molecules [9].
2. The light source should provide low noise levels. Fluctuations in the light source can contribute noise to the signal; therefore the light source must have sufficient intensity so that the signal is not buried in background noise and be sufficiently stable so that it does not contribute significantly to the noise.
3. The light source should provide adequate light intensity. Due to the relatively long optical path lengths found in the RAS spectrometer, the limited reflectance from the sample itself, and the absorption of light in optical components, it is necessary to choose a light source that is intense enough to provide a measurable signal at the detector after the associated losses have been taken into account.

The light sources that are widely available are lasers, incandescent bulbs, low-pressure gas lamps and high-pressure gas lamps. High-pressure gas lamps, like, Xenon lamps fulfill all the requirements. Therefore a 75 W high-pressure Xenon lamp (Hamamatsu C2174) was used with a stabilized power supply (Hamamatsu C6979). This provided adequate light intensity over the wavelength range of interest, as shown in the spectral output curve in figure 3.3 [18].

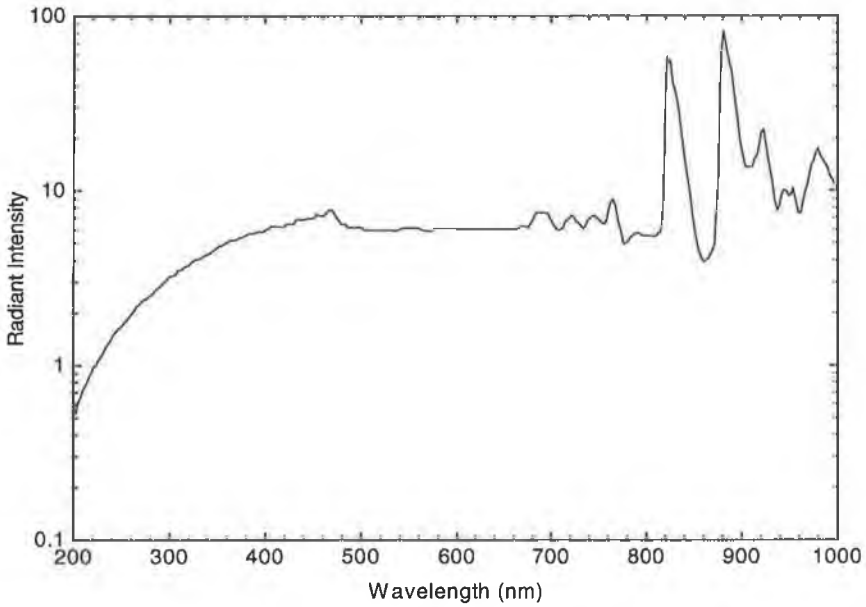

Figure 3.3 *Radiant intensity vs wavelength for the Xenon lamp* [18].

The Xenon lamp and the monochromator were aligned on an optic table and a spectral scan was performed from 1-6 eV to determine the light intensity over the energy range of the lamp. The response is shown in figure 3.4, without the correction

for the response of the grating. This spectrum indicates that there is adequate light intensity in the energy range 1.53-5.0 eV.

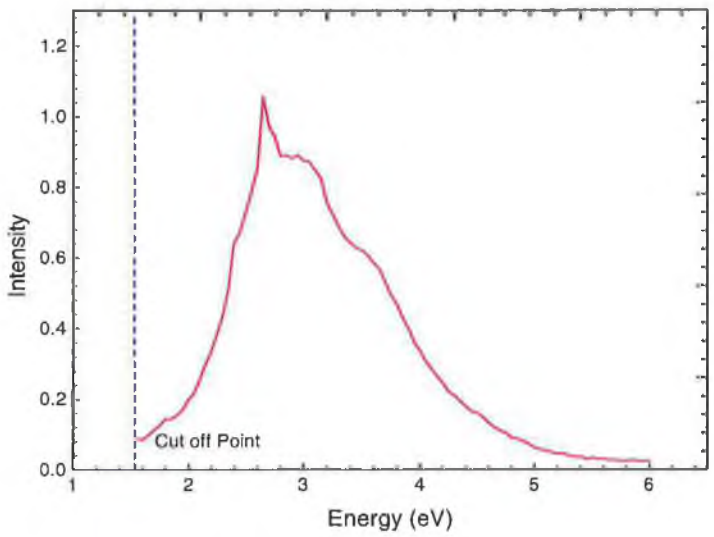

Figure 3.4 *Spectral range of Xenon lamp.*

The Xenon lamp provides a smooth and stabilised signal even after 2000 hours of operation. As a further safeguard against intensity fluctuations, it is normal practice to switch on the lamp for approximately 15-20 minutes before it is used, so that it can reach stable working temperature.

3.2.2 Mirrors

The reflectivity of the mirrors is of crucial importance. A normal concave mirror does not reflect over the entire wavelength range required. Ultraviolet enhanced aluminium coated mirrors (Coherent-Ealing Optics) with a spectral range of 1.6-5 eV were used to enhance reflection in the ultraviolet and the infrared region. The mirrors reflect about 85-90% of the incident radiation depending on the coating used, thus as few mirrors as possible should be used to maintain a useable beam intensity. Figure 3.5 shows the basic optical physics and notation that will be used in this section for calculating image distances and the mirror and sample positions.

It is essential for the light beam to be approximately parallel in order to avoid losses due to divergence. The light from the Xe-lamp must be focused onto the sample and the light from the sample must be focused onto the entrance slit of the monochromator. The geometry of the experiment limits the focal length of the mirror to specific values. It was found that a mirror of focal length 200 mm was appropriate. The diameter of the mirror is limited by the spot size from the Xenon lamp, which is about 5mm. A 50mm diameter mirror was used. The arc of the Xe lamp is directed through

an adjustable circular aperture onto the mirror. The mirror then focuses an image of the arc onto the sample. The size of the image on the sample must also be taken into account, typical sample sizes range from 5 mm-2 cm.

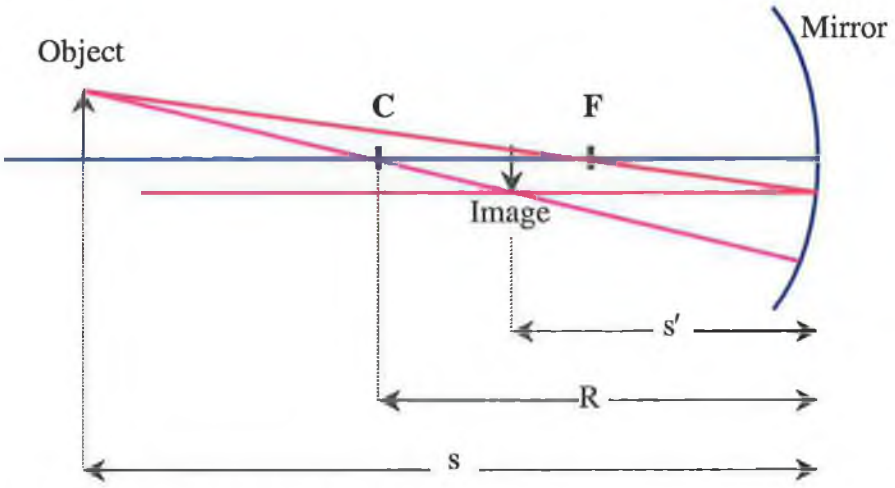

***Figure 3.5** diagram of notation used for optics.*

The relevant equations are:

$$\frac{1}{s}+\frac{1}{s'}=\frac{1}{f} \tag{3.1}$$

$$\frac{1}{s}+\frac{1}{s'}=\frac{2}{R} \tag{3.2}$$

$$\beta=-\frac{s'}{s} \tag{3.3}$$

where s is the distance from the mirror to the object, s' is the distance from the mirror to the image, f is the focal length of the mirror, R is the radius of curvature of the mirror and β is the magnification.

Table 3.1 shows a range of calculations for s, s' and β for different focal length mirrors. R and s_1 are negative due to a sign convention. s_1' is the positive going distance from the mirror to the image focused on the sample and s_1 is the negative going distance from the light source to the mirror. Due to space limitations, the distance from the mirror to the sample can be varied between 400 mm and 1000 mm. A suitable mirror can be chosen in the specified range.

f (mm)	**R** (mm)	s_1' (mm)	s_1 (mm)	β
150	-300	400	-240.0	1.7
		500	-214.3	2.3
		600	-200.0	3.0
		700	-190.9	3.7
		800	-184.6	4.3
		900	-180.0	5
		1000	-176.0	5.7
200	-400	400	-400.0	1.0
		500	-333.3	1.5
		600	-300.0	2.0
		700	-280.0	2.5
		800	-266.7	3.0
		900	-257.2	3.5
		1000	-250.0	4.0
		1200	-240.0	5.0
250	-500	400	-666-7	0.6
		500	-500.0	1.0
		600	-428.6	1.4
		700	-388.9	1.8
		800	-363.6	2.2
		900	-346.2	2.6
		1000	-333.3	3.0

Table 3.1 *Distances s, s′ and magnification β for mirrors of varying focal lengths.*

When designing a RAS apparatus a plot of s (object distance) versus s' (image distance) along with a plot of β versus s' can be helpful in finding the best compromise of distance to the lamp (compact setup) and size of the image. Examples of such plots are shown in figures 3.6 and 3.7 [13].

It is found that the best compromise is a mirror of focal length 200 mm and distance from mirror to sample ($l_{m\rightarrow sample}$) of approximately 800 mm. Figure 3.6 shows how the position of the mirror can be varied to keep the image of the lamp in focus on the sample for various sample positions, for a mirror of focal length f_1=200 mm. A movement of about 150 mm is required to cover sample distances from 400mm to beyond 1000 mm.

After passing through the analyser the light is focused onto the aperture of a fibre optic cable and coupled through the fibre into the monochromator. The lens and fibre are manufactured from quartz and transmit over the photon energy range required. The diameter of the spot illuminating the aperture of the optic fibre is approximately 3-4 mm. The light passes through the fibre to the entrance slit of the monochromator.

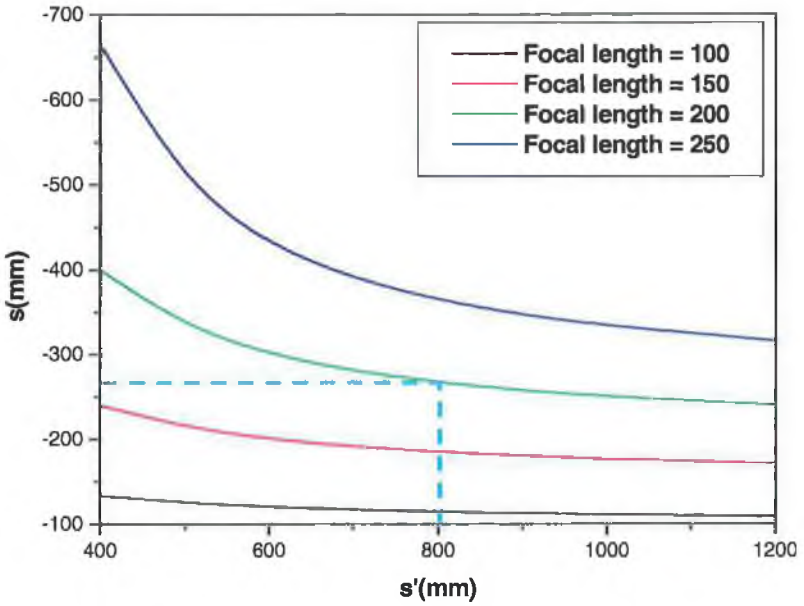

Figure 3.6 *Plot of position of lamp s as a function of the distance between the mirror and the sample.*

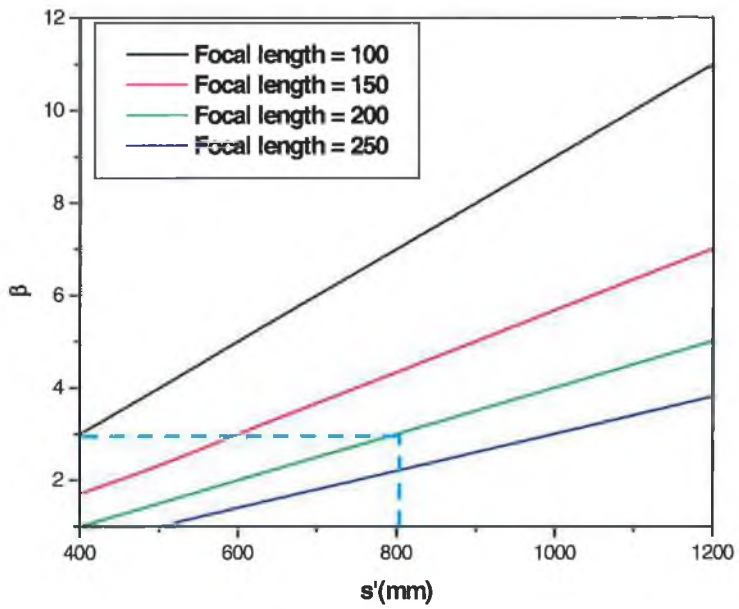

Figure 3.7 *Magnification β versus s′ for varying focal lengths of the mirror. The dotted line denotes the tolerable upper limit for β with the arc size used in the experiment.*

After the positions and focal lengths of the mirror and fibre optic have been determined the other components are arranged on the optic table. If space is very limited a compact setup can be implemented by folding the light path with the use of additional mirrors, but the reduction in light intensity must be taken into account. This reduction will depend on the mirrors used and the value depends on the angle at which the light beam is incident on the mirrors. The mirrors can only be placed between lamp and

polariser or between analyser and monochromator because they can influence the polarisation of the light.

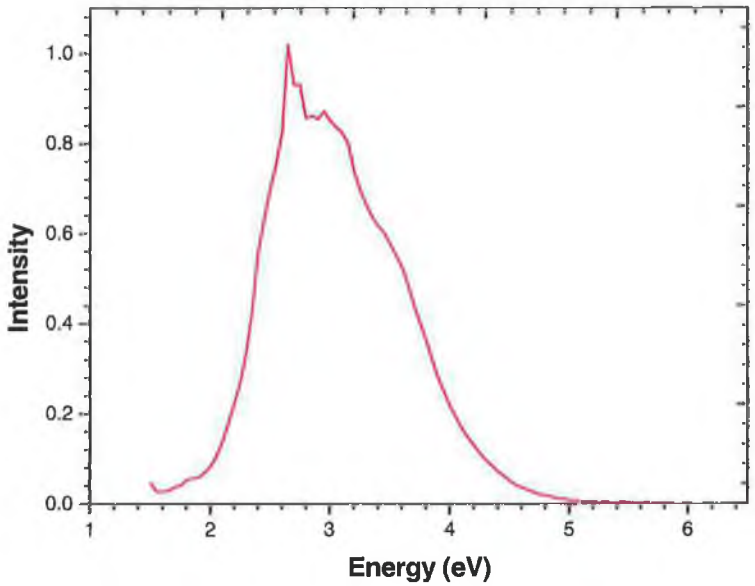

***Figure 3.8** Intensity of light reflected from mirror as a function of photon energy.*

A spectral scan was performed on the mirror to prove that there was adequate light intensity over the required energy range. The Xenon lamp, the monochromator, and the mirror were aligned on the optic table and a spectral scan was performed from 1.5-6eV. The measured reflectivity curve is shown in figure 3.8 and demonstrates that the mirror has sufficient intensity between 1.6-5 eV. The mirror was positioned using an adjustable mirror mount (Newport Optics).

3.2.3 Polariser / Analyser

The necessary requirements for a suitable polariser and analyser are

1. The polariser and analyser should have good transmission in the 1.5 eV-5.0 eV energy range.
2. The polarizer should have a high extinction ratio. The extinction ratio of a polariser is defined, as the extent to which light is transmitted on passing through crossed polarizers. Typical values are approximately 10^{-5}.

Polarisers that are widely available include 'Sheet Polarisers' and 'Prism Polarisers' namely, Glan-type, Rochon Polarisers and Wollaston Polarisers. Where possible, the polariser and analyser should be of similar quality.

Sheet polarisers do not have a high extinction ratio (~10^{-2}) and therefore are unsuitable. Prism polarisers take advantage of double refraction, a phenomenon

observed in birefringent crystalline materials which have different refractive indices for light polarised in different directions. In uniaxial crystals two refractive indices are observed. One, n_e, is observed for rays polarised parallel to the unique symmetry axis of the crystal (extraordinary rays) and the other, n_o, is observed for rays polarised perpendicular to the symmetry axis (ordinary rays). Therefore, two in-phase components entering a birefringent material will be out of phase after passing through it. After analysis of all the different types of prism polarisers available, it was decided that the quartz Glan-Taylor polariser was the most suitable polariser for the spectrometer.

3.2.3.1 Glan-Taylor Polariser

The Glan-Taylor polariser is composed of two calcite or quartz prisms separated by an air gap. Their optic axes are parallel as shown in figure 3.9. This type of prism takes advantage of the fact that the critical angle for the extraordinary ray is greater than that of the ordinary ray. Thus for suitable angles the extraordinary ray suffers total internal reflection, but the ordinary ray does not.

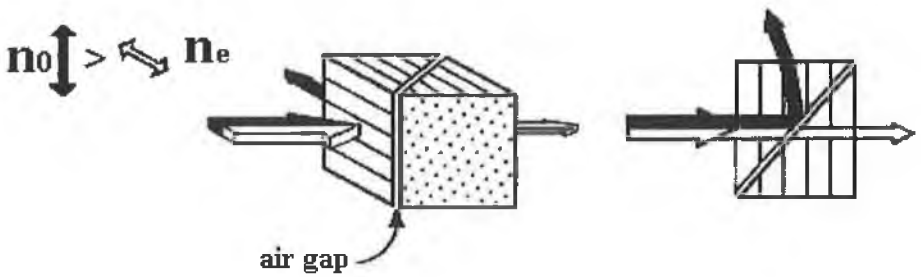

Figure 3.9 *Glan-Taylor Polariser.*

These air spaced polarisers are suited for a wide variety of applications, particularly with collimated input beams. Standard Glan-Taylor polarisers with no side escape windows are suitable for low to medium power applications where the rejected beams are not required. The spectral transmission range of Glan-Taylor polarisers is from 220 nm to beyond 2600 nm depending on the manufacturing material. Because the total internal reflection method works for only a small range of angles, the acceptance angle of this type of polariser is very small. At best, light outside the acceptance cone is lost even though it is of the desired polarization. This leads to loss of efficiency. Therefore the acceptance angle should be limited for Glan-Taylor polarisers to 5°. See figure 3.10 [19] for pictorial representation of the acute acceptance angle for this polariser. Glan-Taylor polarisers have an extinction ratio of the order of ~10^{-5}.

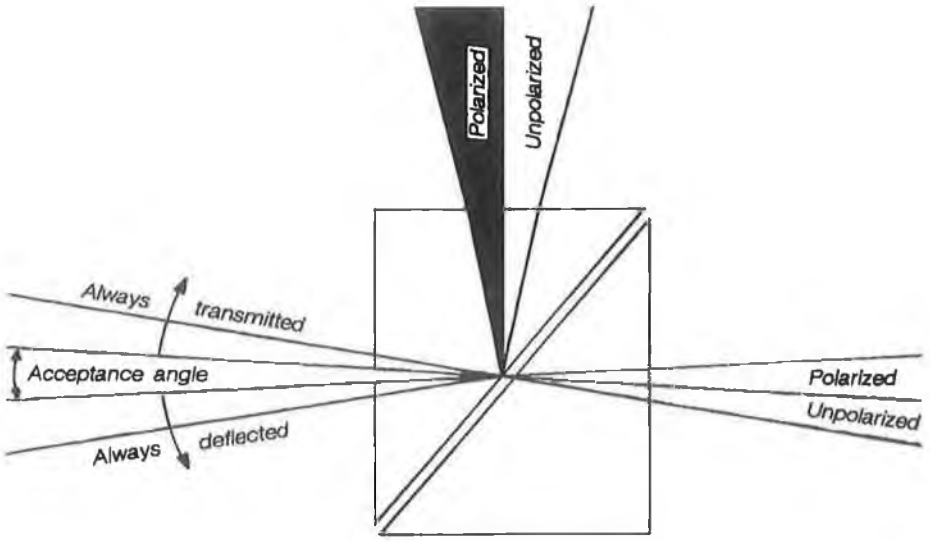

Figure 3.10 *Diagram of Acceptance angle of Glan-Taylor Polarisers*[19].

A spectral scan, figure 3.11, was performed on the polarising prisms to show that there was adequate light intensity over the required energy range and that the polarisers purchased were in agreement with the manufacturers specifications.

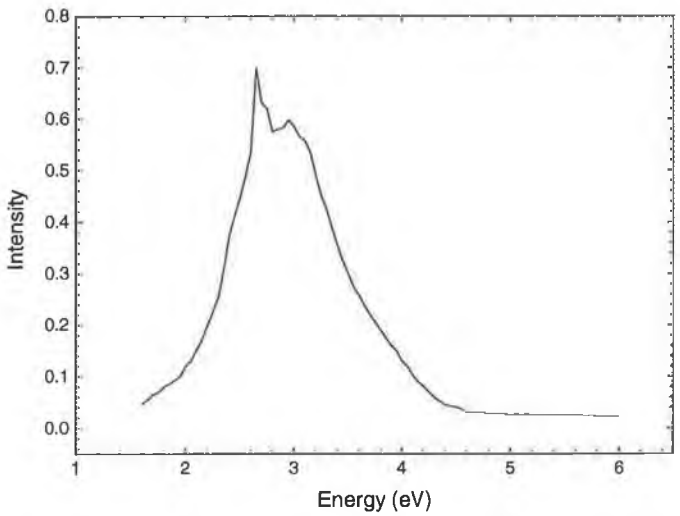

Figure 3.11 *Spectral Scan of polariser and Analyser.*

3.2.4 Low-Strain Window

Light entry to a vacuum chamber is though a view-port, which may have a strain-induced birefringence and this can cause a large offset in the signal. The view port birefringence is due to many factors including the manufacturing process of the window and also securing the flange to the vacuum vessel.

It is possible to obtain windows that are specially fabricated to reduce the strain effects (Bomco). The usual arrangement is cylindrical in shape with the quartz entrance/exit window protruding about 10 cm from the secured flange, as shown in

figure 3.12. This configuration distributes pressure along the length of the cylinder rather than across the face of the cylinder, which is manufactured from fused silica for transmission in the ultraviolet.

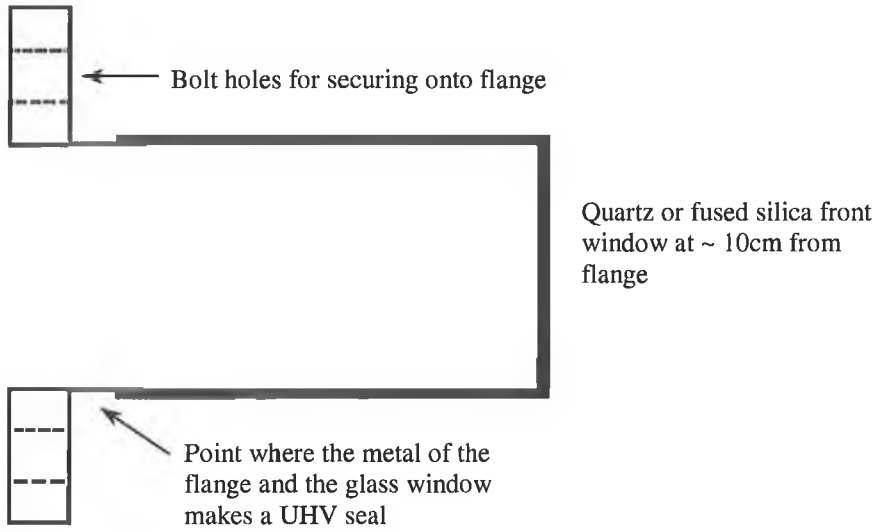

***Figure 3.12** Low-Strain Window.*

Although, this configuration improves the signal quality, it does not remove the strain completely. If the strain is assumed to be small, calibration spectra may be recorded to correct the detected signal.

If the sample is aligned so that the axes of interest are lined up along the x and y axes, the RAS signal is:

$$\left.\frac{\Delta r}{r}\right|_{0^\circ} = \frac{r_x - r_y}{r_{bulk}}$$

$$r_{bulk} = \frac{r_x + r_y}{2}$$

If the sample is then rotated through 90° such that the x and y axes are interchanged, the signal becomes:

$$\left.\frac{\Delta r}{r}\right|_{90^\circ} = \frac{r_y - r_x}{r_{bulk}} = -\frac{r_x - r_y}{r_{bulk}}$$

This is the inverse of the original signal. If the two signals are added together they should equal to zero. However, if the strained window lies in the optical path of the beam it adds an additional window response to the detected signal. Since the window is not rotated with the sample, the window response remains the same at 0° and 90°. Adding two sample responses cancel each other out completely but the two window responses add together. Although this method of finding the correction factor for the

window is not strictly correct mathematically, it works well in practice. The correction factor is therefore

$$\frac{\Delta r_{window}}{r} = \frac{RAS_{0°} + RAS_{90°}}{2} \tag{3.4}$$

where $RAS_{0°}$ and $RAS_{90°}$ are the RAS responses at 0° and 90° respectively. The effect of window strain can be corrected for in the software (c.f. section 3.5).

3.2.5 Photoelastic Modulator

A photoelastic modulator (PEM) is an instrument used for modulating or varying the polarization of a beam of light. A PEM90 photoelastic modulator from Hinds Instruments with an I/FS50 oscillator head was chosen. The principal of operation of the PEM is based on the photoelastic effect, in which a mechanically stressed sample exhibits birefringence proportional to the induced strain.

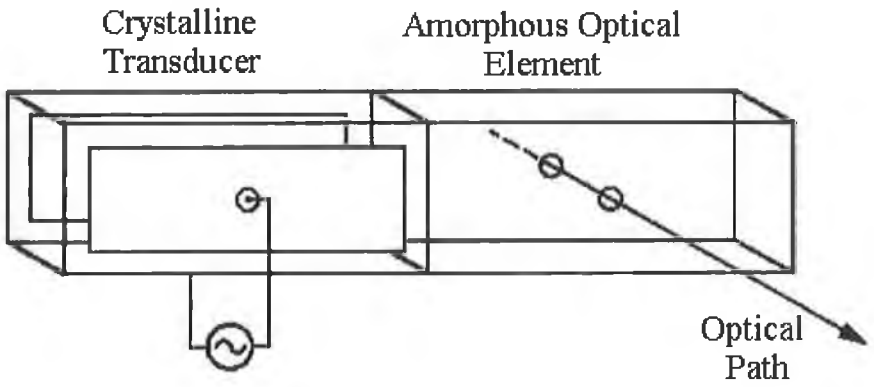

***Figure 3.13** Photoelastic Modulator* [20].

During operation, the PEM quartz crystal is compressed by a piezoelectric transducer, which is driven by a control voltage, figure 3.13 [20]. The driving voltage, which is an AC driven piezoelectric quartz transducer, cemented to one end of the crystal, establishes a uniaxial sinusoidal standing wave in a rectangular block of fused quartz. The oscillating strain is accompanied by an oscillating induced birefringence so that the fused quartz crystal acts as a linear retarder with an alternating (time-varying) relative retardation [21]. The direction of the strain determines the direction of the fast or slow axes of the modulated retarder. The amplitude of the sinusoidal retardation is proportional to the strain and, consequently, to the voltage applied to the transducer.

The AC driven voltage may not be purely sinusoidal, resulting in a non-sinusoidal vibration in the crystal. As a result there are higher harmonics in the PEM.

To analyse the content of higher harmonics in the signal a fast Fourier transform (FFT) of the transmitted light was measured as shown in figure 3.14. The FFT shows the relative strength of the first, second and third harmonics.

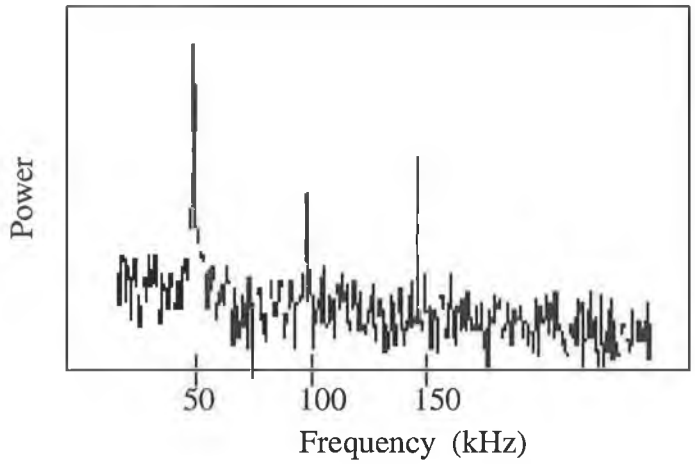

Figure 3.14 *FFT of a signal transmitted through the PEM showing 1st, 2nd and 3rd harmonics.*

The PEM may also have some residual birefringence associated with it as a result of the mounting. This will add a constant value on to the PEM retardation, which can be represented by the equation:

$$\varphi = \delta_m \sin(\omega t) + \delta_0 \tag{3.5}$$

Where δ_0 is the constant strain and δ_m is the phase amplitude, such that $\delta_m = \pi$ corresponds to half-wave modulation. There is very little that can be done to correct this, as it is inherent to the PEM. However it is not an important factor when using PEM for RAS measurements.

3.2.6 Monochromator

Listed below are all the necessary requirements for obtaining a suitable monochromator:

1. The monochromator should cover the energy range from 1.6 eV to 5.0 eV.
2. The monochromator should be able to step in energy increments of ~0.005 eV or greater.
3. The monochromator should have RS232 or IEEE interface capabilities.

The SpectaPro-150 Monochromator (SP-150) from Acton Research Corporation fills all the criteria needed for a RAS system. It features a rotating turret table that can hold two gratings, a single grating was chosen to cover the energy range required. There

are 1200 grooves/mm with a blaze of 300 nm on the grating. Figure 3.15 shows the response of this grating [20]

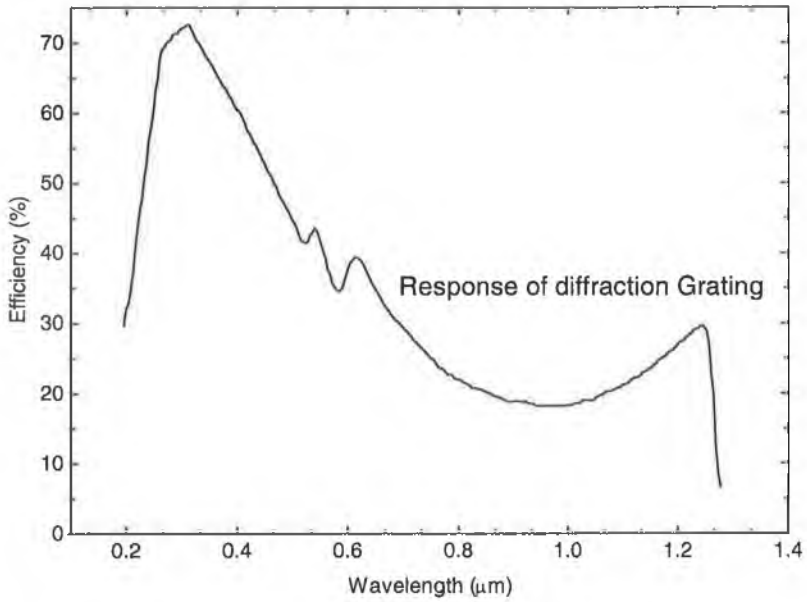

Figure 3.15 *Response of monochromator diffraction grating* [20]

The monochromator also features adjustable entrance and exit slits, which can be used to provide a suitable trade-off between spectral resolution (improved by using smaller slit width) and light intensity (improved by using larger slit width).

3.2.7 Photodetector

The criteria for choosing a detector are:

1. The detector operates from 1.5 eV to 5.5 eV.
2. The detector should have a frequency response as determined by the PEM.
3. The detector should have a linear relationship between light level and output current.
4. The detector should have low noise levels.

A photomultiplier tube was chosen. The required frequency response is determined directly from the photoelastic modulator. The PEM operates at ω = 50 kHz and 2ω = 100 kHz, therefore it is necessary for the detector to have a frequency response that is flat up to at least 100kHz. An ARC photomultiplier tube P2(R928) and high voltage power supply PD-439 were purchased from the Acton Research Corporation.

3.2.8 Preamplifier, Low-Pass & High-Pass Filter

After the light has passed through the monochromator and is detected by the photomultiplier tube, the ω and 2ω (Im and Re respectively) parts of the signal must be separated using a filtering and pre-amplifier circuit.

The preamplifier consists of two additional filter circuits, a low-pass filter is used to separate out the DC component and a high-pass filter is used to separate out the AC component of the signal. The preamplifier has a gain of twenty-five which is chosen to match the 13 bit resolution (± 10.54 V) on the lock-in amplifier.

The preamplifier and filter gains are adjusted so that the AC and DC outputs are not affected by an offset that would lead to sizable errors in the measured signal.

The preamplifier converts the photodetector current into a voltage output that is connected to the lock-in amplifier input. The preamplifier, and low and high-pass circuits were constructed and diagrams of these are shown in Appendix A [22].

3.2.9 Lock-In Amplifier

A lock-in amplifier is used to measure the AC signal from the detector output. A 50 KHz drive signal from the PEM controller is used as the reference signal for the lock-in amplifier. An Analog to Digital Converter (ADC) on the lock-in amplifier is used to detect the DC offset in the signal, in order that the quantity $\Delta U_{\omega,2\omega}/U_{dc}$ is the AC signal at ω and 2ω divided by the DC signal can be evaluated. To maximise the output from the lock-in, the input signal must be in phase with the reference wave, therefore a phase adjustment has to be performed before a full spectrum can be recorded.

A SR510 lock-in amplifier was purchased from Stanford Research Systems. It featured two digital to analog converter and four analog to digital converters. One of these was used to measure the DC signal. This lock-in has both an RS232 and an IEEE interfaces.

3.2.10 Serial Port Multiplexer

The RAS spectrometer requires three serial ports to operate automatically but the computer has only two serial ports. Therefore a serial port multiplexer was constructed [23]. Four serial ports on the multiplexer can be controlled from one serial port and one parallel port on the computer.

The parallel port controls the link from the computer to each of the three controllable devices, the PEM, the lock-in amplifier and the monochromator. When the

link is open information can be sent to the device via the serial port. Receiving any information from the devices operates in the same way. The parallel port opens the link and information is sent to the computer via the serial port. Therefore each of the devices can be operated sequentially to record a spectrum. A circuit diagram for the serial port divider can be found in appendix A [23].

3.3 Operation of Spectrometer

The output from the photomultiplier tube consists of an AC signal superimposed on a DC offset shown in figure 3.16. The high-pass and low-pass filters split the signal up into AC and DC components. The lock-in amplifier measures the amplitude of the AC component. An ADC on the rear of the lock-in amplifier records the DC component. The drive signal from the PEM is connected to the input reference on the lock-in amplifier.

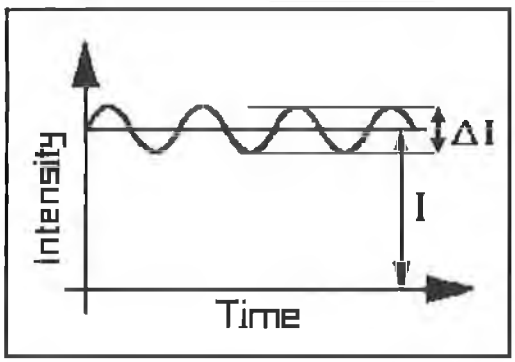

Figure 3.16 *DC signal superimposed on AC signal.*

RAS measurements are performed with the spectrometer using the following procedure:

1. The lock-in amplifier is set to the correct frequency, f or 2f depending on whether the imaginary or real signal is measured. The phase must also be set correctly and in general it is different for the ω and 2ω signals. The software can perform the phase setting automatically for the ω and 2ω signals before the scan is run.
2. The time constant on the lock-in amplifier is set to an appropriate value. The time step between successive data acquisitions should be at least a factor of three greater than the time constant of the lock-in.
3. The retardation of the PEM is set to the correct value for the ω and 2ω signals, (as outlined in section 2.4.1) and the voltage on the modulator is adjusted to the appropriate value, which depends on the photon energy.

4. The high voltage level on the photomultiplier tube is set to an appropriate value so that the DC level is measurable and the signal does not saturate. A DC level of approximately 250 V is sufficient for this.
5. The AC and DC components of the signal are measured with the lock-in amplifier. In the absence of alignment errors and window strain the real signal (2ω component) is calculated according to

$$(1.4544)\left(\frac{AC}{DC}\right) = \mathrm{Re}\left(\frac{\Delta\hat{f}}{\hat{f}}\right) J_2 \delta_m \tag{3.6}$$

and the imaginary signal (ω component) according to

$$(1.2162)\left(\frac{AC}{DC}\right) = \mathrm{Im}\left(\frac{\Delta\hat{f}}{\hat{f}}\right) J_1 \delta_m \tag{3.7}$$

The RAS spectra scan can be performed in two ways. Either the real and imaginary signals can be obtained together during a single scan or the real and imaginary signals can be obtained individually in separate scans.

3.3.1 Computer & Control Software

An IBM 386SX computer was used to control the RAS spectrometer. The data acquisition program was developed in-house using Basic45 as the programming language. Basic45 was chosen because it is an uncomplicated language to learn and it has built-in graphics.

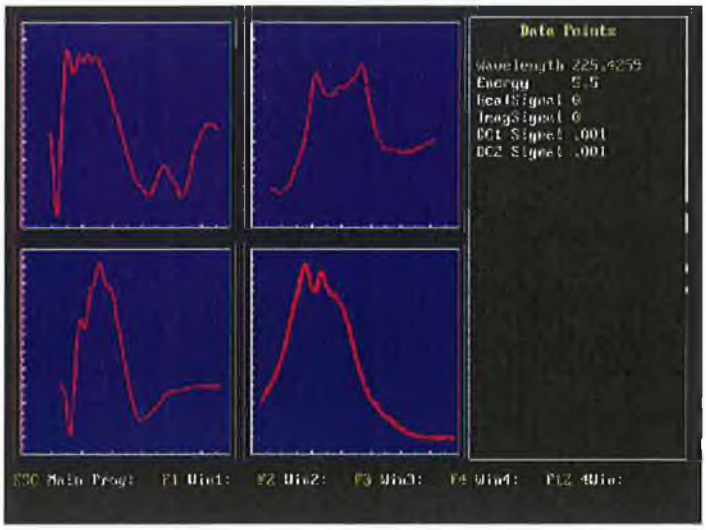

Figure 3.17 *Picture of Acquisition software for RAS spectra.*

The software controls the lock-in amplifier settings, the photoelastic modulator, the monochromator and the high voltage supply for the photomultiplier tube. It features subroutines in drop down menus for changing the settings on the monochromator, the

lock-in amplifier and the photoelastic modulator. It also features a 'phase' scan subroutine; this calculates the phase difference between the reference signal from the PEM and the detected signals at ω and 2ω. The AC and DC signals are read in from the lock-in amplifier and recorded in an output file and plotted in real time during data acquisition as shown in figure 3.17.

3.3.2 Calibration

Aspnes measured the reflectance anisotropy of the (110) surfaces of Silicon and Germanium. Mochán and Barrera [24] performed calculations of the predicted anisotropy for the Ge(110) surface due to the local surface field effects. There is remarkably good agreement between the calculated anisotropy due to the local surface field effects and the experimentally measured anisotropy. Aspnes developed this further [1] and concluded that additional contributions to the anisotropy are surface excitonic effects and a bulk related effect due to the non-zero momentum of incident photons.

Experimental spectra for the real and imaginary signals of naturally oxidized Si(110) are shown in figure 3.18. These reflectance anisotropy lineshapes are regularly used as calibration curves for RAS spectrometers.

In order to calibrate the spectrometer for experimental measurements, naturally oxidized silicon (110) was used as a test sample. The calibration curves obtained experimentally from our spectrometer are shown in figures 3.19 and 3.20. They agree well with the experimental lineshapes measured by Aspnes et. al. [1] shown in figure 3.18.

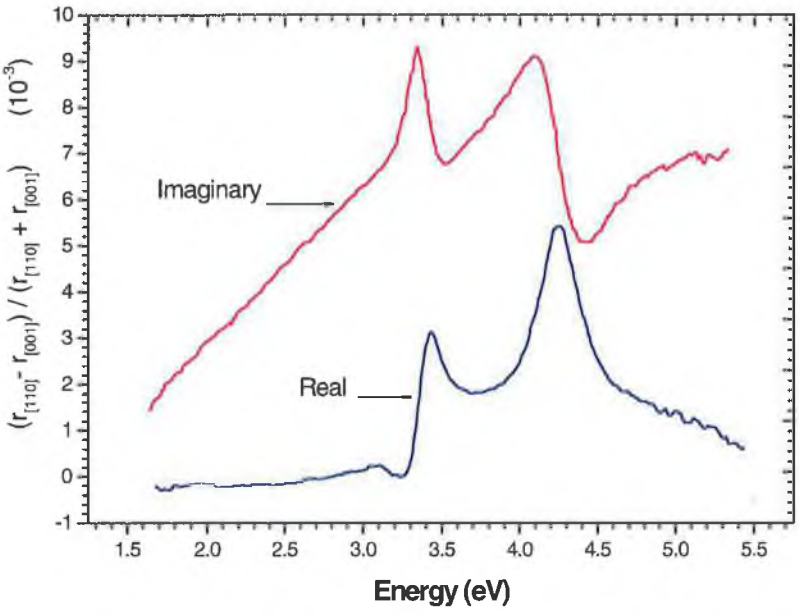

Figure 3.18 *Real and Imaginary spectra for naturally oxidized Si(110)* [1].

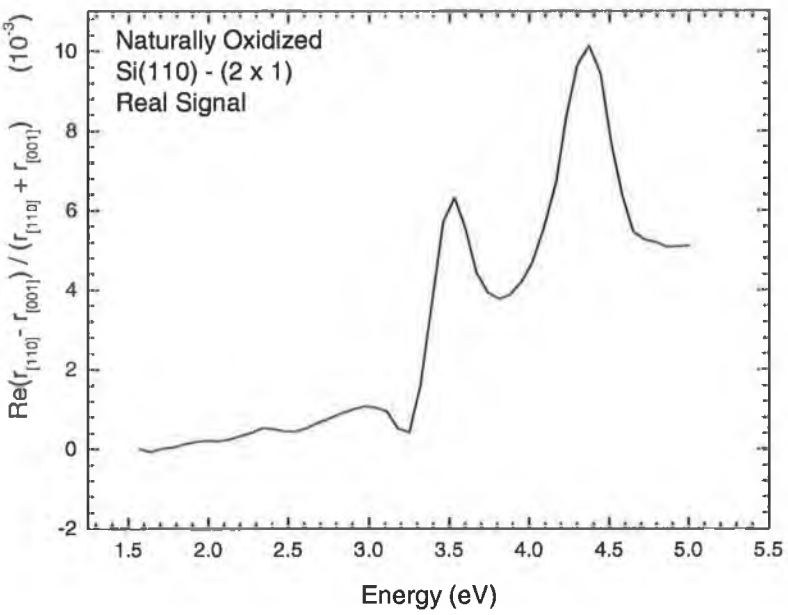

Figure 3.19 *Experimentally obtained real signal for Si(110).*

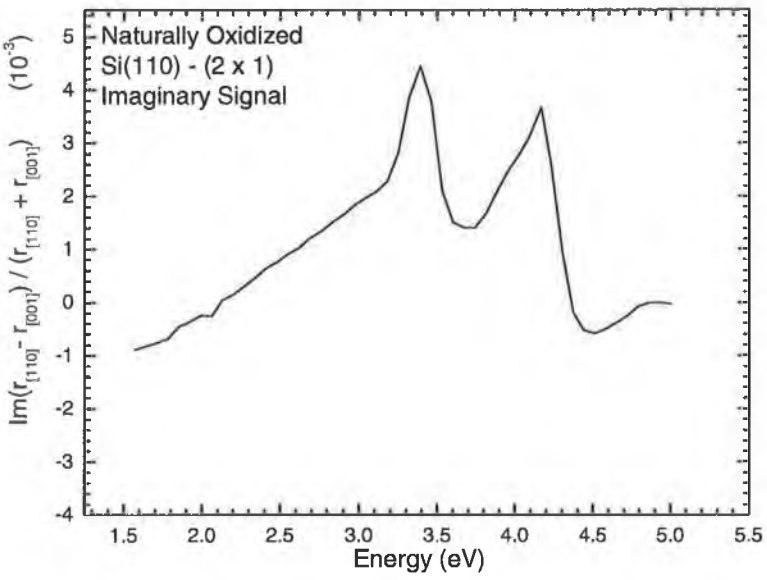

Figure 3.20 *Experimentally obtained imaginary signal for Si(110).*

3.4 RAS Experimental Setup

The RAS system is mounted on an Ultra High Vacuum chamber by means of an adjustable table, figure 3.21. The table can be adjusted in the x, y and z directions. It is possible to position the RAS apparatus so that measurements can be carried out on samples in UHV. Once the RAS system was aligned with the sample it was not moved from that position until the conclusion of the experiment. The sample was moved during the experiment to argon bombard and anneal but more precise positional control on the

manipulator allowed the sample to be replaced in the same position after each movement.

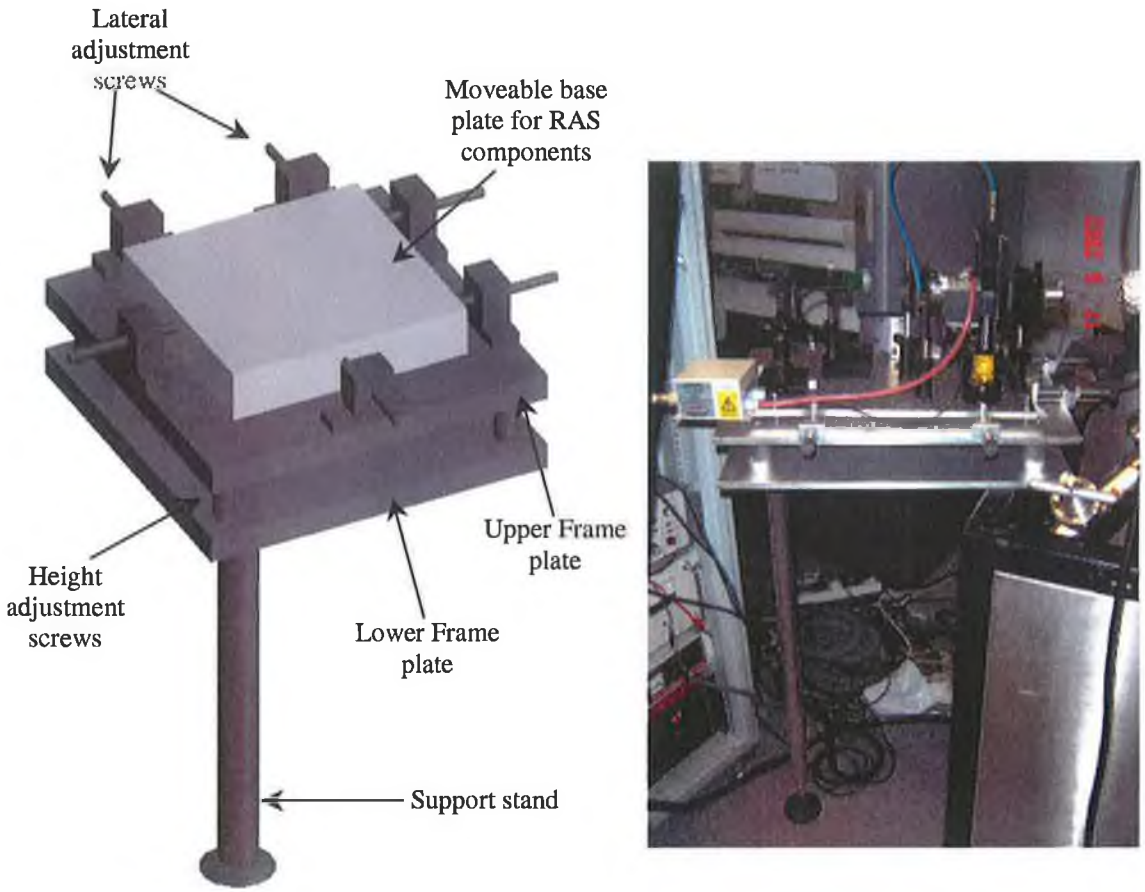

Figure 3.21 *diagram and picture of the position table.*

3.5 STM Experimental Setup

An STM operates by measuring a small tunnel current (~0.1-10 nA) between two electrodes spaced a few angstroms apart with a potential difference (1 mV to ~5 V) applied between them. One of the electrodes is the sample under investigation; the other is an atomically sharp tip (usually made of tungsten or a platinum iridium alloy). As shown in chapter two the current decays exponentially with the distance between the two electrodes. At a specific separation a tunnel current can be measured. A topographic image of the sample surface can be obtained by measuring the current as the tip is scanned across the surface. STM tips manufactured from tungsten and Pt/Ir were purchased from Omicron and were used to acquire atomic scale images of the surfaces under investigation.

3.5.1 Piezo Scanner

Scanning is achieved by using a piezoelectric transducer, which is used to control the small vertical (z) and lateral (x, y) displacements of the tip. The tip is placed at the top of the piezo tube as shown in figure 3.22. By convention the z-axis is taken as normal to the sample surface and the surface itself is then the xy plane.

The ceramic scanner is manufactured from lead zirconate titanite (PZT), metallized on the outer and inner surfaces and poled in the radial direction [25]. The outside metal coating is sectioned into four quadrants. The extension of a block of piezoelectric material of length L and thickness h if a voltage V is applied across h is given by

$$\Delta L = \frac{d_{31} V L}{h} \tag{3.9}$$

For commercial piezo-ceramics the d_{31} coefficients lie in the range 1-3 Å/V. Vertical (z) motion can be achieved by applying the same voltage to all four outer electrodes and grounding the inner electrode. Lateral (x or y) motion can be achieved by applying equal and opposite voltages to the two opposite vertical outer electrodes while keeping the other two horizontal electrodes grounded or at constant voltage. In practice, the STM control unit produces four high voltage outputs: Z-X, Z+X, Z-Y and Z+Y. The Z voltage typically ranges from –130 V to +130 V and the X and Y voltages range from –135 V to + 135 V on the Omicron Scala system.

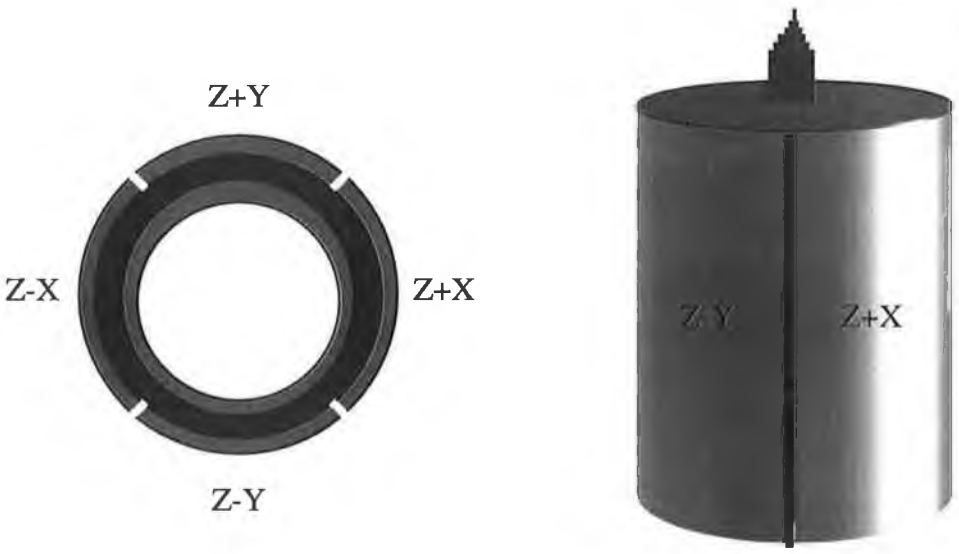

Figure 3.22 *Piezo tube scanner, (a) Top View, (b) side view.*

3.5.2 Vibration Isolation System

Effective vibration isolation is one of the most critical elements needed in order to maintain the tunneling gap of a few angstroms between the tunneling tip and the sample surface [26]. The typical corrugation amplitude on a metal surface is approximately 0.1-0.5 Å. Therefore disturbances from external vibrations must be reduced to less than 0.01 Å [27]. Two conditions must be fulfilled to achieve low external vibration.

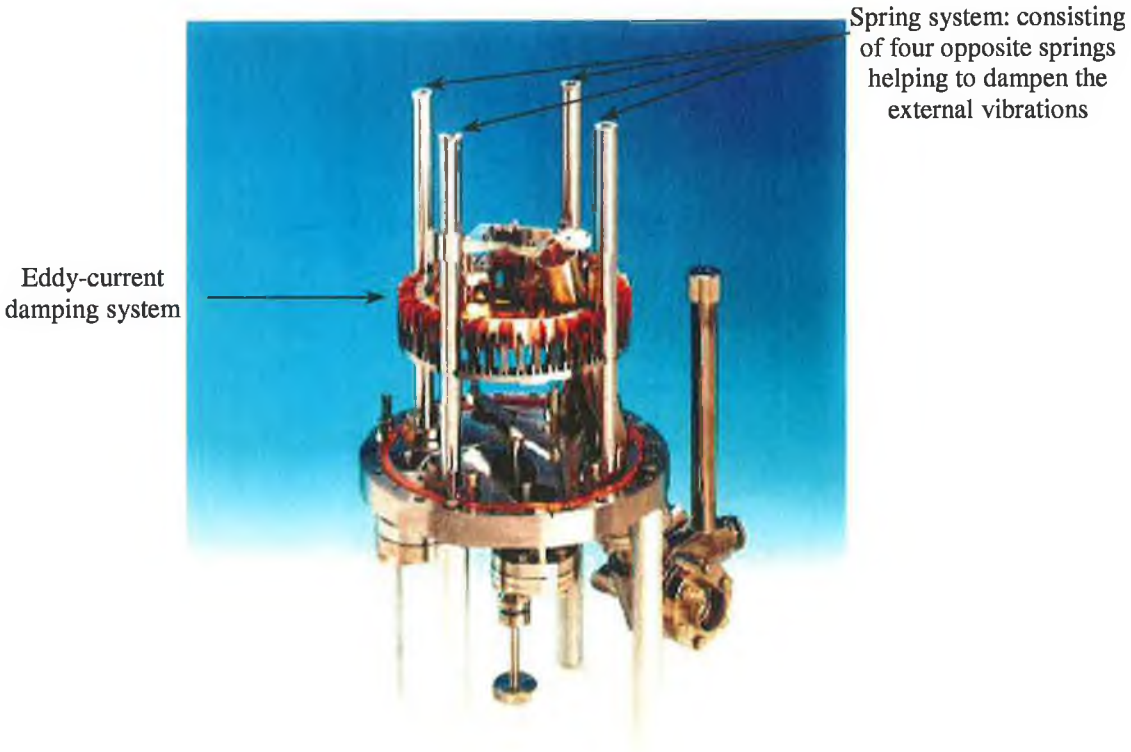

Figure 3.23 *Picture of STM showing spring damping system and eddy current damping system* [29].

- The STM head should have a high resonance frequency (>1 KHz) i.e. it should be small, light and rigid as possible.
- The STM should be mounted on a vibration isolation system, which has a low resonance frequency (~1 Hz), which effectively damps out vibrations.

Most modern STMs use coiled spring systems [26] with eddy-current damping [28] or else viton-metal stack isolators. Spring systems can be designed with resonance frequencies of 1Hz or lower but do not provide much damping. For this reason, eddy-current damping is usually used in conjunction with these systems. The spring system and the eddy current damping system on the Omicron VT-STM is shown in figure 3.23 [29].

3.5.3 Scanning Modes

There are two modes of operation of the STM: constant current mode or constant height mode. Both modes are shown in figure 3.24. In constant height mode, a constant voltage is applied to the z-piezo and the tip is scanned across the surface at a constant height while the current varies with tip-sample separation. Although this method allows rapid scanning, it can only be performed on atomically flat surfaces to avoid the tip crashing into step edges or other protrusions. Since the tunnel current varies by an order of magnitude for a tip sample separation of 1 Å, this mode requires a tunnel current amplifier with a large input dynamic range.

In constant current mode, the tunnel current is kept constant by a feedback system, as shown in figure 3.25. The tip traces out the shape of the surface as it scans across the sample. The changes in the tip displacement (caused by the z-piezo extending or contracting in order to stabilize the tunnel current) provide a topographic image of the surface.

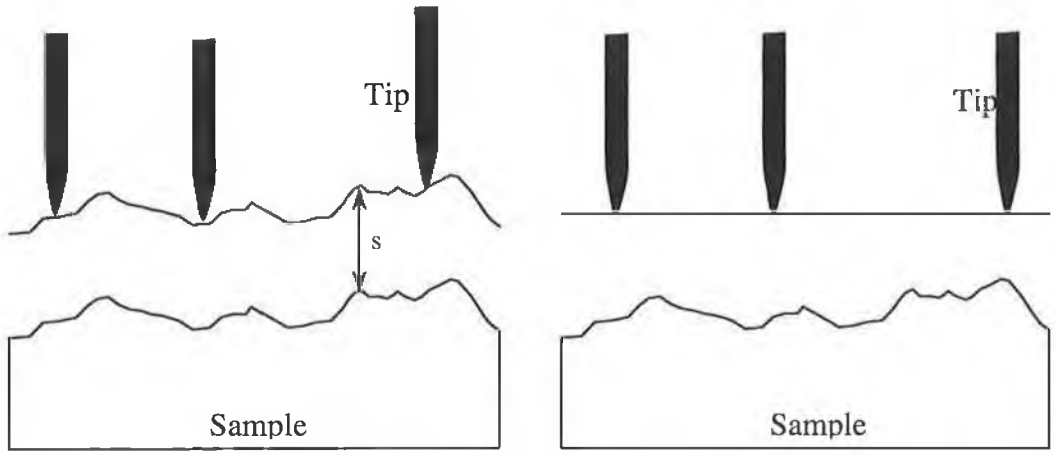

Figure 3.24 *shows the two modes, (a) constant current mode, (b) constant height mode, that the STM can operate.*

3.5.4 Feedback Mechanism

The tunnel current is first amplified and then converted into a voltage. The distance dependence is then extracted by passing the signal through a logarithmic amplifier and the output signal is compared to a preset value, which corresponds to a desired gap width, s. The difference signal is fed into the z-piezo high voltage amplifier and the tip is moved towards or away from the surface to bring the gap width (and hence the tunnel current) back to the desired value, i.e. the system operates in negative feedback mode. A topographic image can be attained from the changes in the z-piezo displacement during the scan assuming the barrier height remained constant over the

scan area. In practice, the logarithmic amplifier, the comparator and the high voltage amplifiers shown in figure 3.25 are contained in the STM Scala control unit, which also handles data acquisition and image display.

The main limitation of the constant current mode is the stability of the feedback loop. If the total phase shift of the system exceeds 180°, the feedback becomes positive and the tip begins to oscillate. In practice, the cut off frequency of the feedback loop i.e. the maximum frequency at which it can operate in negative feedback is in the kHz range. Therefore the output of the I-V converter is fed into a low pass filter to suppress the high frequency signals. The scan speed is limited by time delays within the circuit, for example the finite time delays of the piezos, which could cause oscillations. Ideally the overall gain of the feedback loop should be as large as possible so that the tip accurately follows the contours of the sample surface. However, a compromise value is often chosen to ensure that the gain is less than unity, above the cut off frequency. The cut off frequency must be below the mechanical resonance frequencies of the STM head to prevent feedback instability due to transmitted vibrations.

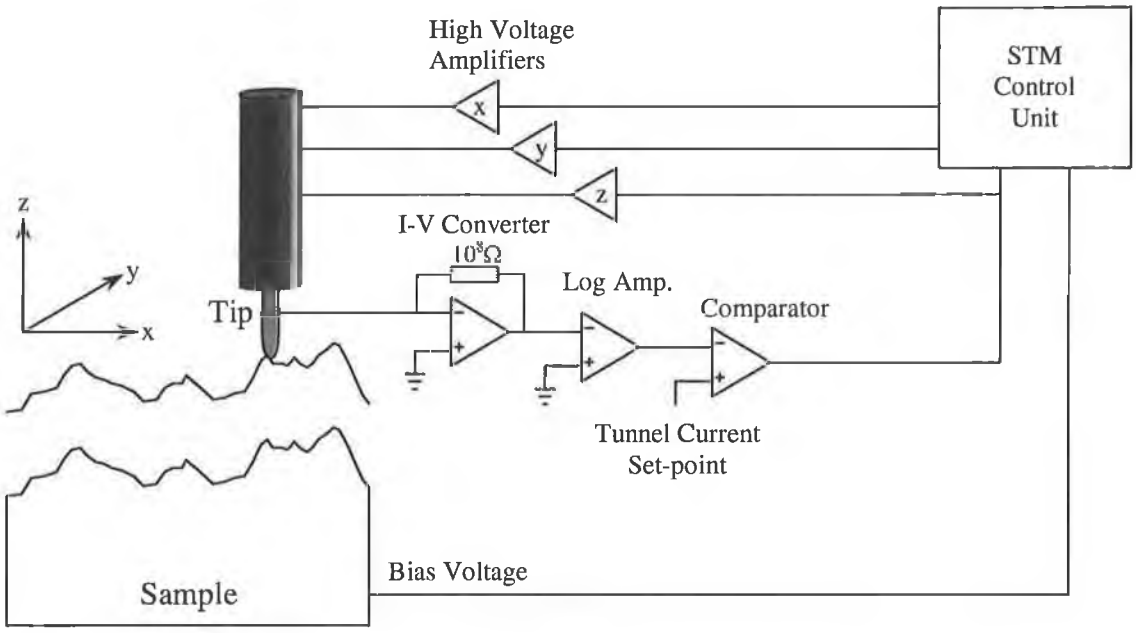

Figure 3.25 *Feedback mechanism for constant current mode STM.*

3.5.5 UHV System

The UHV system consists of three main chambers: the preparation chamber, the analysis chamber and the room temperature STM chamber. Samples and tips can be

loaded through a fast-entry lock attached to the preparation chamber. The layout of the system is shown in figure 3.26(a), (b) and (c) [29].

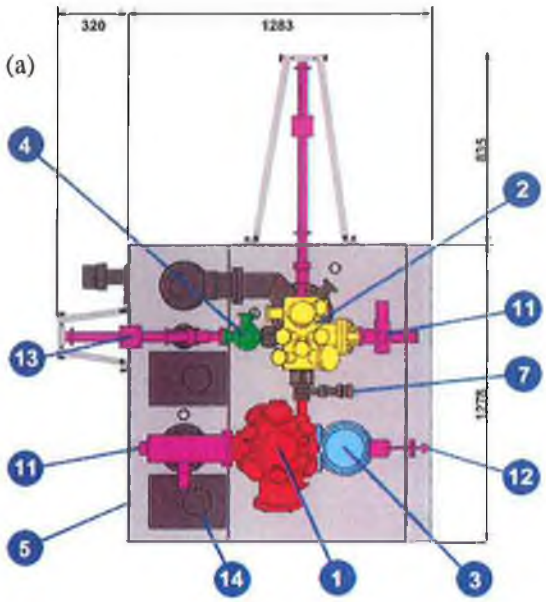

1. Analysis Chamber
2. Preparation Chamber
3. Room temperature STM chamber
4. Fast entry load lock
5. Bench Assembly
6. Gate Valve (pneumatic)
7. Gate Valve
8. All metal Angle Valve
9. Turbo Molecular Pump
10. Titanium Sublimation Pump
11. Manipulator
12. Wobble Stick
13. Magnetic Transfer Rod
14. Heater Assembly

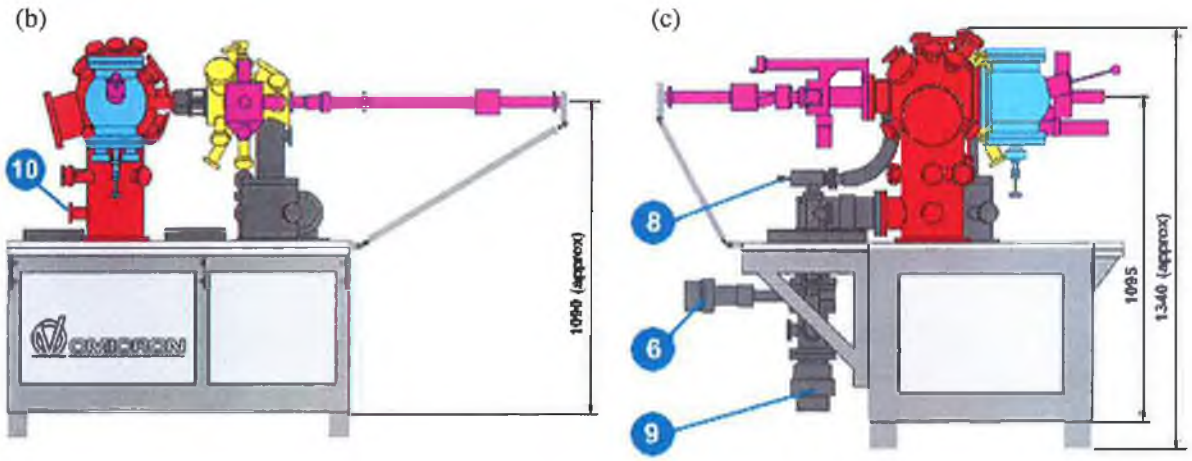

Figure 3.26 *Diagram of UHV system showing (a) top, (b) side and (c) end views*[29].

3.5.6 STM Sample Holders

The sample plate is manufactured from tantalum with a keyhole at the front so that it can be captured and moved within the UHV system. The Au sample was reworked so that two tubular incisions were inscribed in the back of the single crystal, shown in figure 3.34. For STM mounting tantalum wire was threaded through and spot-welded to the sample plate, thus fixing the sample to the plate, shown in figure 3.27. A different type of sample holder with direct current heating was used to mount the Si(111). The sample holders were purchased from Omicron Vacuumphysik [29].

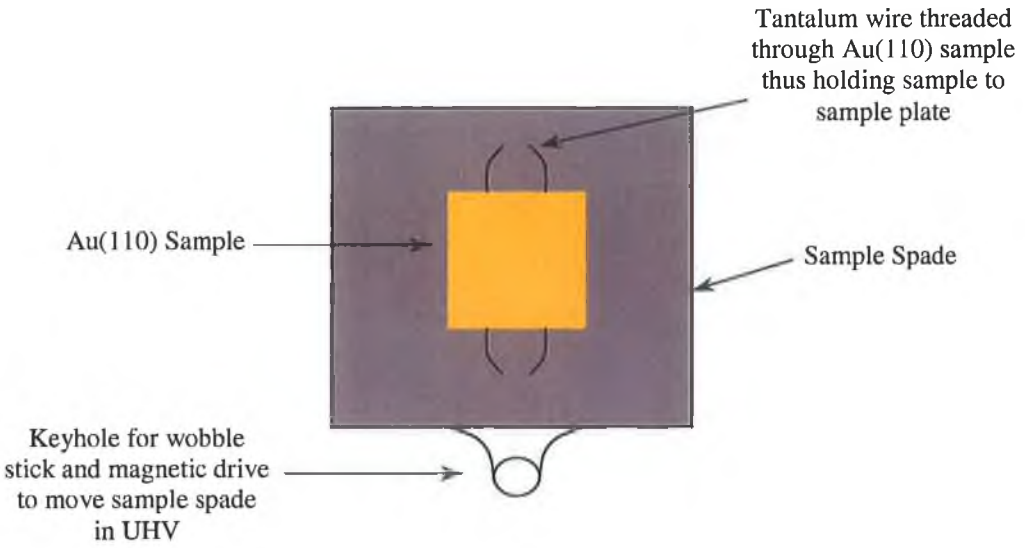

Figure 3.27 *Sample Plate showing how Au(110) sample was fixed to it.*

3.6 Low Energy Electron Diffraction (LEED)

3.6.1 LEED Experimental Setup

LEED experiments were performed in a titanium sublimation pumped ultra high vacuum chamber shown in figure 3.26 equipped with a rear view Omicron Spectaleed system, with an operating base pressure of 1×10^{-10} mbar. The LEED apparatus is shown in fig 3.28 together with a schematic diagram.

The LEED has been fitted with a Lanthanum Hexaboride Filament (LB_6). This filament has good emission characteristics at low power inputs. It yields a higher emission current and lower energy spread than a thoriated tungsten filament.

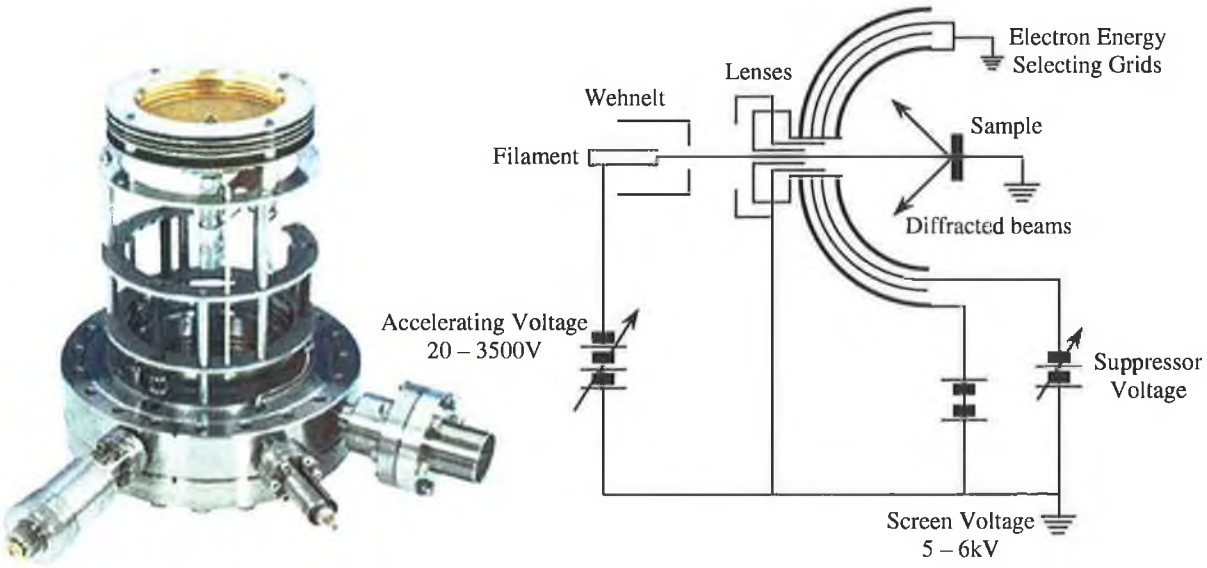

Figure 3.28 *Picture and schematic diagram of LEED system* [29].

The electrons are themionically emitted by the heated LB_6 filament and collimated by the Wehnelt, which has a small negative bias with respect to the filaments. The lenses are used to focus the electron beam. This beam backscatters from the sample surface, passes through a set of grids, which functions to select only the electrons which are elastically scatter from the surface and are then accelerated to a fluorescent screen. When they strike the screen, they cause the phosphor to glow, revealing the diffraction pattern. These images are stored at different electron energies with the help of a CCD camera.

3.7 Photoelectron Spectroscopy

3.7.1 Synchrotron Radiation [30]

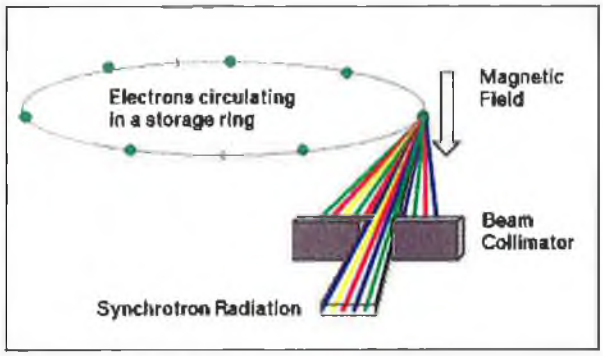

Synchrotron radiation is emitted when charged particles moving at relativistic speeds are forced to follow curved trajectories. The first visual observation of Synchrotron Radiation was in 1948 from the General Electric synchrotron in the USA during investigations into the design and construction of accelerators suitable for the production of very high-energy electrons. Over the next 50 years, an explosive growth in the building of accelerators optimised for synchrotron radiation production has turned this interesting radiative energy loss into a valuable research tool.

The radiation emitted is extremely intense and extends over a broad wavelength range from the infrared through the visible and ultraviolet, and into the soft and hard x-ray regions of the electromagnetic spectrum. This is the energy range of radiation used in photoemission. Synchrotron radiation sources produce x-ray radiation which is of the order of 10^6 times more intense than that from conventional sources and are in addition, continuously tuneable. A schematic diagram of the synchrotron is shown in figure 3.29.

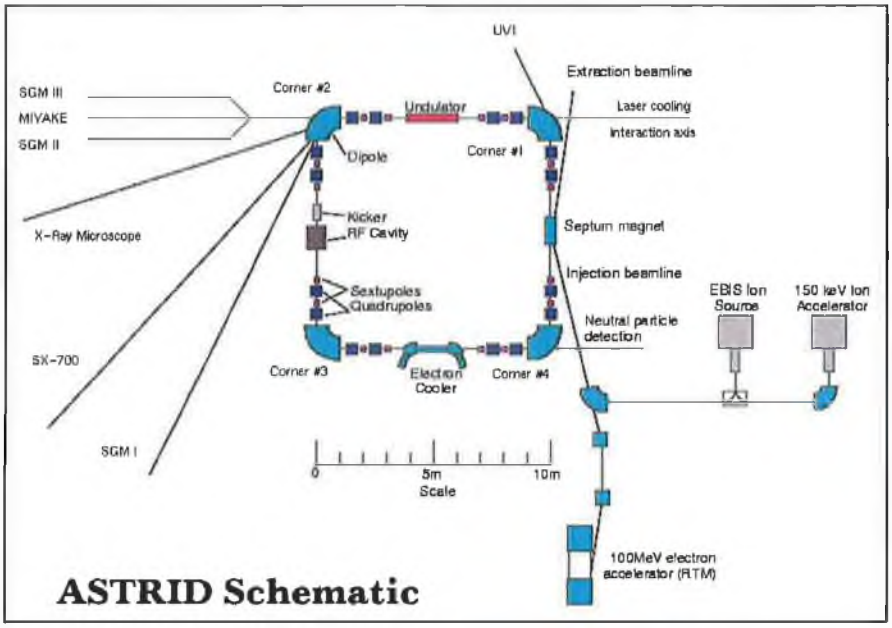

Figure 3.29 *Schematic diagram of ASTRID Synchrotron* [30].

Although the storage ring itself is under high vacuum, electrons are removed by collisions with gas molecules, so the beam current decays. At Aarhus, a new beam is injected every 24 hours during normal operation. The radiation frequency required is selected using a monochromator. The broad range of frequencies available means that synchrotron radiation is suitable for a wide variety of experiments [30], [31].

Finally synchrotron radiation has in addition to its high intensity and collimation two other desirable characteristics.

1. The radiation is almost linear polarized in the plane of the storage ring in contrast to the unpolarised light from conventional ultraviolet and X-ray sources.
2. Since the electrons in the ring are "bunched" the radiation will come as short (of the order 10^{-9} s) pulses, which is useful for timing experiments.

3.7.2 Monochromator and Grating

Photoemission spectroscopy experiments require well-defined photon energies. The "white" radiation from ASTRID must be monochromatized before entering the experimental chamber.

The SGM1 beamline combines a spherical grating monochromator containing three gratings. A SCIENTA electron energy analyser permits fast acquisition of spectra with high-energy resolution, typically 40 meV.

The monochromator has a usable photon energy range from 30 eV to 400 eV. Typical flux values are $\geq 10^{10}$ photons/second at 130 eV with 50 μm slits and are $\geq 10^{9}$

photons/second at 350 eV with the 100 μm slits. The resolution of the three gratings operating with 50 μm slits is shown in figure 3.30 [30].

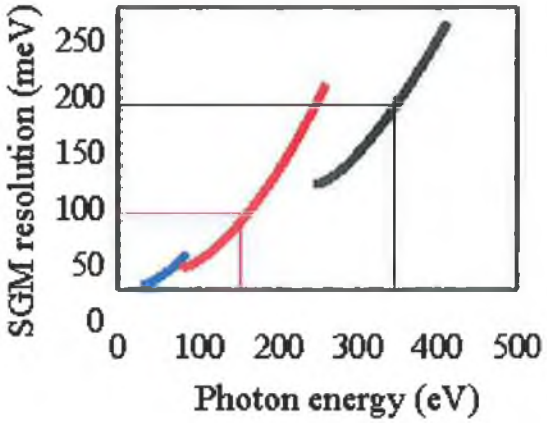

Figure 3.30 *Resolution of the SGM1 monochromator with a typical working setting of the slits at 50 μm* [30].

The core of a soft X-ray monochromator is the diffraction grating shown in figure 3.31, which nearly works in reflection at grazing angles of incidence. A reflection diffraction grating consists of a reflecting surface with a periodic array of lines separated by a distance d. If polychromatic light is incident on the grating at an angle of incidence α, and the exit slit is located at an angle β to the grating, the grating equation

$$n\lambda = d(\cos\alpha - \cos\beta)$$

determines the wavelength passing through the slit. The first order light (n=1) is more intense than the higher order components and is therefore mostly used in experiments.

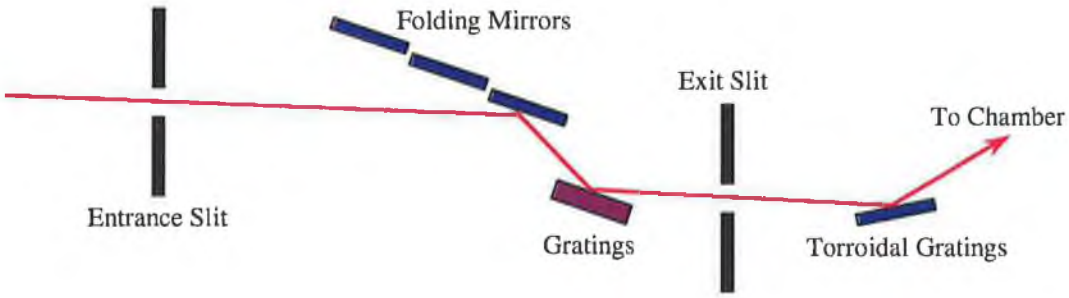

Figure 3.31 *Layout of the SGM1 monochromator.*

3.7.3 The Electron Energy Analyser

The system is equipped with a 200 mm mean radius spherical electron analyser (SCIENTA) with a video based multichannel detector system, shown in figure 3.32. A

resolution of 5meV has been demonstrated, whereas a typical working resolution is about 40 meV.

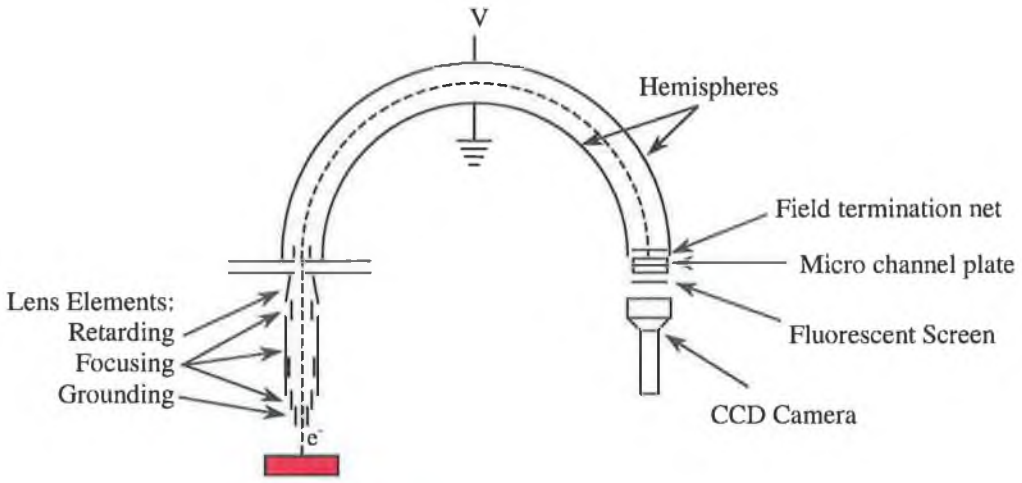

Figure 3.32 *Diagram of SCIENTA spectrometer.*

3.7.4 Experimental Setup

The photoelectron spectroscopy experiments described in this thesis, were performed on the SGM1 beamline at ASTRID in Aarhus, Denmark. This experimental station is designed for surface sensitive experiments. A layout of the experimental chamber is shown in figure 3.33.

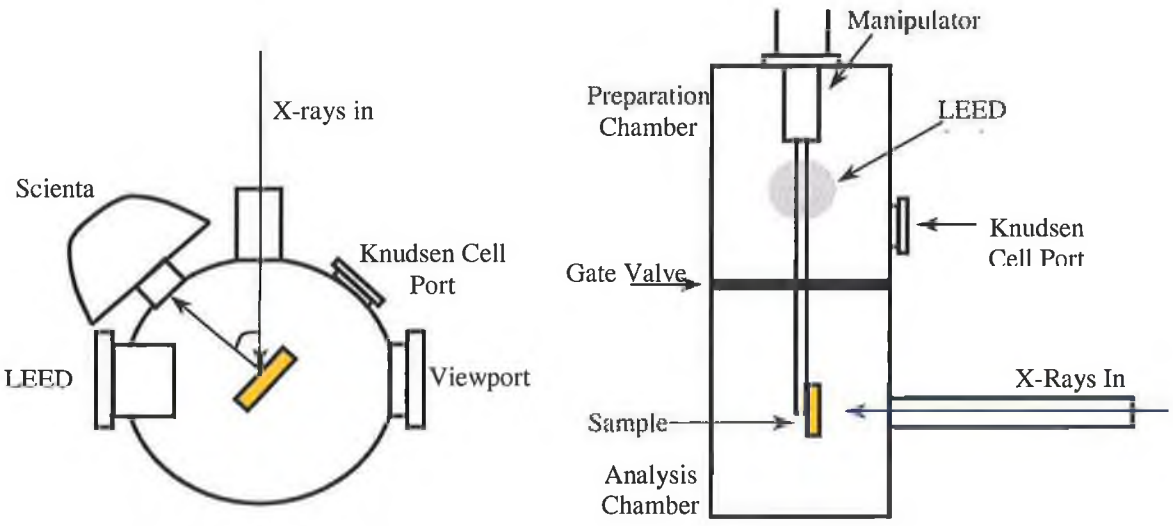

Figure 3.33 *The experimental chamber setup at beamline SGM 1 in Aarhus, for photoelectron studies.*

A base pressure of 10^{-10} mbar was readily achieved on this system after a 24-hour bakeout. The end-station consists of two mu-metal UHV chambers, mounted on top of each other, the upper chamber is used for surface preparation, and the lower chamber is used for photoemission experiments. The preparation chamber is equipped with an Ar^+

gas sputter gun, LEED optics, a mass spectrometer and a gas inlet system. At present there are two sample holders, one with direct current heating (up to 20 A) for thin (~0.5mm) wafers, and one with electron bombardment heating. Both can be cooled via a LN_2 flow cryostat. The sample manipulator has x, y, z movement as well as polar and azimuthal rotations. A Knudsen cell operating at 150°C was mounted on the chamber for pentacene evaporation.

3.8 Au(110) Crystal

The Au(110) crystal was purchased from Metal Crystals and Oxides, Ltd. Two holes of diameter 1mm were drilled through the back of the Au(110) crystal parallel to the front face as shown in figure 3.34(a) and (b). Tungsten wire was threaded through the two holes in the shape shown in figure 3.34(b) and mounted onto the manipulator. In order to heat the Au(110) sample, a current was passed through the tungsten wire.

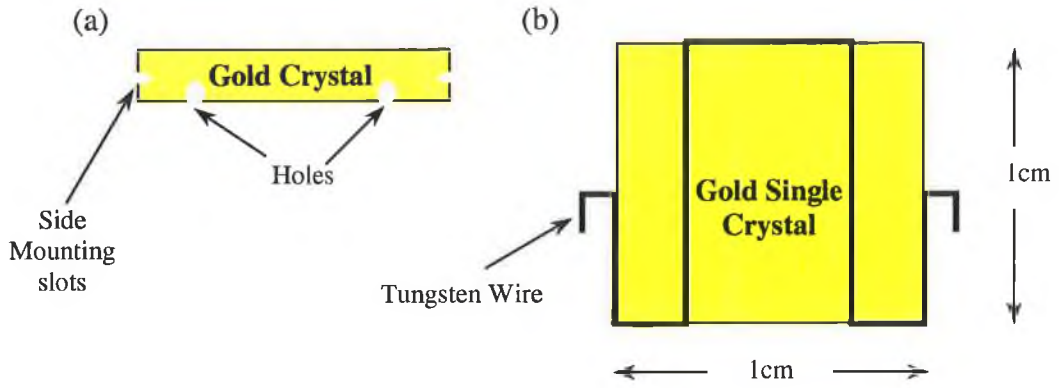

Figure 3.34 *Sample Mounting incorporating resistive heating filament.*

3.9 Knudsen Cell Evaporator

An organic evaporator was built to deposit the pentacene onto the Au(110) sample. A small sheet (3 cm × 2.5 cm) of tantalum foil of thickness 0.125 mm was cut and folded along the x-axis so that the two corners meet.

Then two tantalum wires of thickness 0.5 mm were spot-welded along the sides of the tantalum sheet. The edges were then folded back over the tantalum wire. The sides were spot-welded to form a seal along the edges and secure the tantalum wire. The top section is also spot-welded from both ends leaving a circular orifice in the middle so that the organic molecule can be evaporated from the pouch, shown in figure 3.35. An Alumel/Chromel thermocouple was spot welded to the pouch for accurate temperature control. The tantalum wire was attached to a UHV compatible dual feedthrough flange

and the thermocouple was also attached to a smaller UHV compatible dual feedthrough flange, as shown in figure 3.35. Pentacene was initially degassed at ~423 K for 24 hours to remove water vapour before use.

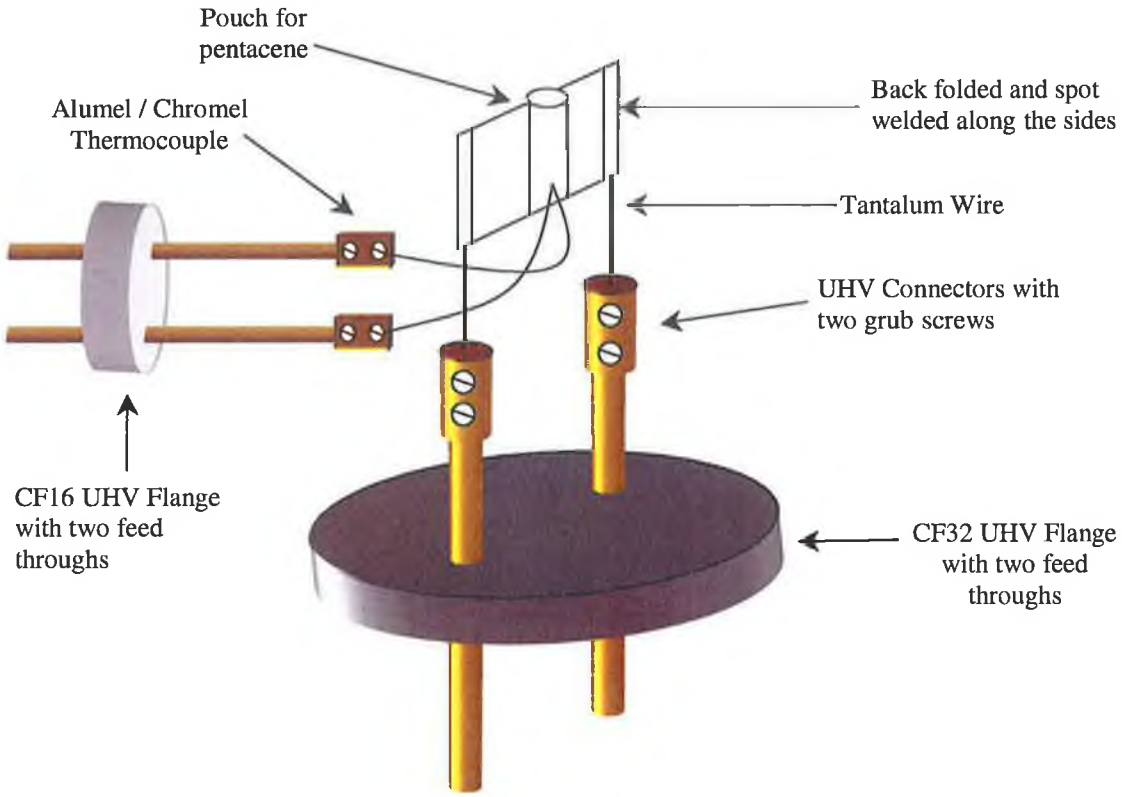

Figure 3.35 *Construction diagram of pentacene evaporator.*

3.10 Summary

Sections 3.1-3.4 have established a setup for a RAS spectrometer from ideas and theory presented in the chapter two. It has included details of a standard model and of requirements for optimum selection of components and comparisons to other available components. Also included is a method to perform experiments with the RAS spectrometer and a structure for affixing the spectrometer for RAS *in-situ* measurements. Section 3.5 introduced experimental details of the STM. Scanning modes, feedback mechanisms and a system of vibration isolation are described. LEED and synchrotron radiation are detailed in sections 3.6 and 3.7. A method of mounting the Au(110) crystal is described in section 3.8 and the construction of a Knudsen cell that is used to evaporate an organic material is described in section 3.9.

Chapter 3 References

1. D.E. Aspnes, J. Vac. Sci. Technol. B3 (5), (1985) 1498.
2. D.E. Aspnes, J.P. Harbison, A.A. Studna, L.T. Florez, J. Vac. Sci. Technol. A6 (1988) 1327.
3. Zettler J-T, Prog. Crystal Growth Charact., 35, 27, (1997).
4. V.L. Berkovitz, I.V. Makarenko, T.A. Minishvili, V.I. Safarov, Solid State Comms. 56 (1985) 449.
5. Z. Sobiesierski, D.I. Westwood, C.C. Matthai, J. Phys. Condens. Matter 10 (1998) 1 – 43.
6. D.E. Aspnes, J.P. Harbison, A.A. Studna, L.T. Florez, J. Vac. Sci. Technol. A6 (1988) 1327.
7. J-T. Zettler, K. Haberland, M.Zorn, M.Pristovsek, W.Richter, P.Kurpas, M.Weyers, J. of Crystal Growth, 195 (1998) 151.
8. Z. Sobiesierski, D.I. Westwood, Thin Solid Films, 318 (1998) 140.
9. B.G. Frederick, J.R. Power, R.J. Cole, C.C. Perry, Q. Chen, S. Haq, Th. Bertrams, N.V. Richardson, P. Weightman, Phys. Rev. Lett. 80(20), (1998) 4490.
10. Y. Borensztein, W.L. Mochan, J. Tarriba, R.G. Barrera, A. Tadjeddine, Phys. Rev. Lett. 71 (1993) 2334.
11. S.M. Scholz, F. Mertens, K. Jacobi, R. Imbihl, W. Richter, Surf. Sci. 340 (1995) L945.
12. B. Sheridan, D.S. Martin, J.R. Power, S.D. Barret, C.I. Smith, C.A. Lucas, R.J. Nichols, P. Weightman, Phys. Rev. Lett. 85 (2000) 4618.
13. D.E. Aspnes, A.A. Studna, Phys. Rev. Lett. 54, 1956, (1985).
14. J. Rumberg, ***Dip. Thesis in Physics***, TU Berlin, (1996).
15. V.L. Berkovits, V.N. Bessolov, T.N. L'vova, E.B. Novikov, V.I. Safarov, J. Appl. Phys., 70(7), (1991), 3707.
16. J.S. Luo, J.M. Olson, K.A. Bertness, M.E. Raikh, E.V. Tsiper, J. Vac. Sci. Technol., B 12(4), (1994), 2552.
17. Dr.Steve Morris, ***thesis.***
18. Hamamatsu Manual, http://www.hamamatsu.com.
19. D.S. Kliger, J.W. Lewis, C.E. Randell, ***Polarized Light in Optics and Spectroscopy***, Academic Press, (1990).
20. http://www.hindsinstrument.com.
21. R.M.A. Azzam and N.M. Bashara, ***Ellipsometry and Polarized Light***, North Holland, Amsterdam (1987).

22. Pat Wogan, private communication.
23. F. Thompson, Electronics World, December 2000, 943.
24. W.L. Mochán, R.G. Barrera, Phys. Rev. Lett. 55, 11, (1985), 1192.
25. C.J. Chen, ***Introduction to Scanning Tunneling Microscopy***, Oxford University Press, 1993.
26. G. Binnig, H. Rohrer, Surface Science, 126, 236 – 244, (1983).
27. D.W. Pohl, IBM Journal of Res. Develop. 30, 417 – 427, (1986).
28. K. Nagaya, H. Kojima, J. Dynam. Syst. Meas. Control, 106, 46 – 51, (1984).
29. Omicron Vacuumphysik, http://www.omicron.de.
30. http://www.isa.au.dk/astrid/astrid.html.
31. J.C. Vickerman, Surface Analyis: ***The principal Techniques***, John Wiley and Sons, 2002.

Chapter 4 Molecular Induced Surface Reconstruction: Pentacene on Au(110)

4.1 Introduction

The structural ordering mechanism for large organic molecules (with masses above 200amu) on crystalline metal or semiconductor surfaces has recently become of great interest for a number of reasons. From a technological point of view thin films of large π-conjugated molecules are promising candidates for the design of optoelectronic devices [1] and organic thin film transistors [2]. For the structural optimization of both, the films and the corresponding interfaces with inorganic contacts [3], a detailed knowledge of the adsorption and ordering on different substrate surfaces is essential. The ordering of the first monolayer is considered as a major parameter for device optimization for a true epitaxial growth of organic films on inorganic substrates [4]. For example, the efficiency of organic photovoltaic cells can be dramatically affected by the molecular morphology of the interfacial layer [5], [6]. It has been demonstrated that for organic molecular crystals or thin film of π-conjugated planar polyacene molecules, the geometry and electronic structure are strongly correlated [7], [8]. Disorder in the film or stacking imperfections can lead to a reduction in carrier mobility [9]. Consequently, a noticeable improvement may be achieved by controlling the molecular orientation in the organic film. A more fundamental motivation for the present study is that little is known about the basic mechanisms, which control the adsorption, and the lateral ordering of large molecules on crystalline surfaces.

In this chapter a structural analysis of the molecular adsorption of pentacene on Au(110) for sub monolayer and multi layer depositions is reported. Au(110) was selected as a substrate, as noble metals with a small density of states near the Fermi edge exhibit a non-dissociative bonding of the molecules to the surface which allows sufficient lateral mobility for the formation of long range ordered structures [10].

4.2 Experimental Details

The experiments were performed using a Scanning Tunneling Microscope (STM) (Omicron, VT-STM) operated in a ultra-high vacuum chamber with a base pressure better than 1×10^{-10} mbar. The STM measurements were made at room temperature (RT) using a Pt/Ir tips. STM images were acquired in constant current tunneling mode. The chamber was equipped with a 4-grid reverse-view Omicron LEED optics.

The Au(110) surface (Metal Crystals and Oxides, Ltd.) was mechanically polished to a mirror finish. Clean Au(110) surfaces were obtained by cycles of Ar^+ sputtering 1000eV and annealing to 400°C. The cleanliness of the Au(110) was assessed

by the appearance of a sharp (1×2) LEED pattern and confirmed with STM images. Pentacene (Aldrich Chemical) was evaporated from a homemade tantalum deposition cell described in section 3.9. The temperature of the cell was monitored by an Al/Cr thermocouple in contact with the Ta crucible. Pentacene evaporation was performed in a preparation chamber isolated from the STM chamber. Before evaporation the pentacene was degassed at 170°C for about 12 hours to remove water vapour. The pentacene was evaporated at a temperature of 195°C and the coverage was deduced from STM images at low and high coverage.

4.3 STM study of pentacene/Au(110)-(2×1)

4.3.1 Clean Au(110)-(2×1)

The missing row reconstruction of noble metal (110) surfaces has been the subject of much theoretical [11] and experimental [12] attention. Since the discovery of the (2×1) reconstruction of the Au(110) surface [13] many experimental studies have been devoted to understanding this surface structure. These studies have included low energy electron diffraction [14], grazing incidence x-ray diffraction [15], high-resolution electron microscopy [16] and scanning tunneling microscopy [17]. It is now well established that the reconstruction involves a missing row structure in which every second row of close packed atoms in the $(1\bar{1}0)$ direction is missing and that the unit cell is doubled in the (001) direction. This surface was confirmed by early STM work [18].

A model of the Au(110)-(2×1) surface is shown in figures 4.1(a) and (b). These show the measurements of the Au(110)-(2×1) surface obtained from the literature [11], [20], [19].

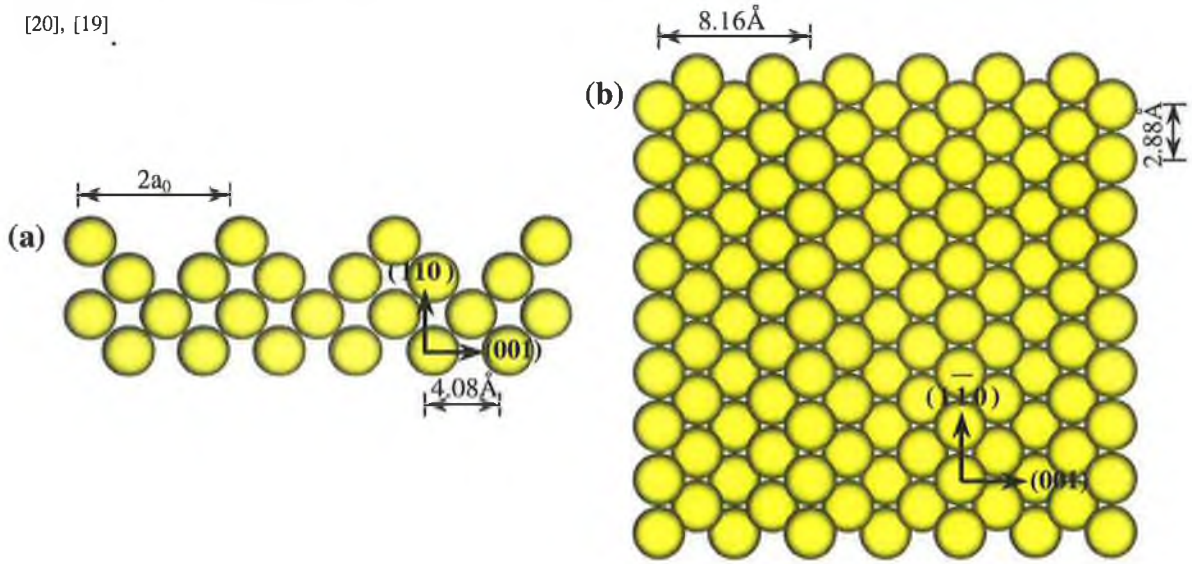

Figure 4.1 *(a) model of the (2×1) missing row reconstruction at the (110) surface of Au (side view), (b) missing row reconstruction at the (110) surface of Au (top view).*

An STM image taken at room temperature of the Au(110)-(2×1) surface is shown in figure 4.2(a). The characteristic missing row reconstruction of this surface can be seen. STM atomic resolution of the rows of close packed atoms in the $(1\bar{1}0)$ direction is not resolved because the images of the Au surface are taken at room temperature and due to thermal drift the gold atoms cannot be resolved. A line profile is obtained across the Au rows in the (001) direction, shown by a thick black line in figure 4.2(a), to determine the Au row separation of 8.16Å [19] indicated in figure 4.1(a) and (b). Figure 4.2(b) shows this line profile and indicates that the experimentally measured value is in good agreement with models, predicting a row separation of 8.16Å ± 1Å [19].

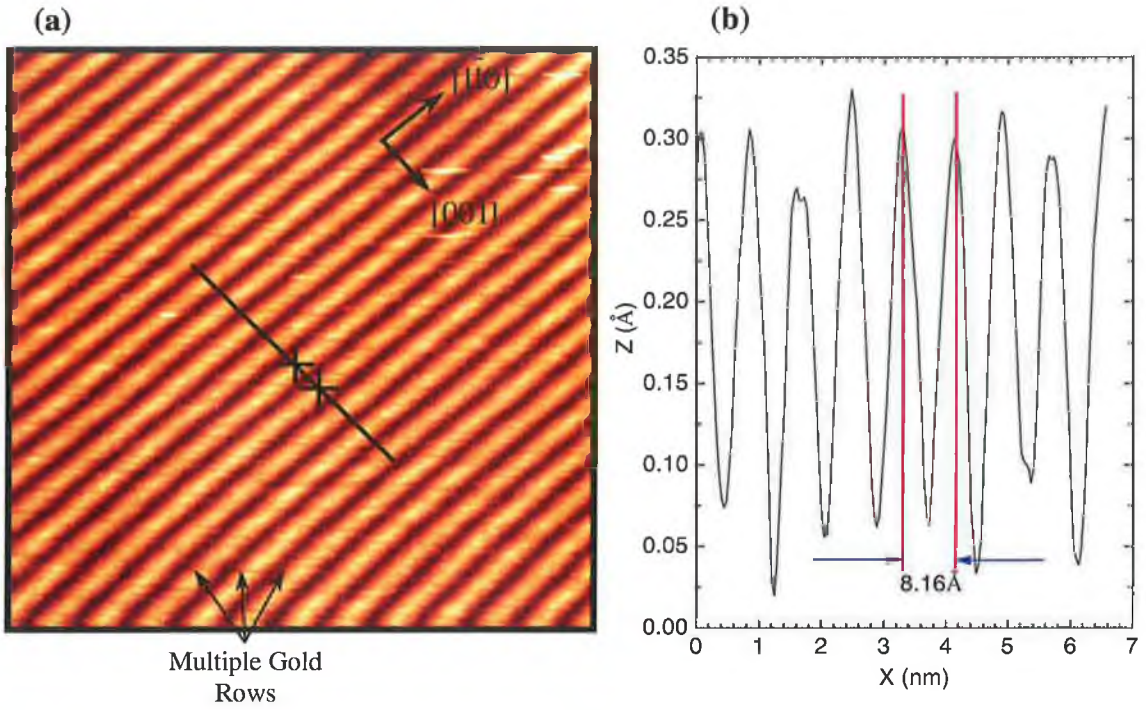

Figure 4.2 *(a) STM image (15nm^2) of clean Au(110)-(2×1) surface featuring the missing row reconstruction and (d) line profile of single scan in (a) showing row separation of 8.16Å ± 1Å. STM image parameters: V_{sample} = 190 mV; I_t = 100 pA.*

4.3.2 The Pentacene Molecule

The pentacene molecule is composed of twenty-two carbon atoms and 14 hydrogen atoms arranged in a linear chain, as shown below in figure 4.3. The measurements of the molecule are also shown in figure 4.3.

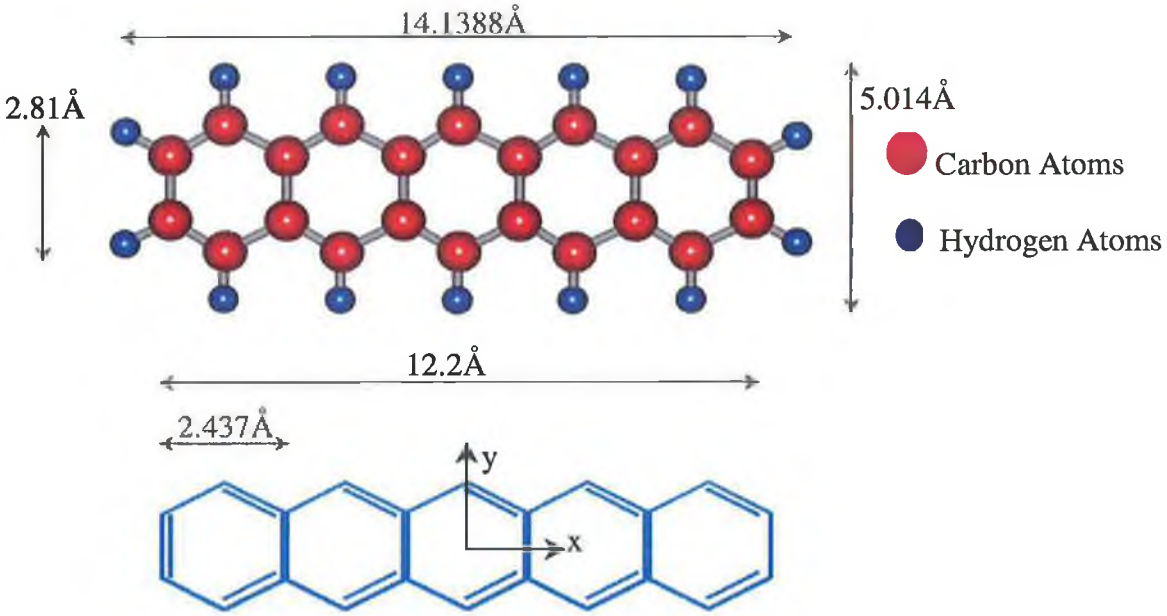

Figure 4.3 *ball and stick model and skeletal structure of pentacene molecule in x-y plane, including dimensions.*

4.3.3 STM of Low Coverage Pentacene on Au(110)-(2×1)

Figure 4.4(a) shows an STM image of the Au(110) surface after a deposition of 0.8ML of pentacene. In this image the gold rows appear as bright lines as indicated in figure 4.4(a). The initial layer of molecules, which have a packing density of 0.057 molecules/gold atom, are mostly resolved as rectangular structures between the close packed gold rows and orientated along the $[1\bar{1}0]$ direction.

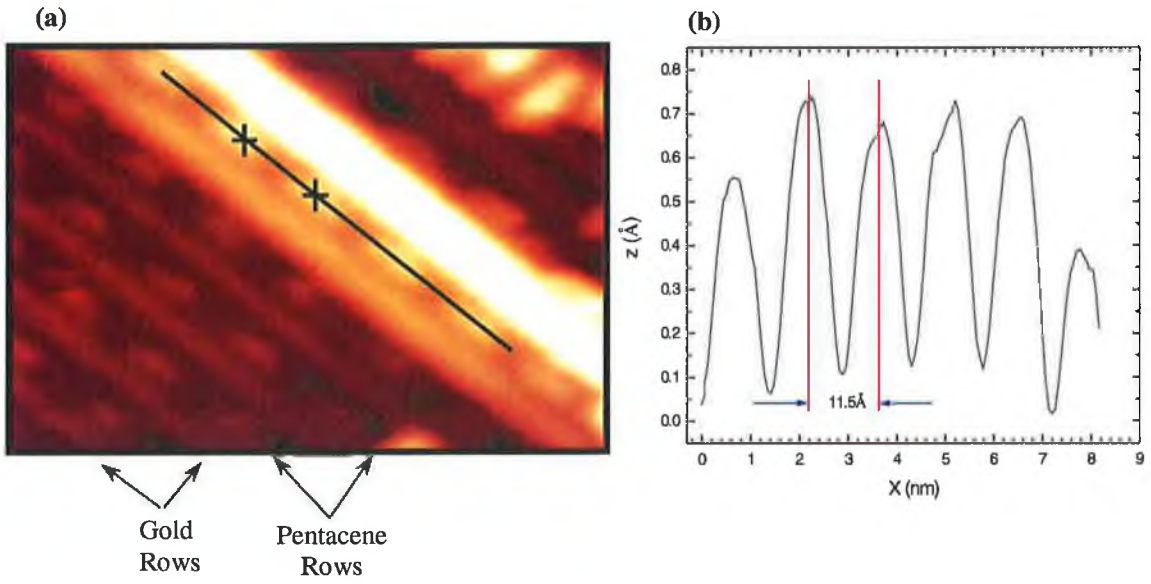

Figure 4.4 *(a) shows STM image (9.0nm x 5.0nm) with pentacene molecules aligned in between the Au(110)-(2×1) channels, (b) shows the line profile of the section in (a) with intermolecular distance of 11.5 Å ± 0.7 Å. STM image parameters:* V_{sample} *= 190 mV;* I_t *= 100 pA.*

The apparent height of the molecules measures ~0.3 Å implies that the pentacene molecules are lying flat. In this dilute phase it is difficult to obtain high-resolution images in which the molecules can be seen clearly, the molecules can appear as fuzzy features, even in images recorded at high impedance (low tunneling current and high voltage). This observation is attributed to their high mobility and molecular diffusion at room temperature [21]. The molecules self-organize into a head-to-head orientation and fill up the gold channels with an intermolecular distance of 11.5 Å ± 0.7 Å, as shown in the line profile in figure 4.4(b). This head to head orientation has also been observed on the Ag/Si(111)-($\sqrt{3}\times\sqrt{3}$)R30° surface [22], discussed in chapter 6.

To define a monolayer and subsequent layer coverages for the Au(110)-(2×1) surface a packing density calculation of the pentacene molecule is employed. The bulk crystal has a (1×1) unit cell and it occupies an area of $a^2/\sqrt{2}$ nm^2. Using the interatomic spacing of 4.08 Å for Au, then there are 8.5 x 10^{18} gold atoms/m^2.

On the Au(110)-(2×1) substrate only half the surface contains gold atoms. Therefore half a monolayer deposition of pentacene will effectively cover the surface. For a half-monolayer coverage of pentacene and averaging distances over approximately 50 pentacene molecules (figures 4.4 and 4.5) the area of the unit cell of the molecule is calculated as 2.06×10^{-18} m^2. For this coverage there are 4.83×10^{17} pentacene molecules/m^2. Therefore a deposition of 0.5ML of pentacene corresponds to one complete layer and has a corresponding packing density of 0.057 molecules/gold atom. For the second and subsequent layer coverages, the area of the unit cell of the pentacene is calculated as 1.43×10^{-18} m^2. For this coverage there are 6.95×10^{17} pentacene molecules/m^2. Above 0.5ML the second layer begins and this has a higher packing density of 0.082 molecules/gold atom.

Several other molecular orientations are resolved on top of the gold rows in figure 4.5(a). In this case, molecules adopt the side-by-side orientation along the $[1\bar{1}0]$ direction reflecting the initial formation of the thin film structure with a packing density of 0.082 molecules/gold atom, shown in figure 4.5(a). STM measurements reveal an intermolecular distance of 8.1 Å ± 0.7 Å from center to center along $[1\bar{1}0]$ direction shown in the line profile in figure 4.5(b) labeled E in figure 4.5(a).

Two preferential adsorption configurations can be identified. In the first orientation the molecules are lying across two gold rows, an example is indicated by the arrow labeled A in fig. 4.5(a). In the second orientation the molecules are lying perpendicular to or on top of a single gold row, an example is indicated by the arrow

labeled B in fig. 4.5(a). Finally, there is a third induced reconstruction where the molecular row starts lying across two gold rows and ends lying across a single row, an example is indicated by the arrow labeled C in Fig. 4.5(a). The unresolved bright lines in figure 4.4(a) are lines of gold atoms displaced from the surface.

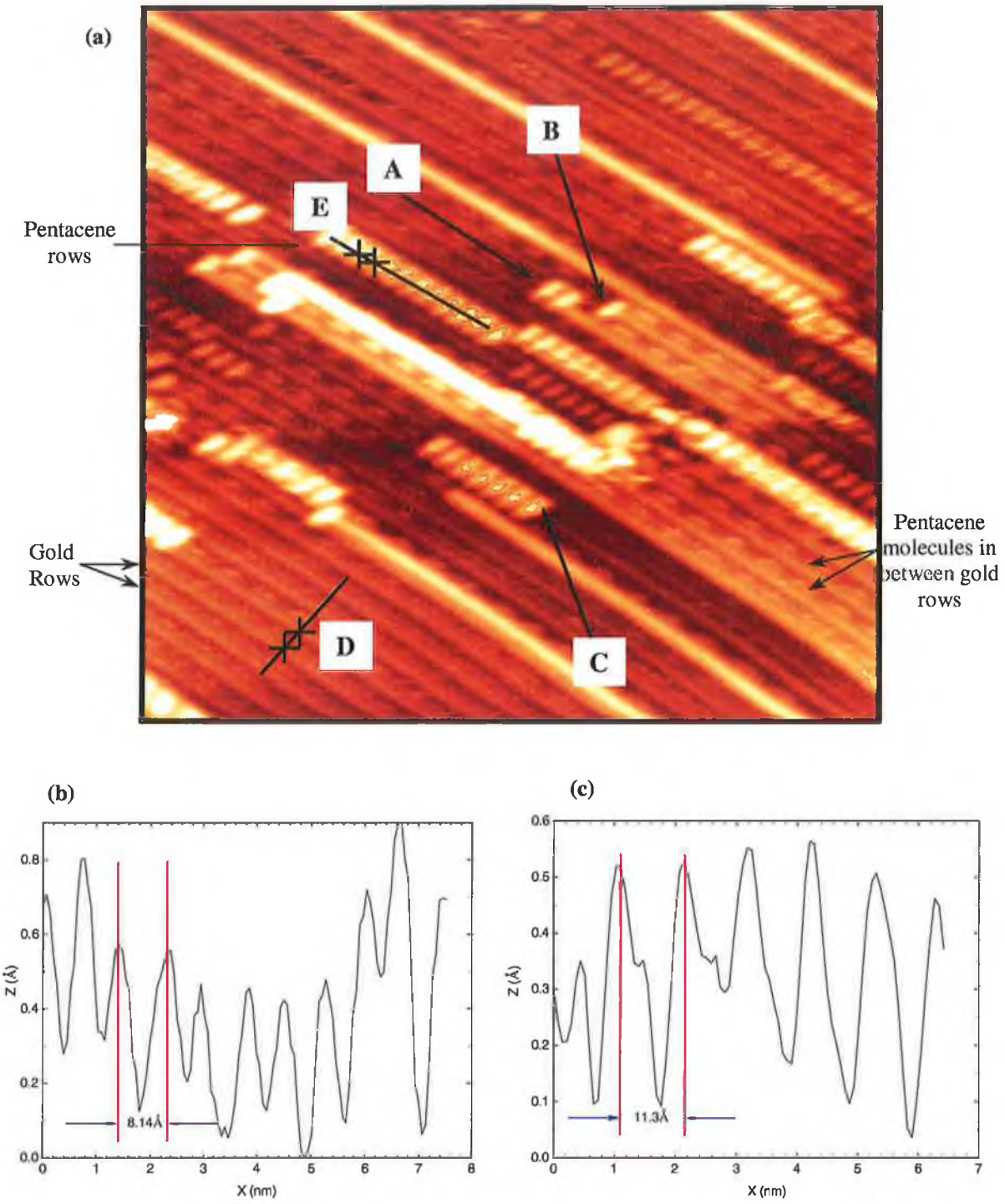

Figure 4.5 *(a) shows an STM image (28nm×28nm) with 0.8 ML pentacene coverage showing the molecular arrangement of pentacene across one and two gold rows, (b) shows the line profile of the section labelled E with intermolecular distance of 8.14 Å ± 0.7 Å and (c) shows the line profile of the section labelled D, the gold row separation of 11.3 Å ± 1 Å. STM image parameters:* V_{sample} *= 190 mV;* I_t *= 100 pA*

Measurements from STM images give an average value for gold row separation of 11.3 Å ± 1 Å, shown in figure 4.5(a) labeled D together with the line profile shown in figure 4.5(c), which is significantly larger than the row separation on the clean Au(110)-(2×1) surface, where the row spacing is measured at 8.14 Å ± 0.7 Å [19]. This indicates that the pentacene induces a reconstruction of the Au(110) surface. This provides an explanation for the lines of gold displaced from the surface.

The initial molecular adsorption, where the molecules lie in the gold channels, produces a new missing row reconstruction. A LEED experiment has been reported [23] for the pentacene/Au(110)-(1×2) interface. Using LEED Corradini et. al. [23] found that deposition of pentacene on this surface revealed a 2-dimensional ordered phase, and showed the presence of a (1×3) pentacene induced long-range periodicity, at room temperature. Repeating this experiment LEED images revealed a similar (1×3) reconstruction of the Au(110) surface, see Fig. 4.6(b). Comparison with the LEED pattern of the clean gold, see figure 4.6(a) acquired at the same primary electron beam energy, shows that a reduction of the distance between two consecutive spots in the [100] directions of the reciprocal lattice occurs while the spots distance in the $[1\bar{1}0]$ direction remain unchanged. This corresponds to a new separation 12.2 Å ± 0.9 Å between the gold rows and agrees well with the STM data shown in figure 4.5(c).

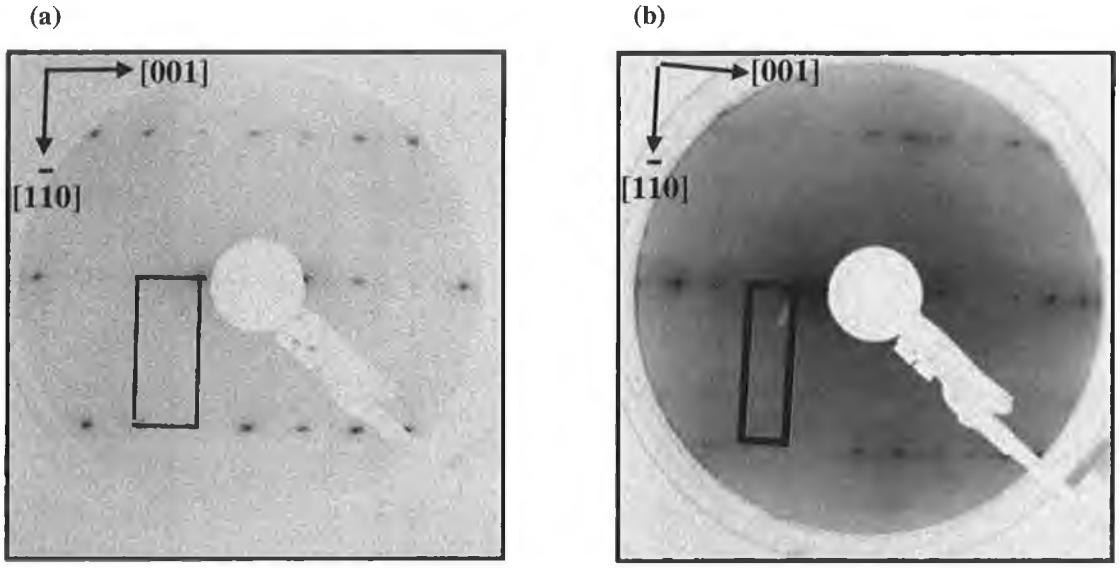

Figure 4.6 *A comparison of the LEED patterns of (a) the clean gold (1 × 2) surface and, (b) on the low coverage phase acquired at the same beam energy of 70eV. A reduction of the spacing between the diffraction spots in the [001] direction occurs showing the formation of the (1× 3) missing atomic gold row reconstruction induced by the pentacene adsorption. The rectangular boxes indicate the unit cell of the reciprocal lattice.*

Adsorption of C_{60} molecules on the Au(110) surface also produced a similar adsorption-induced (1×3) missing row reconstruction [24]. Moreover, density functional calculations of Au(110) surface structure show that the (1×3) reconstruction is slightly energetically favorable (by a difference of 0.015 Jm^{-2}), however the energy difference is small enough that any kind of defect or adsorbate on the surface can influence the result [25].

The low coverage pentacene arrangement is clearly different from the structure of the bulk crystal [26] leading to a unique pentacene structure produced by the Au(110) surface that can act as a template for molecular ordering on the macroscopic scale.

4.3.4 STM of High Coverage Pentacene on Au(110)-(2×1)

There have been extensive investigations of the growth of thin pentacene films on a variety of substrates including semiconductors [27], passivated semiconductors [2], [28], [22], [29] and metallic surfaces [30], [21], [23], [31]. However, attempts to growth highly ordered multilayer epitaxial thin films have been largely unsuccessful. This is primarily due to the fact that the molecular orientation depends on a subtle competition between the intermolecular and molecule-substrate interactions particularly those occurring in the first monolayer. Therefore, novel molecular arrangements, different to that in the bulk organic crystal, can be obtained in the organic epitaxial film [32]. A sensible choice of surface is a critical factor in the fabrication of highly ordered molecular films with a minimum of structural imperfections. As an example, pentacene deposition on the Ag/Si(111)-($\sqrt{3}\times\sqrt{3}$)R30° surface [22] reveals three molecular domains oriented at 120° with respect to each other. The symmetry and orientation of these structural domains are caused by the hexagonal symmetry of the substrate. Consequently, structural defects in the substrate, such as grain boundaries can prevent high molecular ordering.

Lukas et.al. [21] have shown that a single pentacene monolayer adsorbed on the Cu(110) surface leads to long-range ordering, of up to several hundreds nanometers in one-dimension and they suggest that a highly ordered epitaxial pentacene multilayer could subsequently be grown on this layer. On the other hand, a π-stacked multilayer pentacene film can be formed on the Ag(111) surface but in this case a large number of domains boundaries are produced [30].

Single domain pentacene films have been grown with nearly perfect order, over a large area of the Au(110) substrate. The crucial factor in the successful production of this highly ordered epitaxial multilayer structure is the choice of the Au(110) surface as a substrate. The clean surface has a (1×2) missing row reconstruction, which upon

adsorption of a submonolayer coverage of pentacene changes to a (1×3) reconstruction with a packing density of 0.057 molecules/gold atom, detailed in previous section. This new reconstruction acts as a template for the formation of unidirectional π-stacked molecular rows, as shown in figure 4.7 and 4.8(a).

Typical STM images with molecular resolution of the multilayer structure are shown in figure 4.7 and 4.8(a). These images reveal the real space of the structure of the epitaxial organic thin film after a pentacene evaporation of approximately 7 ML on the clean Au(110)-(1×2) surface. After deposition, the surface was annealed to approximately 100°C for several minutes in order to promote molecular ordering. In Organic Molecular Beam Epitaxy (OMBD) in which the film cohesion is due to weak interaction (van der Waals) forces, annealing the substrate, significantly improves the molecular self-arrangement. After annealing to 100°C the pentacene molecules arrange themselves in a well-ordered, evenly spaced molecular rows, shown in figure 4.7. The highly ordered pattern of molecular rows remains stable up to temperatures of 150°C after which the molecules start to desorb from the surface. It is also evident from other surface analysis techniques such as photoemission and RAS, detailed in section 4.4 and in chapter 5 respectively, that the molecules may dissociate on the surface with increasing temperature as the spectra of the clean Au(110) surface is always unattainable without repeating an Ar^+ sputtering process. This would indicate that the molecular rows are in part due to kinetic stabilization, which occurs during the growth and also suggests that it corresponds to a thermodynamically stable structure [21].

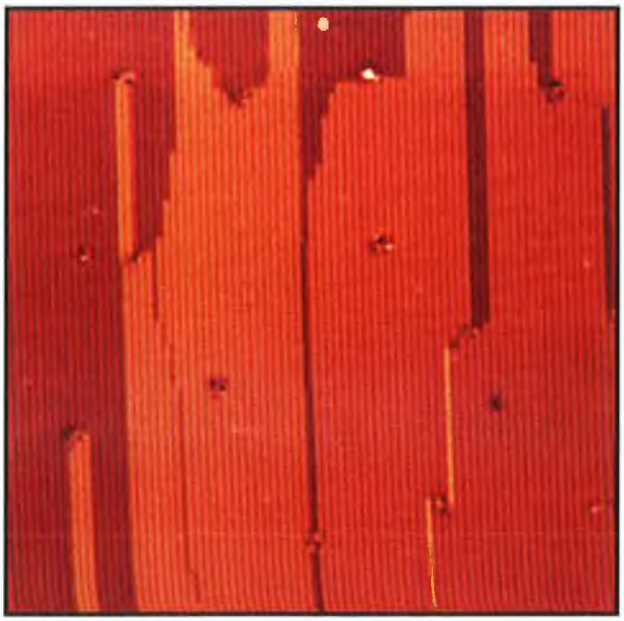

Figure 4.7 *STM image (500 nm^2) of the Au(110) surface after pentacene deposition of ~ 7 ML. Image parameters: V_{sample} = 190 mV; tunnelling current I_t = 180 pA.*

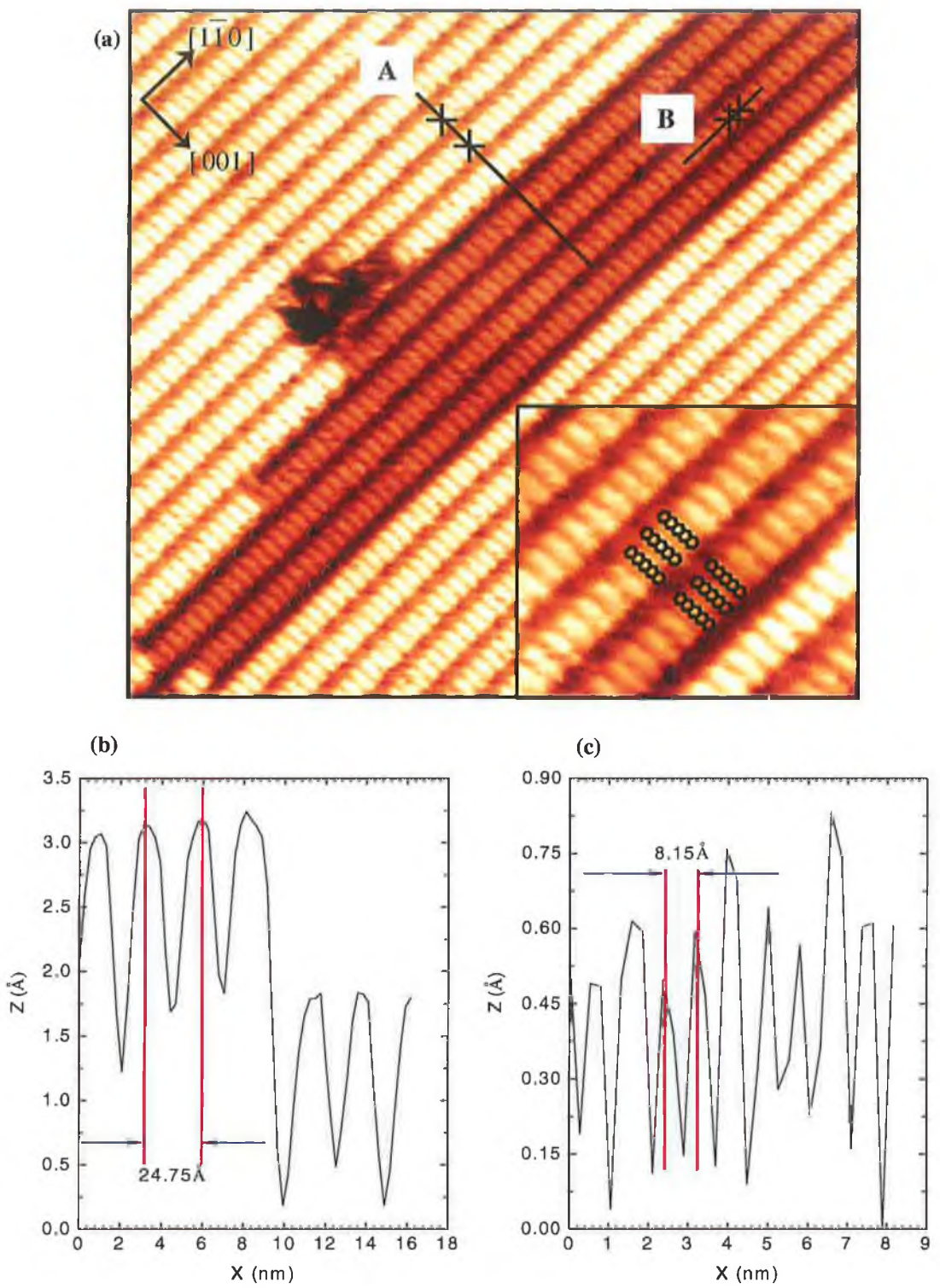

Figure 4.8 *(a) High resolution STM images (45 nm^2, insert = 10 nm^2) showing the molecular structure of the multilayer pentacene film. Schematic black shapes represent the side-by-side orientation in the molecular arrangement. Image parameters: V_{sample} = 190 mV; I_t = 100 pA, (b) Line profile of row separation distance, marked A, showing the distance measured at 24.75 Å ± 1 Å, (d) Line profile of intermolecular distance, marked B, showing the distance measured at 8.15 Å ± 0.7 Å (from center to center of the molecules).*

The large-scale image, in figure 4.7 shows a single domain pentacene thin film in which growth occurs along the $[1\bar{1}0]$ direction. In this image the multilayer formation is well resolved and terraces separated by single molecular step heights are observed. The structural arrangement of the individual molecules is shown in the high resolution STM image and inset image in figure 4.8(a). Within this single domain the molecules adopt a side-by-side orientation and self-organize to form molecular rows with long-range order. Such ordering has been observed previously for pentacene adsorption on metal substrates [30], [21]. The apparent height of the individual molecule resolved in this STM image is ~0.3Å which suggests that the molecules are lying flat on the surface [22], [30], [21]. The intermolecular distance along the $[1\bar{1}0]$ direction is measured to be 8.15 Å ± 0.7 Å (from center to center of the molecules), shown in figure 4.8(c). This corresponds to the distance induced by the van der Waals interaction and is in good agreement with previous STM measurements [21]. The molecular rows, growing along the $[1\bar{1}0]$ direction, are separated by a large distance of 24.7 ± 1 Å, a line profile of such is shown in figure 4.8(b). Each row grows on top of the one underneath as revealed in the STM image at high-resolution, figure 4.8(a), leading to a stacked molecular row formation.

Note that the molecular rows can form either on top of the underlying row or between two molecular rows in the [100] direction, however the latter configuration is rarely observed. Within a row, (i.e. along the $[1\bar{1}0]$ direction), the molecules predominately adsorb on the bridge site between two underlying molecules, although some instances of top site adsorption are also observed. Consequently, highly ordered multilayers are produced leading to a (1×1) molecular structure growing in a layer-by-layer (Frank-van der Merwe) mode.

A typical LEED pattern, recorded at 35 eV, obtained from this multilayer structure is shown in figure 4.9. The LEED image shows a rectangular array of sharp diffraction spots, confirming the (1×1) structure of the multilayer pentacene film. This LEED image was taken at 35 eV and not 70 eV, as was figure 4.6 because the clean gold diffraction spots would not fit into the LEED screen at 35 eV. This is due to the deBroglie relation, indicating that as the beam energy is increased, θ decreases and the spots move closer together. Therefore to obtain correct measurements of the diffraction spots it was necessary to obtain the LEED image at 70 eV. LEED measurements averaged over several samples gives an organic surface unit cell of 25.1Å ± 1Å × 8.3 ± 1 Å in agreement with the real space STM observations, where these LEED distances

are calibrated using LEED patterns obtained on the clean Au(110)-(1×2) structure acquired at 70 eV shown in figure 4.6.

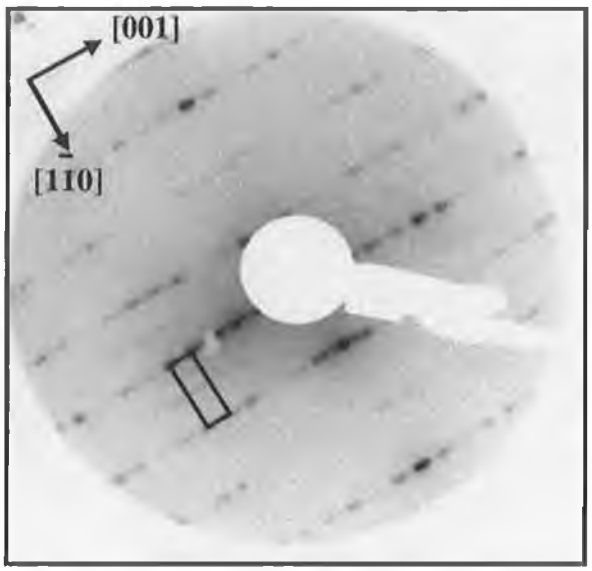

Figure 4.9 *Typical Diagram LEED Pattern, acquired in-situ with an electron beam energy of 35 eV, showing the reciprocal space structure of the thin organic film. This LEED pattern is observed all across the sample (1cm^2 size) and shows that the multilayer formation is produced on a large scale. Rectangular shape indicates the reciprocal unit cell.*

Because of the preferential molecular adsorption configurations described in section 4.3.3, the minimum distance allowed between two consecutive molecular rows along the [001] direction, in a side-by-side orientation is 24.4Å. The intermolecular distance observed in the higher coverage pentacene film of 24.75Å corresponds well to the underlying Au(110)-(1×3) structure. This explains the large separation of the molecular rows in the multilayer organic film.

On the basis of these arguments, it is concluded that the (1×3) reconstruction induced by the pentacene molecules acts as a template for the subsequent formation of the unidirectional rows of pentacene along the [100] direction. Moreover, this thin film shows a high degree of structural perfection on a microscopic scale where the main defects are identified as molecular vacancies. Judging from these considerations, this unique hybrid interface should be a very good candidate for the purpose of performance improvement especially in optical organic device application such as organic Schottky-diode.

4.4 Core level photoemission of pentacene/Au(110)-(2×1)

The discussion of photoemission from the pentacene/Au(110)-(2×1) interface is divided into two main sections. The first examines the core level photoemission data and the second examines the valence band data. A work function analysis is performed and a band diagram for the pentacene/Au(110)-(2×1) interface is established in the core level photoemission section. The C 1s (binding energy of 284.3 eV [33]) and the Au $4f_{7/2}$ (binding energy of 84.0 eV [33]) core levels are measured and energy shifts are correlated to distinct molecular orientations observed in STM as described in sections 4.3.3 and 4.3.4. Analysis of variations of the areas under the core levels with increasing pentacene deposition provides a measurement of a monolayer and subsequent layer coverage times. This correlates with the packing density calculations in section 4.3.3.

Analysis of the valence band photoemission demonstrates that features in the pentacene/Au(110)-(2×1) interface spectra, can be attributed to π and σ transitions shown in the pentacene gas phase spectrum. In order to determine the pentacene orientation on the surface group theory is applied to this interface.

4.4.1 Work Function Analysis

An energy level configuration including the highest occupied molecular orbital (HOMO), the lowest unoccupied molecular orbital (LUMO), the Fermi level (E_F) and the vacuum level of the pentacene/Au interface was measured using photoemission spectroscopy performed at the Aarhus synchrotron. A bias of 9.07 V was applied to the sample during the workfunction measurements and the high binding energy cutoff for pentacene depositions on Au(110)-(2×1) was studied to ascertain changes in the work function, ϕ as a function of the pentacene deposition. An estimate of the pentacene coverage can be found from this experiment.

A plot of the work function of the clean Au surface and the work function for the pentacene/Au interface for increasing pentacene depositions is shown in figure 4.10. It can be clearly seen that as the pentacene is deposited onto the sample there is a shift in the high binding energy cutoff for this sample towards lower kinetic energy. This indicates the presence of a significant interface dipole. This interface dipole is most likely attributed to charge transfer from the pentacene into the Au since a molecular dipole moment is not possible due to a lack of a permanent dipole on the pentacene molecule [34].

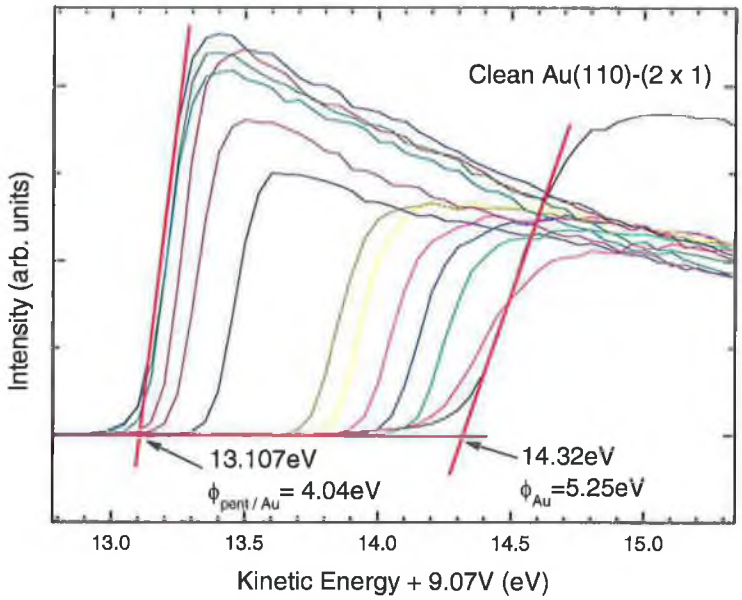

Figure 4.10 *showing the high binding energy cutoff for increasing pentacene depositions on a clean Au(110)-(2×1) surface.*

The work function of the clean gold surface was determined to be approximately 5.25 ± 0.04 eV and the work function for the pentacene terminated Au surface was determined to be approximately 4.04 ± 0.04 eV. Therefore the interface dipole can be estimated to be 1.21 ± 0.04 eV. The onset of the HOMO (see section 4.5) was found to be ~0.85 ± 0.04 eV, it is therefore possible to build up a band diagram for the pentacene/Au(110)-(2×1) interface a shown in figure 4.11. The position of the LUMO was obtained from the literature [35].

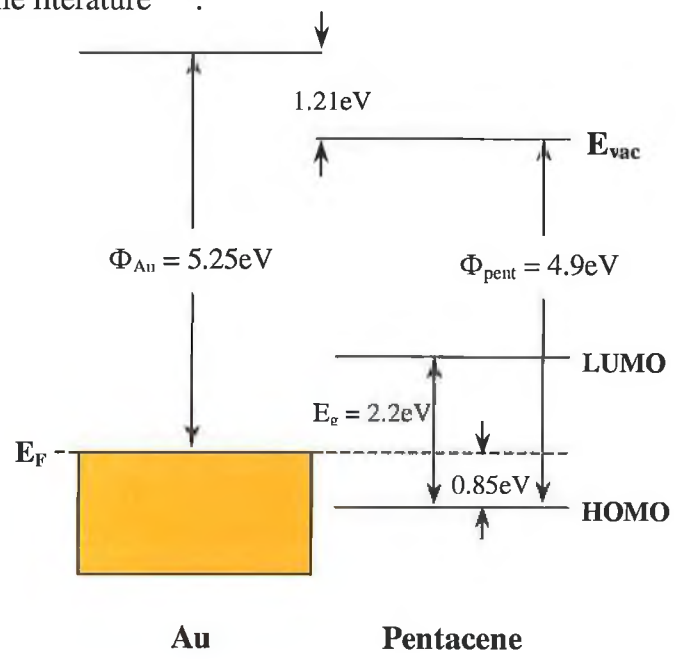

Figure 4.11 *Band diagram for the pentacene / Au(110) interface. The interface dipole is shown to be 1.21eV.*

From this experiment it is also possible to approximately estimate the coverage of pentacene on the Au(110)-(2×1) substrate. If the work function changes are plotted against the deposition time, shown in figure 4.12 and two straight lines are fitted to each of the linear regions, where they intersect is taken as a complete monolayer. Figure 4.12 shows that a deposition corresponding to ~250 seconds is a monolayer.

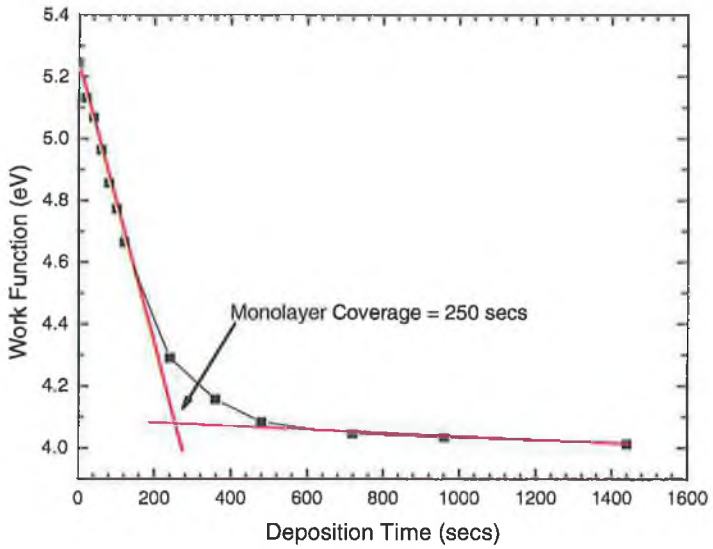

Figure 4.12 *plot of work function versus deposition time to estimate a monolayer coverage.*

4.4.2 Au $4f_{7/2}$ core level

The decomposition of the Au $4f_{7/2}$ spectra is based on the Doniach-Sunjic lineshape [36], [37], incorporating an asymmetry parameter, a Gaussian lineshape representing the experimental broadening and the Lorentzian width representing the intrinsic lineshape. The Doniach-Sunjic lineshape was unavailable in the fitting program in Origin 7.0 [38], therefore the Au $4f_{7/2}$ peaks have all been resolved into components using a deconvolution program as described earlier. Two Voigt lineshapes representing the bulk and surface components were used. The parameters used to fit the peaks are shown in table 4.1. Figure 4.13(a)-(l) is a plot for increasing pentacene coverage on the Au(110)-(2×1) surface, this figure also shows the decomposition of the Au $4f_{7/2}$ peaks and the contributions of the surface and bulk lineshapes to the overall fit. The small broadening at this early coverage rules out a strong chemical interaction at the interface.

The width of the Gaussian lineshape can be approximated from the instrumental broadening, which is a combination of the SGM 1 beamline broadening and the SCIENTA analyzer broadening. From figure 3.30 the resolution of the SGM 1 beamline at the photon energies required are used. The SCIENTA analyzer has a resolution of approximately 40 meV. The equations for calculating the Gaussian widths are

$$E = \sqrt{\Delta E_{SCIENTA}^2 + \Delta E_{SGM1}^2} \quad (4.1)$$

therefore the approximate Gaussian widths needed to fit the Au $4f_{7/2}$

$$E = \sqrt{(40meV)^2 + (100meV)^2}$$

$$E = 0.108 \text{ eV}$$

This is an approximate value because there are other factors, which can influence the broadening, but can be used as a good start to begin the fitting process.

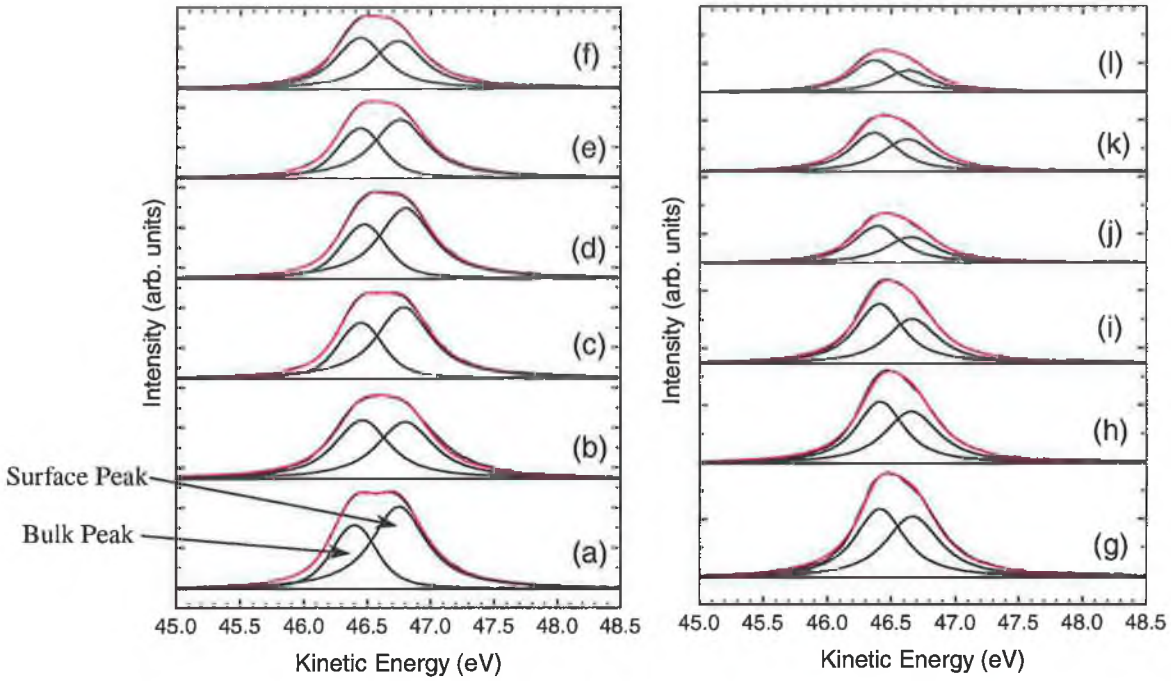

Figure 4.13 *Au $4f_{7/2}$ spectra taken with photon energy of 130eV of (a) clean gold, and after a deposition of (b) 20 secs, (c) 40 secs, (d) 60 secs, (e) 100 secs, (f) 120 secs, (g) 240 secs, (h) 360 secs, (i) 480 secs, (j) 720 secs, (k) 960 secs and (l) 1440 secs. Also shown are the fitting spectra and the fitted curve.*

It was found that increasing the pentacene coverage, the gold signal decreased as shown in figure 4.13. It can be seen that as the pentacene molecules are deposited on the Au surface, the bulk and surface contributions both shift to lower kinetic energy. The surface contribution shifts by 0.18 ± 0.04 eV and the bulk contribution shifts by 0.11 ± 0.04 eV towards lower kinetic energy.

From the STM images in section 4.3.3 a change in the arrangement of the molecules on the Au(110)-(2×1) surface was observed. Therefore the shifts in the peaks can be attributed to the molecules initially assembling between the Au rows and after half a monolayer assembling on top of the Au rows at 90° to their original arrangement. Also evident from figure 4.13 is that the intensity changes for the surface peak during

the deposition of the first 0.5 ML. This is consistent with the (2×1) to (3×1) surface reconstruction change.

Peak		Voigt 1 - Bulk Peak				Voigt 2 - Surface Peak				Total		
	Cover (secs)	E (eV)	A	G (eV)	L (eV)	E (eV)	A	G (eV)	L (eV)	ΔE (eV)	$Area_{total}$	χ^2
(a)	0	46.43	24.16	0.14	0.4	46.78	28.33	0.15	0.45	0.34	52.49	0.29
(b)	20	46.46	23.10	0.16	0.46	46.79	23.55	0.16	0.48	0.34	46.65	0.43
(c)	40	46.46	21.00	0.14	0.42	46.79	25.17	0.16	0.47	0.33	46.17	0.32
(d)	60	46.49	20.48	0.12	0.43	46.79	24.56	0.16	0.47	0.31	45.04	0.42
(e)	100	46.46	19.71	0.15	0.42	46.78	19.56	0.15	0.46	0.31	39.28	0.23
(f)	120	46.45	18.22	0.15	0.42	46.76	18.20	0.15	0.45	0.30	36.42	0.22
(g)	240	46.45	17.03	0.14	0.42	46.76	16.62	0.15	0.46	0.31	33.65	0.32
(h)	360	46.41	14.67	0.14	0.4	46.66	14.04	0.15	0.46	0.24	28.71	0.17
(i)	480	46.41	14.20	0.14	0.4	46.66	11.34	0.15	0.43	0.25	25.53	0.09
(j)	720	46.40	8.73	0.14	0.4	46.65	6.56	0.15	0.42	0.25	15.29	0.03
(k)	960	46.38	8.33	0.14	0.4	46.62	6.26	0.15	0.44	0.24	14.59	0.04
(l)	1440	46.39	7.65	0.14	0.4	46.63	5.27	0.15	0.40	0.24	12.91	0.03

Table 4.1 *Fitting parameters for Au $4f_{7/2}$ peak.*

4.4.3 C 1s core level

It was found that with increasing pentacene coverage, the carbon signal increased. The carbon 1s peaks are resolved into two components using a deconvolution program in Origin 7.0 [38] as described in chapter 3.

Increasing the pentacene coverage on the Au(110)-(2×1) surface, it was found that the carbon peak can be fitted with a single Voigt function (consisting of a Gaussian and a Lorentzian) for pentacene coverages up to a monolayer, shown in figure 4.14(a)-(f). A single Voigt function does not adequately fit the carbon peak after a monolayer coverage and a second Voigt function is required to fit the peak after a monolayer, shown in figure 4.14(g)-(k). The requirement of a second peak to fit the carbon spectra after a monolayer this again shows that the pentacene is in a different bonding environment. The parameters for the fits are given in table 4.2.

From figure 4.14 it can be seen that all the carbon atoms in the pentacene molecule remain at the same kinetic energy of 54.44 eV ± 0.04 eV on the Au(110)-(2×1) surface for coverages up to 240 seconds. After that coverage the kinetic energy of the carbon atoms decrease to 54.17 eV ± 0.04 eV and remain at that energy. Therefore

an energy shift of approximately 0.27 ± 0.04 eV is observed. The C 1s peak shift is consistent with the change in the orientation of the pentacene molecules on the surface.

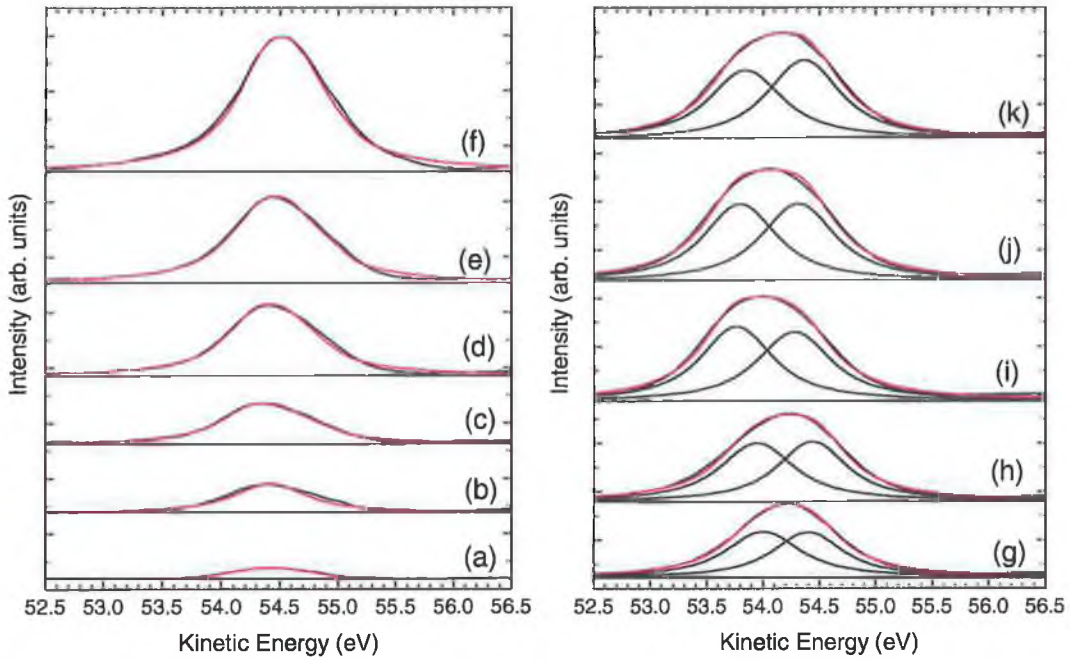

Figure 4.14 *carbon 1s core level photoemission spectra taken with photon energy of 340eV after a deposition of (a) 60 secs deposition, (b) 100 secs, (c) 120 secs, (d) 240 secs, (e) 360 secs, (f) 480 secs, (g) 720 secs, (h) 960 secs and (i) 1440 secs on a clean Au(110)-(2×1) surface. Also showing are the fitting spectra.*

Peak		Voigt 1 – Bulk Peak				Voigt 2 – Surface Peak				Total		
	Cover (secs)	E (eV)	A	G (eV)	L (eV)	E (eV)	A	G (eV)	L (eV)	ΔE (eV)	$Area_{tot}$	χ^2
(a)	20	54.43	9.608	0.2	0.7	-	-	-	-	-	9.608	0.3
(b)	40	54.42	28.53	0.25	0.65	-	-	-	-	-	28.53	1.16
(c)	60	54.41	47.02	0.25	0.7	-	-	-	-	-	47.02	1.54
(d)	100	54.41	82.26	0.25	0.7	-	-	-	-	-	82.26	1.75
(e)	120	54.42	99.39	0.25	0.7	-	-	-	-	-	99.39	1.83
(f)	240	54.44	156.59	0.25	0.7	-	-	-	-	-	156.59	1.90
(g)	360	54.00	112.11	0.25	0.7	54.40	103.71	0.25	0.65	0.4	215.82	1.62
(h)	480	53.95	142.39	0.25	0.7	54.42	136.47	0.25	0.65	0.47	278.85	1.36
(i)	720	53.96	178.96	0.25	0.68	54.45	169.64	0.25	0.7	0.49	348.60	1.34
(j)	960	53.94	166.83	0.25	0.69	54.41	195.90	0.25	0.7	0.47	362.73	1.24
(k)	1440	53.96	188.71	0.25	0.69	54.41	190.58	0.25	0.7	0.46	379.29	1.19

Table 4.2 *Fitting parameters for carbon 1s peak.*

From the STM image of pentacene adsorption on Au(110)-(2×1) in figure 4.5(a), it can be seen that the initial layer of molecules are resolved as rectangular structures between the gold rows and orientated along the $[1\bar{1}0]$ direction. When they have completed filling the channels in the gold they begin to lie across the top of the channels

in the [001] direction. Therefore due to a different geometrical structure between 0.5 ML and higher coverages, the change in the arrangement of the molecules is consistent with the shift in energy of the carbon 1s peak. Figure 4.12 shows a monolayer is completed at approximately 250 seconds deposition. This provides further evidence that the shift in the carbon 1s peak is consistent with a change in the geometry of the molecule on the surface.

From the total area under the peak it is possible to estimate the coverage of a monolayer of pentacene on the Au(110)-(2×1) substrate. The peaks have to be normalized for this calculation. The Au $4f_{7/2}$ core level peak can be normalized by dividing all the areas by the clean gold core level. By plotting the C 1s core levels for each coverage and extrapolating until the C 1s saturates, it is then possible to normalize the C 1s by dividing the area under the core level by its saturation area. Plotting the normalized areas for the Au $4f_{7/2}$ and the C 1s core levels as a function of the deposition time and following the same procedure as in figure 4.12 for best-fitting lines, their intersection point corresponds to approximately a complete monolayer. The plots are shown in figure 4.15 for the two core levels. For each of the core level curves it can be seen that there are three distinct sections and careful calculation of the packing density for the submonolayer regime from section 4.3.3 shows that at ~170 seconds a half-monolayer is completed which agrees very well with the plots shown in figure 4.15. Also considering the first monolayer and the higher packing density for this coverage it is found that after approximately 244 seconds another layer is complete. The packing density of the molecules on the Au(110)-(2×1) surface is the same after the second monolayer has been completed. Therefore subsequent layers are complete as multiples of ~245 seconds. These results differ slightly with figure 4.12 but agree within experimental error with the changes observed in the Au $4f_{7/2}$ and C 1s core levels. One extra feature about the cross section plot in figure 4.15 is that following four monolayers deposition the areas of the Au $4f_{7/2}$ and the C 1s core levels have approximately reached their maximum and minimum respectively. This reveals a Stranski-Karastanov growth pattern [39], where the first layers are grown as complete monolayers but after a specific coverage, growth continues as islanding, (see chapter 2). This would account for the Au $4f_{7/2}$ core level not saturating after 1440 secs of pentacene deposition.

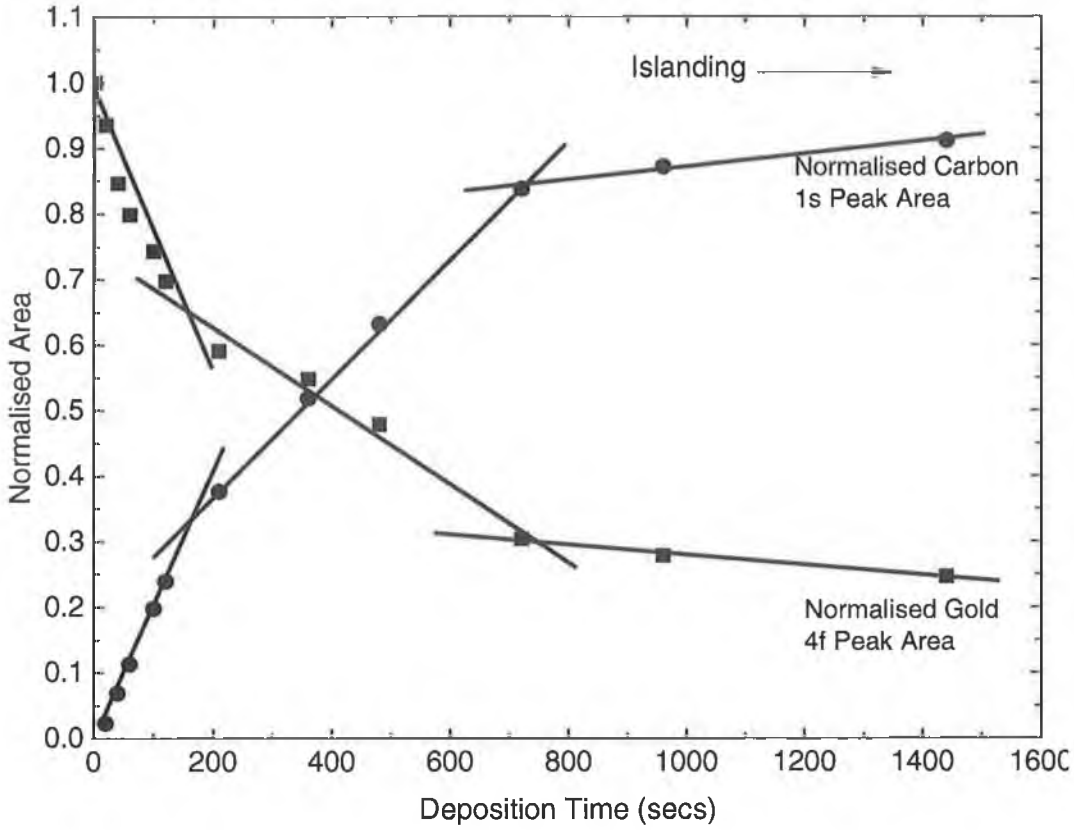

Figure 4.15 *cross section corrected areas for C 1s peak (●) and Au $4f_{7/2}$ peak (■) plotted as a function of deposition time. Also shown by the lines are the calculated times for a complete monolayer.*

4.5 Valence Band Photoemission

4.5.1 Results

As was previously discussed in section 2.5.5 a complete analysis of the valence band spectra requires a full molecular orbital calculation, which was not available. Instead Group Theory was explored to try and explain the changes in the valence band spectra with increasing pentacene coverage and to solve the molecular orientation of the pentacene molecule on the Au(110)-(2×1) surface.

Figure 4.16 shows a gas phase spectrum of pentacene [40], [41] (D_{2h} symmetry species) with the seven π orbitals assigned to the molecule, starting with the lowest kinetic energy $3b_{2g}$, $2a_u$, $3b_{1g}$, $2b_{2g}$, $3b_{3u}$, $1a_u$, $1b_{2g}$, and the features labeled f, g, h, i and j are the observable σ orbitals. A software package called Hyperchem [42] was used to confirm the π orbital assignments with the literature and to determine the σ orbital assignments. The σ orbital assignments are shown at the bottom of figure 4.16. It was found that the f feature in the gas phase spectrum can be composed of $2b_{1g}$ and $7b_{3g}$ orbitals, the g feature can be made up of $7b_{1u}$, $6b_{3g}$ and $2b_{3u}$ orbitals. The h peak can be

composed of $5b_{3g}$, $6b_{1u}$, $5b_{1u}$ and $1b_{3u}$ symmetry orbitals. The i and j features are made up of $7a_g$, $6b_{2u}$ and $4b_{1u}$ symmetry orbitals.

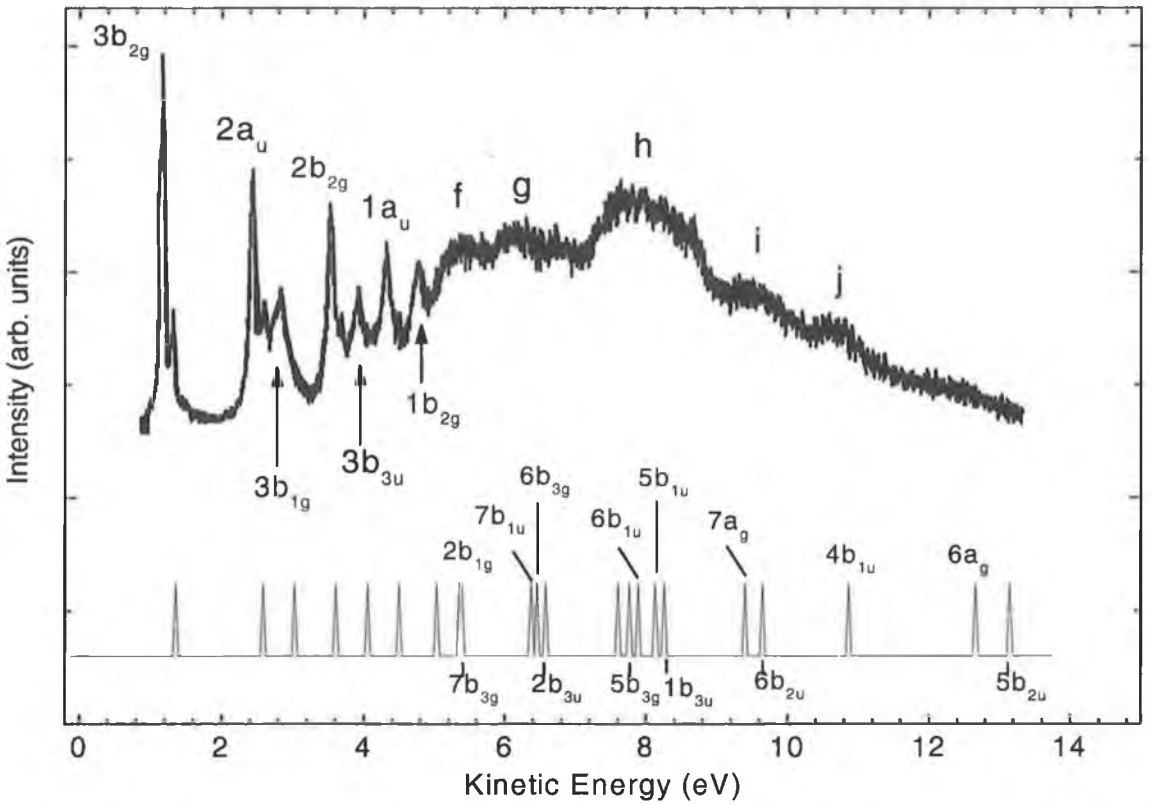

Figure 4.16 *Gas phase spectrum of the pentacene molecule with π and σ orbital assignments* [40], [42].

It was found that for increasing amounts of pentacene on the Au(110) surface, several distinct emission features attributed to the pentacene became evident in the valence band spectra at normal, s and p-polarized emission. All spectra are obtained at incident photon energy of 34 eV, this energy was chosen as it was found to reveal the most resolved features in the valence bands. Figure 4.17 shows a comparison between the valence band spectra at normal emission and s and p-polarized emission for a multilayer (<3 ML) pentacene coverage on Au(110)-(2×1). The Au 5d peaks at ~2.5-3 eV dominate the spectra. The features labelled a – j indicate the intensity and positions of the valence peaks for the bulk pentacene and correspond closely to the gas phase spectrum of the pentacene, shown above the pentacene/Au(110) interface spectrum of figure 4.17.

The photoemission feature that appears to be the HOMO of pentacene at kinetic energy 0.85 eV is labelled a in figure 4.17 and it can be seen in the inset in figure 4.18 that it remains at this energy throughout the deposition sequence for normal emission. Close inspection of the deeper lying molecular orbitals shows that these levels do not shift in energy during deposition. This is an indication of a weak interaction between a

metal substrate and organic overlayer. The formation of interfacial covalent bonds would result in a substantial change in the kinetic energy and line shape of the molecular orbitals, especially those of purely π-derived molecular orbital such as the HOMO [35], [43].

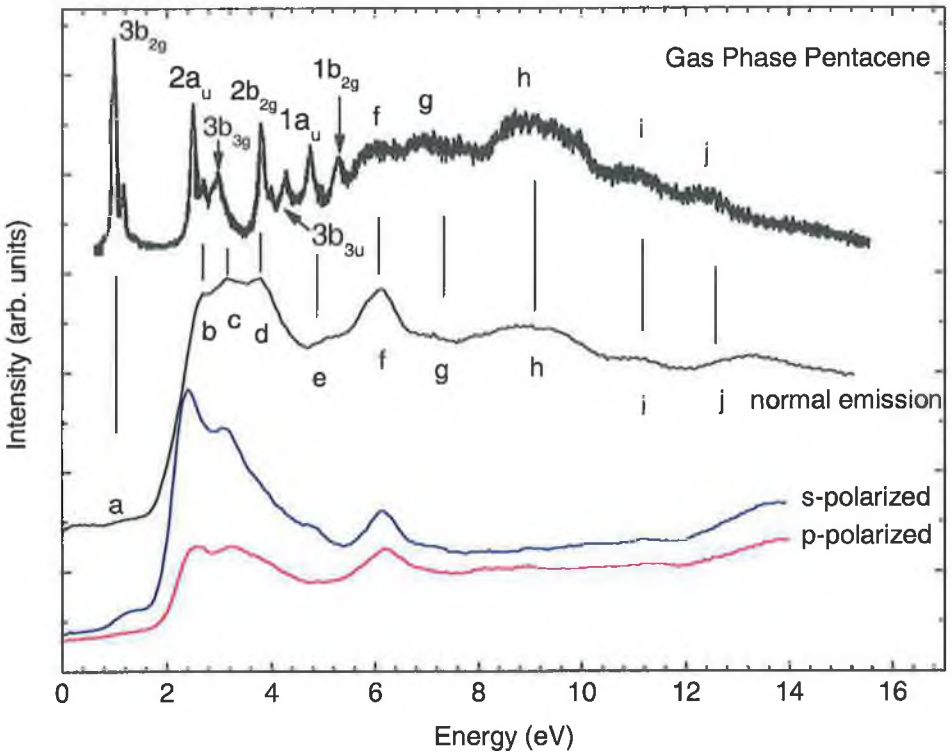

Figure 4.17 *Valence band spectra for clean Au(110) and pentacene covered Au(110) in normal, s and p-polarised emission.*

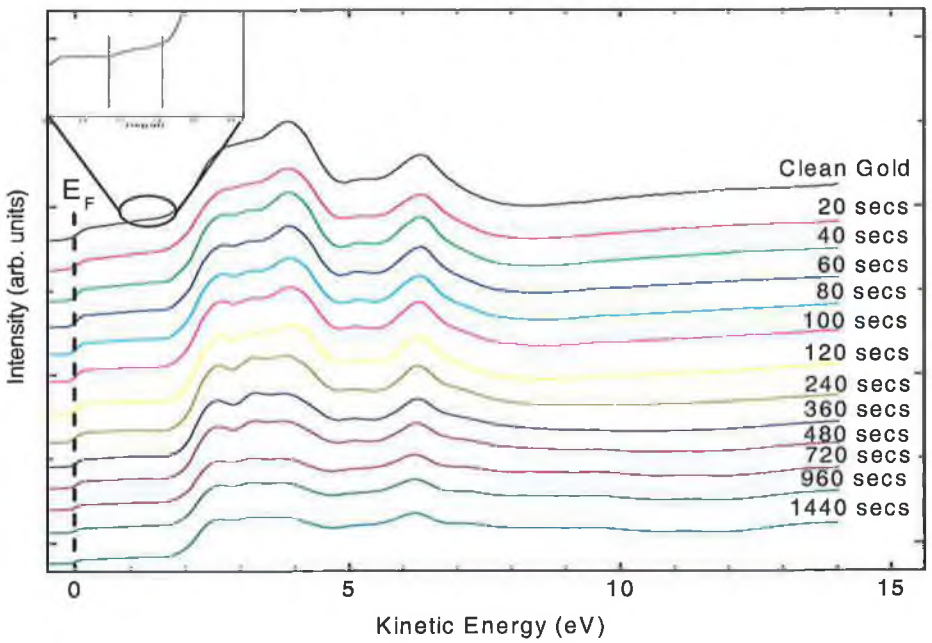

Figure 4.18 *Valence Band spectra for increasing coverages of pentacene on Au(110)-(2×1).*

4.5.2 Group Theory Analysis

To correctly interpret the valence band spectra and evaluate the orientation of the pentacene molecule with respect to the surface, group theory was applied to the pentacene/Au(110)-(2×1) interface. Group theory makes extensive use of symmetry. In general the more symmetric the molecule, the fewer different energy levels it has, and the greater the degenercies of those levels. The study of symmetry can help to decide which transitions between energy levels are possible, a molecule may not be able to absorb light even if that light has precisely the correct energy to span two energy levels of the molecule. The symmetries of the states involved must be compatible in order that the molecule may absorb the light. The selection rules which discriminate between allowed and forbidden transitions are one of the most important uses of symmetry. The selection rules governing the uv-photoemission process from the clean and pentacene covered Au(110)-(2×1) surface, as a consequence of the symmetry properties of the system will be discussed.

Using the simplified one-dimensional model (equation 2.52) it is now possible to obtain the selection rules mentioned in section 2.7.1. To calculate the basis of the selection rules it is necessary to have a direct product of the irreducible representations table for the point group D_{2h}. These are necessary to accurately determine the selection rules for the allowed and forbidden transitions.

D_{2h}	A_g	B_{1g}	B_{2g}	B_{3g}	A_u	B_{1u}	B_{2u}	B_{3u}
A_g	A_g	B_{1g}	B_{2g}	B_{3g}	A_u	B_{1u}	B_{2u}	B_{3u}
B_{1g}		A_g	B_{3g}	B_{2g}	B_{1u}	A_u	B_{3u}	B_{2u}
B_{2g}			A_g	B_{1g}	B_{2u}	B_{3u}	A_u	B_{1u}
B_{3g}				A_g	B_{3u}	B_{2u}	B_{1u}	A_u
A_u					A_g	B_{1g}	B_{2g}	B_{3g}
B_{1u}						A_g	B_{3g}	B_{2g}
B_{2u}							A_g	B_{1g}
B_{3u}								A_g

Table 4.3 *Direct Products of Representation Table.*

By taking the x, y and z polarization directions from the right column in table 2.2 it is possible to construct a basis for the selection rules. Therefore x-polarization is represented by B_{3u}, y-polarization by B_{2u}, and z-polarization by B_{1u}. By performing a direct product of these polarizations (table 4.3) with the initial states (table 2.2), the

final state wavefunctions can be predicted. If the final state contains a totally symmetric irreducible representation A_g of the D_{2h} point group then the transitions are allowed.

$$\int \psi_e^* \hat{\mu} \psi_e \, d\tau_e$$

$$A_g \begin{pmatrix} B_{3u} \\ B_{2u} \\ B_{1u} \end{pmatrix} A_g = \begin{pmatrix} B_{3u} \\ B_{2u} \\ B_{1u} \end{pmatrix} \leftarrow \text{Forbidden} \qquad A_u \begin{pmatrix} B_{3u} \\ B_{2u} \\ B_{1u} \end{pmatrix} A_g = \begin{pmatrix} B_{3g} \\ B_{2g} \\ B_{1g} \end{pmatrix} \leftarrow \text{Forbidden}$$

$$B_{1g} \begin{pmatrix} B_{3u} \\ B_{2u} \\ B_{1u} \end{pmatrix} A_g = \begin{pmatrix} B_{2u} \\ B_{3u} \\ A_u \end{pmatrix} \leftarrow \text{Forbidden} \qquad B_{1u} \begin{pmatrix} B_{3u} \\ B_{2u} \\ B_{1u} \end{pmatrix} A_g = \begin{pmatrix} B_{2g} \\ B_{3g} \\ A_g \end{pmatrix} \leftarrow \text{Allowed}$$

$$B_{2g} \begin{pmatrix} B_{3u} \\ B_{2u} \\ B_{1u} \end{pmatrix} A_g = \begin{pmatrix} B_{1u} \\ A_u \\ A_u \end{pmatrix} \leftarrow \text{Forbidden} \qquad B_{2u} \begin{pmatrix} B_{3u} \\ B_{2u} \\ B_{1u} \end{pmatrix} A_g = \begin{pmatrix} B_{1g} \\ A_g \\ B_{3g} \end{pmatrix} \leftarrow \text{Allowed}$$

$$B_{3g} \begin{pmatrix} B_{3u} \\ B_{2u} \\ B_{1u} \end{pmatrix} A_g = \begin{pmatrix} A_u \\ B_{1u} \\ B_{2u} \end{pmatrix} \leftarrow \text{Forbidden} \qquad B_{3u} \begin{pmatrix} B_{3u} \\ B_{2u} \\ B_{1u} \end{pmatrix} A_g = \begin{pmatrix} A_g \\ B_{1g} \\ B_{2g} \end{pmatrix} \leftarrow \text{Allowed}$$

Referring back to figure 4.17, the allowed and forbidden transitions do not correspond very closely to the valence band peaks that appear in the pentacene/Au(110)-(2×1) interface spectrum. Therefore, the analysis has been further detailed. In table 4.5 it was possible to break down the allowed and forbidden transitions and assign orbital quantum numbers to the final state. Therefore it is easier to consider the outgoing wave in the vacuum as a superposition of spherical harmonics $\langle|L\,M|\rangle$ centered at an origin on the surface. It is clear that for non-zero photocurrent at the detector, it is necessary for M in equation 2.52 to be non-zero but also that the detector does not lie in a nodal plane of the outgoing wave. For normal emission the final state must contain $|L\,0\rangle$ components (s, p_z, d_z^2,....) in order to be detected [44]. That is, the final state belongs to the totally symmetric representation. This places a restriction on the nature of the initial state, only those initial states which have the same symmetry as a component of the operator can contribute to the detected photoemission signal.

The spherical harmonics were obtained from the literature and are listed in table 4.4. Table 4.5 shows the orbital numbers of the final states and the predicted final states allowed for the pentacene molecule up to L = 3 partial waves with the z-axis perpendicular to the substrate. Each $\langle|L\,M|\rangle$ quantum number in table 4.4 can be incremented by +2.

D_{2h}	$\langle \lvert L\ M \rvert \rangle$
A_g	$\lvert 0\ 0 \rangle_+$
B_{1g}	$\lvert 2\ 2 \rangle_-$
B_{2g}	$\lvert 2\ 1 \rangle_-$
B_{3g}	$\lvert 2\ 1 \rangle_+$
A_u	$\lvert 3\ 2 \rangle_-$
B_{1u}	$\lvert 1\ 0 \rangle_+$
B_{2u}	$\lvert 1\ 1 \rangle_+$
B_{3u}	$\lvert 1\ 1 \rangle_-$

Table 4.4 *Table showing symmetrized bases.*

Utilising group theory table 4.5 is constructed for normal emission in both s and p polarisations. But due to experimental constraints the analyser on the UHV chamber at the Aarhus synchrotron was not moveable, and therefore normal emission in s and p polarizations was not obtainable. Normal emission is obtainable for the sample at ~37° with respect to the incident light, but this spectrum contains both s and p-polarisations. Therefore the sample was moved so that normal incidence reflects s-polarised light and grazing incidence reflects p-polarised light. For the s-polarized orientation the detected spectrum is composed of features derived entirely from of s-polarised light. For the p-polarized orientation the detected spectrum is composed mostly from p-polarized light but contains a small component of s-polarized light aswell. It can now be seen that table 4.5 is not essentially accurate for the selection rules needed to determine the orientation of the pentacene molecule on the Au(110)-(2×1) surface, but in most cases it can be used to assist the analysis of the photoemission spectra.

It can be seen from table 4.5 that nearly all states are allowed in normal emission; most contain a $\lvert L\ 0 \rangle$ component in the final state. This is a result of the low symmetry of the pentacene molecule and therefore it is very difficult to differentiate between allowed and forbidden states.

For p-polarized light the final state wavefunction must belong to the a_g or the b_{1u} symmetry species of the D_{2h} point group, shown in column three table 4.5. The z-axis is chosen as normal to the surface and the molecule is assumed to lie flat on the surface in the xy plane, therefore the x-axis is aligned along the long molecular axis and the y-axis is aligned across the long molecular axis. Initial states with symmetry b_{2u}, b_{3u}, b_{3g} and b_{2g} are expected to contribute to the s-polarized spectrum [45] shown in columns one and two table 4.5.

Initial State	x-polarisation	y-polarisation	z-polarisation
a_g	$b_{3u} \rightarrow [1, 1\rangle_-$ $[3, 1\rangle_-$ $[3, 3\rangle_-$	$b_{2u} \rightarrow [1, 1\rangle_+$ $[3, 1\rangle_+$ $[3, 3\rangle_+$	$b_{1u} \rightarrow [1, 0\rangle_+$ $[3, 0\rangle_+$ $[3, 2\rangle_+$
b_{1g}	$b_{2u} \rightarrow [1, 1\rangle_+$ $[3, 1\rangle_+$ $[3, 3\rangle_+$	$b_{3u} \rightarrow [1, 1\rangle_-$ $[3, 1\rangle_-$ $[3, 3\rangle_-$	$a_u \rightarrow [3, 2\rangle_-$
b_{2g}	$b_{1u} \rightarrow [1, 0\rangle_+$ $[3, 0\rangle_+$ $[3, 2\rangle_+$	$a_u \rightarrow [3, 2\rangle_-$	$b_{3u} \rightarrow [1, 1\rangle_-$ $[3, 1\rangle_-$ $[3, 3\rangle_-$
b_{3g}	$a_u \rightarrow [3, 2\rangle_-$	$b_{1u} \rightarrow [1, 0\rangle_+$ $[3, 0\rangle_+$ $[3, 2\rangle_+$	$b_{2u} \rightarrow [1, 1\rangle_+$ $[3, 1\rangle_+$ $[3, 3\rangle_+$
a_u	$b_{3g} \rightarrow [2, 1\rangle_+$ $[2, 3\rangle_+$	$b_{2g} \rightarrow [2, 1\rangle_-$ $[2, 3\rangle_-$	$b_{1g} \rightarrow [2, 2\rangle_-$
b_{1u}	$b_{2g} \rightarrow [2, 1\rangle_-$ $[2, 3\rangle_-$	$b_{3g} \rightarrow [2, 1\rangle_+$ $[2, 3\rangle_+$	$a_g \rightarrow [0, 0\rangle_+$ $[2, 0\rangle_+$ $[2, 2\rangle_+$
b_{2u}	$b_{1g} \rightarrow [2, 2\rangle_-$	$a_g \rightarrow [0, 0\rangle_+$ $[2, 0\rangle_+$ $[2, 2\rangle_+$	$b_{3g} \rightarrow [2, 1\rangle_+$ $[2, 3\rangle_+$
b_{3u}	$a_g \rightarrow [0, 0\rangle_+$ $[2, 0\rangle_+$ $[2, 2\rangle_+$	$b_{1g} \rightarrow [2, 2\rangle_-$	$b_{2g} \rightarrow [2, 1\rangle_-$ $[2, 3\rangle_-$

Table 4.5 *Table showing initial states →final states →partial states allowed.*

For p-polarization, the transitions a_g and b_{1u} are the only allowed transitions, therefore according to figure 4.16 the only features that should be observable are the features g, h, i and j. Comparing this to figure 4.17 it can be seen that none of the π-orbitals are seen in this spectrum, as expected but in the σ-orbital part of the spectrum there are very weak peaks in the spectrum for the features g, h, i, and j.

For s-polarization, the transitions b_{2u}, b_{3u}, b_{3g} and b_{2g} are the only allowed transitions, therefore according to figure 4.16 the only features that should be observable are the π features $3b_{2g}$, $2b_{2g}$, $3b_{3u}$ and $1b_{2g}$, the σ features observable should be f, g, h and i. Comparing this to figure 4.16 it can be seen that the π orbitals that should be seen are seen but there are no observable σ transitions in the spectrum.

The normal emission spectrum has both π and σ transitions. From figure 4.17 it can be clearly seen that there is direct correspondence between the gas phase pentacene spectrum and the pentacene/Au(110)-(2×1) interface. The HOMO (feature a) in figure

4.17 has B_{2g} symmetry from the gas phase spectrum. The other features b, c, and d all correspond to pentacene transitions and have a_u, b_{3g} and b_{2g} symmetries respectively. In the σ region labeled f-j there is indeed a good correspondence to the gas phase spectrum. Unfortunately a molecular orientation could not be determined from this spectrum. A full analysis of this surface would best be suited to an angle resolved photoemission experiment to determine the angle that each of the transitions is strongest. From that analysis a molecular orientation could be derived.

All the analysis that has been performed so far has been based on the assumption that the pentacene molecule is lying flat on the Au(110)-(2×1) surface. This was assumed because the STM images in section 4.3.3 and 4.3.4 revealed what looked like a pentacene molecule lying flat on the surface but there is a possibility that the molecule might be lying on its side in a tilted orientation. Table 4.6 was constructed for normal emission from various orientations of the pentacene molecule on the gold surface. It shows allowed states $[L, 0\rangle_+$ and some of the other possible allowed states $[L, 1\rangle_+$ that have a transition that can be detected for various orientations of the pentacene molecule with respect to the Au(110)-(2×1) surface when z-polarized synchrotron light is incident on it, as shown in figure 4.19. What is shown in each of the columns are the polarization component that the molecule would have with z polarized light incident on the sample. The molecular axes are, z-direction perpendicular to the plane of the molecule, the x-direction is along the long axis of the molecule and the y-direction is across the width of the molecule.

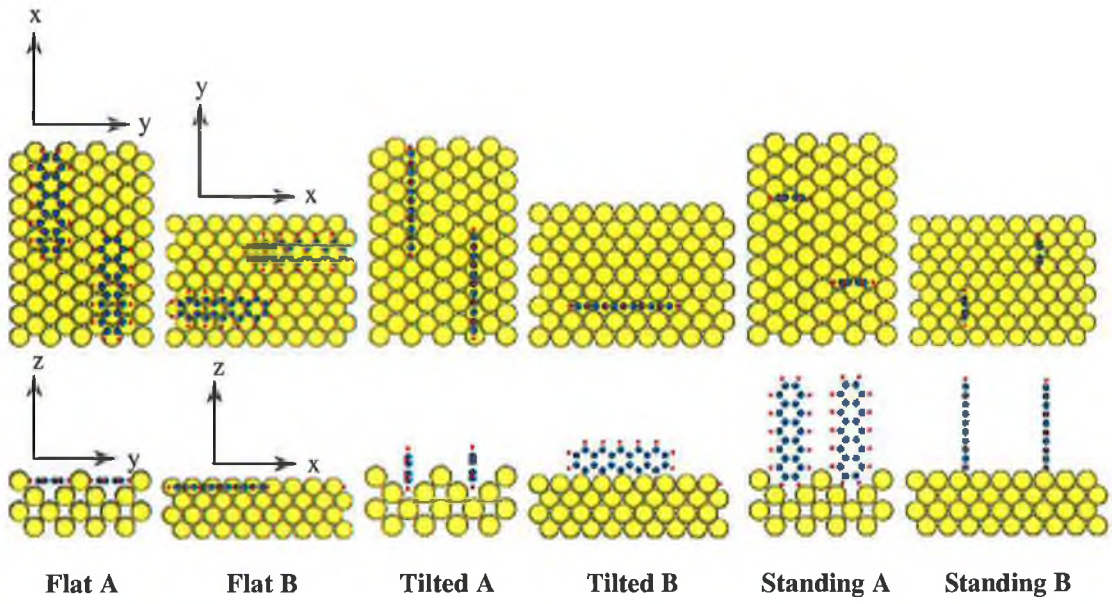

Figure 4.19 *Schematic diagram for various configurations of the pentacene molecule on the Au(110)-(2×1) surface.*

The π-states can now be assigned from the gas phase diagram of pentacene in figure 4.16 [40].

By comparing the allowed states in table 4.6 to figure 4.17, it can be seen that the orientation tilted A has the best correspondence to the pentacene states. In the π-region the HOMO and features b, c, d and e in figure 4.16 can be account for. They have symmetries b_{2g}, b_{3g}, a_u and b_{1u}. In the π-σ and σ region the features f-i can also be accounted for and they have symmetries b_{1g}, b_{3u}, b_{1u} and b_{2u}. Although the correspondence is not always correct the majority of the transitions can be accounted for by this method of orbital analysis. The STM images in sections 4.3.3 and 4.3.4 confirm that the molecule is lying parallel to the surface, either in a flat A or flat B orientation. The STM images cannot account for the molecule in a tilted A orientation. Therefore it is concluded that the group theory analysis has not been conclusive about the orientation of pentacene on the Au(110)-(2×1) surface.

π-Orbitals:

Orbit	*Flat A*		*Flat B*		*Tilted A*		*Tilted B*		*Standing A*		*Standing B*	
	Y	Z	X	Z	Y	Z	X	Y	X	Z	X	Y
π_{11}			$[1, 0\rangle_+$			$[1, 1\rangle_-$				$[1, 1\rangle_-$		
π_{10}						$[2, 2\rangle_-$				$[2, 2\rangle_-$		
π_9					$[1, 1\rangle_-$		$[1, 1\rangle_+$	$[1, 1\rangle_-$	$[1, 1\rangle_+$		$[1, 1\rangle_+$	$[1, 1\rangle_-$
π_8			$[1, 0\rangle_+$			$[1, 1\rangle_+$				$[1, 1\rangle_+$		
π_7			$[0, 0\rangle_+$		$[2, 2\rangle_-$		$[0, 0\rangle_+$	$[2, 2\rangle_-$	$[0, 0\rangle_+$		$[0, 0\rangle_+$	$[2, 2\rangle_-$
π_6						$[2, 2\rangle_-$				$[2, 2\rangle_-$		
π_5			$[1, 0\rangle_+$			$[1, 1\rangle_-$				$[1, 1\rangle_-$		

π + σ - Orbitals

Orbit	*Flat A*		*Flat B*		*Tilted A*		*Tilted B*		*Standing A*		*Standing B*	
	Y	Z	X	Z	Y	Z	X	Y	X	Z	X	Y
$2B_{1g}$					$[1, 1\rangle_-$			$[1, 1\rangle_-$				$[1, 1\rangle_-$
$2B_{3u}$			$[0, 0\rangle_+$		$[2, 2\rangle_-$		$[0, 0\rangle_+$	$[2, 2\rangle_-$	$[0, 0\rangle_+$		$[0, 0\rangle_+$	$[2, 2\rangle_-$
$1B_{1g}$					$[1, 1\rangle_-$			$[1, 1\rangle_-$				$[1, 1\rangle_-$
$1B_{3u}$			$[0, 0\rangle_+$		$[2, 2\rangle_-$		$[0, 0\rangle_+$	$[2, 2\rangle_-$	$[0, 0\rangle_+$		$[0, 0\rangle_+$	$[2, 2\rangle_-$

σ - Orbitals

Orbit	*Flat A*		*Flat B*		*Tilted A*		*Tilted B*		*Standing A*		*Standing B*	
	Y	Z	X	Z	Y	Z	X	Y	X	Z	X	Y
$4B_{1u}$		$[0, 0\rangle_+$		$[0, 0\rangle_+$		$[0, 0\rangle_+$				$[0, 0\rangle_+$		
$4B_{2u}$	$[0, 0\rangle_+$				$[0, 0\rangle_+$		$[2, 2\rangle_-$	$[0, 0\rangle_+$	$[2, 2\rangle_-$		$[2, 2\rangle_-$	$[0, 0\rangle_+$
$3B_{3g}$	$[1, 0\rangle_+$					$[1, 1\rangle_+$				$[1, 1\rangle_+$		
$4A_g$		$[1, 0\rangle_+$		$[1, 0\rangle_+$	$[1, 1\rangle_+$		$[1, 1\rangle_-$	$[1, 1\rangle_+$	$[1, 1\rangle_-$		$[1, 1\rangle_-$	$[1, 1\rangle_+$
$3B_{1u}$		$[0, 0\rangle_+$		$[0, 0\rangle_+$		$[0, 0\rangle_+$				$[0, 0\rangle_+$		

Table 4.6 *Allowed states of various orientations of pentacene with incident synchrotron light for σ orbitals.*

4.6 Conclusion

The pentacene/Au(110)-(2×1) interface was studied using STM, LEED and synchrotron photoemission. It was found using the STM that the pentacene molecules adsorbed parallel to the surface between the gold rows until the gold surface rows were filled or half a monolayer was completed. After a half monolayer is completed it was found that the molecules change orientation. From the STM images the molecules are still adsorbed flat on the surface but now the orientation is across the gold rows in the [001] direction.

Using the LEED technique it was found that the initial adsorption of pentacene onto the Au(110)-(2×1) surface changes the reconstruction from a (2×1) to a (3×1). Measuring with STM shows that the distances between the Au rows has increased from 8 Å to 12 Å, which corresponded to the change observed in the LEED pattern.

Using photoemission it was possible to probe the core levels, the valence bands and perform a work function analysis. From the work function analysis a band diagram was constructed for the pentacene/Au(110)-(2×1) interface. An interface dipole of 1.21 ± 0.04 eV was found. From both the C 1s and the Au $4f_{7/2}$ core levels it was possible to correlate the change in orientation of the molecules after half a monolayer with a shift in energy. The valence band measurements were difficult to analyze. Utilizing group theory to explain the features in the valence band spectra gave inconclusive results. Even after an extensive analysis of the interface it was found that a model of tilted A orientation, figure 4.19, provided the best fit with group theory but it is not convincing. The low symmetry of the molecule prevented the assignment of states because of the lack of selection rules associated with the pentacene molecule for this interface. From the STM images the orientation of the molecules is flat on the surface, but this could be a LDOS effect in the STM. Therefore the STM is also not conclusive.

Chapter 4 References

1. X. Crispin, V. Geskin, A. Crispin, J. Cornil, R. Lazzaroni, W.R. Salaneck, J.L. Bredas, J. Am, Chem Soc, 124, (2002), 8131.
2. Frank-J. Meyer zu Heringdorf, M.C. Reuter, R.M. Tromp, Nature, 412, 517, (2001).
3. C. Seidel, C. Awater, X.D. Liu, R. Ellerbrake, H. Fuchs, Surf. Sci. 371, 123, (1997).

4. J. E. Anthony, J.S. Brooks, D.L. Eaton, S.R. Parkin, J. Am. Chem. Soc., 123, 9482, (2001).
5. S.E. Shahenn, C. J. Brabec, N. S. Sariciftci, F.P. Padinger, T. Fromherz, J. C. hummelen, Appl. Phys. Lett. 78(6) 2001, 841.
6. C. Videlot, D. Fichou and F. Garnier, Synt. Met.101 (1999) 618.
7. J.L. Brédas, J.P. Calbert , D.A. da Silva Filho and J. Cornil, PNAS vol. 99 (2002), 5804.
8. N. E. Gruhn, Demetrio A. da Silva Filho, Tonja G. Bill, Massimo Malogoli, Veacslav Coropceanu, Antoine Kahn and Jean-Luc Brédas, J. Am. Chem. Soc 124 (2002), 7918.
9. S.R. Forrest, Chem. Rev. 97 (1997), 1793.
10. K. Glockler, C. Seidel, A. Soukopp, M. Sokolowski, E. Umbach, M. Bohringer, R. Berndt, W. –D. Schneider, Surf. Sci., 405, 1, (1998).
11. A. Nduwimana, X.G. Gong, X.Q. Wang, Appl. Surf. Sci., 219, (2003), 129 and K.-M. Ho, K.P. Bohnen. Phys. Rev. Lett., 59,16, (1987), 1833.
12. M. Sturmat, R. Koch, K.H. Rieder, Phys. Rev. Lett., 77, 25, (1996), 5071.
13. D.G. Fedak, N.A. Gjostein, Surf. Sci. 8, (1967), 77.
14. W. Moritz, D. Wolf, Surf. Sci. 163, (1985), L655 and W. Moritz, D. Wolf, Surf. Sci. 88, (1979), L29 and references therein.
15. E. Vlieg, I.K. Robinson, K. Kern, Surf. Sci. 166, (1990), 248.
16. D. Marks, D.J. Smith, Phys. Rev. Lett., 51, (1983), 1000.
17. T. Gritsch, D. Coulman, R.J. Behm, G. Ertl, Surf. Sci. 257, (1991), 297.
18. G. Binning, H. Rohrer, Ch. Gerber, E. Weibel, Surf. Sci. 131, (1983), L379 .
19. A. Kühnle, T.R. Linderoth, B. Hammer, F. Besenbacher, Nature 415, 891, (2002).
20. C. Kittle, ***Introduction to Solid State Physics***, Wiley, New York, (1986).
21. S. Lukas, G. Witte, Ch. Woll, Phys. Rev. Lett., 88, 2, 028301, (2002).
22. Ph.Guaino, A.A. Cafolla, D. Carty, G. Sheerin, G. Hugues, Surf. Sci. 540 (2003) 107.
23. V. Corradini, C. Menozzi, M. Cavallini, F. Biscarini, M. G. Betti and C. Mariani, Surf. Sci. 532 (2003), 249.
24. S. Modesti, J.K. Gimzewski and R.R. Schlittler, Surf. Sci. 331 (1995) 1129.
25. K.-P. Bohen and K. M. Ho, Electrochimica Acta. 40, (1995), 129.
26. E.A. Silinsh, V. Capek, ***Organic Molecular Crystals***, American Institute of Physics Press, New York, 1994.
27. M. Kasaya, H. Tabata and T. Kawai, Surf. Sci. 400 (1998) 367.

28. C.D. Dimitrakopoulos, A.R. Brown and A. Pomp, J. Appl. Phys. 80(4) (1996) 2501.
29. Ricardo Ruiz, Bert Nickel , Norbert Koch, Leonard C. Feldman, Richard F. Haglund, Antoine Kahn and Giacinto Scoles, Phys. Rev. B 67 (2003) 125406.
30. Joo H. Kang and X.-Y. Zhu., Appl. Phys. Lett. 82, (2003) 3248.
31. C.B. France, P.G. Schroeder and B.A. Parkinson, NanoLetters 7 (2002), 693.
32. Q. Chen, T. Rada, A. McDowall and N.V. Richardson, Chem. Mater. 14 (2002), 743.
33. L. Ley, M. Cardona, Topics in Applied Physics Volume 27: ***Photoemission in Solids II***, Springer-Verlag New York, 1979.
34. P.G. Schroeder, C.B. France, J.B. Park, B.A. Parkinson, J. of Appl. Phys., 91, 5, (2002), 3010.
35. N. Koch, J. Ghijsen, R.L. Johnson, J. Schwartz, J.-J. Pireaux, A. Kahn, J. Phys. Chem. B, 106, (2002), 4192.
36. P.A. Bruhwiler, S.E. Schnatterly, Phys. Rev. Lett, 61, 3, (1988), 357.
37. N. Marsot, R. Belkhou, F. Scheurer, B. Bartenlian, N. Barrett, M.A. Delaunay, C. Guillot, Surf. Sci. 377, (1997), 225.
38. OriginLab Corporation, Origin© 7.0 SR0, One Roundhouse Plaza, Northampton, MA 01060, USA.
39. P.G. Schroeder, C.B. France, J.B. Park, B.A. Parkinson, J. Phys. Chem. B, 107, (2003), 2253.
40. N.O. Lipari, C.B. Duke, J. Chem Phys, 63(5), (1975), 1768.
41. P.A. Clark, F. Brogli, E. Heilbronner, Helvetica Chimica Acta, 55(5), (1972),1415.
42. Hyperchem (TM) Professional 7.0, Hypercube Inc., 1115 NW 4th Street, Gainsville, Florida 32601, USA.
43. C. Shen, A. Kahn, J. Schwartz, J. of Appl. Phys., 89, (2001), 449.
44. N.V. Richardson, D.R. Lloyd, C.M. Quinn, J. of Electron Spectroscopy and Related Phenomena, 15, (1979), 177.
45. P. Yannoulis, K.-H. Frank, E.-E. Koch, Surf. Sci., 241, (1991), 325.

Chapter 5 RAS on Au(110)-(2×1)

5.1 RAS on Clean Au(110)-(2×1): a probe of surface states

5.1.1 Experimental Setup

The RAS measurements were carried out in an ultra high vacuum chamber with base pressure better than 2×10^{-10} mbar. The Au(110) sample was subjected to repeated cycles of Ar^+ bombardment (~1 keV for 15 minutes) and annealing (~673K [1] for 15 minutes). This procedure produced a clean Au(110)-(2x1) surface as confirmed by LEED measurements.

5.1.2 Clean Au(110)-(2×1) Surface:

Important contributions to the RAS spectra of Cu(110)[4],[5] and Ag(110)[6],[7] arise from transitions involving surface states, therefore it is expected that the RAS response of Au(110) can be explained in a similar way. But unlike the Cu(110) and Ag(110), the Au(110) surface adopts a (2×1) missing row reconstruction. Xu et. al. [2] have suggested that this reconstruction changes the surface states available for RAS. The electronic structure of Au(110) surface has been investigated previously both theoretically[2] and experimentally[3] and is detailed in chapter 2.

The RAS response from metal surfaces has not been treated well theoretically and therefore an empirical approach is employed based on a three phase model, in which medium 1 is vacuum, medium 2 is a thin overlayer of thickness d, and medium 3 is an infinitely thick isotropic solid, (refer chapter 2) [8], [9]. In this model transitions associated with surface states are combined with a representation of the bulk optical properties of the metal to produce an empirical RAS spectrum. Following Cole et. al. [8] the bulk dielectric response, ε_b is represented by

$$\frac{1}{1-\varepsilon_b} = A(\omega) - iB(\omega) \tag{5.1}$$

where A(ω) and B(ω) are calculated from the bulk properties of the gold.

$$A(\omega) - iB(\omega) = \frac{1}{1-\varepsilon_b} = \frac{1-\varepsilon_3'(\omega) - i\varepsilon_3''(\omega)}{(1-\tilde{\varepsilon}_3(\omega))^2} \tag{5.2}$$

where

$$\tilde{\varepsilon} = \varepsilon' - i\varepsilon''$$

$$\varepsilon' = n^2 - k^2$$

$$\varepsilon'' = 2nk$$

Taking the real and imaginary parts

$$A(\omega) = \frac{\varepsilon_3'(\omega) - 1}{(1-\varepsilon_3'(\omega))^2 + (\varepsilon_3''(\omega))^2}, \qquad B(\omega) = \frac{\varepsilon_3''(\omega)}{(1-\varepsilon_3'(\omega))^2 + (\varepsilon_3''(\omega))^2} \tag{5.3}$$

These parameters are crucial to the interpretation of reflectance anisotropy measurements. In this work they are calculated from n and k values of the Au(110) given by Palik [10], and are shown in figure 5.1. Note that the real part of the reflectance difference spectra observed for the clean Au(110)-(2×1) follows B(ω) quite closely in the energy range 1.5-3.5 eV.

The principal axes of the optical response, x and y are chosen along the ⟨001⟩ and ⟨$\bar{1}$10⟩ crystal directions respectively. An optical transition arising from incident light polarised along the x-axis in the surface is represented by a Lorentzian contribution

$$\varepsilon_s^x(\omega) = 1 + \frac{S/\pi}{\omega_t - \omega + i\Gamma/2} \qquad \varepsilon_s^y(\omega) = 1 \tag{5.4}$$

where S is the intensity, ω is the energy, ω_t is the transition energy and Γ is the full width at half maximum of the transition. The real and imaginary parts of the RAS response [9], [8], [11] can be expressed in terms of A(ω) and B(ω), as

$$\Re(\omega) = -\frac{2\omega d}{c}\left[A(\omega)\Delta\varepsilon_S''(\omega) + B(\omega)\Delta\varepsilon_S'(\omega)\right] \tag{5.5(a))}$$

$$\Im(\omega) = \frac{2\omega d}{c}\left[A(\omega)\Delta\varepsilon_S'(\omega) - B(\omega)\Delta\varepsilon_S''(\omega)\right] \tag{5.5(b))}$$

where $\Delta\varepsilon_S' = \varepsilon_S^{x'} - \varepsilon_S^{y'}$ and $\Delta\varepsilon_S'' = \varepsilon_S^{x''} - \varepsilon_S^{y''}$ are the differences between the real and imaginary components of ε_S^x and ε_S^y.

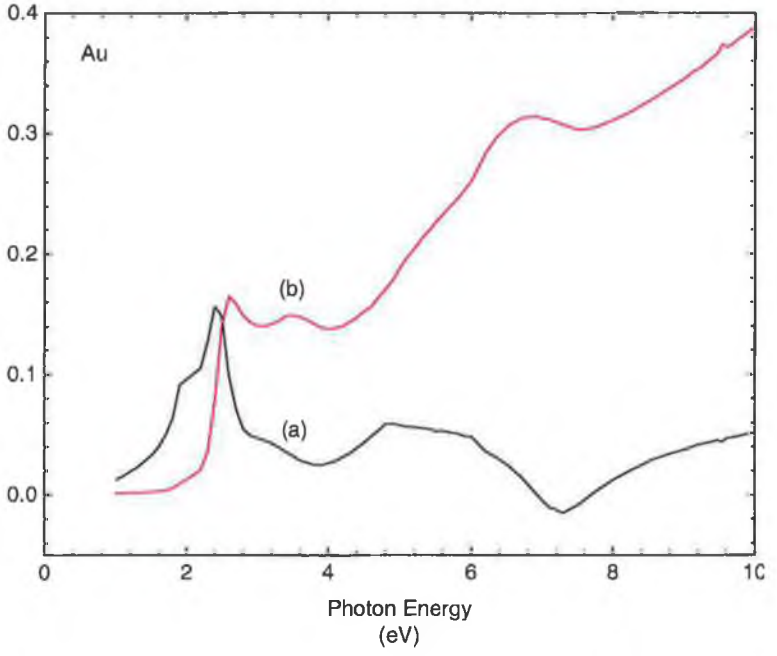

Figure 5.1 *(a) A(ω) and (b) B(ω) coefficients calculated from the n and k values in Palik* [10].

Figure 5.2 shows the RAS spectrum (real part) of the clean Au(110)-(2×1) and the simulated RA spectrum. The key spectral features are found at 1.9 eV, 2.5 eV, 3.5 eV, and 4.5 eV as indicated.

The Re(Δr/r) spectrum is fitted using three Lorentzian peaks. The first peak at ~1.7 eV is reproduced with a peak that has a transition energy of 1.7 eV ± 0.4 eV and is orientated along the [001] direction corresponding to a transition polarised along the x-direction. The next peak at ~2.5 eV is reproduced by a transition at 2.53 eV ± 0.2 eV polarised along the y-axis in the model. These two transitions model the RAS spectrum of the Au(110) very well below 3.7 eV. However a third peak at 3.5 eV ± 0.2 eV, polarised along the y-axis, is required to model the data over the entire range.

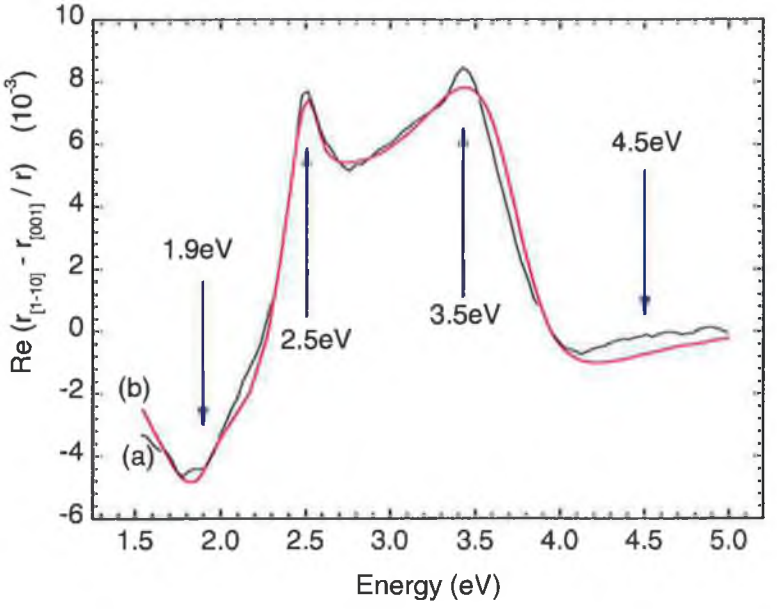

Figure 5.2 *(a) RAS spectra of clean Au(110)-(2×1) reconstruction with relevant features indicated by arrows and (b) the fitted model with the fitting contributions.*

Combining these three transitions the model fitted the experimental spectrum of the clean Au(110) well, as shown in figure 5.2. Table 5.1 summarises the parameters used to model the Re(Δr/r) Au(110)-(2×1) spectrum.

	PEAK 1	PEAK 2	PEAK 3
Direction	[001]	[1-10]	[1-10]
ω_t / eV	1.7 ± 0.4	2.56 ± 0.2	3.75 ± 0.2
Transition ($\bar{\Gamma} - \bar{X}$) [2]	F→A	Interband	R→I
Γ / eV	0.7	0.24	0.72
S	1.05	0.065	0.4

Table 5.1 *parameters of the fits to well ordered Au(110)-(2×1).*

The optical transitions can be interpreted in terms of the Au(110)-(2×1) electronic band structure derived from a first principals calculation by Xu et. al. [2] and from experimental work [3]. Transitions between surface bands at the $\bar{\Gamma}$ and $\bar{X}$ points account for all the transitions seen in the clean Au(110) RAS spectra. At the $\bar{\Gamma}$ point the calculation indicates the presence of an occupied surface resonance, F, of even symmetry at 1.7 eV below E_F. An unoccupied surface state of odd symmetry, A, lies at ~0.3 eV above E_F. These two states have the correct symmetry for an optical transition with an expected value of 2.0 eV. At the $\bar{X}$ point, a surface band, I, of predominantly d-character lies within the bulk band region starting at ~1.5 eV below E_F. The band, R, is a surface resonance, which lies ~2.2 eV above E_F. A transition between these two states has the correct symmetry for a RAS transition and an expected value of 3.7 eV. These two transitions are incorporated into the simulation of the RAS spectra, as shown in table 5.1.

5.2 Effect of Surface Disorder in Au(110)

There are many ways to introduce surface disorder in a crystal. Introducing a small amount of a gas, such as oxygen or nitrogen on the Cu(110) and Ag(110) surfaces can induce surface disorder [7],[5]. Stahrenberg et. al. [5], [7] measured the RAS response of these modified surfaces, and recorded the difference in the spectral features, observing a quenching of the surface states.

The Au(110) surface can be disordered by introducing a contaminant or evaporating another atom or molecule onto the sample surface. Stahrenberg et. al. [7] introduced a small amount of potassium onto the Au(110)-(2×1) surface in order to modify the surface electronic structure and to experimentally distinguish between the surface and bulk contributions in the RA spectra. Evaporating potassium on the Au(110) sample induced surface disorder, as was confirmed by LEED. RAS measurements showed that a number of features in the potassium/Au(110)-(2×1) spectra were different from that of the clean Au(110)-(2×1) spectra. In the real part of the potassium/Au(110)-(2×1) RAS spectrum, the signal was quenched below the 2.5 eV peak. This is mainly in the area below the onset of the Au 5d bands. The peaks at 1.9 eV and 2.5 eV are surface states or surface resonances with mainly p-like character. These peaks were reduced significantly in intensity. At energies greater than 2.5 eV, above the onset of the Au 5d bands, the Au(110)-(2×1) features were still clearly visible but slightly reduced in intensity. Annealing of the disordered, potassium covered, Au(110) surface to 673K

resulted in an ordered c(2×2) LEED pattern. The peak at 1.9 eV goes negative in the $Re(\Delta r/r)$ spectrum and the peak at 2.5 eV returns to its original intensity. Above the onset of the Au 5d bands, the bulk interband contributions were similar to that of the clean Au(110) surface.

The Au(110) surface organises itself naturally at room temperature in the (2×1) missing row reconstruction but at ~673K the surface reconstructs in a (1×1) disordered phase. The (2×1) to (1×1) transition is a continuous order-disorder transition, therefore there is a non-abrupt phase change. The results of LEED [12], [13] and ion scattering [14] experiments support the fact that at all temperatures the surface contains an adsorbed half monolayer of Au atoms. In the (1×1) phase the adatoms randomly occupy regular lattice sites and this overlayer becomes ordered by short-range atomic jumps. The RAS data is completely consistent with this model for the (2×1) to (1×1) phase transition. If the transition takes place by the random displacement of adatoms, a range of local (2×1) environments will occur and the resulting disorder will broaden the energy states probed by RAS, particularly the surface state, A, and states below 2.5 eV.

Figure 5.3 shows $Re(\Delta r/r)$ spectra of Au(110) recorded at increasing sample temperatures. The spectra at higher temperatures show similar changes to those observed in the potassium covered Au(110). The part of the spectrum above 2.5 eV is reduced in intensity but by a much smaller factor than the part of the spectrum below 2.5 eV. In the energy region above 2.5 eV transitions are dominated by atoms in the second Au layer [11] and are therefore not as surface sensitive as the transitions below 2.5 eV. RAS is a local probe and the surface sensitive peaks at and below 2.5 eV, which arise from transitions at the $\bar{\Gamma}$ point, (state F and state A) are clearly reduced in intensity as the sample is annealed to higher temperatures. The above interpretation of the transition from (2×1) to (1×1) agrees with the RAS spectrum in figure 5.3, where the spectrum becomes broader as a consequence of increased disorder as temperature is increased.

Sheridan et. al. [11] performed a similar experiment with Au(110) but they induced the (2×1)-(1×1) phase transition electrochemically in an electrolyte solution of 0.1M H_2SO_4. At an electrode potential of approximately 0.2 V a change in the spectra was observed that was very similar to that shown in figure 5.4 and those measured by Stahrenberg et. al [15].

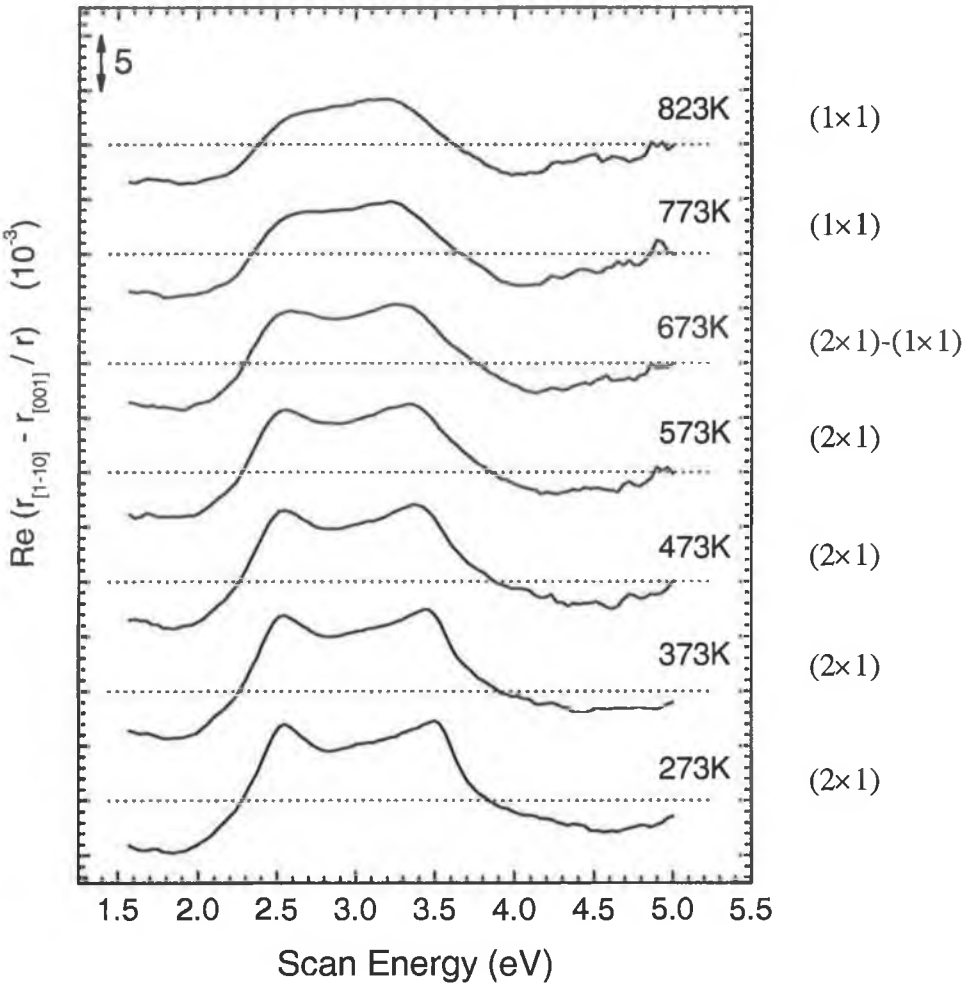

Figure 5.3 *RAS spectra of the Au(110)-(2×1) to (1×1) transition at various temperatures. The dashed lines indicate zero levels. All temperatures ± 5 K.*

5.3 Effect of Surface Roughness

In this experiment the effect of surface roughness on the Au(110)-(2×1) RAS spectra is investigated.

Weightman et. al. [18] previously performed RAS and STM experiments on this surface after Ar^+ bombardment [18]. For the clean Au(110), large and well ordered terraces with (1×2) reconstruction and continuous monatomic steps are observed. After argon bombarding for 16 minutes it was found that the surface had an undulating morphology consisting of elevated islands and valley regions [18]. Domains of (1×2) reconstruction were found following longer bombardment times, but the structure of the undulating morphology was not well resolved, suggesting a disordered structure at these sites. The STM data is consistent with the view that the surface is a disordered arrangement with local (1×2) environments. LEED experiments on Au(110) showed a good (2×1) pattern with resolved spots. But LEED experiments [18] on the argon

bombarded surface showed streaks developing along the rows of diffraction spots indicating the [001] direction. These streaks indicate that a number of the atoms in the "atom chains" of the (2×1) reconstruction along the $[1\bar{1}0]$ direction randomly shift position in the [001] direction; and occupy sites in between neighbouring $[1\bar{1}0]$ rows, resulting in the loss of the periodicity along the $[1\bar{1}0]$ direction.

Similar work investigating the effect of surface roughness has also been performed on the Cu(110) surface [16],[17].

Surface roughness in the clean Au(110)-(2×1) surface was induced by repeated argon ion bombardment at 500 eV without annealing the Au crystal. In this case it was found that the RAS technique is particularly sensitive to changes in the surface morphology in the photon energy range 3.0-5.0 eV. To examine the effect of surface roughness, the clean Au(110) surface was subjected to successive Ar^+ bombardment (500 eV, 6.2 μA, 300 K) for one minute time intervals.

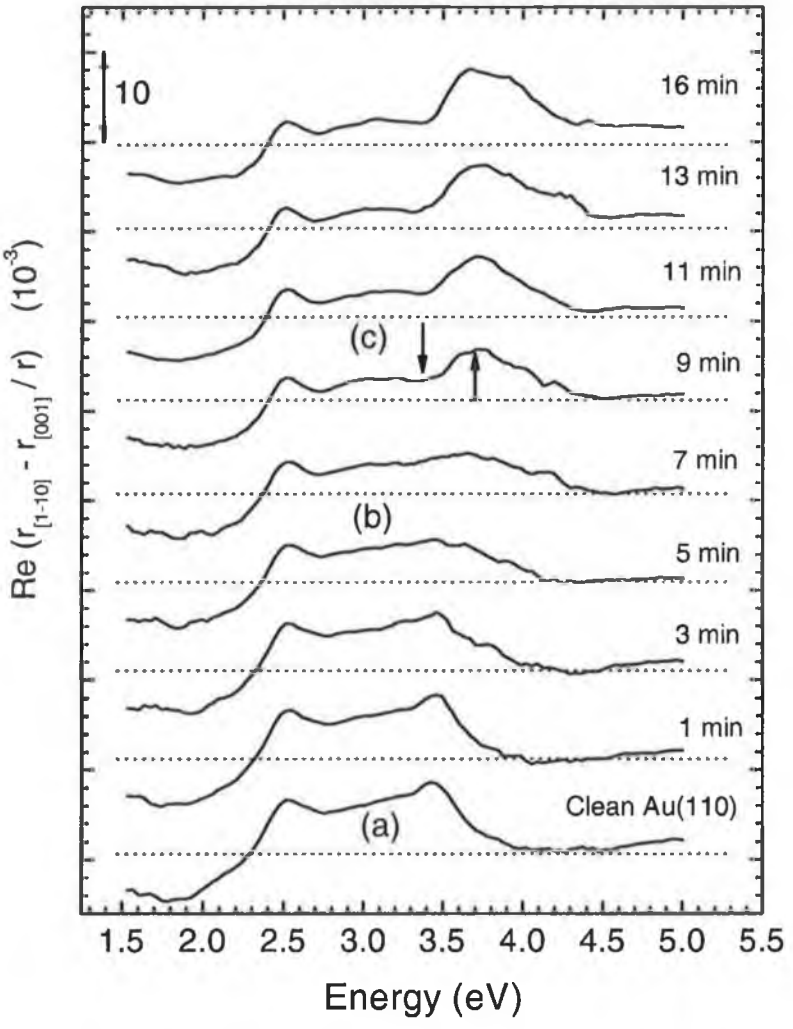

Figure 5.4 *RAS spectra of Argon bombarded Au(110) for increasing bombardment times as indicated.*

The RAS spectrum of the clean, ordered Au(110)-(2×1) is shown in figure 5.4(a), the familiar positive going peaks at 2.5 eV and 3.5 eV are evident. The change in the Re(Δr/r) with increasing surface roughness is shown in successive spectra in figure 5.4.

The positive going feature between 2.1 eV and 2.5 eV is reduced in intensity but retains a similar slope with increasing bombardment time. Features between 3.0 eV and 5.0 eV change dramatically with increasing bombardment time with the peak at 3.5 eV reduced in intensity until it is unobservable after ~5 minutes (figure 5.4(b)). Further bombarding produces a broad negative going feature at 3.4 eV and a positive going feature centered at 3.55 eV after 9 minutes, indicated by the arrows in figure 5.4(c). The feature centered at 3.55 eV has a similar gradient to the feature between 2.1 eV and 2.5 eV.

The changes observed in the response below 2.5 eV (figure 5.4) are explained by the loss of the (2×1) reconstruction. This result is in agreement with the results found in section 5.2 where it was shown that the intensity of the Re(Δr/r) spectrum below 2.5 eV decreased at elevated temperatures due to the (2×1)→(1×1) phase transition. The peak at 2.5 eV maintains a similar intensity (figure 5.5) and this indicates the lack of sensitivity of this feature to increasing surface roughness. Between 3.0 eV and 5.0 eV the spectra are sensitive to surface roughness. Therefore the peaks in this region can act as an indicator as to the quality of the surface under investigation. The simulated spectra for heavily bombarded Au(110)-(2×1) is shown in figure 5.5.

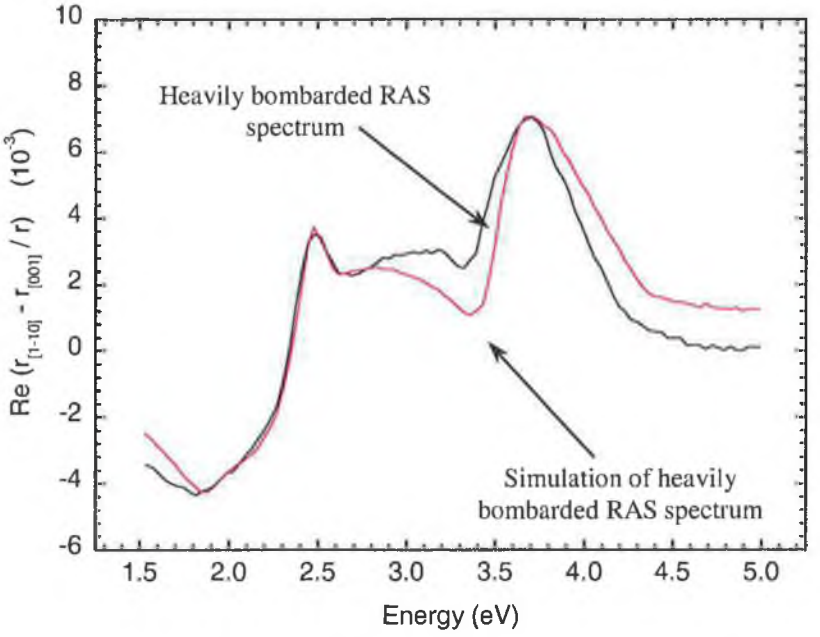

Figure 5.5 *Spectra of heavily bombarded Au(110)-(2×1) and a calculated spectrum of this curve.*

	PEAK 1	PEAK 2	PEAK 3
direction	[001]	[1-10]	[001]
ω_t / eV	1.7 ± 0.03	2.53 ± 0.03	3.7 ± 0.03
Transition ($\bar{\Gamma} - \bar{X}$) [2]	F→A	Interband	R→I
Γ / eV	1.0 ± 0.10	0.17 ± 0.05	0.3 ± 0.05
S	1.7 ± 0.04	0.06 ± 0.01	0.23 ± 0.01

Table 5.2 *Fitting parameters for the heavily Ar^+ bombarded Au(110)-(2×1)* Re(Δr/r) *spectrum.*

It is possible to generate a simulated spectrum for the heavily bombarded surface by varying the energy, width, and intensity of the third component in the model. The model for the heavily bombarded surface shows good agreement in the region 1.5 eV to 2.9 eV. At approximately 3.35 eV, the generated spectrum is lower in intensity than the experimental data, the peak at 3.7 eV is reproduced in magnitude. Above 3.7 eV the generated spectrum is higher in intensity than the experimental profile. This may be due to the fitting procedure or there may be the need to use a fourth component. In the literature only three components are used to fit this peak [18]. On the heavily bombarded surface the loss of long range order is reflected in the increased width of the peak at ~1.7 eV. The parameters for the peak at 2.5 eV are identical to those used for the clean surface, this indicates that this feature is insensitive to surface roughness.

5.4 Pentacene on Au(110)-(2×1)

In this experiment the RAS technique is employed to investigate pentacene evaporated onto the Au(110)-(2×1) surface. It is found that increasing the pentacene coverage on the clean Au(110)-(2×1) surface, shows a change in the orientation of the molecule on that surface. Coverages above and below half a monolayer can be detected and interpreted using RAS.

Pentacene was chosen because it has intermolecular electronic transitions in the visible-infrared region and therefore are appropriate to the spectral range of the RAS spectrometer. Structural investigations of the missing row reconstruction on the Au(110)-(2×1) surface show that the row separation (shown in figure 5.6) is on the order of the width of an acene molecule. The missing row separation on the Au(110)-(2×1) surface from atom centre to centre is 8.16 Å[19], (figure 5.6) the width of the pentacene molecule is approximately 5.04 Å and the length is 14.21 Å[20], [21]. It may therefore be possible for the molecule to adsorb between the Au rows in the [1$\bar{1}$0] direction for coverages of approximately half a monolayer.

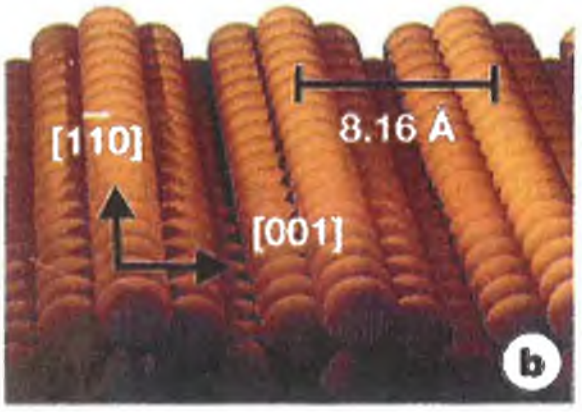

***Figure 5.6** Image of the Au(110)-(2×1) reconstruction*[19].

5.4.1 The Visible-IR spectrum of pentacene

A visible-near infrared absorption spectrum of pentacene is shown in figure 5.7. As with other large conjugated molecules, the totally symmetric (D_{2h} symmetry) vibrational modes are expected to dominate the vibronic transitions in pentacene[22]. The electronic spectrum of pentacene exhibits three adsorption band systems in the range 2-6 eV (250-1000 nm) associated with transitions from the X^1A_g ground state to the (1^1B_{2u}), (1^1B_{3u}) and (2^1B_{3u}) states respectively. The observed transitions and their assignments are listed in table 5.3 [22], [23], [24].

Wavelength (nm)	*Energy(eV)*	*Assignment*
578	2.147	$1^1B_{2u} \leftarrow X^1A_g$
533	2.328	ν_{CCC} | | bend
498	2.492	ν_{CC} stretch
467	2.657	$2\nu_{CC}$ stretch
427	2.906	
403	3.079	
381	3.257	
346	3.586	$1^1B_{3u} \leftarrow X^1A_g$
330	3.76	
303	4.095	ν_{CH} stretch
292	4.24	$2^1B_{3u} \leftarrow X^1A_g$
287	4.32	ν_{CH} bend
277	4.47	ν_{CC} stretch

***Table 5.3** shows the optical transitions of pentacene and some of their assignments* [23], [22]

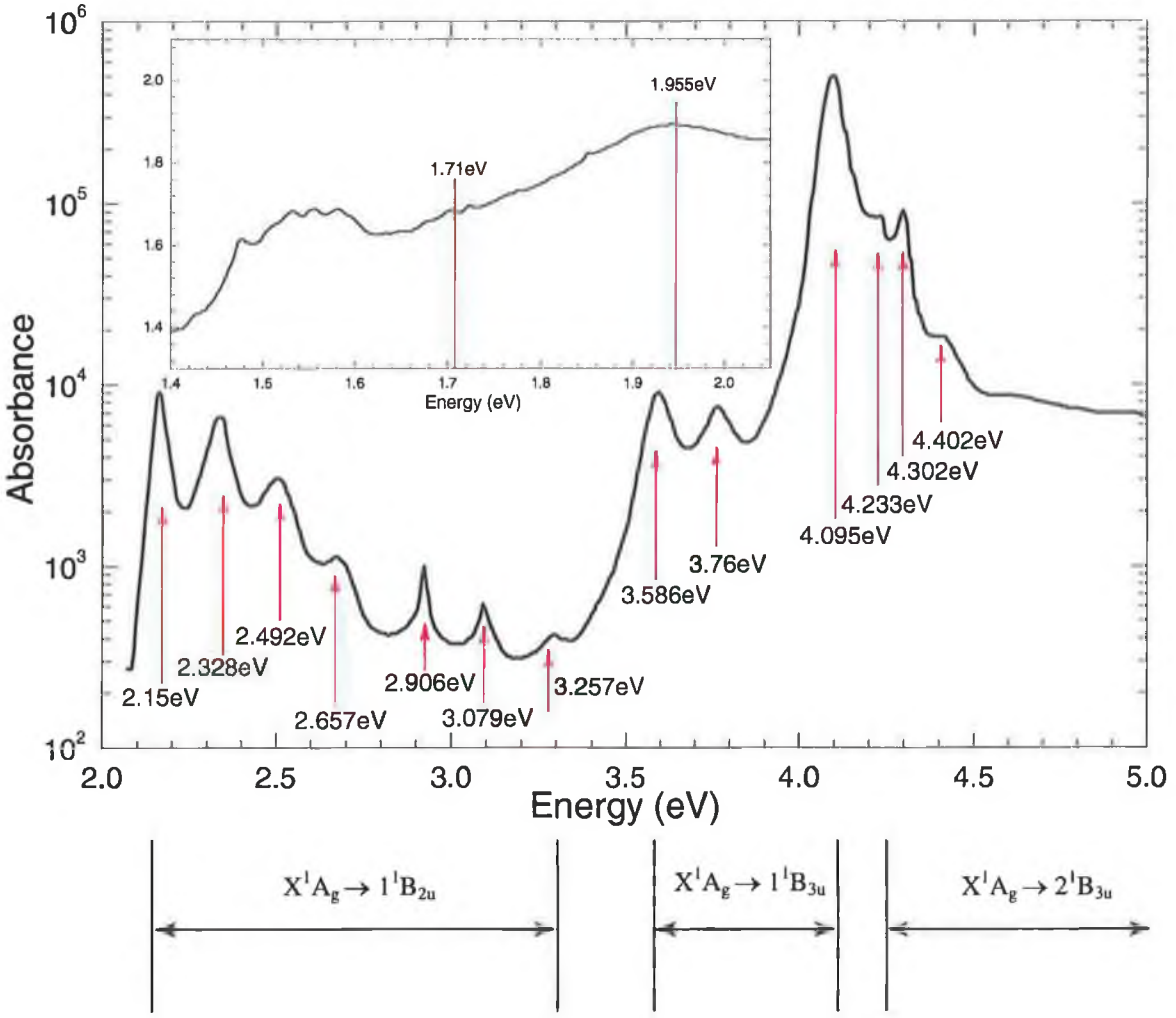

***Figure 5.7** Absorption spectrum of pentacene from the near infrared to the near ultraviolet* [22],[23],[24].

In principal the azimuthal orientation of an adsorbate can be determined from the RA spectrum if a well-defined transition dipole, relative to the molecular coordinates, exists within the available energy range and the metal does not screen the E field of the light parallel to the metal surface. In favourable cases, such as the one chosen here, the application of RAS to molecular adsorbates requires an understanding of [25] whether an adsorbate transition causes an increase or decrease in the reflectivity, because an increase or a decrease corresponds to a 90° rotation of the adsorbate relative to the substrate.

5.4.2 Low Coverage to Monolayer Coverage:

Pentacene was deposited on the clean Au(110)-(2×1) surface at room temperature for coverages up to half a monolayer. In chapter 4 it was seen using STM and photoemission that adsorption of the pentacene molecule on the Au(110)-(2×1)

surface for a coverage of half a monolayer results in a change in reconstruction from a (2×1) to a (3×1). Therefore the reconstruction change will be reflected in the RAS response by a change in the $\mathrm{Re}(\Delta r/r)$ lineshape of the clean Au(110)-(2×1).

Figures 5.8(a)-(f) shows the RA spectra for several depositions for increasing coverages up to half a monolayer of pentacene deposited on the Au(110)-(2×1) surface in 0.1 ML increments. Figure 5.8(a) shows the RA spectrum for the clean Au(110)-(2×1) reconstruction. It can be seen that the RAS response does change for the initial deposition of 0.1 ML. From successive depositions of pentacene it can be seen that the RAS spectra remain approximately unchanged in the energy region of 1.5-1.9 eV. But significant changes occur for the two Au(110)-(2×1) peaks at ~2.5 eV and ~3.5 eV even though they remain visible throughout the deposition sequence. The peak at 2.5 eV has shifted in energy by about 0.1eV and the peak 3.5 eV remains in the same position. The positive going change in intensity of the two peaks increases with the coverage. There is a significant change in the RAS response between 0.3 ML and 0.4 ML. At 0.4 ML coverage a positive going shoulder at ~3.85 eV and a broad peak with a negative going change in intensity at ~4.4 eV develops. For the following coverage of 0.5 ML the shoulder at 3.81 eV develops into a prominent peak and the broad peak at 4.4 eV increases in intensity. Also two more peaks at 3.11 eV and 3.25 eV become apparent in the spectrum.

In general there is an increase in the intensity of the RAS response, which shows that the surface is becoming gradually more reflective for light polarized along the $[1\bar{1}0]$ direction and gradually less reflective for light polarized along the [001] direction.

Features indicated by arrows in figure 5.8 can be assigned to electronic transitions in the pentacene molecule with energy positions and assignments as listed in table 5.3. There is good agreement between the peaks observed with RAS figure 5.8 and the absorption spectrum shown in figure 5.7. It is important to note that these energies do not necessarily coincide with transition energies observed in optical absorption, but the optical absorption spectra reveals good correspondence confirming the assignment to optical transitions in pentacene.

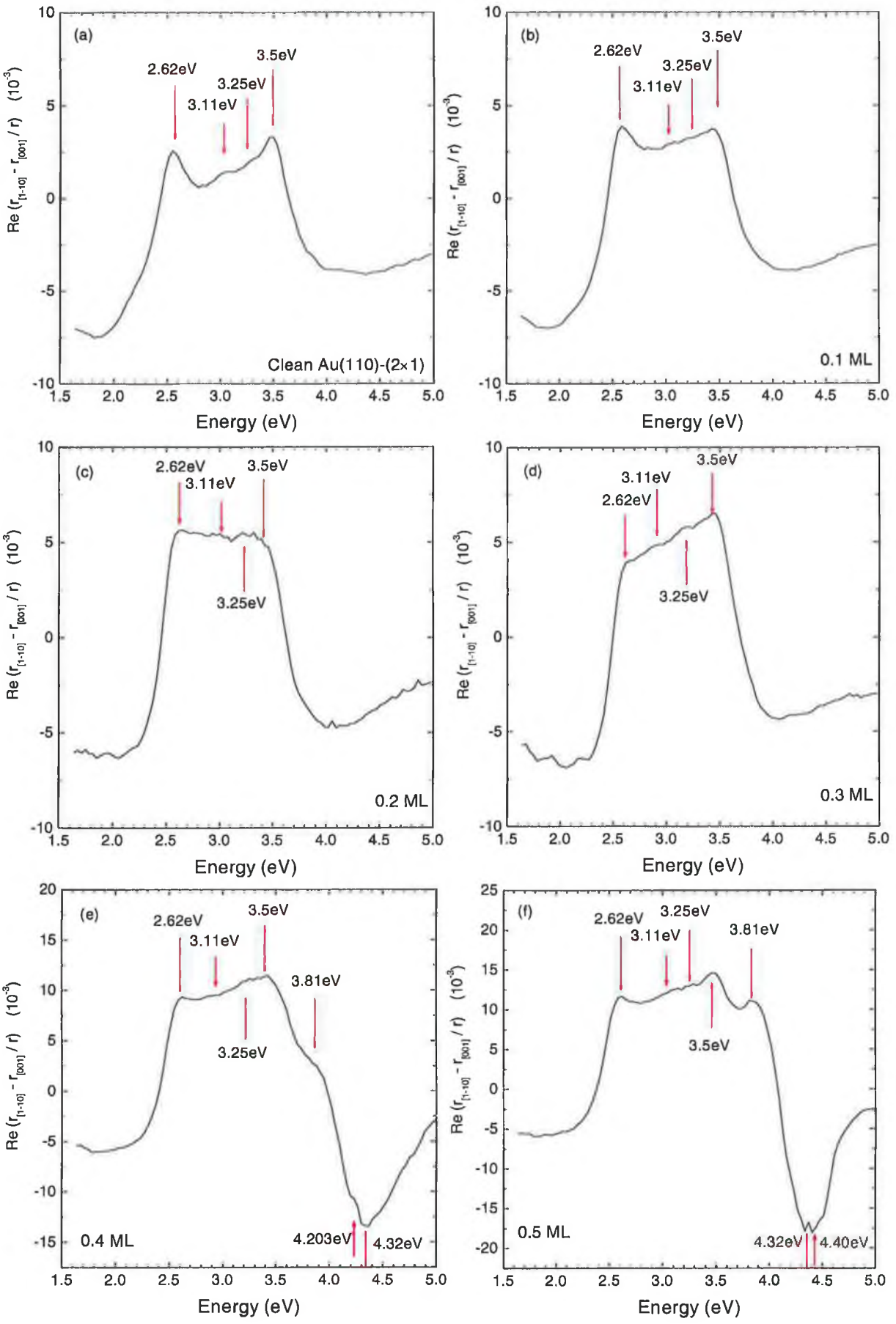

Figure 5.8 *real RAS spectra for increasing coverages of pentacene on Au(110)-(2×1) (a)clean Au(110)-(2×1), (b) 0.1 ML, (c) 0.2 ML,(d) 0.3 ML, (e) 0.4 ML, (f) 0.5 ML.*

5.4.3 Intermediate Pentacene Coverage:

Figure 5.9 shows the RAS spectra for a series of pentacene depositions from ~0.6 ML to ~1.1 ML. A new negative going peak is observed at 1.78 eV appears at 0.6 ML. At this coverage the peak is small, but the negative change in intensity continues to increase with increasing coverage. In the energy range from 1.9 eV to 2.5 eV a shoulder begins to develop with several peaks becoming more resolved on the shoulder as a function of the pentacene coverage. The peak observed at 2.62 eV from the low coverage phase has shifted in energy again to 2.53 eV and is increasing in intensity throughout the deposition sequence. Between 2.53 eV and 3.93 eV the RA spectrum has begun to decrease. One broad peak takes the place of the 3.11 eV and the 3.25 eV peaks. The original peak observed at 3.5 eV for the clean gold spectrum, has begun to decrease in intensity. The peak at 3.85 eV in the low coverage phase has decreased in intensity but become more prominent. Therefore a better measurement of the energy position has revealed it to be at 3.93 eV. Also the peaks at ~4.4 eV have become more intense.

The RA lineshape of the Au(110)-(2×1) peak at ~2.53 eV is still visible and has hardly changed at this coverage, this suggests that the underlying Au surface is intact and chemical interaction between the organic molecules and the substrate is weak [26] . The most significant change for this intermediate coverage is in the energy range from 3.5 eV to 4.0 eV, where the change in intensity is in the opposite direction compared to the low coverage phase. This shows that the surface has become gradually more reflective for light polarized along the [001] direction and gradually less reflective for light polarized along the $[1\bar{1}0]$ direction. According to Frederick et al [25] this change in direction of the reflectivity corresponds to an azimuthal rotation of 90° of the molecule relative to the substrate.

From the STM experiment in chapter 4, we see that after half a monolayer the molecules preferentially align across the rows, in the [001] direction, therefore at a coverage above 0.6 ML of pentacene, it is possible that the component of the electronic transition along the long axis of pentacene has now changed to the component of the transition across the pentacene molecule and vice versa. There is again remarkable agreement between the position of the peaks observed with RAS in figure 5.9 and the absorption spectrum shown in figure 5.7.

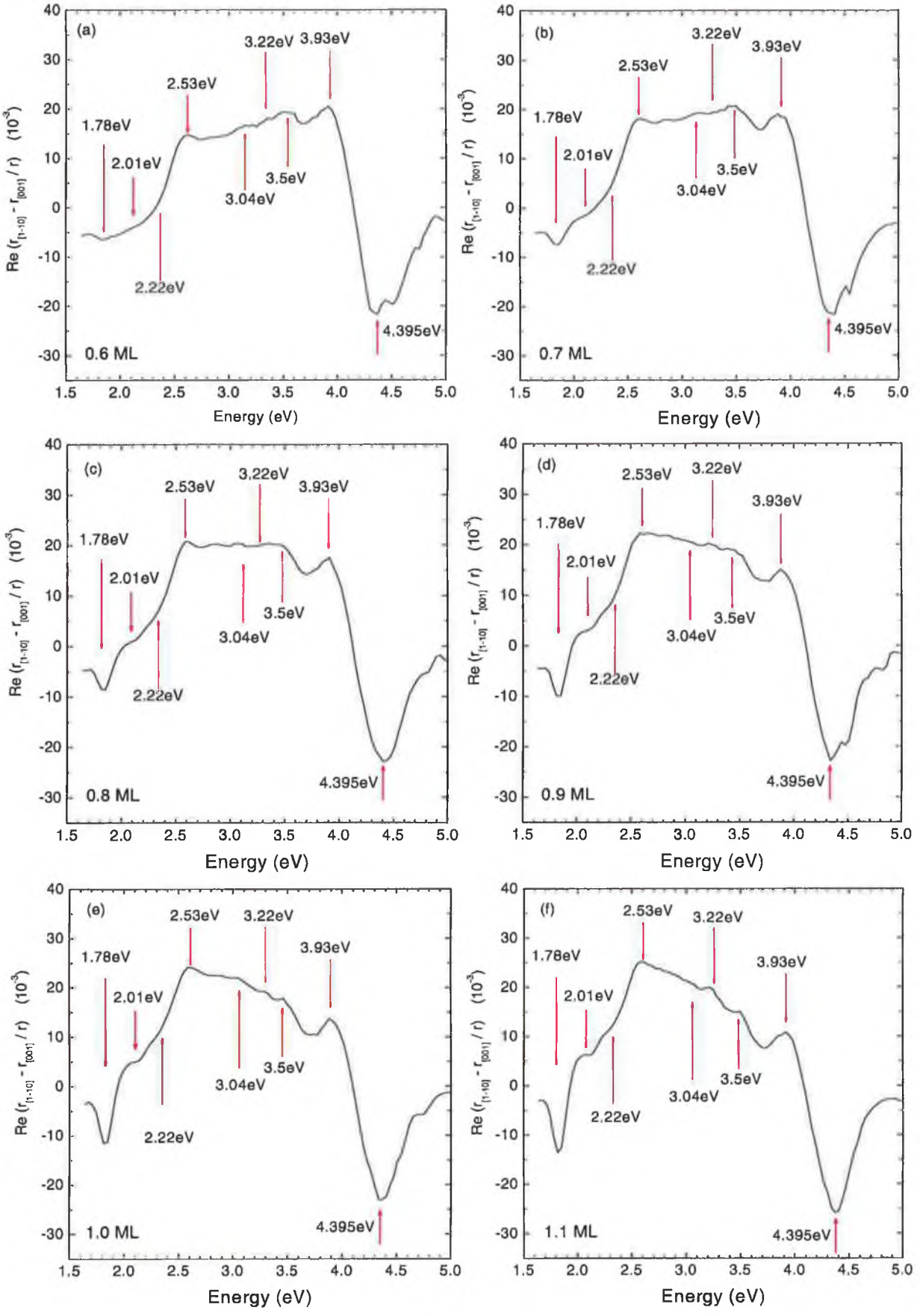

Figure 5.9 *real Re($\Delta r/r$) spectra for increasing coverages of pentacene on Au(110)-(2×1) (a) 0.6 ML, (b) 0.7 ML, (c) 0.8 ML,(d) 0.9 ML, (e) 1.0 ML, (f)1.1 ML.*

5.4.4 High Pentacene Coverage:

Figure 5.10 shows the $Re(\Delta r/r)$ spectra for a high coverage of pentacene on Au ranging from ~2.3 ML to ~3.5 ML.

The peak at 1.78 eV in the intermediate coverage has become more resolved and continues to grow in intensity during all the evaporations. The spectral range from 1.9 eV to 2.5 eV has changed dramatically. The peaks seen developing on the shoulder intermediate coverage become four resolved peaks at energies 1.955 eV, 2.21 eV, 2.35 eV and 2.52 eV for a pentacene coverage of ~2.3 ML and above. The peaks, which were previously seen in the medium coverage spectra in the energy range 2.55 eV to 3.5 eV, are almost gone. In the higher energy range of the spectra the change in intensity has continued to increase in the negative direction. The two peaks at 1.78 eV and 3.6 eV have approximately the same negative change in intensity. The peak at 3.93 eV retains the same shape throughout the high coverage deposition, but decreases in intensity at a very slow rate. The negative going peak at 4.285 eV has essentially remained at the same intensity for the range of depositions covered.

From the STM images of this surface at high coverages, the molecules are aligned along the [001] direction. Similarly to the medium coverage surface where the molecules start to align across the missing row reconstruction, the higher coverages are found to follow the same growth mode and preferentially align in the same direction but form a reconstruction either on top of the underlying molecules or on a bridge site between two molecules.

Again there is good agreement between the peaks position observed with RAS and the absorption spectrum shown in figure 5.7.

Energy Peaks from Absorption Spectrum (eV)	***Experimentally Measured RAS peak Energy(eV)***	***Assignment***
1.72	1.78	
1.955	1.955	
2.147	2.21	$1^1B_{2u} \leftarrow X^1A_g$
2.328	2.35	ν_{CCC} ⊥ bend
2.492	2.52	ν_{CC} stretch
3.586	3.528	$1^1B_{3u} \leftarrow X^1A_g$
3.76	3.6	
4.095	3.932	ν_{CH} stretch
4.24	4.285	$2^1B_{3u} \leftarrow X^1A_g$

Table 5.4 *Optical transitions of pentacene and their assignments and the energies of the peaks derived from RAS experiments.*

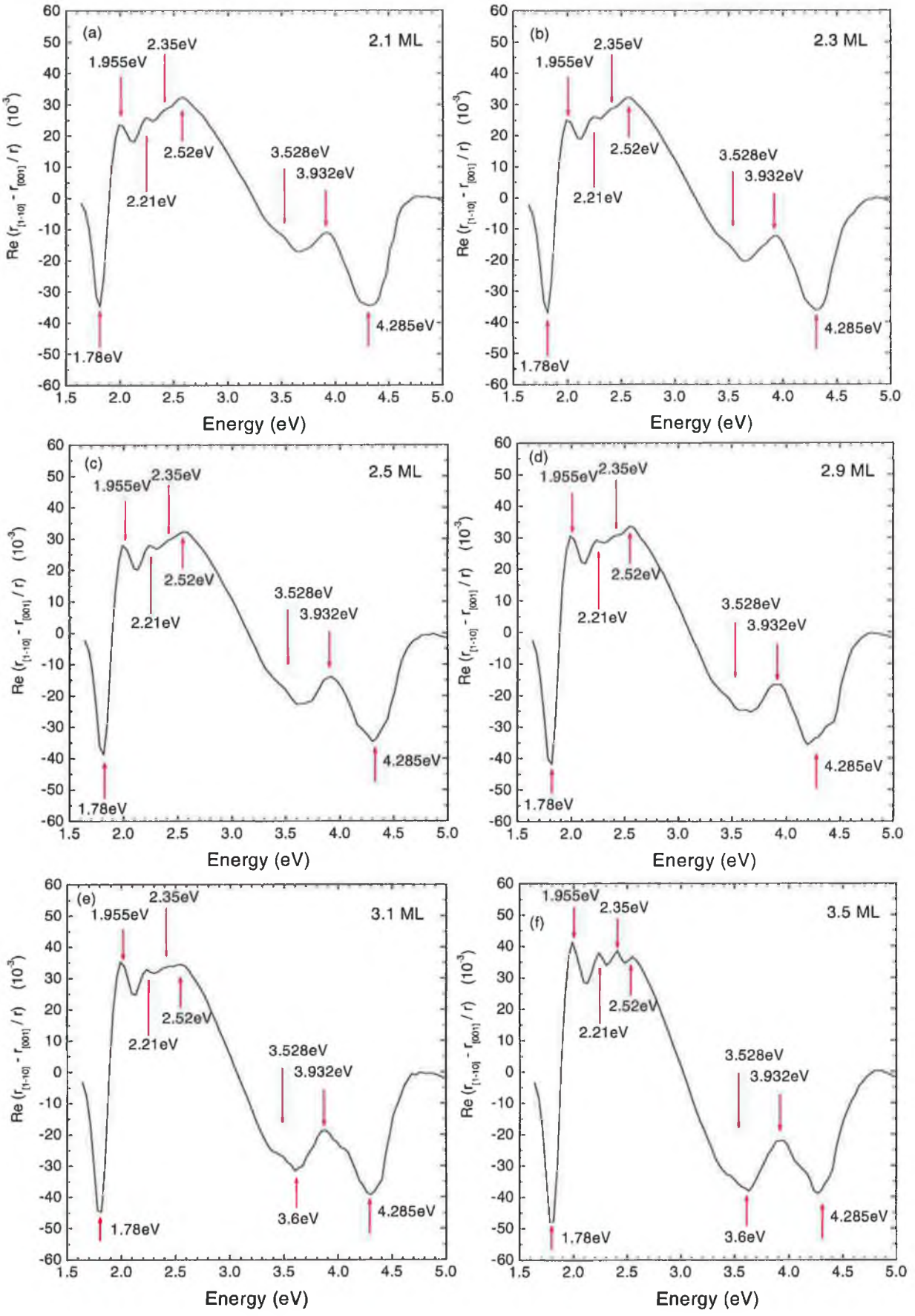

Figure 5.10 *real Re($\Delta r/r$) spectra for increasing coverages of pentacene on Au(110)-(2×1) (a) 2.1 ML, (b) 2.3 ML, (c) 2.5 ML,(d) 2.9 ML, (e) 3.1 ML, (f)3.5 ML.*

Figure 5.11 shows a contour map of the all the data acquired for pentacene adsorbed on the Au(110)-(2×1) surface. This provides a picture to view the development of all the peaks with increasing pentacene coverage seen in figures 5.8, 5.9 and 5.10.

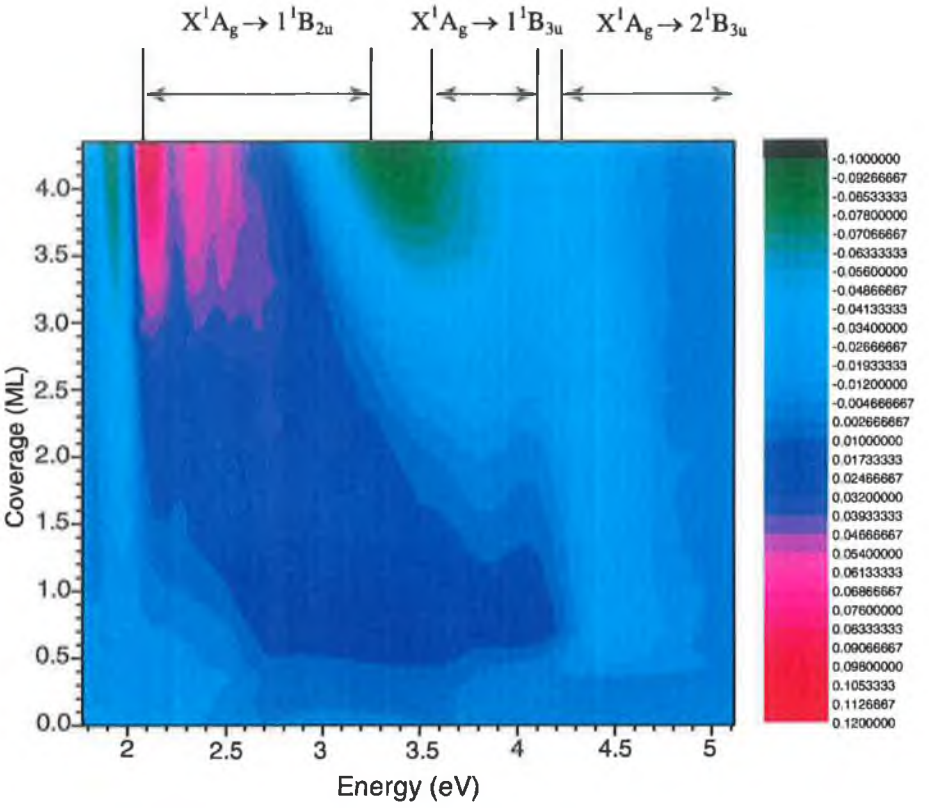

Figure 5.11 *colour contour plot for increasing coverages of pentacene on Au(110)-(2×1).*

5.4.5 Annealing the pentacene covered Au(110)-(2×1) surface

After the final deposition of pentacene the substrate was annealed to various temperatures between 60°C and 140°C, at which temperature the pentacene desorbs from the surface. From the STM experiments on the same surface it was found that at a temperature of ~100°C long range ordering of the pentacene (200 nm×200 nm) is achieved. The ordering of an organic molecule on Cu(110) [25] was detected using RAS. Frederick et. al. [25] found that the anisotropy continued to grow and the intensity increased.

The results of the annealing experiment observed by STM as described in chapter 4 are not observed in the RAS experiment. It is found that the anisotropy does not grow with increasing temperature. It is found that annealing causes thermal desorption of the pentacene. The higher temperature spectra which did not change upon further annealing also do not correspond to the clean Au(110)-(2×1) surface. It was found in chapter 4 that the initial deposition of pentacene causes a change in the

reconstruction from a (2×1) to a (3×1). Therefore after the pentacene has desorbed from the surface the Au(110)-(3×1) reconstruction remains. The changed spectra could be consistent with a Au(110)-(3×1) surface reconstruction. Another reason for the change in the spectra could be that the pentacene has dissociatively bonded to the surface as carbon and it would take higher temperatures or an Ar^+ bombard to desorb it fully and return to the clean Au(110)-(2×1) surface.

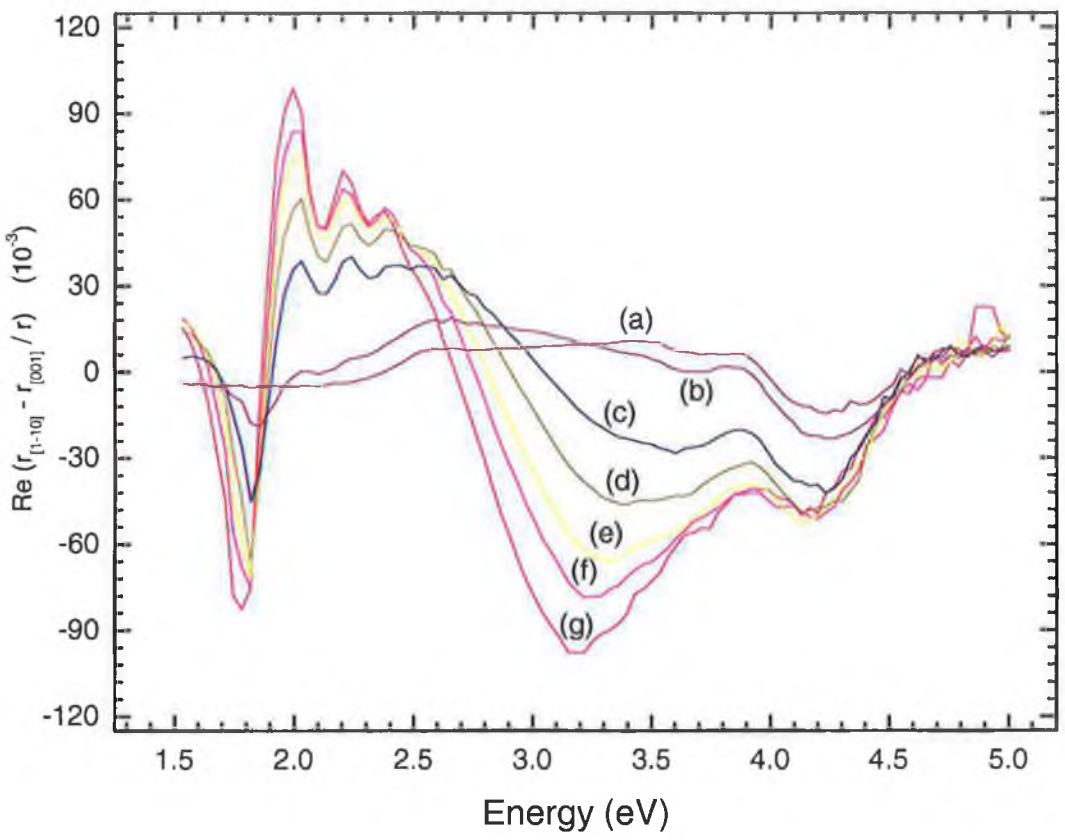

Figure 5.12 *real RAS spectra for increasing sample temperatures of a high coverage of pentacene on Au(110)-(2×1) (a) 413 K, (b) 393 K, (c) 373 K, (d)363 K, (e)353 K, (f) 323, (g) 273 K.*

5.5 Conclusion

In this chapter it is shown that the RAS technique is sensitive to surface states and interband bulk transitions on the Au(110)-(2×1) surface. This has been shown through a number of experiments ranging from introducing surface disorder to identify surface states to surface roughening in order to find the transitions that are not related to the surface. Pentacene was deposited on the Au(110)-(2×1) surface and studied using RAS. For low coverages (up to half a monolayer) it was found that the pentacene molecule aligned between the Au(110)-(2×1) rows. At approximately 0.3ML to 0.4ML

a change from a (2×1) to (3×1) reconstruction is detected. Above half a monolayer coverage the orientation of the pentacene molecules rotates by 90° and aligns preferentially across the rows in the [001] direction. A change in the direction of the intensity can correspond to a change in the azimuthal orientation of the molecule on the surface. This change can be seen in the spectra for the intermediate coverage of pentacene. At higher coverages the pentacene has terminated the Au surface and several peaks in the RAS spectra appear that are at the same energy as the peaks observed in the absorption spectrum of pentacene. These transitions are attributed to three optical transitions from the ground state with symmetry X^1A_g and several vibronic transitions associated with each optical transition. The results of the annealing experiment are not consistent with the STM results presented in chapter 4. It is found that the pentacene molecule either desorbs from the surface with the (3×1) reconstruction remaining or that the pentacene has dissociatively bonded to the surface as carbon.

These four experiments have shown the validity of the RAS technique as a powerful tool for the study of the growth of organic molecules on metal surfaces.

Chapter 5 References

1. R.G. Musket, W. McLean, C.A. Colmenares, D.M. Makowiecki, W.J. Siekhaus, Applied Surface Science, 10, 143, (1982).
2. C.H. Xu, K.M. Ho, K.P. Bohnen, Physical Review B, 39, 9, 5599 (1989).
3. R.A. Bartynski, N. Gustafsson, Physical Review B, 33, 6588, (1986).
4. Ph. Hofmann, K.C. Rose, V. Fernandez, A.M. Bradshaw, W. Richter, Physical Review Letters, 75, 10, (1995).
5. K. Stahrenberg, Th. Herrmann, N. Esser, W. Richter, Physical Review B, 61, 4, (2000).
6. Y. Borensztein, W.L. Mochan, J. Tarriba, R.G. Barrera, A. Tadjeddine, Physical Review Letters, 71, 14, (1993).
7. K. Stahrenberg, T. Herrmann, N. Esser, J. Sahm, W. Richter, S.V. Hoffmann, Ph. Hofmann, Physical Review B, 58, 16, (1998).
8. R.J. Cole, B.G. Frederick, P. Weightman, Journal of Vacuum Science and Technology A, 16, 5 (1998).
9. J.D.E. McIntyre, D.E. Aspnes, Surf. Science, 24, 417, (1971).
10. ***Handbook of Optical Constants of Solids***, edited by E.D. Palik (Academic, New York 1985 and 1991), Vol 1.

11. B. Sheridan, D.S. Martin, J.R. Power, S.D. Barrett, C.I. Smith, C.A. Lucas, R.J. Nichols, P. Weightman, Physical Review Letters, 85, 21, (2000).
12. W. Moritz, D. Wolf, Surf. Sci. 163, L655, (1985).
13. W. Moritz, D. Wolf, Surf. Sci. 88, L29, (1979).
14. M. Copel, T. Gustafsson, Phys. Rev. Lett. 57, 723, (1986).
15. K. Stahrenberg, Th. Herrmann, N. Esser, W. Richter, Physical Review B, 65, 035407, (2001).
16. D.S. Martin, A. Maunder, P. Weightman, Phys. Rev. B, 63, 155403, (2001).
17. J. Bremer, J. –K. Hansen, O. Hunderi, Surf. Sci. Lett. 436, L735, (1999).
18. D.S. Martin, N.P. Blanchard, P. Weightman, Surf. Sci., 1-7, (2003), 532.
19. A. Kühnle, T.R. Linderoth, B. Hammer, F. Besenbacher, Nature 415, 891, (2002).
20. R.G. Endres, C.Y.Fong, L.H.Yang, G. Witte, Ch. Woll, Computational Materials Science, 29(3), (2004), 362.
21. Hyperchem (TM) Corporation, Professional 7.01, Hypercube Inc., 1115 NW 4th Street, Gainsville, Floride, 32601, USA.
22. T.M. Halasinski, D.M. Hudgins, F. Salama, L. J. Allamandola, T. Bally, Journal of Physical Chemistry A 104, 7484, (2000).
23. C. Hellner, L. Lindqvist, P.C. Roberge, Journal of Chemical Society Faraday Transactions II 68, 1928, (1972).
24. N.O. Lipari, C.B. Duke, Journal of Chemical Physics, 63, 5, 1768, (1975).
25. B.G. Frederick, J.R. Power, R.J. Cole, C.C. Perry, Q. Chen, S. Haq, Th. Bertrams, N.V. Richardson, P. Weightman, Physical Review Letters, 80, 20, 4490, (1998).
26. A.M. Paraian, U. Rossow, S. Park, G. Salvan, M. Friedrich, T.U. Kampen, D.R.T. Zahn., J. Vac. Sci. Technol. B, 19(4), 1658, (2001).

Chapter 6 An Investigation of the Interaction and Ordering of Pentacene Molecules on the Ag/Si(111)-($\sqrt{3}\times\sqrt{3}$)R30° Surface

6.1 Introduction

The focus in state-of-the-art nanoscale science and technology is increasingly on the exploitation of organic molecules not only as the building blocks of novel nanostructured materials but as circuit elements (wires, gates, switches, etc...) in a new generation of molecular electronic devices. In order to control the formation of electronic devices at a molecular scale, it is necessary to understand the behaviour of molecules deposited on surfaces. Molecules such as pentacene have shown high potential in the quest to build a new generation of devices based on organic semiconductors. Several groups have investigated the interactions of pentacene molecules on both semiconductor [1], [2], [3], [4] and metallic surfaces [5], [6], [7].

The growth of organic films on semiconductor surfaces is generally controlled by the competition between molecule-substrate and molecule-molecule interactions. On atomically clean silicon surfaces the molecule-substrate interaction plays a major role as the molecules are chemisorbed [8] and are unable to diffuse at room temperature. On metallic surfaces [9], the molecules are not tightly bonded, interacting through van der Waals type forces and can diffuse on the surface at room temperature. In this case the molecule-molecule interactions are no longer negligible and may drastically influence the molecular reconstruction on the surface.

The ordering of organic molecules evaporated on the Ag/Si(111)-($\sqrt{3}\times\sqrt{3}$)R30° surface (henceforth abbreviated Ag/Si-$\sqrt{3}$) has been investigated previously. C_{60} molecules [10] are found to bond preferentially at defect sites and step edges and molecular domains are formed which are ordered in a double domain configuration. Cobalt phthalocyanine (CuPc) molecules form a close packed structure at a coverage close to a monolayer [10]. The substrate-adsorbate interaction on this surface is expected to be intermediate in strength between the clean Si(111)-(7×7), on which the molecules are usually chemisorbed, and the hydrogen passivated Si(111) surface on which the molecules are physisorbed and molecule-molecule interactions are significant.

In this chapter, the use of Ultra-high-vacuum scanning tunnelling microscopy (STM) to determine the structure of the S1, S2 and S3 ordered phases of pentacene on Ag/Si(111) is described. Sections 6.2 and 6.3 examines the Si(111)-(7×7) and Ag/Si-$\sqrt{3}$ surfaces and their reconstructions. Synchrotron photoemission is used to investigate the pentacene/Ag/Si-$\sqrt{3}$ interface in section 6.5.

6.2 Si(111)-(7×7) Reconstruction

The discovery of the Si(111)-(7×7) structure was a milestone of the surface crystallography of semiconductors. Schlier and Farnsworth [11] observed it as early as 1959 by LEED. Binnig, Rohrer and co-workers reported its real space STM images in 1982 [12], [13], in the first STM micrographs of a semiconductor surface ever made.

Silicon is a favourite of experimentalists because it cleaves easily along the (111) planes. Each Si-Si bond in the bulk is directed along one of the <111> axes, so that a {111} plane cuts as few bonds per area as possible in the crystal. Each atom on the ideal Si(111)-(1×1) surface is back bonded to three subsurface atoms. Its fourth sp^3 orbital points towards the vacuum and is half occupied. Atoms with dangling bonds are second nearest neighbours. Cleaving produces a metastable (2×1) reconstruction built around π-bonded chains. Annealing the sample and cooling slowly results in the (7×7) reconstruction.

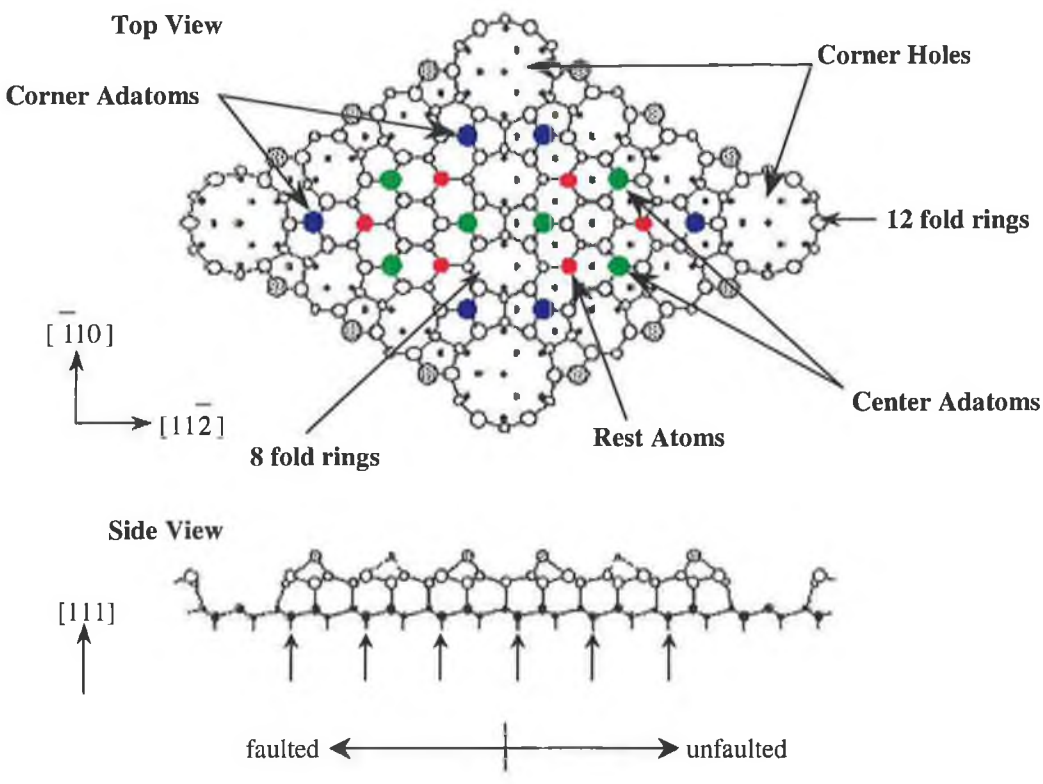

Figure 6.1 *The (7×7) dimer-adatom-stacking fault model (DAS). The stacking fault is in the right half of the (7×7) cell.*

The structure of the Si(111)-(7×7) was determined by Takayanagi et. al. [14] after a detailed analysis of transmission electron diffraction data. It is a very complex surface

with nine-dimer bonds, twelve adatoms of two types (centre and corner adatoms), and a subsurface stacking fault in each surface cell. Additional features of this Dimer-Adatom-Stacking fault (DAS) [14] reconstruction are corner holes and six unsaturated "rest atoms" dangling bonds exposed in the layer below the adatoms, shown in figure 6.1. Around the corner holes the atoms are arranged in twelvefold rings, and there are also eightfold rings along each boundary between faulted and unfaulted areas. The difference between the faulted and unfaulted areas can be seen in the bottom section of figure 6.1 (marked by arrows). In the unfaulted half of the unit cell the third layer of atoms are exposed to the surface. In the faulted half the third layer of atoms marked in the diagram are not exposed to the surface. A complete set of LEED coordinates was later deduced from LEED spectra by Tong et. al. [15]. The Si(111)-(7×7) surface is metallic; with the corner adatoms on the faulted half having the highest DOS near the Fermi energy [16], [15].

Upon flashing to ~1200°C, rapidly cooling to 950°C and slowly cooling in approximately 100°C/minute the periodicity changes to (7×7) as shown in the STM images figure 6.2(a) and (b). Also, annealing to ~1000°C and cooling down slowly leads to a metastable (5×5) periodicity [17].

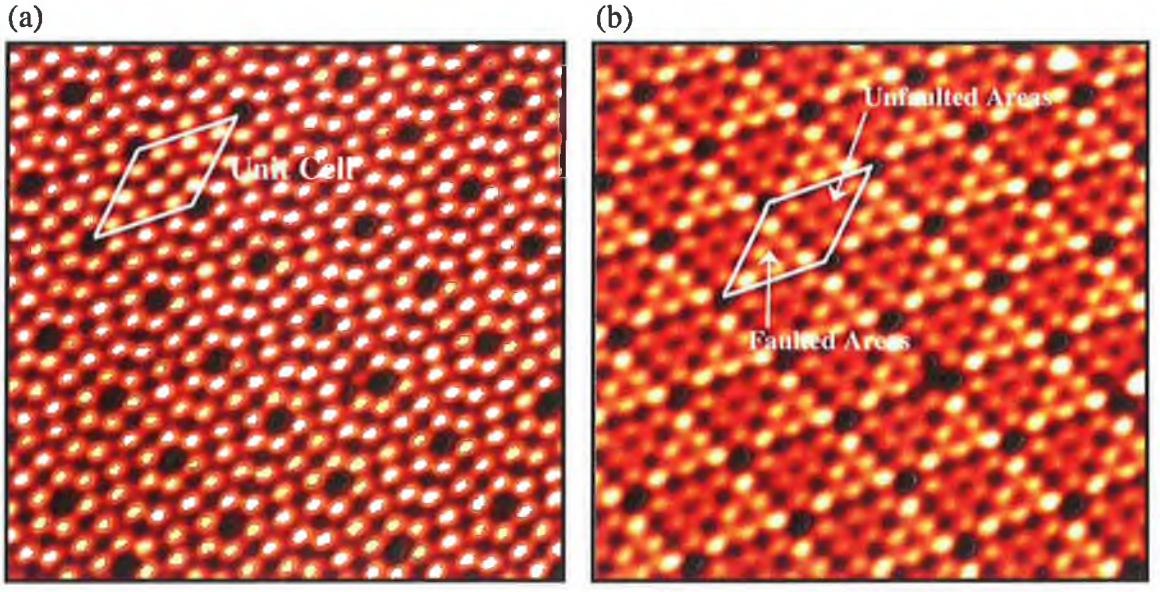

Figure 6.2 *(a) Filled and (c) Empty state images of the (7×7) reconstruction, (15 nm^2) I_t = 0.5 nA, V_s = 1.5 V.*

6.3 The Ag / Si(111)-($\sqrt{3}\times\sqrt{3}$) Surface

Silver deposition on the Si(111)-(7×7) surface at elevated temperatures leads to the formation of a $\left(\sqrt{3}\times\sqrt{3}\right)$-R30° reconstruction. This structure has been studied extensively [18], [19], [20]. The honeycomb-chain-trimer (HCT) model, shown in figure

6.3(a), has been confirmed as the most reasonable model for this structure. A typical STM empty state image of this reconstruction at room temperature is shown in figure 6.3(b). This image, recorded at V_s = 1.0 V, reveals a hexagonal structure consisting of six protrusions (honeycomb structure), relating to the charge density at the centre of the Ag trimers, while the dark regions are related to the underlying Si trimers. Measurements from high resolution STM images of the Ag/Si(111)-√3 surface are in agreement with previous STM measurements [18], [19], [20]. The average length of the unit cell is measured to be 6.8 Å ± 0.5 Å with the error in the measurements arising mainly from thermal drift or piezo creep.

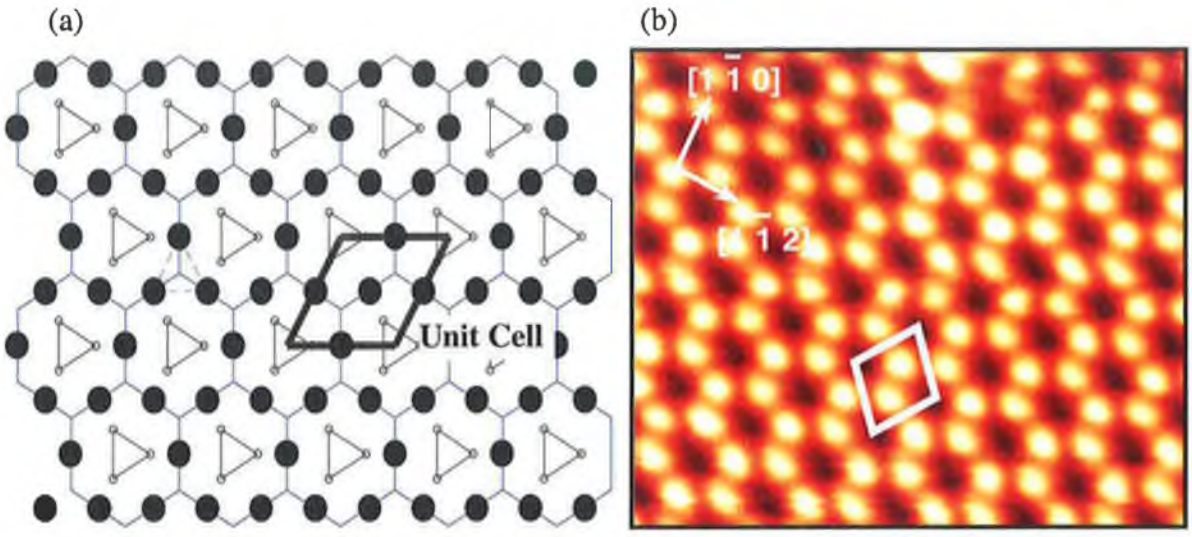

Figure 6.3 *(a) Schematic illustration of the Honeycomb-Chain-Trimer (HCT) model of the Ag/Si(111)-$(\sqrt{3}\times\sqrt{3})R30°$ surface. Ag atoms are represented by large solid dots, Si atoms are shown as small open circles. The honeycomb structure (solid line) represents a hexagonal structure observed in the STM image (b). Image parameters: size = 5×5 nm^2, V_s = +1.0 V, I_t = 2.0 nA.*

6.4 STM Investigation of Ag/Si(111)-√3-Pentacene Surface

6.4.1 Solid Phase S1:

Figure 6.4(a) shows an STM image of the Ag/Si-√3 surface after deposition of ~0.35 ML of pentacene. This coverage forms the first, low density, solid phase, S1. Three molecular domains are observed at 120° with respect to each other. The symmetry and orientation of these structural domains, and the (√3×√3)-R30° honeycomb geometry, suggest a molecular arrangement, which depends on a molecule-substrate interaction. The molecules absorb lying flat on the surface, which is typical for planar polyacene molecules [21]. This is confirmed by the high resolution STM image.

Within each domain the molecules are observed to form periodic parallel rows. The apparent width of each molecular row is 7.9 Å ± 1.0 Å (figure 6.4(c)) and the inter-row distance is 15.8 Å ± 2.0 Å (figure 6.4(d)). The individual molecules adopt a head-to-head orientation with a separation of 18.4 Å ± 2.0 Å (figure 6.4(b)), measured from centre to centre along the rows.

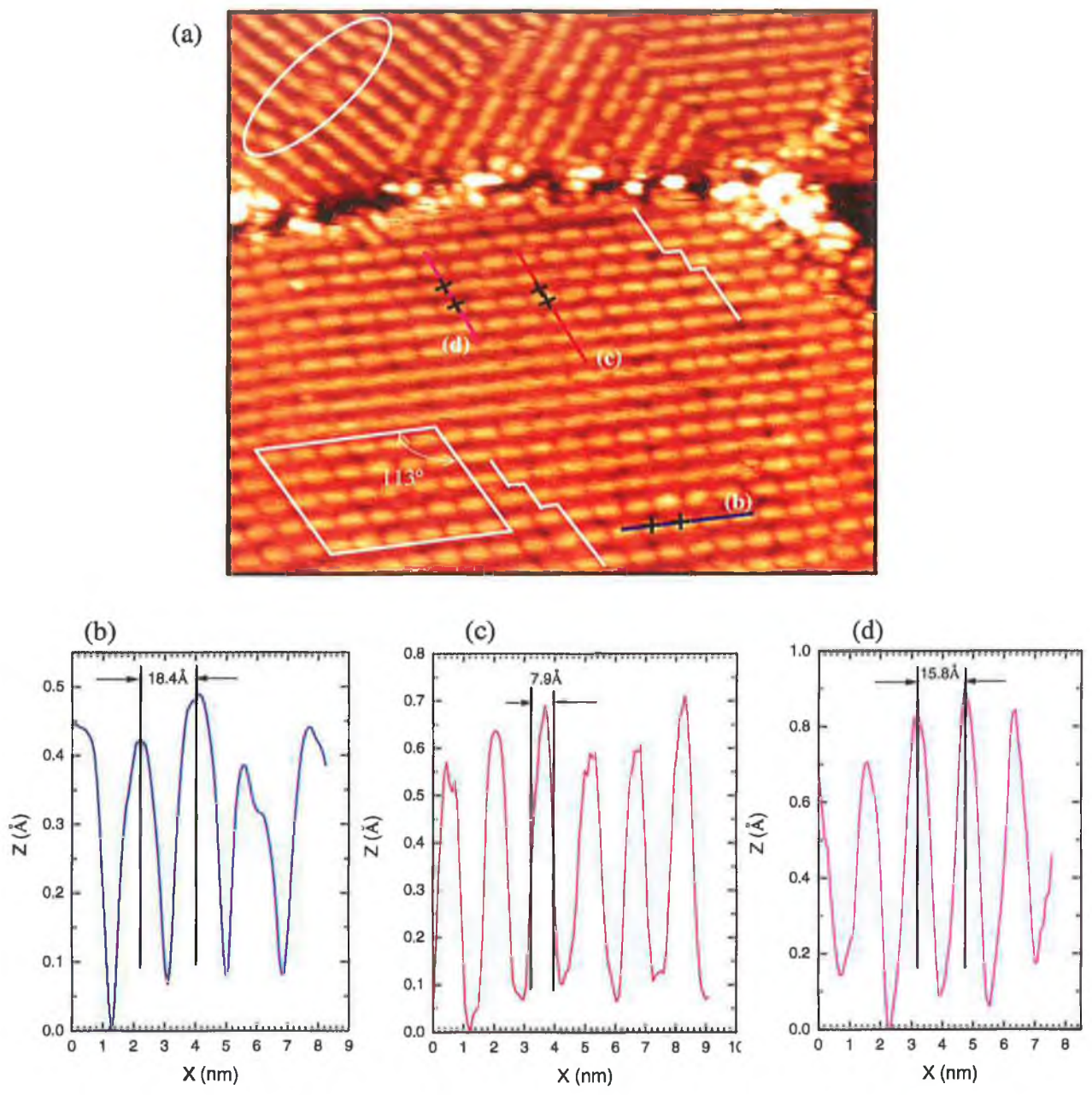

Figure 6.4 *(a) STM image of S1 phase. Molecules are lying flat on the surface. A small ordered region is indicated by the parallelogram. Parallel and perpendicular shifts of the molecular rows are indicated by the white lines and circled regions respectively. Image parameters: size = 40×40 nm^2, V_s = -1.5 V, I_t = 100 pA, (b) line profile of the head-to-head orientation with molecular separation of 18.4 Å, (c) cross section of molecular rows illustrating an apparent width of 7.9 Å and (d) cross section of molecular rows showing an inter-row distance of 15.8 Å*

The pentacene adlayer consist of many small molecular regions one of which is indicated by the white parallelogram in figure 6.4(a). Within these regions, the molecules are regularly spaced both along and perpendicular to the molecular rows, resulting in an angle of 113° ± 3° between the boundaries. This symmetry is disturbed by both small uniaxial translations, (some of which are indicated by the white lines in figure 6.4(a), which occur parallel to the direction of the rows and also by lateral shifts perpendicular to the molecular rows, as circled in figure 6.4(a).

In order to understand the growth mode of the S1 phase, the interface has been studied at lower pentacene coverages. Figure 6.5 shows an STM image of the Ag/Si(111)-√3 surface, with a pentacene coverage of ~0.2 ML. In this image the molecular rows are still observed as bright protrusions aligned along domains oriented at 120°. The average width of a molecular row is 8.3 Å ± 1.0 Å, which is in agreement with the values measured for 0.35 ML coverage. This suggests the same head-to-head orientation of the molecules, however, the individual molecules within a row could rarely be resolved at this dilute coverage. This may be explained by diffusion of the molecules across the surface at room temperature. A similar effect [22] was observed for CuPc molecules on the Ag/Si(111)-√3 surface.

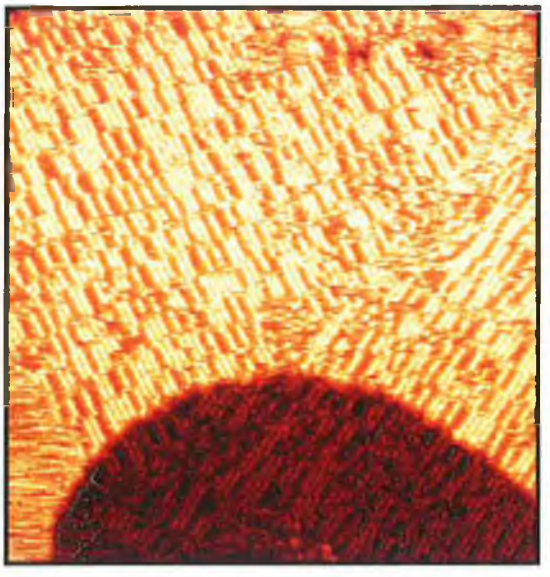

Figure 6.5 *STM image of Ag/Si-√3 coverage after pentacene deposition of ~0.2 ML. The bright protrusions are short parallel rows of pentacene molecules showing the initial stage of the growth of the solid phase S1. Image parameters: size 120×120 nm², V_{sample}= +1.0 V, I_t = 100 pA.*

A typical higher resolution of the image of the surface in figure 6.5 is presented in figure 6.6(a). In this image the underlying Ag/Si-√3 honeycomb structure is resolved in between the pentacene rows. In comparison with the STM image of the clean Ag/Si-

$\sqrt{3}$ surface, figure 6.6(a) shows a reduced resolution of the honeycomb structure in which the features relating to the Ag trimers are not resolved. This change is possibly associated with diffusion of the molecules especially at this dilute coverage, where it is difficult to maintain high resolution. However the relative position and orientation of the molecular rows with respect to the honeycomb structure can be distinguished. Note that no apparent restructuring of the substrate occurs. The average length of the unit cell of the Ag/Si(111)-$\sqrt{3}$ is still measured to be 6.6 Å ± 0.5 Å. From this and similar images, it is determined that the molecular rows are aligned along the $[1\bar{1}0]$ direction and at 120° relative to this direction. From these images it is possible to count the number of hexagonal STM features between the pentacene rows. Three different spacings of 2.5, 5 and 6.5 unit cell lengths are again identified, in agreement with the measured statistical distribution. It is noted that the perpendicular shift observed in the S1 phase, are also present in this low coverage phase, as circled in figure 6.6(a).

A statistical distribution of the spacings between the centres of the parallel rows was measured from a series of images similar to that shown in figure 6.5. A histogram of this distribution, figure 6.6(e), shows that the rows are separated by quantised distances of d_1= 16.2 Å ± 2.0 Å, d_2=33.5 Å ± 2.0 Å and d_3= 44.1 Å ± 2.0 Å. The smallest inter-row distance d_1 corresponds to the inter-molecular row distance of 15.8 Å, measured for the S1 phase, as shown in figure 6.6(b). Moreover, comparison with the Ag/Si-$\sqrt{3}$ substrate shows that these distances are multiples of 2.5 (16.25 Å), 5 (32.5 Å) and 6.5 (42.25 Å) of the silver unit cell length. These multiple distances are shown in figure 6.6(b), figure 6.6(c) and figure 6.6(d) respectively. In addition to the symmetry of the molecular domains, this suggests that the adsorbed layer is in registry with the structure of the substrate.

From these observations, a model is proposed for the arrangement of the molecules with respect to the adsorption sites of the substrate. The parameters for this model are based on small ordered regions similar to those indicated in figure 6.4. Two molecular adsorption sites are identified; the first is a three-fold hollow site at the centre of an Ag-trimer (CA-site); and the second is a six-fold hollow site at the centre of the hexagonal arrangement of silver atoms (CB-site), shown in figure 6.7.

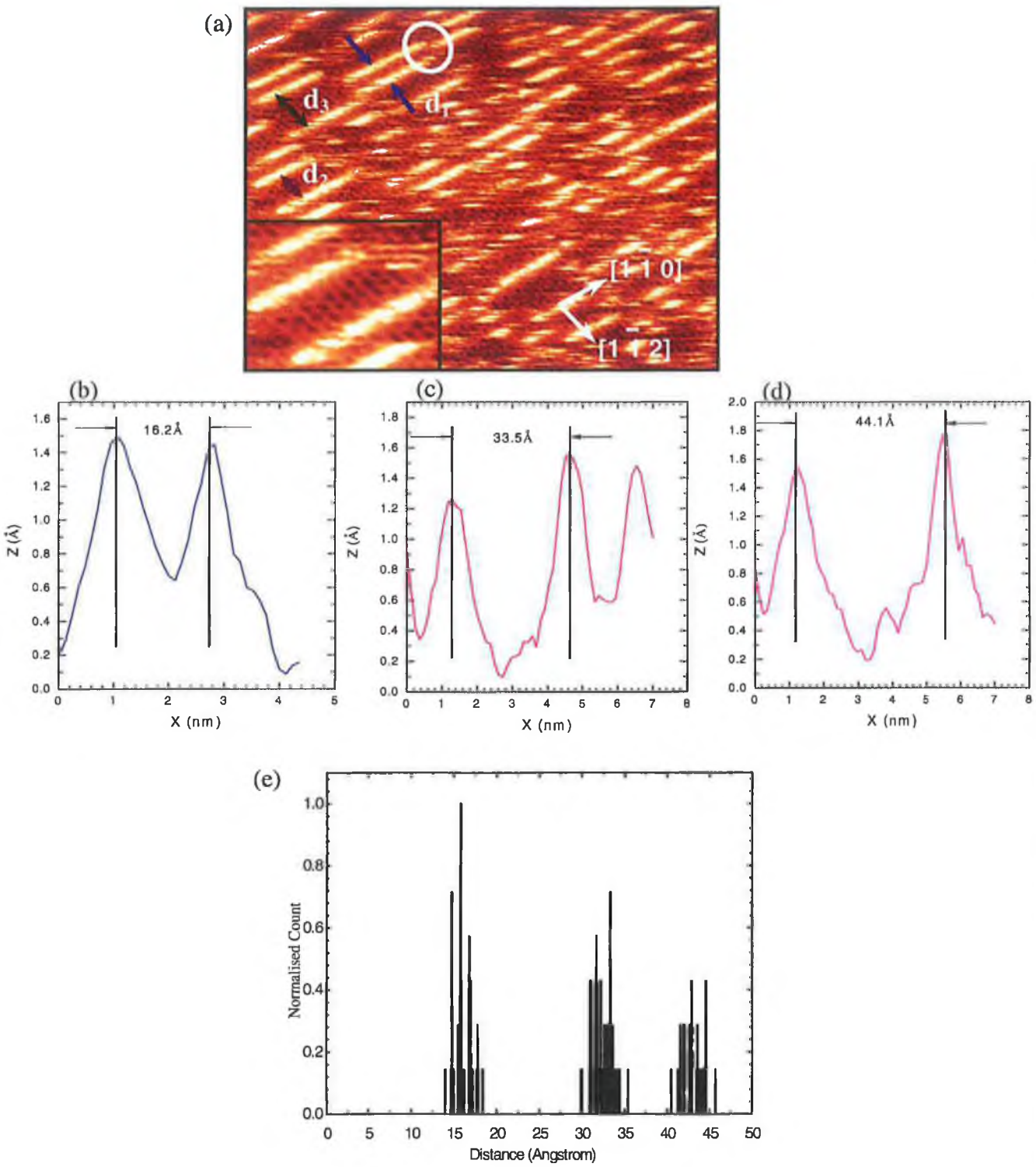

Figure 6.6 *(a) High-resolution image of Ag/Si-√3 after a pentacene deposition of ~0.2 ML. The honeycomb structure of the substrate is resolved between the molecular rows. FFT smoothing has been applied to the image. Examples of the d_1, d_2, d_3 inter-row spacings are indicated in the top left hand corner of the image. Image parameters: size = 40×40 nm^2, V_s = +1.0 V, I_t = 100 pA, (b) cross section of the area indicated by d_1 in figure 6.5(a), (c) cross section of the area indicated by d_2 in figure 6.5(a), cross section of the area indicated by d_3 in figure 6.5(a) and (e) histogram of the statistical distribution of the inter-row spacings, determined from a series of images similar to that shown in figure 6.4. It reveals that the inter-row spacings are separated by quantised distances of d_1= 16.2 Å ± 2.0 Å, d_2=33.5 Å ± 2.0 Å, d_3= 44.1 Å ± 2.0 Å*

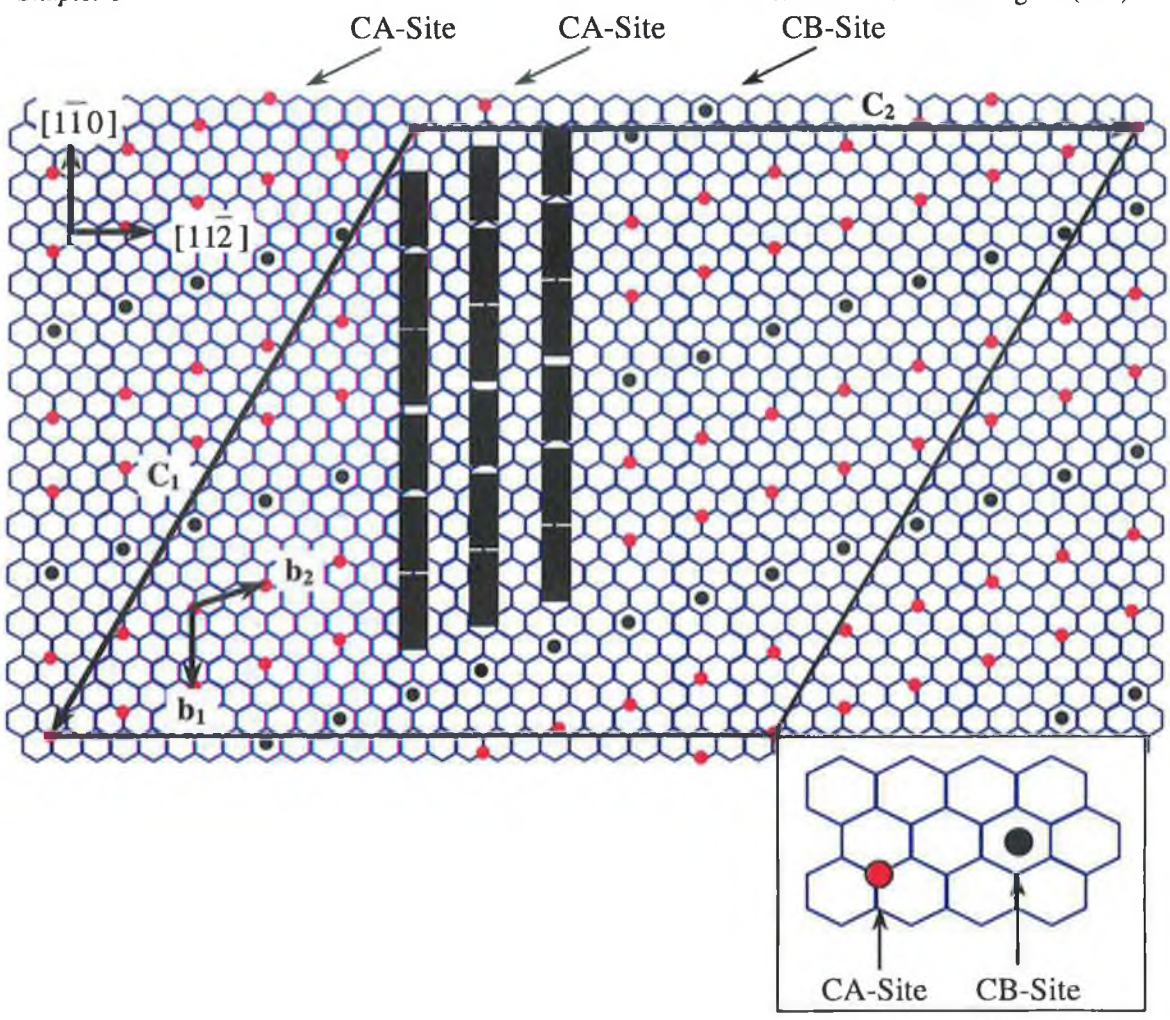

Figure 6.7 *Proposed model for the Ag/Si(111)-(25×25)-pentacene structure, S1 phase. The underlying hexagonal lattice shows that the honeycomb structure observed in the STM image (figure 6.2(b)). Molecules are represented by their centre of mass (•) and (•). The adsorption sites CA (•) and CB (•) are indicated by the arrows and are clearer in the zoomed insert. The smallest cell of the adlayer containing two molecules is indicated by the vectors* $\mathbf{b}_1$ *and* $\mathbf{b}_2$*, which form an angle of 113°. The high order (25×25) commensurate cell is indicated by the vectors* $\mathbf{c}_1$ *and* $\mathbf{c}_2$*.*

The suggested molecular arrangement is drawn schematically in figure 6.7, where the dots, positioned over the adsorption sites, indicate the centre of mass of the molecules. The hexagonal lattice shown in the model represents the honeycomb structure observed in the STM image in figure 6.3(b). From this model the average distance between the adsorption sites is 19.1 ± 2.0 Å where the length scale has been determined from the substrate unit cell. This value is in accord with the centre-to-centre separation of 18.4 Å ± 2.0 Å, measured along the rows. From these measurements, the magnitude of the unit cell vectors, $\mathbf{b}_1$ and $\mathbf{b}_2$ for the S1 phase adlayer are b_1=18.4 Å ± 2.0 Å, b_2=20.0 Å ± 2.0 Å with an angle of $\gamma = 113° \pm 3°$ between the vectors.

This model shows that there exists a high order (25×25) commensurate cell, with respect to the unit cell of the Ag/Si-√3 surface, containing 75 molecules. Knowing how many molecules that there are in the unit cell it is possible to determine the molecular packing density. At this low coverage, the molecular packing density D is 3.4×10^{-3} mol.Å^{-2}. The unit mesh of this coincidence cell is shown in the model, and indicated by the vectors $\mathbf{c_1}$ and $\mathbf{c_2}$.

The ordering and molecular orientations of a number of nonpolar, linear molecules, adsorbed on plane surfaces, have been extensively studied [9]. In the majority of cases the molecules adopt a close packed ordering, which may be either commensurate, high-order commensurate or non-commensurate with the lattice of the underlying substrate [9]. These close packed orderings arise from molecule-substrate and molecule-molecule interactions [23], [24]. Step edges can also play a role in ordering the molecules [25]. For larger acenes, a well defined overlayer structure is seen on vicinal Cu(111) surfaces but not on the flat Cu(111) surface [21]. This is attributed to the larger binding energy at the step site. On the Ag/Si-√3 surface the pentacene molecules do not preferentially decorate the steps and no alignment occurs along the step edges. However, since molecular ordering does occur, this suggests that the film is governed by lateral molecule-molecule interactions.

Bulk pentacene has a triclinic structure with lattice parameters a = 7.9 Å, b = 6.06 Å, c = 16.1 Å, $\alpha = 101.9°$, $\beta = 112.6°$ and $\gamma = 85.8°$ [23] with the molecules lying flat in the ac plane. It is interesting to compare the natural symmetry of the organic molecule to the structure of the film, which is determined by intermolecular interactions. The S1 phase maintains the symmetry of the ac plane of the crystal. In particular the angle between the commensurate cell vectors $\mathbf{c_1}$ and $\mathbf{c_2}$ (figure 6.6) matches the angle β in the crystal. However, molecule-substrate interactions also play a significant role in determining the structure of the S1 phase, in which the molecules exhibit a clear preference for the CA and CB adsorption sites. The average separation of these sites along the $[1\bar{1}0]$ direction is comparable to the separation of the molecules along the c-direction in the crystal. Also, the spacing between the rows is approximately twice the molecular spacing along the a-direction in the crystal. This symmetry only occurs in small regions of the film because of the translations and lateral shifts of the molecular rows, mentioned above.

6.4.2 Solid Phase S2:

Figure 6.8 shows an STM image of the surface at a pentacene coverage of one monolayer. The new solid phase, S2, consists of rows of molecules separated by 6.5 Å ± 0.5 Å. The pentacene molecules now adopt a close packed side-by-side arrangement with molecular domains oriented at 120°.

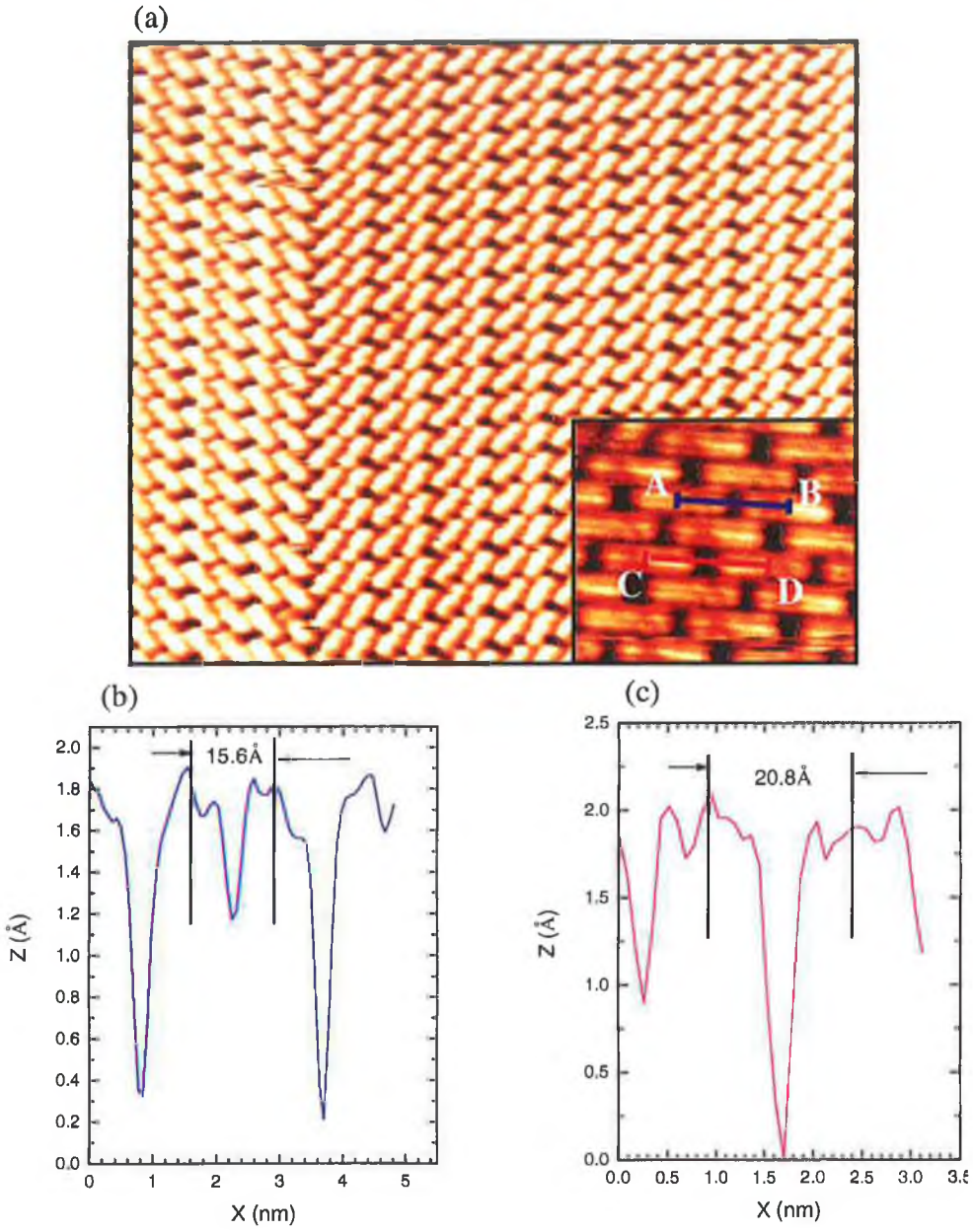

Figure 6.8 *STM image of solid phase S2 formed after deposition of 1ML of pentacene. The molecules form pairs along their major axis as shown in zoomed insert. The lines AB and CD indicate distances referred to in the text. Image parameters: size 21.5×21.5 nm^2, V_s = -1.1 V, I_t = 200 pA, (b) line profile of AB section indicated in figure 6.8(a) and (c) line profile of CD indicated in figure 6.8(a).*

Within this compact structure the molecules form pairs along their major axis. The centre-to-centre distance between two molecules within a pair is 15.6 Å ± 2.0 Å

(the line AB in figure 6.8) and the distance between adjacent molecules in neighbouring pairs is 20.8 Å ± 2.0 Å (the line CD in figure 6.8). The molecular density D of this phase is $(9.6\pm0.2)\times10^{-3}$ mol.Å^{-2}, approximately three times the value of the low coverage phase, S1. This ordering is attributed to the absorption of additional molecules between the molecular rows of the low coverage phase to form a more compact structure. Note that Lukas et. al. [6] report that increasing the pentacene coverage on the Cu(110) surface leads to the formation of multilayers instead of additional adsorption within the pentacene rows.

Because low energy electron diffraction patterns were not obtainable for this surface, bias dependent imaging was exploited as an alternative method of determining the registry of the pentacene molecules with respect to the Ag/Si-√3 surface. Under certain bias conditions the molecular film can appear transparent and it is possible to image the substrate underneath.

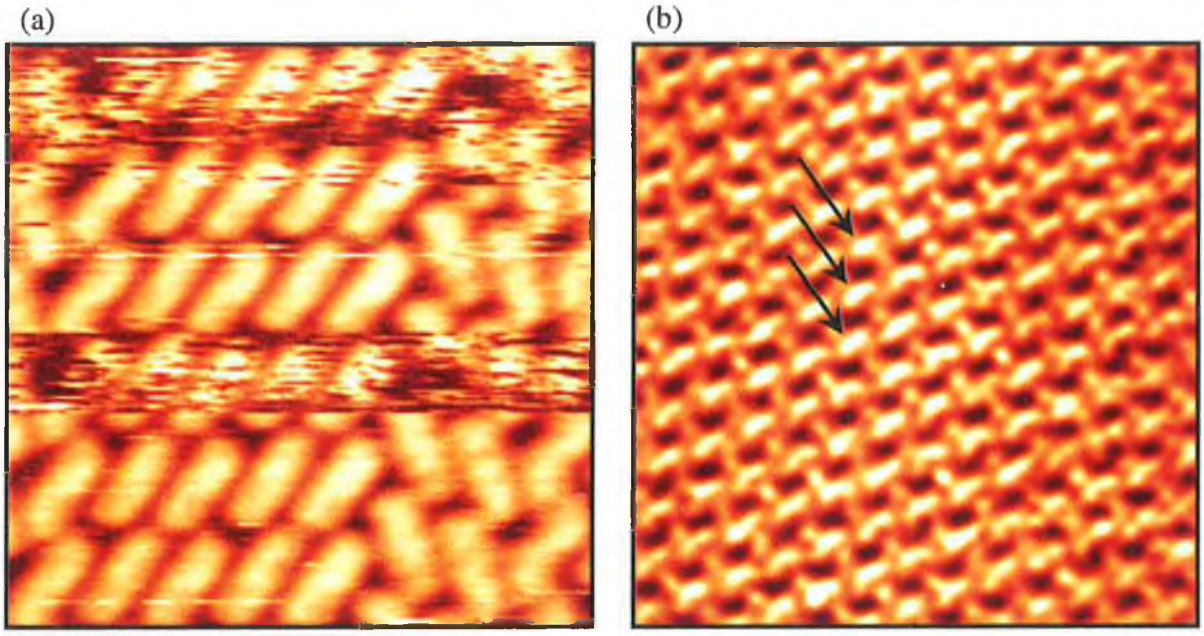

Figure 6.9 *STM images (7.8×7.8nm^2) of solid phase S2 recorded in dual scan mode. (a) image recorded at high bias (V_{sample} = -1.9 V, I_t = 50 pA) in which the pentacene molecules are visible. (b) low bias scan (V_{sample} = 0.3 V, I_t = 190 pA) of substrate imaged through the pentacene molecules. FFT smoothing has been applied to this image. The arrows indicate the brighter features in the substrate structure attributed to pentacene adsorption*

Figures 6.9(a) and (b) shows STM images recorded in dual scan mode. Figure 6.9(a), recorded at a high bias of V_{sample} = -1.9 V in the forward scan direction, shows an image of the S2 structure with the pentacene molecules clearly resolved. Figure 6.9(b), recorded at a low bias of V_{sample} = 0.3 V in the backward scan direction, shows the same area in which the Ag/Si-√3 substrate is imaged through the molecular adlayer. Figures

6.9(a) and (b) have been corrected for a small lateral shift in their registry which occurs in dual scan mode. Viewed simply, the bias can be used as a tuneable parameter to focus on either the molecular film or on the underlying substrate. Imaging of surface features beneath an adlayer has been reported and explained previously [22], [27], [28], [29]. At a sufficiently high bias, resonant tunnelling takes place through the energy levels of the molecule. While at a low bias, tunnelling occurs within the HOMO-LUMO gap, permitting features associated with the underlying surface to be imaged.

At low bias voltage the image reveals brighter features in the Ag/Si-$\sqrt{3}$ structure (examples are indicated by arrows in figure 6.9(b)). An example of this is the adsorption of benzene molecules on the Pt(111) surface [30] where measurements reveal three distinct types of STM images, depending upon the benzene adsorption site. In low bias (<500 mV) images of PTCDA molecules on graphite [31] both the graphite lattice and the PTCDA molecules could be observed in the same image. The brighter features in figure 6.9(b), suggest a charge transfer between the Ag/Si-$\sqrt{3}$ surface and the π electrons of the pentacene, resulting in a significant molecule-substrate interaction [32], [33]. It is difficult to discover the molecular arrangement from the STM features revealed in this single image. However, from both images in figure 6.9 it is possible to determine both the positions and orientations of the pentacene molecules with respect to the Ag/Si-$\sqrt{3}$ surface.

A suggested model for the S2 phase is shown schematically in figure 6.10, in which the molecules are again shown with their centre of mass positioned over the adsorption sites. Compared to the S1 phase, adsorption takes place exclusively on the Ag-trimer sites (CA-site) with no molecular adsorption on the six-fold hollow sites (CB-site).

From this model the distance between the adsorption sites for the paired molecules (AB in figure 6.8) is 15.6 Å. The distance between adjacent molecules in neighbouring pairs (CD in figure 6.8) is 19.5 Å, where the length scale has been determined from the silver substrate unit cell in figure 6.9(b). These values are in good agreement with the model separations determined from the STM images in figure 6.8. This molecular arrangement leads to smaller commensurate overlayer, Ag/Si(111)-(2×3)-pentacene, with two molecules per unit cell, denoted by the vectors $\mathbf{b_1}$ and $\mathbf{b_2}$ in figure 6.10.

In the S2 phase the symmetry of the ac-plane is absent and rearrangement occurs both along and perpendicular to the molecular rows. The densest packing along a row, resulting in a pairing of the molecules, is a direct consequence of adsorption taking

place exclusively on the CA adsorption site. In this compact phase the inter-row separation corresponds to the measured van der Waals interaction radius of 6.5 Å [6]. This interaction produces an attractive force between the molecules leading to a lateral rearrangement, which results in a decrease of the inter-row spacing. In addition, the molecules do not line-up side by side across the rows but are uniformly shifted by the vector $\mathbf{b_1}$.

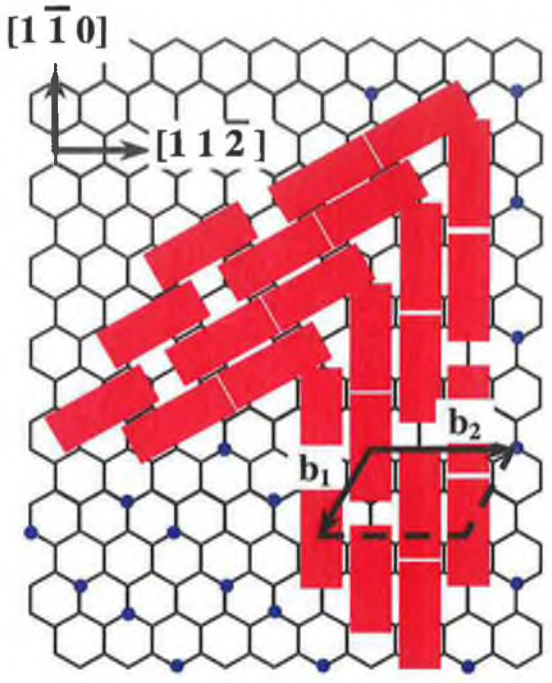

Figure 6.10 *Proposed model for the Ag/Si(111)-(2×3) pentacene structure, S2 phase. The underlying hexagonal lattice shows the honeycomb structure observed in the STM image (figure 6.2). Molecules are represented by their centre of mass (•). The arrow indicates the single adsorption site CA. The vectors* $\boldsymbol{b_1}$ *and* $\boldsymbol{b_2}$*, forming an angle of 118° ±2°, indicate the unit cell of the adlayer containing two molecules*

6.4.3 Solid Phase S3:

The STM image in 6.11(a) shows the surface with a pentacene coverage of >1.0 monolayer. The inter-row spacing of 6.5 Å ± 0.5 Å observed for the S2 phase is not large enough to accommodate additional molecules within the monolayer. At the centre of this image, a molecular reorganization is observed as a series of bright parallel protrusions, arranged in a line. Two peaks are observed within each protrusion, with an average distance between them of 5.65 Å ± 0.6 Å. Similar bight protrusions have also been observed when pentacene is deposited on the Au(111) surface [5]. Moreover, it is possible to see this molecular reorganization occurring during the scanning process. A cross sectional profile along the A-A line reveals an increase in the contour height across the region of molecular reorganization. The magnitude of the corrugation

measured across the bright protrusions is approximately twice that measured for the close packed side-by-side orientation.

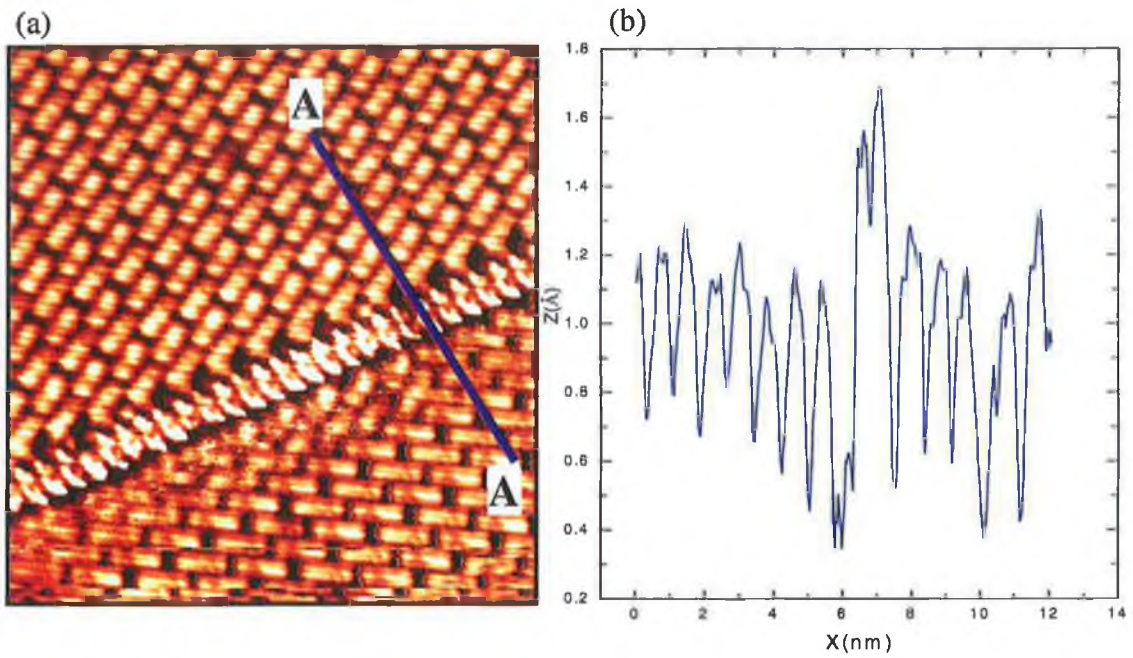

Figure 6.11 *(a) STM image (15×15 nm^2, V_s=-1.3 V, I_t=300 pA) of >1.0 ML coverage showing a reorganization of the molecules, (b) cross sectional profile along the A-A line showing a single protrusion composed of two peaks induced by the tilting of a pair of molecules.*

Figure 6.12 shows a series of images taken from a sequence recorded with the same tunnelling conditions and scan speed of 177 nm/s. The images shown here correspond to the 2nd, 3rd, 4th 5th, 6th and 8th frames in the sequence (note that figure 6.11 corresponds to the first frame in this sequence and that no drift correction has been performed). Each of the protrusions is formed from a rearrangement of two flat lying molecules as seen in the region of figure 6.12(a)-(f).

From these observations it is proposed that the molecules are tilted, in a standing-on-end position, with each of the bright protrusions corresponding to a single molecule. The molecular density for the tilted phase is D = (2.15 Å ± 0.6 Å)×10^{-2} mol.Å^{-2}, which is approximately twice the density found for the second planar phase, S2. The average distance of 5.65 Å ± 0.6 Å between the protrusions is close to the inter-planer spacing of 6.06 Å along the b direction of the unit cell of the pentacene crystal [34]. This indicates that the molecules are aligned facing each other, however the precise molecular orientation has not been determined.

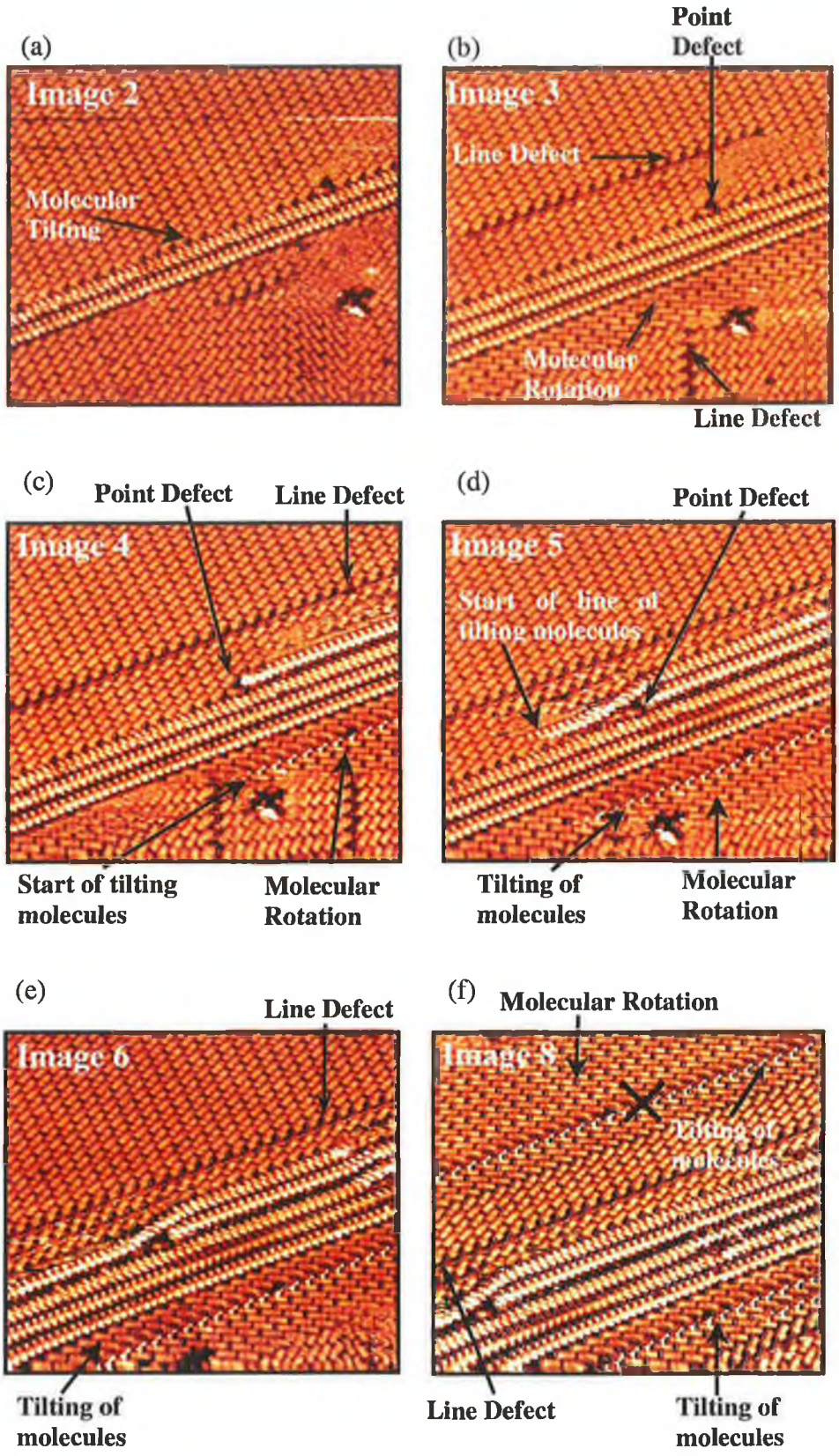

Figure 6.12 *(a), (b), (c), (d), (e) and (f) are frames 2, 3, 4, 5, 6 and 8 from a sequence of images recorded with the same tunnelling conditions (V_s=-4.2 V, I_t=20 pA) and with a scan speed of 177 nm/s (no drift control has been applied).*

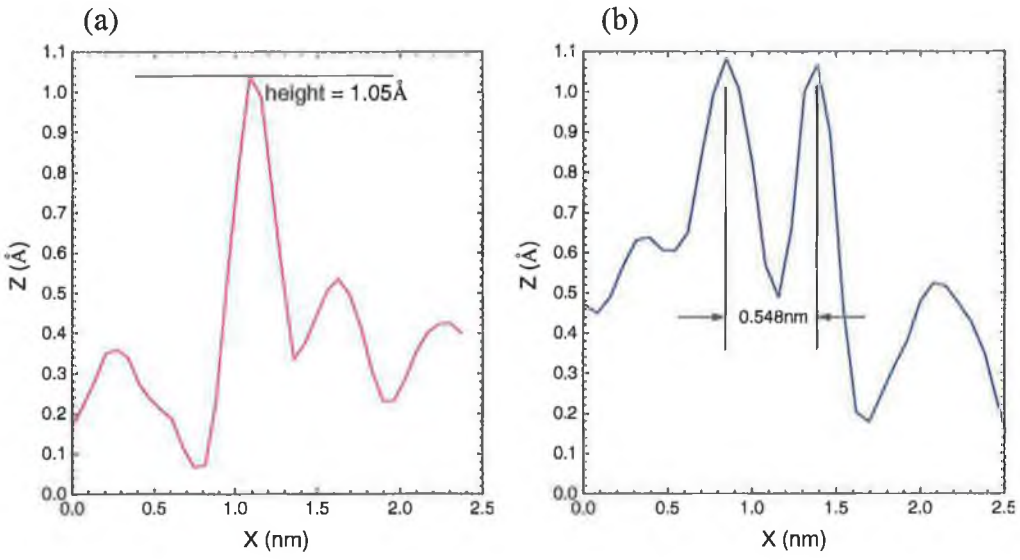

Figure 6.13 *(a) and (b) are the cross sections of the area indicated in 6.12(f).*

It can be seen just beneath the main tilting lines in figure 6.12(a) and (b) a part of the molecular plane has rotated by 120°, indicated on the image, and a line defect has appeared at the bottom of figure 6.12(b). Also another line defect has begun to develop at the top of figure 6.12(b). In figure 6.12(c), it can be seen that in the centre area another main line of tilting molecules has begun but it seems to be pinned by the point defect, as indicated on the image. In the same figure another section of the molecular plane has rotated by 120°, indicated on the image, to match the previously rotated section in figure 6.12(b). A second line defect has appeared just beneath that rotated section. In the centre of the rotated section in figure 6.12(c) a single line of molecules has begun to tilt. In figure 6.12(d), it can be clearly seen that another line of molecules in the centre area have begun to tilt into the upright position but interestingly the new line has coupled to where the previous line pinned at the defect has stopped. It can also be seen that another section of the molecular plane has rotated to again match the initial rotation in all the previous images. Interestingly the two line defects at the bottom of the previous image have disappeared and the line of tilting molecules in that section has developed further. Comparing figures 6.12(e) and (f) it is seen that the molecular plane above the main tilting molecules has rotated by 120° to the initial orientation. This has occurred just as another single line of pentacene molecules, indicated by the arrow in figure 6.12(e), has begun to tilt into the upright position. A line profile of the tilting molecules is shown in figures 6.13(a) and (b). This shows that the width of the pentacene molecule standing-on-end is ~5.5 Å and the height is ~1.0 Å.

It seems that the molecular plane is reorganized itself to accommodate more molecules into a single monolayer. This is a clear indication of the weak molecule-substrate interaction and of the extent of the molecular physisorption.

Tilting of pentacene molecules has previously been observed by Penning Ionisation Electron Spectroscopy (PIES) on a graphite surface [35]. The relative intensity of the π and σ bands is seen to change as a function of the pentacene coverage with the intensity of the σ band increasing with increasing overlayer thickness. Harada et. al. [35] proposed that the molecules are deposited flat onto the substrate at low coverage and gradually tilt with increasing coverage. There is also considerable evidence from the STM studies that the scanning process itself has a significant effect on the molecular ordering observed. At coverages in excess of one monolayer, the orientation of the pentacene molecules changes as a function of the scanning [36], [37]. This could suggest that the ordering observed in the pentacene films cannot be separated from the measurement technique induced ordering, especially on the surface where the strength of the molecule-substrate interaction is very weak. A recent study by Eremtchenko et. al. [38] of the factors which control the epitaxial growth of organic molecules on Ag(111) surface suggested that the weak bonding interaction between perylene and the substrate resulted in the STM dragging the molecule across the surface during scanning. It can be seen in figure 6.12 that the molecules are definitely tilted but the reason for the tilting is still unresolved. Two possible suggestions are that the molecules increase their packing density by tilting to accommodate more molecules on the surface with increasing pentacene coverage or that the STM scanning process itself is responsible for the tilting.

6.5 Photoemission Pentacene /Ag/Si(111)-($\sqrt{3}\times\sqrt{3}$)R30°

The discussion of photoemission from the pentacene/Ag/Si(111)-($\sqrt{3}\times\sqrt{3}$)R30° interface has been divided into two main sections; the first examines the core level photoemission including an analysis of the shifts in the work function, and a study of the Si 2p, Ag 3d and C 1s core levels. The second section examines the valence bands for this surface. A gas phase spectrum of the pentacene molecule was acquired from the literature and peaks was assigned as π and σ symmetry states. A set of selection rules appropriate for this surface was constructed and the differences in the valence band spectra for s and p-polarized light are explained. Consequently, it has also been possible to determine the orientation of the molecule on this surface from the selection rules.

6.5.1 Work Function Analysis

The high binding energy cutoff is recorded with the sample biased negatively at 9.07 V with respect to the analyzer. The high binding energy cutoffs for each pentacene deposition on the Ag/Si(111)-($\sqrt{3}\times\sqrt{3}$)R30° surface are studied to ascertain changes in the work function with pentacene coverage. Shifts in the work function are determined by applying a best-fit line to the background, as shown in figure 6.14.

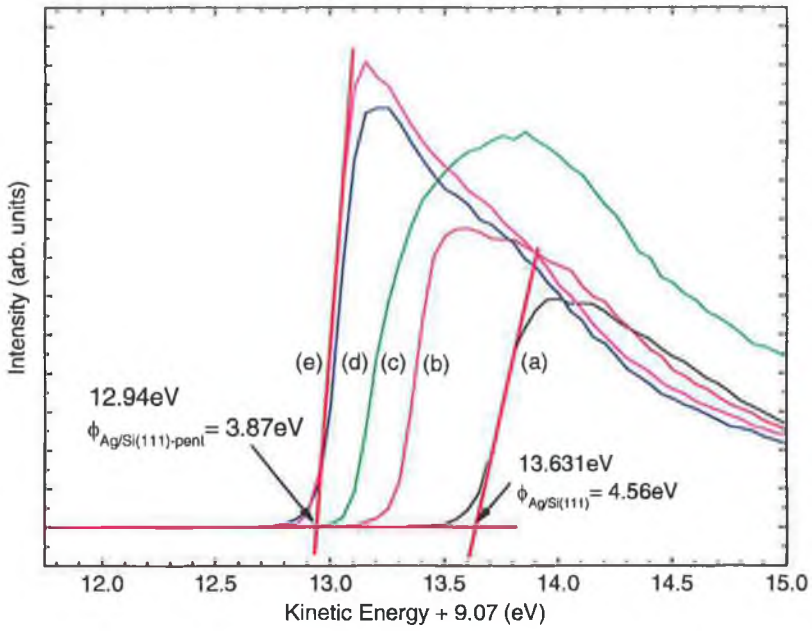

Figure 6.14 *Change in high binding energy cutoff as a function of pentacene deposition, (a) clean Ag/Si(111)-$\sqrt{3}$, (b) 120 secs pentacene deposition, (c) 240 secs, (d) 480 secs and (e) 960 secs*

The work function changes from the clean Ag/Si(111)-$\sqrt{3}$ surface value of 4.56 ± 0.02 eV to a final value of 3.87 ± 0.02 eV as a function of pentacene coverage. It can be seen that there is a difference of ~0.7 eV for a coverage of approximately 960 secs deposition, this approximately corresponds to the magnitude of the interface dipole. It is now well accepted that conventional band bending models cannot fully explain peak shifts at initial stages of metal/organic interface formation, particularly for submonolayer coverages [39], [40]. Therefore the 0.7 eV change in the workfunction can be attributed to small band bending, charge transfer from the pentacene into the substrate since a molecular dipole moment is not possible due to a lack of a permanent dipole on the pentacene molecule [5], changes in the ionisation potential [5] of the adsorbed molecule or final state screening effects [5], [41].

It is therefore possible to build up a band diagram for the Ag/Si(111)-$\sqrt{3}$ pentacene interface as shown in figure 6.15. The onset of the HOMO (see section 6.3.4)

was found to be ~1.6 ± 0.05 eV below the Fermi level E_F and the interface dipole was found to be approximately 0.5 eV.

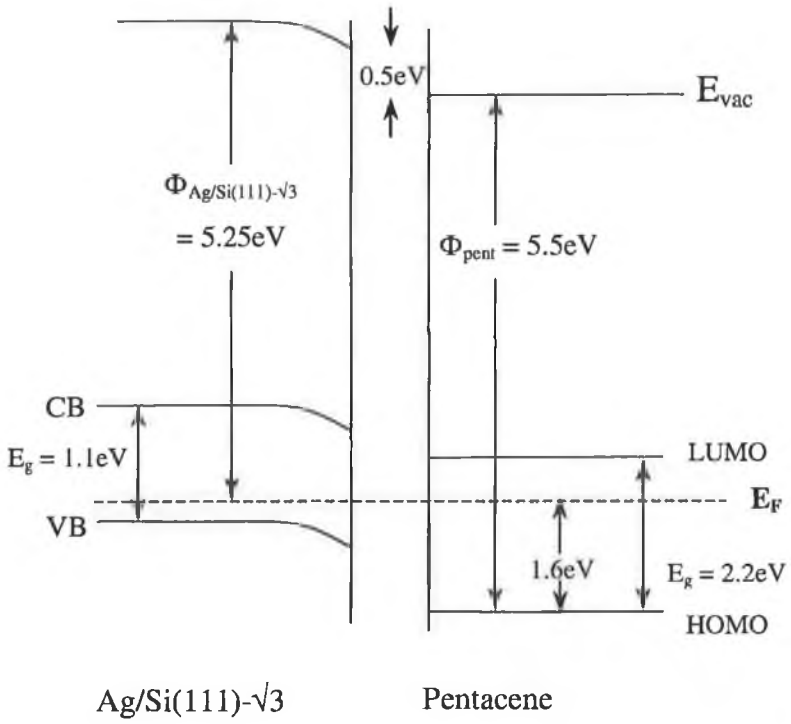

Figure 6.15 *Band diagram for the Ag/Si(111)-√3 pentacene interface. The interface dipole is shown to be ~0.5 eV.*

The optical band gap of the pentacene is ~2.2 eV [42], and from this value the position of the LUMO is found. The ionisation potential for the pentacene thin film is determined from the work function in figure 6.14 and the position of the HOMO. The ionisation potential for these thin pentacene films is 5.5 ± 0.05 eV, which is 0.6 eV larger than the reported ionisation value of pentacene [42].

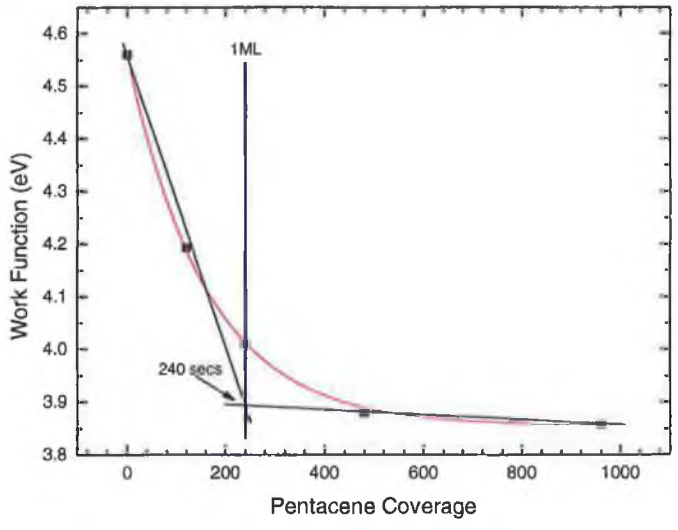

Figure 6.16 *Change in workfunction as a function of pentacene coverage.*

It is possible to estimate the coverage of pentacene on the Ag/Si(111)-$\sqrt{3}$ substrate if the work function changes are plotted against the deposition time, as shown in figure 6.16. Two straight lines are fitted to each of the linear regions. It is found that the two linear lines intersect at approximately 240 secs deposition and this is taken as a complete monolayer.

6.3.2 Core Level Peaks

After the first pentacene deposition (120 secs) it can be seen in figure 6.17 that there is an immediate shift of the peak to lower kinetic energy. This can be explained in terms of the Fermi level movement back towards the midgap position. The clean metallic Si(111)-(7×7) has a Fermi level position of 0.63 eV above the valence band minimum [43]. When this is added to the workfunction value of 4.6 eV [44] the resultant ionization potential value of 5.23 ± 0.05 eV agrees well with the known ionization potential value 5.32 eV for silicon [41], [45]. When silver is deposited, the Si 2p core level shifts 0.4 eV towards higher kinetic energy. This is equivalent to the Fermi level moving down the band gap to a final state at 0.25 ± 0.05 eV above the valence band minimum, which for the boron doped samples used in this experiment approximates to a flat band position. This is in agreement with the result from previous studies [46].

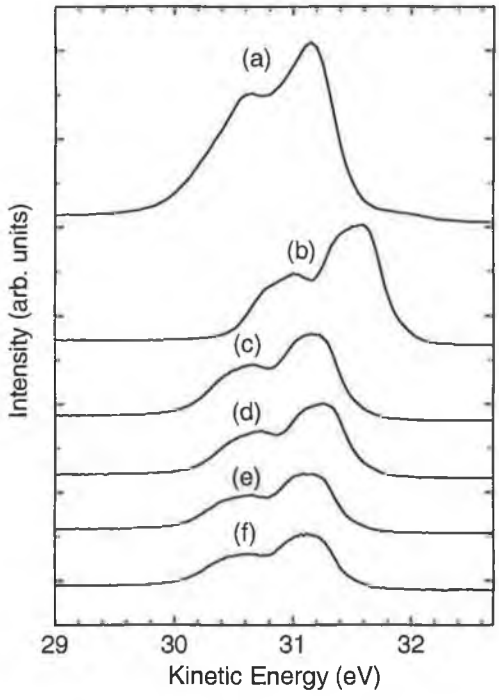

Figure 6.17 *(a) Si 2p core level spectra of the clean Si(111)-(7×7), (b) the clean ($\sqrt{3}\times\sqrt{3}$) silver terminated Si(111) surface and subsequent pentacene coverages, (c) 120 secs pentacene deposition, (d) 240 secs, (e) 480 secs and (f) 960 secs.*

Following a pentacene deposition of approximately 0.5 ML the Si 2p peak shifts back to lower kinetic energies by 0.3 eV. This is again equivalent to the Fermi level moving back up the band gap to a final state at 0.55 eV above the valence band minimum. Therefore the Fermi level has again moved back to the midgap position for coverages above half a monolayer. For subsequent pentacene depositions the Si 2p peak shifts slightly to lower kinetic energies by approximately 0.1 eV, indicating that the Fermi level moves slightly further up the band gap. The movement of the Fermi level back to approximately the same position indicates that there is little or no interaction between the silicon substrate and the pentacene molecules.

For the Ag 3d core level peak a similar shift of 0.3 ± 0.05 eV is again observed after the first pentacene deposition, shown in figure 6.18. It can be seen that the Ag 3d peak attenuates consistently with increasing coverage of pentacene on the surface, indicting layer-by-layer growth. Between the 480 seconds and the 960 seconds deposition there is no change in the intensity. This would indicate that the pentacene is islanding at high coverages resulting in a Stranski-Krastanov growth mode.

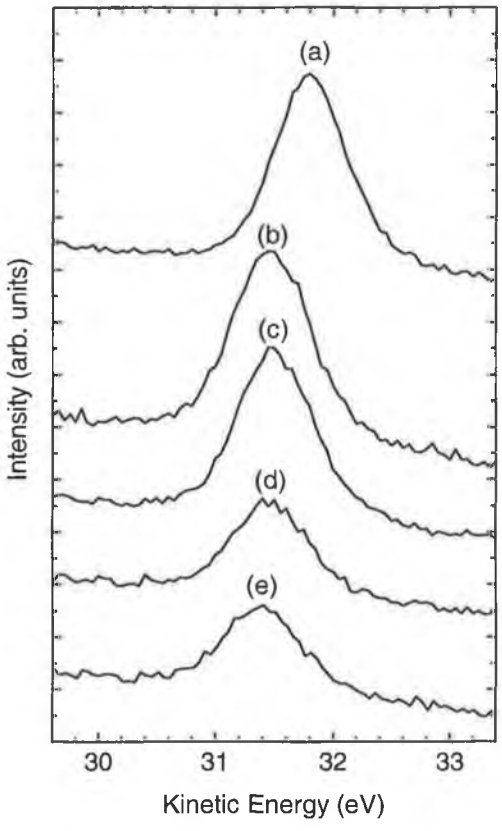

Figure 6.18 *Ag 3d core level spectra of (a) the clean (√3×√3) silver terminated Si(111) surface and subsequent pentacene coverages, (b) 120 secs pentacene deposition, (c) 240 secs, (d) 480 secs and (e) 960 secs.*

From the evolution of the C 1s spectra shown in figure 6.19 the peaks gradually but consistently shifts to lower kinetic energy as a function of pentacene coverage. There is an asymmetry in the C 1s peak from the lowest pentacene coverage, which is reduced with increasing pentacene thickness. These results contrast with the recently reported study by Watkins et. al. [47] for the deposition of pentacene on a Au surface, where the binding energy of the C 1s peak was observed to decrease as a function of layer thickness. But Prisert et. al. [40] have convincingly shown that a contribution from final state screening to the photoemission peak position at submonolayer coverages on a metallic surface can explain these contrasting results. The effectiveness of the screening is reduced the further the molecule is from the surface, thereby explaining the increase in binding energy of the C 1s peak as the pentacene film increases in thickness.

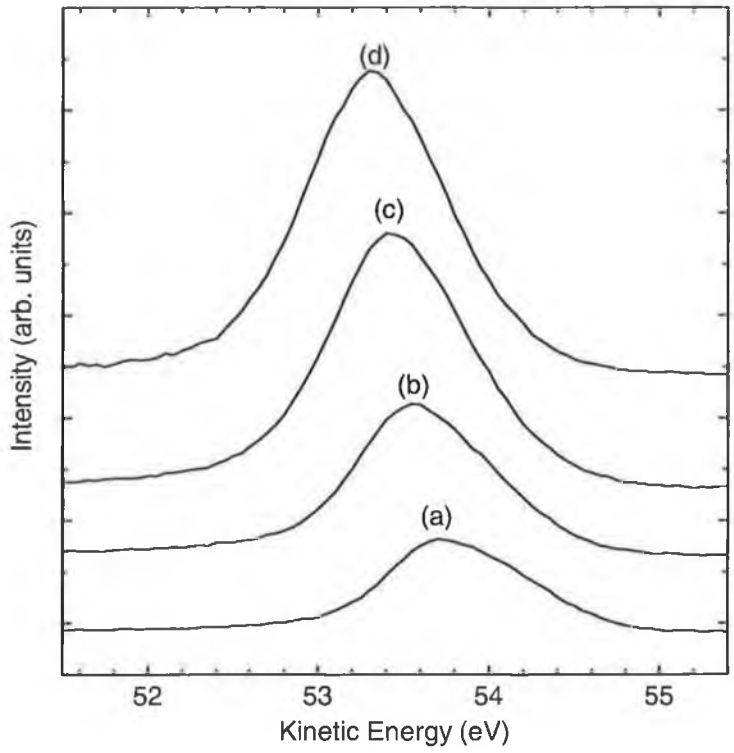

Figure 6.19 *C 1s core level spectra of pentacene coverages on the clean (√3×√3) silver terminated Si(111) surface for (a) 120 secs pentacene deposition, (b) 240 secs, (c) 480 secs and (d) 960 secs.*

6.3.1 Valence Band Photoemission

Synchrotron photoemission is a powerful method used to determine electronic structure and orientation of molecules on a surface [48], [49]. The valence band of pentacene includes 7π- and many σ-like orbitals extends over a binding energy range of approximately 20 eV, as shown in figure 4.16, which shows a gas phase spectrum of pentacene [50], [51] (D_{2h} symmetry species) with the seven π orbitals assigned to the

molecule, starting with the lowest kinetic energy $3b_{2g}$, $2a_u$, $3b_{1g}$, $2b_{2g}$, $3b_{3u}$, $1a_u$, $1b_{2g}$. The features labeled f, g, h, i and j are the observed σ orbitals. The software package Hyperchem [52] was used to confirm the π orbital assignments with the literature and to determine the σ orbital assignments shown at the bottom of figure 4.16. It was found that the f feature in the gas phase spectrum can be composed of $2b_{1g}$ and $7b_{3g}$ orbitals, the g feature is made up of $7b_{1u}$, $6b_{3g}$ and $2b_{3u}$ orbitals. The h peak is composed of $5b_{3g}$, $6b_{1u}$, $5b_{1u}$ and $1b_{3u}$ symmetry orbitals. The i and j features are made up of $7a_g$, $6b_{2u}$ and $4b_{1u}$ symmetry orbitals.

Figure 6.20 shows a set of synchrotron photoemission spectra for an ordered multilayer of pentacene deposited on Ag/Si(111)-√3 compared to the gas phase spectrum of the pentacene. A one-to-one correspondence exists between both the multilayer pentacene film and the gas phase spectrum. A small shift of the pentacene gas phase spectrum of approximately 0.1 eV was performed to align this spectrum correctly with the photoemission spectra. According to reference [53], [51] the first seven orbitals are composed definitively of π character (see table 6.1) and the remaining features are (σ - π) and σ orbitals.

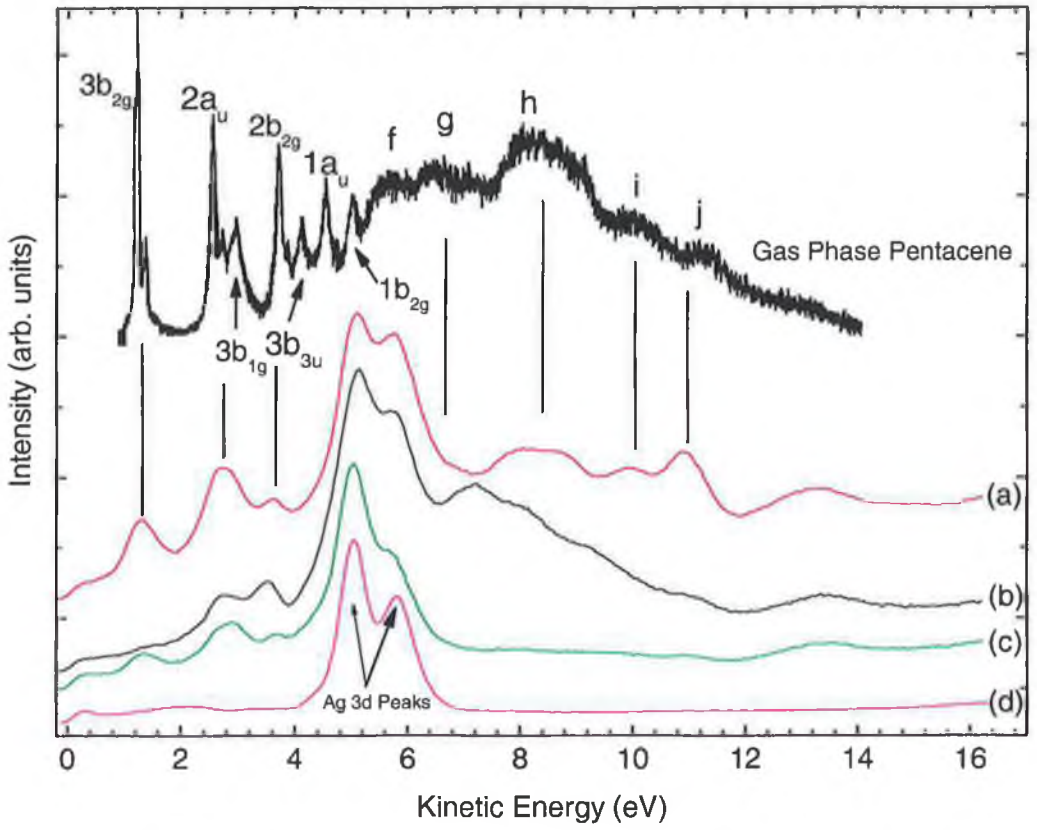

Figure 6.20 *(a) p-polarised emission spectra for pentacene terminated Ag/Si(111)-√3, (b) normal emission spectra for the Ag/Si(111)-√3 pentacene surface, (c) s-polarised emission spectra and (d) the Ag/Si(111)-√3 spectrum is also shown for comparison.*

A set of emission spectra for a high pentacene deposition on Ag/Si(111)-$\sqrt{3}$ taken in normal, s and p-polarizations at a photon energy of 37 eV are also displayed in figure 6.20. Due to experimental constraints the analyser on the UHV chamber at the Aarhus synchrotron was not moveable, and therefore normal emission in s and p polarizations was not obtainable. Instead the sample was moved so that normal incidence reflects s-polarised light and grazing incidence reflects p-polarised light. The s-polarized spectrum is composed purely of s-polarisation but the p-polarized spectrum contained a small component of s-polarization, the geometry is shown figure 6.21.

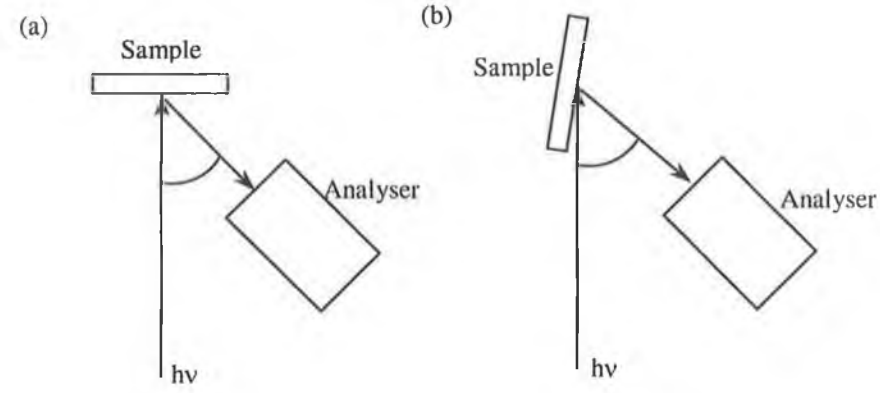

Figure 6.21 *(a) configuration for s-polarization spectra, (b) configuration for p-polarized spectra.*

The photoelectron spectra from the clean Ag/Si(111)-$\sqrt{3}$ surface is also shown for reference. In the lower binding energy region between 4 and 7eV the Ag 3d peaks are dominant. In the s-polarized spectrum very few σ features from the molecule are detected, the p-polarized spectrum exhibits, due to the smaller penetration depth of the incident photons, several adsorbate induced emission features.

For p-polarized normal emission the final state wavefunction must belong to the a_g or the b_{1u} symmetry species of the D_{2h} point group. The z-axis is chosen as normal to the surface and the molecule is assumed to lie flat on the surface in the xy plane, so that the x-axis is aligned along the long molecular axis and the y-axis aligned across the long molecular axis. Initial states with symmetry b_{2u}, b_{3u}, b_{3g} and b_{2g} are expected to contribute to the s-polarized spectrum [49]. Because of the three fold symmetry of the Ag/Si(111)-($\sqrt{3}\times\sqrt{3}$)R30°surface domains, with axes aligned in three different directions around the z-axis, it is not possible to distinguish between x- and y- polarizations. Utilising group theory as in chapter 4, table 6.1 is constructed for normal emission in both s and p polarisations. In table 6.1 the allowed transitions within the D_{2h} point group for both xy and z-polarizations at normal emission are indicated by (+).

D_{2h}	x, y	z	Energy (eV)	
$3b_{2g}$ (π)	+	–	1.61	
$2a_u$ (π)	–	–	2.52	
$3b_{3g}$ (π)	+	–	3.05	
$2b_{2g}$ (π)	+	–	3.65	
$3b_{3u}$ (π)	+	–	4.04	
$1a_u$ (π)	–	–	4.50	
$1b_{2g}$ (π)	+	–	5.02	
$2b_{1g}$ (π+ σ)	–	–	5.32	f
$7b_{3g}$ (π+ σ)	+	–	5.41	f
$7b_{1u}$ (π+ σ)	–	+	6.37	g
$6b_{3g}$ (π+ σ)	+	–	6.46	g
$2b_{3u}$ (π+ σ)	+	–	6.59	g
$1b_{1g}$ (π+ σ)	–	–	7.59	
$5b_{3g}$ (π+ σ)	+	–	7.76	h
$6b_{1u}$ (π+ σ)	–	+	7.89	h
$5b_{1u}$ (π+ σ)	–	+	8.14	h
$1b_{3u}$ (π+ σ)	+	–	8.28	h
$7a_g$ (σ)	–	+	9.38	i
$6b_{2u}$ (σ)	+	–	9.65	i
$4b_{1u}$ (σ)	–	+	10.86	j
$6a_g$ (σ)	–	+	12.68	
$5b_{2u}$ (σ)	+	–	13.16	

Table 6.1 *Symmetry Assignment for pentacene.*

Examining table 6.1, it can be seen that states with symmetry b_{2u}, b_{3u}, b_{2g} and b_{3g} are expected to contribute to the s-polarized spectrum. Investigating the s-polarized spectrum in figure 6.18, it can be seen that the π orbitals, namely the $3b_{2g}$, the $3b_{3g}$, and the $2b_{2g}$ symmetry states can be seen clearly. The HOMO with symmetry $3b_{2g}$ is allowed by the selection rules, the $3b_{3g}$ and $2b_{2g}$ states are allowed by the selection rules. This region of the s-polarised spectrum corresponds well with the selection rules. At an energy of 5.02 eV a state with symmetry $1b_{2g}$ exists but features between 4 eV and 7 eV are not resolvable because the Ag 3d peaks dominate that part of the spectrum and therefore this state is not seen. For energies above 7 eV the σ states are very weak. On close examination only small peaks are observable at 7.75 eV and 9.5 eV. These peaks correspond to features h and i respectively in the gas phase spectrum. From table 6.1, for s-polarised light it can be seen that features h and i have allowed states with symmetries $1b_{3u}$, $5b_{3g}$ and $6b_{2u}$ respectively.

For the p-polarized spectrum the final state wavefunction must have a_g or b_{1u} symmetry. Examining table 6.1 and comparing the selection rules with figure 6.20 it can be seen that the π states, again the $3b_{2g}$, $2a_u$ or $3b_{3g}$, and the $2b_{2g}$ can be seen in the spectrum, but in this case the peaks are more intense and better resolved. It can also be seen in table 6.1 that no states should exist in this part of the p-polarized spectrum. An explanation for this discrepancy could be the fact that when performing the p-polarised scans the sample was not at normal emission and these scans contained some s-polarisation. Features around the Ag 3d peaks are again not resolved. There is a state at approximately 6.4 eV, on the falling end of the Ag 3d peaks, which is allowed by the selection rules and attributed to $7b_{1u}$ symmetry state. On close examination it is possible to see that there is a small change in the p-polarized spectrum compared to the s-polarized spectrum in this area.

Most of the differences between the s and p-polarizations occur for the σ orbitals. Features h-j are more resolved in the p-polarised spectrum. For p-polarized light feature h is attributed to symmetry states $5b_{1u}$ and $6b_{1u}$, feature i is attributed to symmetry state $7a_g$ and j is attributed to symmetry state $4b_{1u}$.

Yannoulis et al [49] suggested that if the a_g and the b_{1u} symmetric orbitals are predominantly excited by p-polarisation, then the molecule is orientated parallel to the substrate. Almost all transitions in figure 4.16 have allowed states that contribute to the peaks in the s and the p-polarization spectra. This makes it impossible to assign an orientation to the molecule. However in the σ part of the gas phase spectrum, the j feature is made up completely of only an allowed p-polarization state, the $4b_{1u}$ symmetry state. Comparing the s and p-polarized spectra in figure 6.20 it is clear that this state only exists in the p-polarized position and not in the s-polarised position. Therefore it can be concluded that the molecule is lying parallel to the surface as was seen by the STM investigation in section 6.2.

6.4 Conclusion

In summary the structure of the first two solid phases S1 and S2 for the pentacene molecule ($C_{22}H_{14}$) on the Ag/Si(111)-($\sqrt{3}\times\sqrt{3}$)R30° surface at room temperature has been observed by STM. Both adlayer structures, are found to be commensurate with the Ag/Si-$\sqrt{3}$ substrate, The formation of well-ordered pentacene layers on the Ag/Si-$\sqrt{3}$ substrate depends not only on the competition between intermolecular and molecule-substrate interactions but also on the nature of the

adsorption site. In a study of the lateral order of PTCDA molecules on several metal surfaces, Fink et al [20] conclude that when the substrate interaction is weak the lateral molecular arrangement is governed by the intermolecular interactions but a stronger interaction with the metal substrate leads to the formation of a commensurate superstructure. Two adsorption sites are identified for the S1 phase, a three fold hollow site at the center of a Ag-trimer (CA-site) and a six-fold hollow site at the center of a hexagonal arrangement of Ag atoms (CB-site). For this phase the lateral interaction is weak and adsorption takes place on both the CA and CB-sites, forming a (25×25) commensurate structure. The six-fold hollow site (CB-site) has the weaker reactivity and consequently, no adsorption takes place on this site for the S2 phase, in which the short-range interactions are stronger. The strength of the molecule-substrate interaction at the Ag-trimer sites (CA-site) is sufficient to produce a new commensurate structure, even in the presence of short-range lateral interactions. For the final phase, S3, it was found that increasing pentacene coverage on the close packed side-by-side orientation of phase S2, the molecules tilt from a planar to an upright configuration. This arrangement increases the density D of the molecules in order to occupy the maximum area.

The results on molecular orientation from group theory selection rules are in clear agreement with the STM studies of the same system, which illustrated a high degree of molecular ordering with the molecules orientated parallel to the surface.

Chapter 6 References

1. F.-J. Meyer zu Heringdorf, M.C. Reuter and R.M. Tromp, Nature 412, (2001), 517.
2. M. Kasaya, H. Tabata, T. Kawai, Surf. Sci., 342, (1995), 215.
3. M. Kasaya, H. Tabata, T. Kawai, Surf. Sci., 406, (1998), 302.
4. G. Hughes, J. Roche, D. Carty, A.A. Cafolla, J. Vac. Sci. Technol. B20(4), (2002), 1620.
5. P.G. Schroeder, C.B. France, J.B. Park, B.A. Parkinson, J. Appl. Phys., 91, (2002), 3010.
6. S. Lukas, G. Witte, Ch. Woll, Phys. Rev. Lett., 88, (2002).
7. Ph. Guaino, D. Carty, G. Hughes, P. Moriarty, A.A. Cafolla, Appl. Surf. Sci., 9817, (2003), 1-5.
8. S.F. Bent, Surf. Sci., 500, (2000), 879.

9. W.N. Unertl (editor), ***Handbook of Surface Science*** Vol.1, Physical Structure, Elsevier Science (the Netherlands), 1996.
10. M.D. Upward, P.H. Beton, P. Moriarty, Phys. Rev. B56(4), (1997) R1704.
11. R.E. Schlier, H.E. Farnsworth, J. Chem. Phys. **30**, (1959), 917.
12. G. Binnig, H. Rohrer, Ch. Gerber, E. Weibel, Phys. Rev. Lett., 49(1), 57.
13. G. Binnig, H. Rohrer, Ch. Gerber, E. Weibel, Appl. Phys. Lett., 40(2), 178.
14. K. Takayanagi, Y. Tanishiro, M. Takahashi, M. Takahashi, J. Vac. Sci. Technol. A**3**, (1986), 1502.
15. S.Y. Tong, H. Huanq, C.M. Wei, W.E. Packard, F.K. Men, G.S. Glander, M.B. Webb, J. Vac. Sci. Technol. A**6**, (1988), 615.
16. M. Fujita, H. Nagayoshi, Surf. Sci. **242**, (1991), 229.
17. W. Monch, ***Semiconductor Surfaces and Interfaces***, 2nd Edition, Springer Series in Surface Sciences, Springer Verlag: Berlin, 1995, Vol. 26 and D. Haneman, Rep. Prog. Phys., 50, (1987), 1045.
18. R.J. Wilson, S. Chiang, Phys. Rev. Lett., 58(4), (1987), 369.
19. E.J. van Loenen, J.E. Demuth, R.M. Tromp, R.J. Hamers, Phys. Rev. Lett., 58(4), (1987), 373.
20. J.F. Fia, R.G. Zhoa, W.S. Yang, Phys. Rev, B48, (1993), 18109.
21. S. Lukas, S. Vollmer, G. Witte, Ch. Woll, Journal of Chemical Phys. Rev., 114(22), (2001), 10123.
22. M.D. Upward, P.H. Beton, P. Moriarty, Surf. Sci, 441, (1999), 21.
23. R. Fink, D. Gador, U. Stahl, Y. Zou, U. Umbach, Phys. Rev. B 60(4), (1999), 2818.
24. M. Bohringer, K. Morgenstern, W.D. Schneider, M. Wuhn, C. Woll, R. Berndt, Surf. Sci., 444, (2000), 199.
25. M.M. Kamma, S.J. Stranick, P.S. Weiss, Science, 274, (1996), 119.
26. A.I. Kitaigorodskii, ***Molecular Crystals and Molecules***, Academic Press, New York, 1973.
27. M. Kanai, T. Kawai, K. Motai, X.D. Wang, T. Hashizume, T. Sakurai, Surf. Sci., 329, (1995), L619.
28. C. Dekker, S.J. Trans, B. Oberndorff, R. Meyer, L.C. Venema, Synthetic Metals, 84, (1997), 853.
29. W. Mizutani, M. Shigeno, M. Sakakibara, M. Ono, S. Tanishima, K. Ohmo, N. Toshimo, J. Vac. Sci. Technol. A8(1), 675, (1990).
30. P.S. Weiss, D.M. Eigler, Phys. Rev. Lett., 71, (1993), 3139.
31. A. Hoshino, S. Isoda, H. Kurata, T. Kobayashi, Appl. Phys., 76(7), (1994), 4113.

32. A. Hoshino, S. Isoda, H. Kurata, T. Kobayashi, Journal of Crystal Growth, 146, (1995), 636.
33. M. Schunack, E. Laegsgaard, I. Stensgaard, F. Besenbacher, J. of Appl. Chem. Phys., 117, (2002), 8493.
34. R.B. Campbell, J.M. Robertson, J. Trotter, Acta. Crystallogr. 14, (1961), 705.
35. Y. Harada, H. Ozaki, K. Ohno, Phys. Rev. Lett., 52, (1984), 2269.
36. Ph. Guaino, A.A. Cafolla, D. Carty, G. Sheerin, G. Hughes, Surf. Sci., 540, (2003), 107.
37. Ph. Guaino, D. Carty, A.A. Cafolla, G. Hughes, P. Moriarty, Appl. Surf. Sci., 212-213, (2003), 537.
38. M. Eremtchenko, J.A. Schaefer, F.S. Tautz, Nature, 425, (2003), 602.
39. I.G. Hill, A.J. Makinen, Z. H. Kafafi, J. Appl. Phys., 88, (1994), 889.
40. H. Prisert, M. Knupfer, T. Schwieger, J.M. Auerhammer, M.S. Golden, J. Fink, J. Appl. Phys., 91, (2002), 4872.
41. L.Ley, M. Cardona, ***Photoemission in Solids II***, Topics in Applied Physics, Vol. 27, Springer-Verlag, 1979.
42. N. Koch, J. Ghijsen, R.L. Johnson, J. Schwartz, J.-J. Pireaux, A. Kahn, J. Phys. Chem. B, 106, (2002), 4192.
43. L.S.O. Johansson, E. Landemark, C.J. Karlsson, R.I.G. Uhrberg, Phys. Rev. Lett., 63, (1989), 2092.
44. D. Carty, G. Hughes, A.A. Cafolla, to be published.
45. ***Physics of Semiconductor Devices***, Sze.
46. J.A. Theobold, N.S. Oxtoby, M.A. Phillips, N.R. Champness, P.H. Beton, Nature, 424, (2003), 1029.
47. N.J. Watkins, Li. Yan, Y. Goa, Appl. Phys. Lett., 80, (2002), 4384.
48. E.W. Plummer, W. Eberhardt, Adv. Chem. Phys. 49, (1982), 533.
49. P. Yannoulis, K.-H. Frank, E.-E. Koch, Surf. Sci., 241, (1991), 325.
50. N.O. Lipari, C.B. Duke, J. Chem Phys, 63(5), (1975), 1768.
51. P.A. Clark, F. Brogli, E. Heilbronner, Helvetica Chimica Acta, 55(5), (1972),1415.
52. Hyperchem (TM) Professional 7.0, Hypercube Inc., 1115 NW 4th Street, Gainsville, Florida 32601, USA.
53. H. Ozaki, J. of Chem. Phys, 113(15), (2000), 6361.

Chapter 7 Conclusions and Future Work

The purpose of this work was to investigate the initial stages of interface formation for the pentacene/Au(110) and pentacene/Ag/Si(111)-($\sqrt{3}\times\sqrt{3}$) surfaces. The main structural techniques used in this work were reflectance anisotropy spectroscopy (RAS), scanning tunnelling microscopy (STM), photoelectron spectroscopy (PES) and low energy electron diffraction (LEED).

In chapter two the theoretical background for the techniques used in the course of this work have been detailed. Two RAS equations are derived; one that is used for modelling the RA spectra and the second equation is in a form suitable for analysis of experimental data. The STM, photoemission and LEED theory have been briefly detailed. Group theory was used to analyse the valence bands of pentacene/Au(110) and pentacene/Ag/Si(111)-($\sqrt{3}\times\sqrt{3}$) surfaces to determine the orientation of the molecular plane relative to the surface. Group theory was described briefly, the selection rules used for the point group of the pentacene molecule are also described.

As RAS was the main technique used in the course of this work the construction of the RAS spectrometer is detailed extensively in chapter three. All of the components that make up the spectrometer are described and details about the calibration of the technique are explained. The experimental details regarding all the techniques are also described to a lesser extent in this chapter. In the final part of chapter three, the Knudsen cell for evaporating organic molecules is described.

An STM and photoemission study of pentacene/Au(110)-(2×1) surface is described in chapter four. Three adsorption configurations for pentacene molecules on this surface are identified. In the first configuration, at coverages of approximately 0.5 ML, it is found that the molecules are aligned between the gold rows along the $(\bar{1}10)$ direction. As a consequence of the initial adsorption of pentacene, the Au(110)-(2×1) reconstruction changes to a (3×1) reconstruction, as determined using STM and LEED. The second adsorption configuration is identified above 0.5 ML coverage, when the gold rows are filled, the molecules adopt a higher packing density and align across the gold rows along the (001) direction. The third adsorption configuration is identified as the pentacene molecule lying across a single gold row.

Core level photoemission experiments reveal a work function change for increasing pentacene coverage and a band diagram is shown. The change in the orientation of the molecule after 0.5 ML is also evidenced in the core level spectra. Group theory was applied to the valence bands and selection rules were developed for the molecule/metal interface. The low symmetry of the pentacene molecule and the

analyzer position, prevented conclusive results regarding the orientation of the pentacene molecular plane with respect to the substrate.

In chapter five RAS measurements are recorded for the clean Au(110)-(2×1) substrate. Three peaks are identified and the RAS measurements are correlated with surface state transitions along the $\bar{\Gamma}-\bar{X}$ direction. A simulation of the spectra was performed, which supported the transitions already identified. RAS measurements were recorded as the Au(110)-(2×1) surface was annealed. It was found that the surface reconstructs from a (2×1)→(1×1) at a temperature of approximately 773 K. Induced surface roughness in the Au(110)-(2×1) was achieved by Ar^+ sputtering the surface for small time intervals. Three peaks were identified and assigned to surface state transitions along the $\bar{\Gamma}-\bar{X}$ direction. Again a simulation of the spectrum was performed, supporting the transitions identified. Finally RAS spectra were recorded for the pentacene/Au(110)-(2×1) interface. With increasing pentacene coverage it is found that the peaks appearing in the spectra correlate with the visible-IR spectrum of pentacene. Three electronic transitions with associated vibronic transitions are identified. Azimuthal orientational information supporting the change in direction of the molecule after half a monolayer is provided by this technique.

In chapter six STM measurements recorded for increasing pentacene coverages on the Ag/Si(111)-(√3×√3) surface, are presented. Three adsorption phases are identified. For the first low coverage phase, three domains are identified at 120° with respect to each other. The symmetry and orientation of these structural domains, suggest a molecular arrangement, which depends on a molecule-substrate interaction. A model is proposed for this surface and it is found that there exists a high order (25×25) commensurate cell, with respect to the unit cell of the Ag/Si-(√3×√3) surface, containing 75 molecules. For the second phase, occurring at approximately a monolayer coverage, the molecules have a higher packing density. The pentacene molecules adopt a close packed side-by-side arrangement with the molecular domains remaining oriented at 120°. A model is proposed for this surface and it is found that this molecular arrangement leads to smaller commensurate overlayer, Ag/Si(111)-(2×3)-pentacene, with two molecules per unit cell. For the third phase, greater than a monolayer coverage, a molecular reorganization is observed. The molecules began to tilt so that their molecular plane is orientated perpendicular to the surface. The reason for the tilting is still unresolved. Two possible suggestions are that the molecules increase their packing density by tilting to accommodate more molecules on the surface with

increasing pentacene coverage or that the STM scanning process itself is responsible for the tilting.

Core level Photoemission experiments reveal a work function change for increasing pentacene coverage and an energy band diagram is produced. The core levels also reveal that there is little or no interaction between the molecule and the substrate. Group theory is applied to the valence bands and selection rules are developed for the molecule/metal interface. This surface proved more successful for the application of group theory to the orientation of the molecular plane. It is shown that due to the selection rules a peak with b_{1u} symmetry produced only by p-polarized light, and not evident using s-polarized light, indicates that the molecule is parallel to the substrate. This is clear from the STM images and the photoemission spectra and it is concluded that the molecular plane is parallel to the substrate.

The RAS provides information regarding surface states, optical transitions and the azimuthal orientation of the molecule with respect to the substrate by exploiting symmetry and polarization differences between the substrate and the adsorbed molecule. Much of this work has been taken up with the construction of the RAS technique and its adaptation to a UHV environment to perform quantitative experiments. The detection system of the spectrometer uses a monochromator and photomultiplier tube. A small improvement was incorporated to the spectrometer, a fibre optic was fitted onto the optic table to couple the light effectively to the monochromator. The programming of the spectrometer, though easy to incorporate has many disadvantages. For a first time user the programme is not as easy to learn as windows based programs, also the RAS spectra acquisition time is long. Both of these areas could be improved by reprogramming the spectrometer using Labview [1]. This program is specifically developed for interfacing to equipment. It is windows based and for a first time user, easy to learn.

The photoemission spectroscopy was performed at the Aarhus synchrotron in Denmark. The results obtained for the core levels provided information about bonding environments and coverages of the molecule on the substrate. The valence bands proved more difficult to analyse. Group theory was used in an attempt to explain the orientation of the molecule with respect to the substrate. The selection rules, based on the molecular symmetry and the sample surface, are only applicable for normal emission. Therefore to obtain conclusive orientational information regarding the molecule on the sample surface a moveable analyser is needed. To obtain conclusive results about the

orientation of the pentacene molecular plane on the substrates two types of experiments can be performed.

The first is an angle resolved photoemission study. Angle resolved detection adds a new dimension to photoelectron spectroscopy. The intensity and energy dependence can be measured as a function of the collection angle with respect to some fixed axes. The tilt angle of the molecular plane (if any) with respect to the surface can be detected using this type of experiment.

A more appropriate technique is near edge X-ray absorption fine structure (NEXAFS). By measuring the polarization dependence of the C 1s $\rightarrow \pi^*$ transitions (for carbon based molecules) in the NEXAFS spectra, it is possible to determine the orientation of the molecular plane with respect to the substrate. By comparing the strong variation of the adsorbate-induced bands with the emission angle, as well as the angle of incidence, i.e. the polarization of the incident light, selection rules can be derived about the orientated molecule. A NEXAFS experiment is planned to determine the precise orientation of the molecular plane on the Au(110)-(2×1) and Ag/Si(111)-$\sqrt{3}$ surfaces.

Chapter 7 References

[1] National Instruments Corporation, 11500 N Mopac Expressway, Austin, Texas, USA. http://www.ni.com.

List of Publications

D. Carty, A.A. Cafolla, **A RAS study of the Pentacene/Au(110)** interface, to be published.

G. Hughes, D. Carty, A.A. Cafolla, Ph. Guaino, **Core Level Photoemission and Scanning Tunneling Microscopy study of the interaction of pentacene with the Si(111) surface,** to be published.

Ph. Guaino, D. Carty, McDonald O, G. Hughes and A. A. Cafolla, **Long range order in a multilayer organic film templated by a molecular induced surface reconstruction: Pentacene on Au(110),** accepted for publication in Applied Physics Letters.

A. A. Cafolla, E. McLoughlin, E. AlShamaileh, Ph. Guaino, G. Sheerin, D. Carty, T. McEvoy, C. Barnes, V. Dhanak and A. Santoni, **Observation of an anti-phase domain structure in the Cu{1 0 0}/Sn surface alloy system** *Surface Science, Volume 544, Issue 1, 10 October 2003, Pages 121-133.*

Ph. Guaino, A. A. Cafolla, D. Carty, G. Sheerin and G. Hughes, **An STM investigation of the interaction and ordering of pentacene molecules on the Ag/Si(111)-($\sqrt{3}\times\sqrt{3}$)*R*30°surface,** *Surface Science, Volume 540, Issue 1, 10 August 2003, Pages 107-116*

Ph. Guaino, D. Carty, G. Hughes, P. Moriarty and A. A. Cafolla, **Scanning tunneling microscopy study of pentacene adsorption on Ag/Si(1 1 1)-($\sqrt{3}\times\sqrt{3}$)R30°,** *Applied Surface Science, Vol 212-213, 15 May 2003, Pages 537-541*

Guaino P, Cafolla AA, McDonald O, Carty D, Sheerin G, Hughes G, Scanning tunnelling spectroscopy of low pentacene coverage on the Ag/Si(111)-(root 3x root 3) surface, J. of Phys Condensed Matter 15 (38): S2693-S2698 OCT 1 2003

Hughes G, Roche J, Carty D, Cafolla T, Smith KE, **Core level photoemission and scanning tunneling microscopy study of the interaction of pentacene with the Si(100)surface,**J. of Vac. Sci. & Technol B 20 (4): 1620-1625 JUL-AUG 2002.

List of Figures

Figure 3.30 Resolution of the SGM1 monochromator with a typical working setting of the slits at 50 μm.

Figure 3.31 Layout of the SGM1 monochromator.

Figure 3.32 Diagram of SCIENTA spectrometer.

Figure 3.33 The experimental chamber setup at beamline SGM 1 in Aarhus, for photoelectron studies.

Figure 3.34 Sample Mounting incorporating resistive heating filament.

Figure 3.35 Construction diagram of pentacene evaporator.

Figure 4.1 (a) model of the (2×1) missing row reconstruction at the (110) surface of Au (side view), (b) missing row reconstruction at the (110) surface of Au (top view).

Figure 4.2 STM image (15nm^2) of clean Au(110)-(2×1) surface featuring the missing row reconstruction.

Figure 4.3 ball and stick model and skeletal structure of pentacene molecule in x-y plane, including dimensions.

Figure 4.4 shows STM image (9.0nm x 5.0nm) with pentacene molecules aligned in between the Au(110)-(2×1) channels.

Figure 4.5 shows an STM image (28nm×28nm) with 0.8 ML pentacene coverage showing the molecular arrangement of pentacene across one and two gold rows.

Figure 4.6 A comparison of the LEED patterns of (a) the clean gold (1 × 2) surface and, (b) on the low coverage phase acquired at the same beam energy of 70 eV.

Figure 4.7 STM image (500 nm^2) of the Au(110) surface after pentacene deposition of ~ 7 ML.

Figure 4.8 (a) High resolution STM images (45 nm^2, insert = 10 nm^2) showing the molecular structure of the multilayer pentacene film.

Figure 4.9 Typical Diagram LEED Pattern, acquired in-situ with an electron beam energy of 35 eV, showing the reciprocal space structure of the thin organic film.

Figure 4.10 showing the high binding energy cutoff for increasing pentacene depositions on a clean Au(110)-(2×1) surface.

Figure 4.11 Band diagram for the pentacene / Au(110) interface. The interface dipole is shown to be 1.21eV.

Figure 4.12 plot of work function versus deposition time to estimate a monolayer coverage.

Figure 4.13 Au $4f_{7/2}$ spectra taken with photon energy of 130eV of (a) clean gold, and after a deposition of (b) 20 secs, (c) 40 secs, (d) 60 secs, (e) 100 secs, (f) 120 secs, (g)

240 secs, (h) 360 secs, (i) 480 secs, (j) 720 secs, (k) 960 secs and (l) 1440 secs. Also shown are the fitting spectra and the fitted curve.

Figure 4.14 carbon 1s core level photoemission spectra taken with photon energy of 340eV after a deposition of (a) 60 secs deposition, (b) 100 secs, (c) 120 secs, (d) 240 secs, (e) 360 secs, (f) 480 secs, (g) 720 secs, (h) 960 secs and (i) 1440 secs on a clean Au(110)-(2×1) surface. Also showing are the fitting spectra.

Figure 4.15 cross section corrected areas for C 1s peak and Au $4f_{7/2}$ peak plotted as a function of deposition time.

Figure 4.16 Gas phase spectrum of the pentacene molecule with π and σ orbital assignments.

Figure 4.17 Valence band spectra for clean Au(110) and pentacene covered Au(110) in normal, s and p-polarised emission.

Figure 4.18 Valence Band spectra for increasing coverages of pentacene on Au(110)-(2×1).

Figure 4.19 Schematic diagram for various configurations of the pentacene molecule on the Au(110)-(2×1) surface.

Figure 5.1 (a) A(ω) and (b) B(ω) coefficients calculated from the n and k values in Palik.

Figure 5.2 (a) RAS spectra of clean Au(110)-(2×1) reconstruction with relevant features indicated by arrows and (b) the fitted model with the fitting contributions.

Figure 5.3 RAS spectra of the Au(110)-(2×1) to (1×1) transition at various temperatures. The dashed lines indicate zero levels. All temperatures ± 5 K.

Figure 5.4 RAS spectra of Argon bombarded Au(110) for increasing bombardment times as indicated.

Figure 5.5 Spectra of heavily bombarded Au(110)-(2×1) and a calculated spectrum of this curve.

Figure 5.6 Image of the Au(110)-(2×1) reconstruction.

Figure 5.7 Absorption spectrum of pentacene from the near infrared to the near ultraviolet.

Figure 5.8 real RAS spectra for increasing coverages of pentacene on Au(110)-(2×1) (a)clean Au(110)-(2×1), (b) 0.1 ML, (c) 0.2 ML,(d) 0.3 ML, (e) 0.4 ML, (f) 0.5 ML.

Figure 5.9 real $Re(\Delta r/r)$ spectra for increasing coverages of pentacene on Au(110)-(2×1) (a) 0.6 ML, (b) 0.7 ML, (c) 0.8 ML,(d) 0.9 ML, (e) 1.0 ML, (f)1.1 ML.

Figure 5.10 real $Re(\Delta r/r)$ spectra for increasing coverages of pentacene on Au(110)-(2×1) (a) 2.1 ML, (b) 2.3 ML, (c) 2.5 ML,(d) 2.9 ML, (e) 3.1 ML, (f)3.5 ML.

Figure 5.11 colour contour plot for increasing coverages of pentacene on Au(110)-(2×1).

Figure 5.12 real RAS spectra for increasing sample temperatures of a high coverage of pentacene on Au(110)-(2×1) (a) 413 K, (b) 393 K, (c) 373 K, (d)363 K, (e)353 K, (f) 323, (g) 273 K.

Figure 6.1 The (7×7) dimer-adatom-stacking fault model (DAS). The stacking fault is in the right half of the (7×7) cell.

Figure 6.2 (a) Filled and (c) Empty state images of the (7×7) reconstruction, (15 nm^2).

Figure 6.3 (a) Schematic illustration of the Honeycomb-Chain-Trimer (HCT) model of the Ag/Si(111)-$(\sqrt{3}\times\sqrt{3})$R30° surface.

Figure 6.4 (a) STM image of S1 phase. Molecules are lying flat on the surface.

Figure 6.5 STM image of Ag/Si-√3 coverage after pentacene deposition of ~0.2 ML.

Figure 6.6 (a) High-resolution image of Ag/Si-√3 after a pentacene deposition of ~0.2 ML.

Figure 6.7 Proposed model for the Ag/Si(111)-(25×25)-pentacene structure, S1 phase.

Figure 6.8 STM image of solid phase S2 formed after deposition of 1ML of pentacene.

Figure 6.9 STM images (7.8×7.8nm^2) of solid phase S2 recorded in dual scan mode.

Figure 6.10 Proposed model for the Ag/Si(111)-(2×3) pentacene structure, S2 phase.

Figure 6.11 STM image (15×15 nm^2, V_s=-1.3 V, I_t=300 pA) of >1.0 ML coverage showing a reorganization of the molecules.

Figure 6.12 (a), (b), (c), (d), (e) and (f) are frames 2, 3, 4, 5, 6 and 8 from a sequence of images recorded with the same tunnelling conditions (V_s=-4.2 V, I_t=20 pA) and with a scan speed of 177 nm/s.

Figure 6.13 (a) and (b) are the cross sections of the area indicated in 6.12(f).

Figure 6.14 Change in high binding energy cutoff as a function of pentacene deposition.

Figure 6.15 Band diagram for the Ag/Si(111)-√3 pentacene interface. The interface dipole is shown to be ~0.7 eV.

Figure 6.16 Change in workfunction as a function of pentacene coverage.

Figure 6.17 (a) Si 2p core level spectra of the clean Si(111)-(7×7), (b) the clean (√3×√3) silver terminated Si(111) surface and subsequent pentacene coverages.

Figure 6.18 Ag 3d core level spectra of (a) the clean ($\sqrt{3}\times\sqrt{3}$) silver terminated Si(111) surface and subsequent pentacene coverages.

Figure 6.19 C 1s core level spectra of pentacene coverages on the clean ($\sqrt{3}\times\sqrt{3}$) silver terminated Si(111) surface for (a) 120 secs pentacene deposition, (b) 240 secs, (c) 480 secs and (d) 960 secs.

Figure 6.20 (a) p-polarised emission spectra for pentacene terminated Ag/Si(111)-$\sqrt{3}$, (b) normal emission spectra for the Ag/Si(111)-$\sqrt{3}$ pentacene surface, (c) s-polarised emission spectra and (d) the Ag/Si(111)-$\sqrt{3}$ spectrum is also shown for comparison.

Figure 6.21 (a) configuration for s-polarization spectra, (b) configuration for p-polarized spectra.

List of Tables

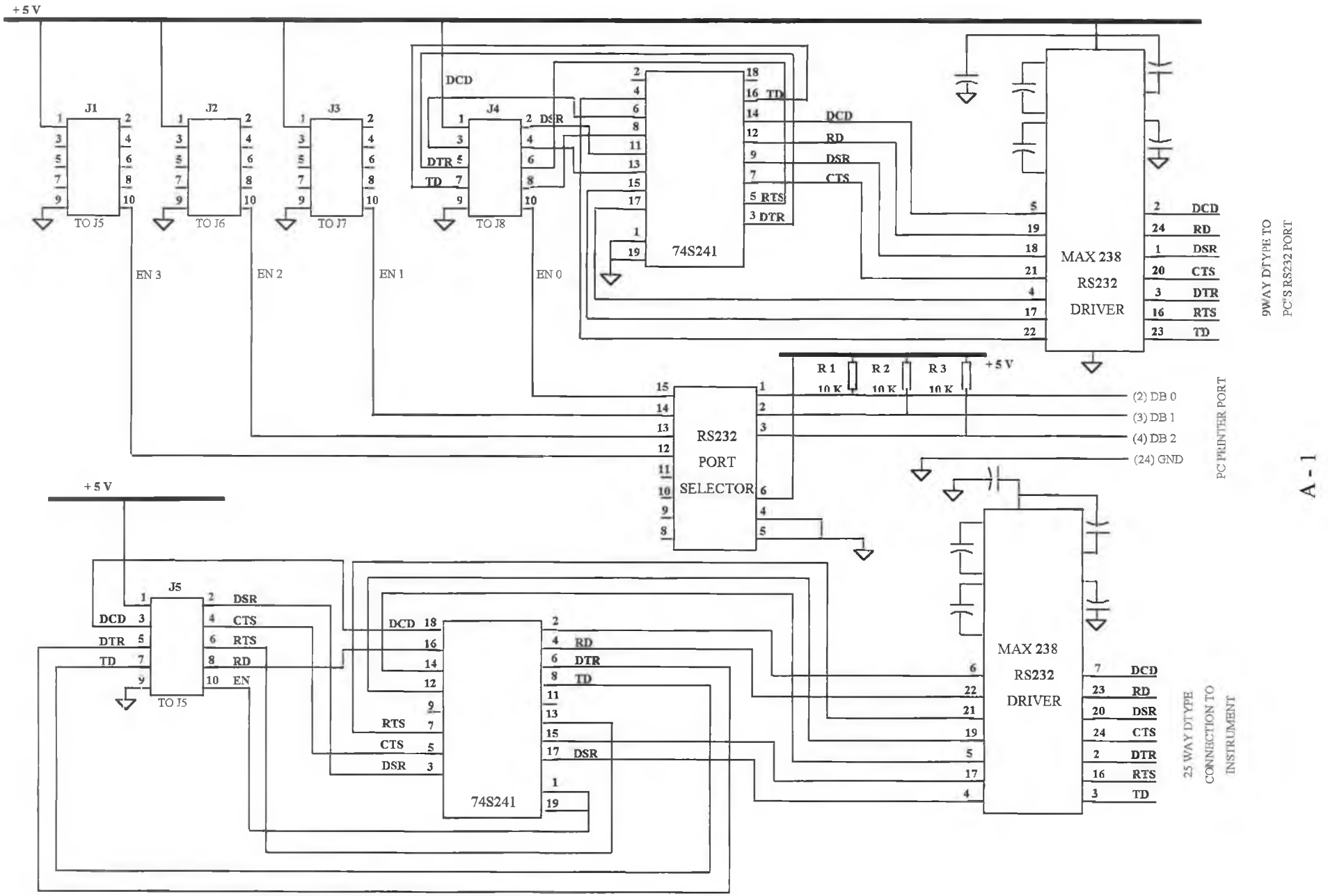
+5 V
J1
J2
J3
J4
TO J5
TO J6
TO J7
TO J8
DCD
DSR
DTR
TD
EN 3
EN 2
EN 1
EN 0
74S241
RTS
CTS
RD
MAX 238
RS232
DRIVER
9WAY DTYPE TO
PC'S RS232 PORT
R 1
R 2
R 3
10 K
RS232
PORT
SELECTOR
(2) DB 0
(3) DB 1
(4) DB 2
(24) GND
PC PRINTER PORT
J5
EN
25 WAY DTYPE
CONNECTION TO
INSTRUMENT

A - 1

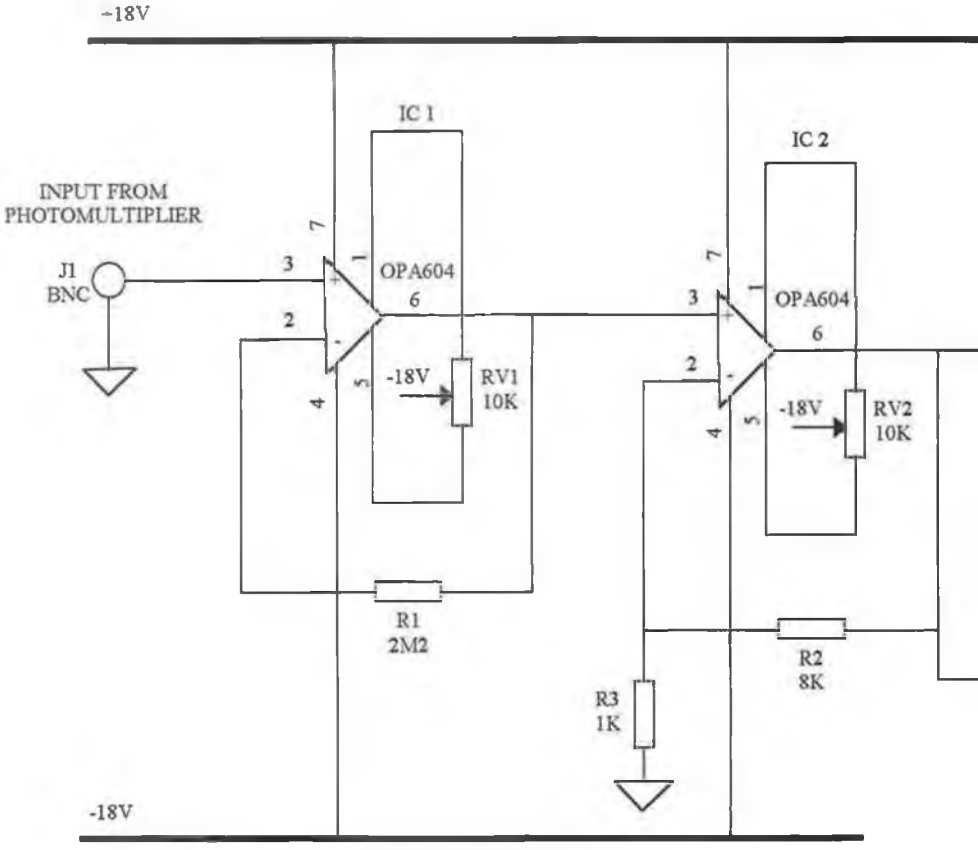
-18V
IC 1
IC 2
INPUT FROM
PHOTOMULTIPLIER
J1
BNC
OPA604
6
OPA604
6
-18V
RV1
10K
-18V
RV2
10K
R1
2M2
R2
8K
R3
1K
-18V

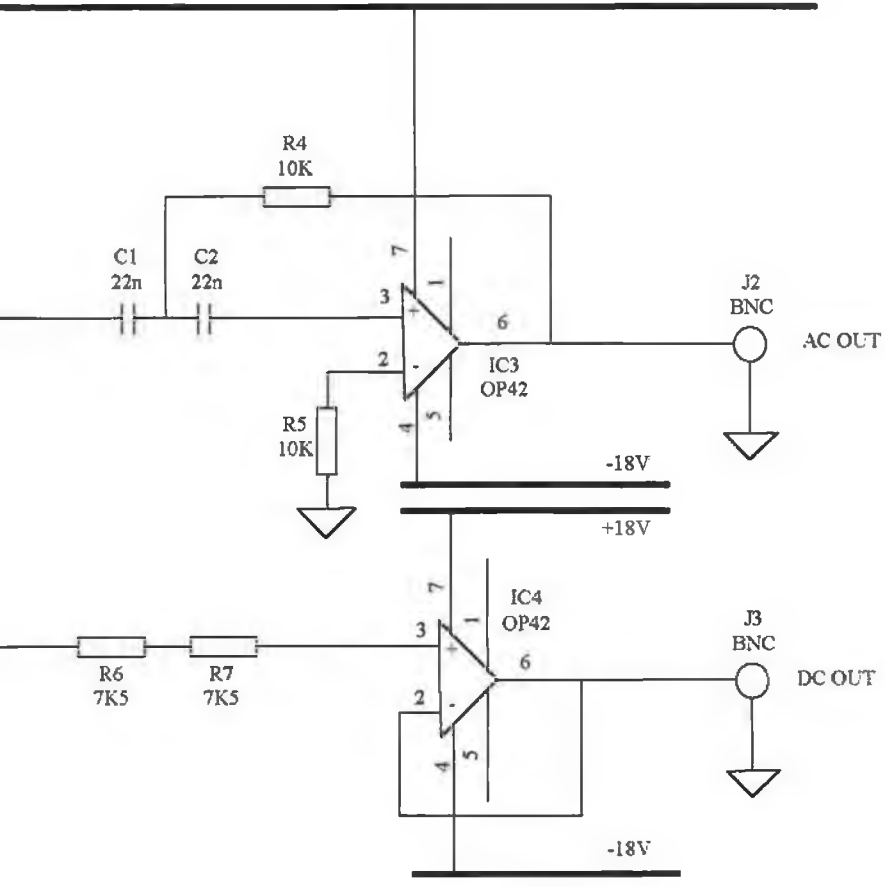
R4
10K
C1
22n
C2
22n
J2
BNC
AC OUT
IC3
OP42
R5
10K
-18V
+18V
IC4
OP42
J3
BNC
DC OUT
R6
7K5
R7
7K5
-18V